UNIVERSITY OF BIRMINGHAM

MODELLING AIR POLLUTION WITHIN A STREET CANYON

by

JIAN ZHONG

A thesis submitted to the University of Birmingham
for the degree of DOCTOR OF PHILOSOPHY

School of Geography, Earth and Environmental Sciences
College of Life & Environmental Sciences
University of Birmingham

September 2015

Abstract

A street canyon is a typical urban configuration with surrounding buildings along the street, where emissions from vehicles are normally released. Buildings are the artificial obstacles to the urban atmospheric flow and give rise to limited ventilation, especially for deep street canyons. This study implements a large-eddy simulation (LES) coupled with a reduced chemical scheme (the LES-chemistry model) to investigate the processing, dispersion and transport of reactive pollutants in a deep street canyon. Spatial variation of reactive pollutants are significant due to the existence of unsteady multiple vortices and pollutant concentrations exhibit significant contrasts within each vortex. In practical applications of using one-box model, the hypothesis of a well-mixed deep street canyon is shown to be inappropriate. A simplified two-box model (vertically segregated) is developed and evaluated against the LES-chemistry model to represent key photochemical processes with timescales similar to and smaller than the turbulent mixing timescale. The two-box model provides the capability of efficiently running a series of emission scenarios under a set of meteorological conditions. In addition, a box model with grid-averaged emissions of street canyons is compared with a two-box model considering each street canyon independently (horizontally segregated) to evaluate uncertainties when grid-averaged emissions are adopted in a grid-based urban air quality model. This study could potentially support traffic management, urban planning strategies and personal exposure assessment.

Acknowledgements

I would like to express my deepest gratitude to my supervisors, Xiaoming Cai and William James Bloss, who have provided excellent PhD supervision. I am thankful to them for giving me constant inspiration and excellent guidance, which have immensely helped me in completing this research work involving both atmospheric dynamics and chemistry. I would like to appreciate Dr Vivien Bright for provision of the Reduced Chemical Scheme (RCS). Many thanks to the University of Birmingham's BlueBEAR HPC service for providing the computational resources. Thanks are also due to Paul Hatton, Simon Thompson, Laurence Hurst for their support and advice of using the BlueBEAR HPC service. I would like to thank Chris Greenshields in the OpenCFD Limited for the providing OpenFOAM advanced training courses. Thanks are also due to Waichi Cheng (Wind Engineering and Renewable Energy Laboratory, Switzerland), Zhengtong Xie (University of Southampton), Hassan Hemida (University of Birmingham) for their advice of OpenFOAM code implementation. I am thankful to Gretchel Coldicott and Jamie Peart for their administrative support to complete a PhD. Thanks to the University Graduate School for providing useful training courses (e.g. Academic writing-Starting to write for your PhD and Time management). Special thanks are to the University of Birmingham for the award of a Li Siguang Scholarship, which is offered in partnership with the China Scholarship Council. Finally, I would like to thank my parents, Jinghua Zhong and Meilan Li, my wife, Congcong Li and the rest of my family for all their supports and encouragement during my overseas study.

Table of Contents

List of symbols

Italicised Alphabets

c_i	Concentration of the i^{th} chemical species
$\overline{c_i}$	Resolved-scale concentration of the i^{th} chemical species
C_{bi}	Background concentration of i^{th} species for box model
$C_{i,m}$	Concentrations of i^{th} species in the box m
C_k	One-equation turbulence sub-grid scale model constant (0.094)
C_ε	One-equation turbulence sub-grid scale model constant (1.48)
Da	Damköhler number
$de_{[pss]}$	Photostationary state defect
E_i	Emission of the i^{th} chemical species
E_{rs}	Resolved-scale turbulent kinetic energy
$E(f)$	Spectra for the turbulent kinetic energy
E	Emission rate
f	Frequency
F_{adv}	Vertical advective flux
F_{turb}	Vertical turbulent flux
F_{total}	Vertical total flux
G	Filter function
H	Building height
I_S	Intensity of segregation
j	Photolysis frequency

k	Reaction rate coefficient
k_{eff}	Effective reaction rate coefficient
k_{ϕ}	Kurtosis of any quantity ϕ
k_{SGS}	Sub-grid scale turbulent kinetic energy
L	Building length
L_i	The chemical loss rate of the i^{th} chemical species
$\hat{n}$	Unit vector normal to the wall
nc	Total number of the chemical species
P_i	Chemical production term of the i^{th} chemical species
PO_3	Ozone production rate
$\overline{p}$	Filtered kinematic pressure
Re	Reynolds number
RJ	Shading ratio coefficient
Sc	Schmidt number (0.72)
s_{ϕ}	Skewness of any quantity ϕ
S_{ij}	Resolved-scale strain rate
t	Time
T_{mix}	Turbulent mixing timescale
T_{chem}	Chemical timescale
$\overline{u}_i$	Filtered velocities
$\overline{u}_{\parallel}$	Resolved scale velocity component parallel to the wall
u_{τ}	Wall friction velocity
V_{d}	Deposition velocity

w_t	Exchange velocity
W	Street width
x_i	Spatial coordinates
z_0	Aerodynamic surface roughness length
$z_\perp$	Distance normal to the wall

Greek Letters

α	Box height ratio of the lower box
δ_ϕ	Standard deviation of any quantity ϕ
δ_{ij}	Kronecker delta
ϕ_i	Percentage of overestimation by the one-box model
ϕ	Any quantity
ε	Heterogeneity of emissions
η	Heterogeneity coefficient
τ_i	Chemical timescale of the i^{th} chemical species
τ_{ij}	Sub-grid scale stresses
κ	von Kármán constant (0.42)
υ	Kinematic molecular viscosity
υ_{SGS}	Sub-grid scale kinematic eddy viscosity
Δ	Filter cutoff width
Δ_i	Local grid spacing in the i^{th} direction
$\frac{\partial P}{\partial x}$	Large-scale kinematic pressure gradient along the x-direction
ΔS_i	Chemical source term of the i^{th} chemical species
Δt	Time step

List of abbreviations

ACH	Air exchange rate
AR	Aspect ratio
APT	Advanced Plume Treatment
BEAR	Birmingham Environment for Academic Research
BUBBLE	Basel urban boundary layer experiment
CACM	Caltech Atmospheric Chemistry Mechanism
CAMx	Comprehensive Air Quality Model with extensions
CBM	Carbon Bond Mechanism
CFD	Computational fluid dynamics
CMAQ	Community Multi-scale Air Quality
CRI	Common representatives Intermediates mechanism
DAPPLE	Dispersion of Air Pollution and its Penetration into the Local Environment
Defra	Department for Environment, food and Rural Affairs
EMEP	European Monitoring and Evaluation Programme
EU	European Union
FFT	Fast Fourier Transformation
FVM	Finite volume method
GEOS	Goddard Earth Observing System
HPC	High performance computing
IRF	Isolated roughness flow
ISL	Inertial sub-layer
LDA	Laser Doppler Anemometer
LES	Large eddy simulation

MCM	Master Chemical Mechanism
MIM	Mainz Isoprene Mechanism
ML	Mixed layer
mph	Miles per hour
MPI	Message Passing Interface
MUST	Mock Urban Setting Test
NAEI	National Atmospheric Emissions Inventory
OpenFOAM	Open Field Operation and Manipulation
OSPM	Operational street pollution model
PBiCG	Preconditioned bi-conjugate gradient
PCG	Preconditioned conjugate gradient
PCH	Pollution exchange rate
PinG	Plume-in-grid
PISO	Pressure Implicit with Splitting of Operators
ppb	Parts per billion (10^9), by volume
ppm	Parts per million (10^6), by volume
ppt	Parts per trillion (10^{12}), by volume
PSS	Photochemical steady state
QSSA	Quasi-steady state approximation
RACM	Regional Atmospheric Chemistry Mechanism
RADM	Regional Acid Deposition Model
RAMS	Regional atmospheric modelling system
RANS	Reynolds Averaged Navier Stokes
RCS	Reduced chemical scheme

RH	Reactive hydrocarbons
RNG	Renormalized-group
RPL	Region Partition Line
RSL	Roughness sub-layer
RSM	Reynolds Stress model
SAPRC	Statewide Air Pollution Research Center
SF	Skimming flow
SGS	Sub-grid scale
TKE	Turbulent kinetic energy
TORCH	Tropospheric organic chemistry experiment
TRES	Typical Real-world Emission Scenario
UBL	Urban boundary layer
UCL	Urban canopy layer
VALIUM	Validation of instruments for environmental policies
VOCs	Volatile organic compounds
WHO	World Health Organisation
WIF	Wake interference flow
WRF	Weather Research and Forecasting

1 Introduction

Air pollution associated with road transport is one of the major environmental issues in urban areas (Murena et al., 2009). The deterioration of urban air quality occurs due to the combined effects of emissions source from vehicles, dynamical processes (reduced dispersion caused by buildings) and chemical processes (evolution of reactive pollutants; formation of secondary pollutants) (Li et al., 2008b). The investigation of urban air pollution has become an interesting area for the environmental research. In this chapter, the scale and structure of the urban boundary layer (UBL) are described. Particular attention is paid to the urban canopy layer (UCL), which includes the generic geometry unit in urban areas, i.e. street canyon. Urban air pollution is also introduced with focus on air pollutants, air quality objectives and atmospheric chemical processing. Finally, the research motivation and thesis overview are presented.

1.1 Urban boundary layer

1.1.1 Scale and structure

The spatial scales can influence the major wind flow features in and above urban surface. Figure 1.1 illustrates schematic topics concerned in urban climatology depending upon the relevant spatial scales (Britter and Hanna, 2003), i.e. street scale (~100 to 200 m), neighbourhood scale (~1 to 2 km), city scale (~10 to 20 km) and regional scale (~100 to 200 km). At the street scale, the interest of aspects concerns building design, pollution dispersion and urban energy balance, which determines the physical and chemical

processes at larger scales. Larger scale processes can in turn influence those processes at smaller scales.

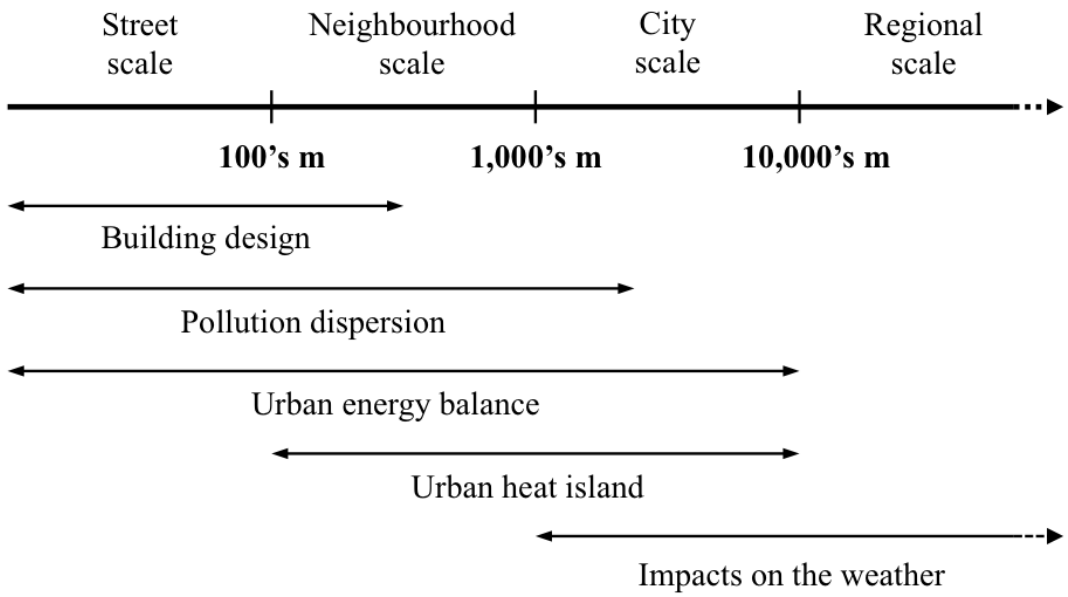

Figure 1.1 Schematic topics concerned in urban climatology to the relevant spatial scales (Britter and Hanna, 2003).

The urban boundary layer (UBL) is of interest as it is the part of the atmosphere where the majority of people dwell (Barlow, 2014). In the presence of a city with arrays of buildings (roughness elements), the urban surface is normally non-homogeneous and possesses very different climatic features from those of the countryside nearby. The UBL can be partitioned into four sub-layers (Figure 1.2) from top to bottom based on the characteristics of turbulent flow (Roth, 2000), i.e. mixed layer (ML), inertial sub-layer (ISL), roughness sub-layer (RSL) and urban canopy layer (UCL). In the ML, the atmospheric flow can be rapidly mixed and relatively independent of the frictional forces and roughness elements in urban areas. The ISL is a constant-flux layer as the vertical fluxes of flow properties are nearly uniform. The RSL is also called the wake layer or the transition layer, which contains the UCL. The flow in the RSL is significantly affected by roughness elements and

the characteristics of the canopy geometry (Oke, 1988). The UCL occupies the lowest part of the RSL (below the mean building height). The atmospheric flow within the UCL exhibits a high spatial and temporal distribution and is highly dependent upon the geometry of roughness elements. Roughness elements (mainly by arrays of buildings) of the urban surface cause considerable drag on the atmospheric flow involved, which plays an important role in determining the characteristics of the turbulence in the UBL. The micro-climates within the UCL directly involving roughness elements are very complex and poorly understood. A better understanding of the micro-climate mechanisms is of vital importance for the city design and planning.

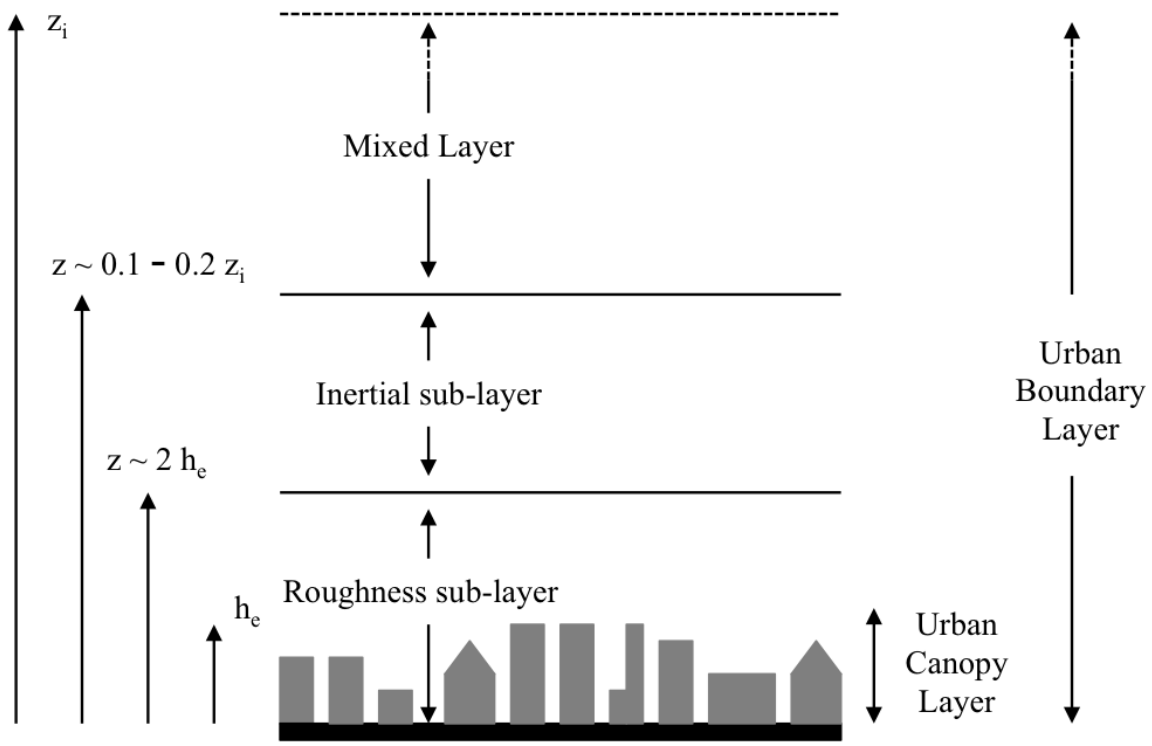

Figure 1.2 Structure of the urban boundary layer. z_i is the height of the urban boundary layer, h_e is the height of the urban canopy layer (Roth, 2000).

1.1.2 Street canyon

The street canyon forms the basic geometry unit of the built environment in urban areas, which typically describes a restricted space in an urban area with surrounding buildings, usually along both sides of a street (Jeong and Andrews, 2002). Figure 1.3 illustrates the schematic of the street canyon geometry (Yazid et al., 2014), which is normally characterized by aspect ratios, i.e. *H*/*W* (the ratio of the building height (*H*) to the street width (*W*), herein referred to *AR*) and *L*/*W* (the ratio of the building length (*L*) to the street width (*W*)). According to Vardoulakis et al. (2003), street canyons might be classified into avenue ($AR \leq 0.5$), regular ($0.5 < AR < 2$) and deep ($AR \geq 2$) street canyons or into short $(L/W \leq 3)$, medium $(3 < L/W < 7)$ and long street canyons $(L/W \geq 7)$ based on the aspect ratios. While *L* (which usually represents the distance between two street intersections) is infinitely large, this corresponds to a 2-dimensional (2D) case (without street intersections); otherwise, it is a 3-dimensional (3D) case. Depending on the differences between the heights of the upwind (H_u) and downwind (H_d) buildings in the approaching wind, street canyons can be also classified into symmetric street canyons ($H_u = H_d$) and asymmetric street canyons, which includes step-up ($H_u < H_d$) street canyons and step-down ($H_u > H_d$) street canyons. The upwind (or downwind) building is also called leeward (or windward) building. Depending on the flow direction towards a street canyon (Yazid et al., 2014), the street canyon flow can be classified into perpendicular flow, parallel flow and oblique flow (Figure 1.3). Wind speed determines the formation and intensity of vortices formed inside street canyons and its direction affects the shape of these vortices (Yazid et al., 2014). Higher wind speed tends to improve air ventilation conditions and thereby enhancing the dispersion of pollutants. Perpendicular flow (discussed below) represents

the worst-case scenario of street canyon ventilation and pollutant dispersion.

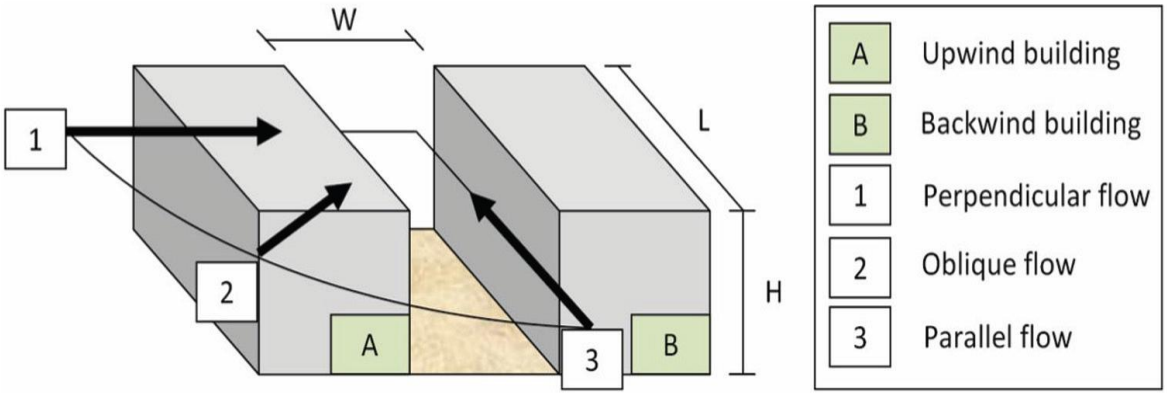

Figure 1.3 Schematic of the street canyon geometry (Yazid et al., 2014).

The most fundamental geometrical model is a single infinitely long street with buildings of the same height on both sides, i.e. the two-dimensional (2D) idealised street canyon (Liu et al., 2011). The characteristics of recirculation in a 2D idealised street canyon are strongly dependent upon the canyon aspect ratio (*AR*). Flow patterns in street canyons under neutral meteorological conditions with perpendicular approaching wind can be classified into three main regimes (Oke, 1987): isolated roughness flow (IRF), wake interference flow (WIF) and skimming flow (SF) (shown as Figure 1.4). The IRF regime is related to widely spaced buildings ($AR<0.3$). The WIF regime is associated with closer spaced buildings ($0.3<AR<0.7$). The SF regime representing the worst-case scenario for pollutant dispersion normally occurs in more tightly spaced buildings, i.e. for regular street canyons ($0.7<AR<1.5$) and deep street canyons ($AR>1.5$) (Murena et al., 2009). A single primary vortex is formed within the regular street canyon (Baker et al., 2004). There are evidences of the formation of multiple vortices within a deep street canyon (e.g. Li et al. (2009)), which may create even poor ventilation conditions for pollutants. Urban air flow pattern plays an important role in the dispersion and transport of pollutants.

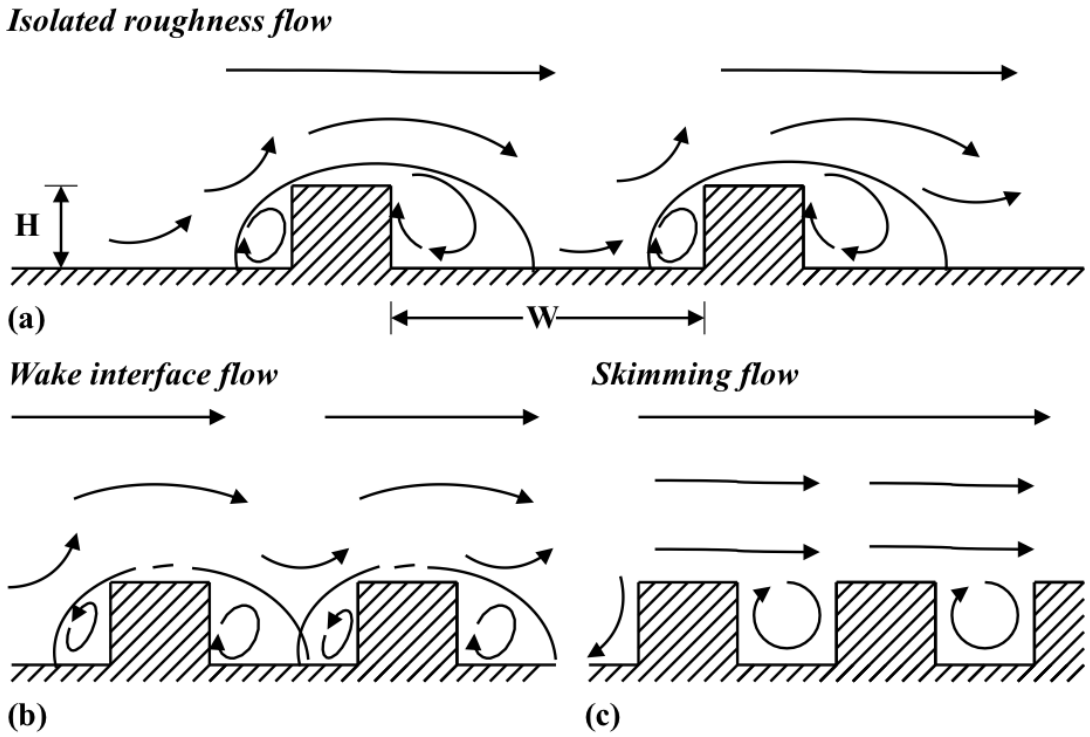

Figure 1.4 Flow regimes in urban canyons with different aspect ratios (Oke, 1987).

1.2 Urban air pollution

1.2.1 Air pollutants

Air pollutants can be classified into two categories: primary air pollutants and secondary air pollutants. Primary air pollutants (Mayer, 1999) are released directly into the atmosphere from emission sources and include mainly nitrogen oxides (NO_x), volatile organic compounds (VOCs) and carbon monoxide (CO). In urban areas, this type of air pollutants normally results from the combustion of fuels.

NO_x are produced when the oxygen (O_2) and nitrogen (N_2) react during any high-temperature combustion processes (Fenger, 1999). The major source of NO_x in urban areas

is the road transport. NO_x emitted from vehicles are mainly in form of nitric oxide (NO) with a small fraction of nitrogen dioxide (NO_2). Advanced technology in controlling the combustion processes can contribute to the reduction of NO_x emissions. NO_2 may pose adverse effects on human health, e.g. the inflammation of the airways, lung problem, respiratory symptoms, and allergens. High levels of NO_x may cause adverse impacts on vegetation and habitats resulting in the loss of biodiversity.

VOCs (including a series of organic air pollutants) in urban areas are mainly formed from incomplete combustion processes and evaporation of fuels, although globally vegetation is the largest source. VOCs may cause serious human health impacts (e.g. cancer, birth defects and dizziness) or damage to ecosystem (e.g. toxicity to plants and animals, accumulation in the food chain). Due to their toxicity, even small concentrations of VOCs are of importance. VOCs play an important role in the formation of O_3 (as O_3 precursors) and have been classified together according the ability to produce O_3 (Sahu, 2012).

CO is formed due to the incomplete combustion of carbon in fuels. Vehicle exhaust is a major source of CO. CO can influence the delivery of oxygen to the tissue from the blood in body, thereby blocking the biochemical reactions (leading to the impairment of the central nervous system). The increase of the air-to-fuel ratio and the use of catalytic converters can effectively decrease CO emissions from vehicles.

Secondary air pollutants are not emitted directly, but are produced into the atmosphere when primary air pollutants undergo chemical processes through chemical reactions (See Table 1.1 for four common forms of atmospheric chemical reactions (Jacobson, 2005), i.e. bimolecular reactions, three-body reactions, photolysis reactions and unimolecular or thermal decomposition reactions). As one of the important secondary air pollutants, ozone

(O_3) is formed by chemical reactions involving primarily the oxidation of VOCs and NO_x in the presence of sunlight. O_3 can pose an adverse impact on human health (such as an irritant to eyes, lung and nose, causing damage to airways and even death) and vegetation (such as loss of crop yields and quality, damage to trees and biodiversity).

Table 1.1 Common forms of atmospheric chemical reactions (Jacobson, 2005).

Type of reaction	Process	Notation
Bimolecular	Two reactants combine to produce two products.	$A + B \rightarrow C + D$
Three-body	Two reactants combine to form one new product. A third, inert molecule (M) stabilizes the end product and removes excess energy.	$A + B + M \rightarrow AB + M$
Photolysis	Solar radiation photon breaks a chemical bond in a molecule	$A + hv \rightarrow B + C$
Thermal decomposition	A molecule decomposes following collision with an inert molecule (M)	$A + M \rightarrow B + C$

1.2.2 Air quality objectives

In order to protect human health, air quality legislation and guidelines should be developed. The European Union (EU) Ambient Air Quality Directive and fourth Daughter Directive have established air quality limit values and target values, which must be complied with by the UK National Air Quality objectives (Defra, 2008). These air quality guidelines can be of vital importance for policy-makers to develop effective air quality strategies. The UK National Air Quality objectives and European Directive limit and target values of selected pollutants for the protection of human health are illustrated in Table 1.2 (Defra, 2008). These air quality objectives reflect health impacts of atmospheric pollutants over different duration of exposure. Both short term exposure to high levels of pollutants and long term exposure to lower levels of pollutants may cause adverse health impacts (WHO, 2000). Air quality objectives applying long term averages may be inadequate to account for real-time nonlinear fluctuations with repeated peaks for short periods, i.e. the exposure that may be typical of an urban street canyon.

According to BBC news (entitled "*Court orders UK to cut NO_2 air pollution*") published in Science & Environment in April 2015 (http://www.bbc.co.uk/news/science-environment-32512152), it was reported that "*The UK's highest court has ruled that the government must take immediate action to cut air pollution*". This case (https://www.supremecourt.uk/cases/uksc-2012-0179.html) was brought by ClientEarth (i.e. an organisation of environmental lawyers). The UK has not successfully met EU air quality limits for NO_2 targets. There were 16 areas in the UK, which have breached the EU air quality limits for NO_2 since 2010. Under existing air quality plans, some cities (e.g. London, Birmingham and Leeds) in the UK are not expected to meet EU air pollution targets until 2030. New air quality plans targeting to cut NO_2 air pollution are required to be submitted to the European Commission by the end of 2015 (Dyer, 2015).

Table 1.2 Selected UK National Air Quality objectives and European Directive limit and target values of selected pollutants for the protection of human health (Defra, 2008).

Pollutant	Concentration measured as	UK National Air Quality objectives	European obligation
NO_2	24 hour mean	200 ug m^{-3} (105 ppb) not to be exceeded more than 18 times a year	200 ug m^{-3} (105 ppb) not to be exceeded more than 18 times a year
	Annual mean	40 ug m^{-3} (21 ppb)	40 ug m^{-3} (21 ppb)
O_3	8 hour mean	100 ug m^{-1} (50 ppb) not to be exceeded more than 10 times a year	Target of 120 ug m^{-1} (60 ppb) not to be exceeded more than 25 times a year averaged over 3 years
CO	Maximum daily running 8 hour mean	10 mg m^{-3} (9 ppm)	10 mg m^{-3} (9 ppm)
Particles (PM_{10})	24 hour mean	50 ug m^{-3} not to be exceeded more than 35 times a year	50 ug m^{-3} not to be exceeded more than 35 times a year
	Annual mean	40 ug m^{-3}	40 ug m^{-3}
Particles ($PM_{2.5}$)	Annual mean	25 ug m^{-3}	Target value 25 ug m^{-3}

1.2.3 Atmospheric chemical processing

(1) NO_x-O_3 interactions

In the absence of VOCs, the atmospheric chemical processing in urban areas is dominated by NO_x chemistry. In the presence of sun light, NO_2 is rapidly photolysed leading to NO and O_3 formation, and NO can react with O_3 to re-form NO_2 through the *photochemical steady state* (PSS) reaction (there is no net production or loss of O_3) as follows (Carpenter et al., 1998):

$$NO_2 + h\nu \rightarrow NO + O(^3P) \quad (1.1)$$

$$O(^3P) + O_2 + M \rightarrow O_3 + M \quad (1.2)$$

$$O_3 + NO \rightarrow NO_2 + O_2 \quad (1.3)$$

where $O(^3P)$ is an oxygen atom without any excess energy or in its ground state and M denotes a third body molecule which absorbs excess energy so that $O(^3P)$ and O_2 may recombine to form an O_3 molecule in the presence of M. These reactions involving the NO-to-NO_2 conversion and O_3 formations are illustrated in Figure 1.5 (Atkinson, 2000). A chemical equilibrium between NO_x and O_3 can be described as:

$$j_{NO_2}[NO_2] = k_{NO+O_3}[NO][O_3] \quad (1.4)$$

where j_{NO_2} is the photolysis frequency of Reaction 1.1 which depends on the intensity of sunlight and k_{NO+O_3} is the rate constant of Reaction 1.3 which depends on temperature.

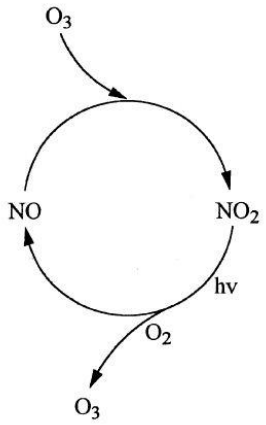

Figure 1.5 NO_x-O_3 interactions in the absence of VOCs.

(2) HO_x chemical processing

In the presence of VOCs, atmospheric chemical processing in urban areas is dominated by the interactions between highly reactive gas-phase radicals (HO_x) and NO_x chemistry. The HO_x radicals include both hydroxyl radical (OH) and hydroperoxy radical (HO_2). OH is one of the most important radicals in the atmosphere. The formation of OH is mainly due to the photolysis of O_3 in the presence of water vapour (H_2O), given as follows:

$$O_3 + h\nu \rightarrow O(^1D) + O_2 \tag{1.5}$$

$$O(^1D) + H_2O \rightarrow OH + OH \tag{1.6}$$

where $O(^1D)$ is the high-energy oxygen atoms which is able to react with H_2O to generate two OH radicals. Alternatively, $O(^1D)$ can be deactivated to $O(^3P)$ through the following reaction:

$$O(^1D) + M \rightarrow O(^3P) + M \tag{1.7}$$

OH drives the atmospheric chemical processing for daytime and initiates the degradation of a variety of VOCs (denoted as RH which is the hydrocarbons containing hydrogen (H) and carbon (C)) with high reactivity to generate organic peroxy radicals (RO_2):

$$OH + RH \rightarrow H_2O + R \tag{1.8}$$

$$R + O_2 + M \rightarrow RO_2 + M \tag{1.9}$$

OH can also react with CO to form HO_2 through following reactions:

$$OH + CO \rightarrow H + CO_2 \tag{1.10}$$

$$H + O_2 + M \rightarrow HO_2 + M \tag{1.11}$$

The fate of peroxy radicals (RO_2 and HO_2) is determined by the atmospheric environmental conditions. Under clean environments (low NO_x conditions), the self- and cross-reactions between RO_2 and HO_2 are dominant:

$$RO_2 + HO_2 \rightarrow ROOH + O_2 \tag{1.12}$$

$$HO_2 + HO_2 + M \rightarrow H_2O_2 + M \tag{1.13}$$

where ROOH represents organic hydroperoxides and H_2O_2 is hydrogen peroxide. Under polluted environments (high NO_x conditions), radical propagation takes place through a series of reactions:

$$RO_2 + NO \rightarrow RO + NO_2 \tag{1.14}$$

$$RO + O_2 \rightarrow R'CHO + HO_2 \tag{1.15}$$

where RO represents alkyl radicals and R'CHO denotes aldehydes. In the presence of NO, OH is formed through the following reaction:

$$HO_2 + NO \rightarrow OH + NO_2 \tag{1.16}$$

The radical propagation driven by NO therefore results in the conversion of NO to NO_2 (leading to the overall production of O_3 through photolysis reactions) and the increase of OH (enhancing the overall chemical processing of VOCs).

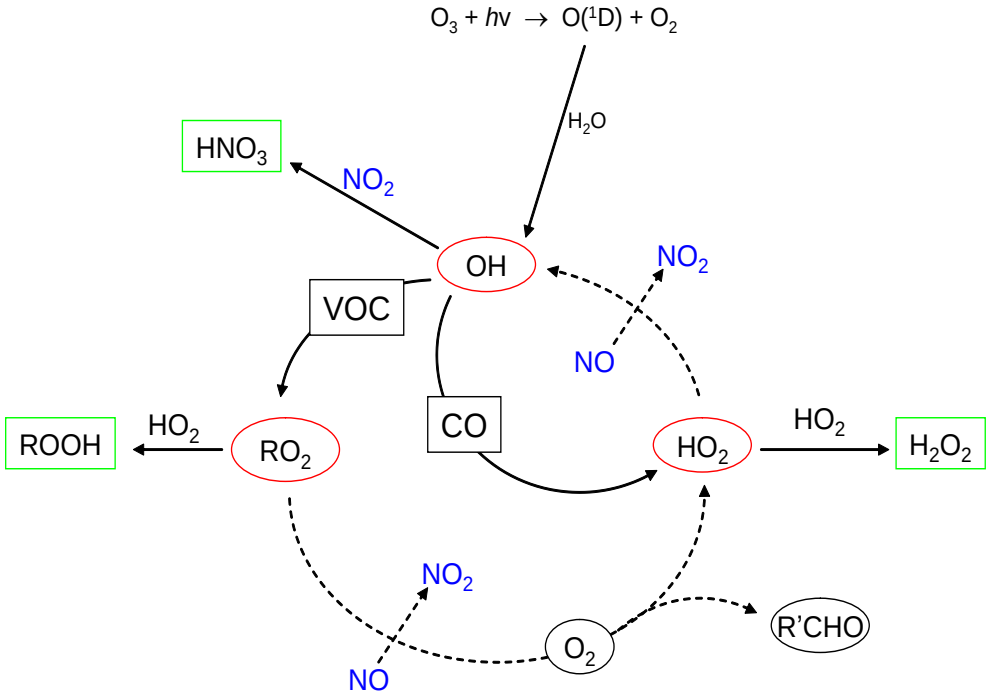

Figure 1.6 HO_x chemical processing of VOCs oxidation with the additional processing of radical propagation under polluted environments (dashed lines), adopted from Bloss (2009).

The cycle of HO_x chemical processing of VOCs oxidation (Bloss, 2009) is shown as Figure 1.6 together with the additional processing of radical propagation under polluted environments (represented by the dashed lines). This reaction cycle is limited by the removal of reactive radical species, such as the following reaction:

$$OH + NO_2 + M \rightarrow HNO_3 + M \tag{1.17}$$

where HNO_3 denotes nitric acid which is stable and highly soluble so as to be converted into condensed phase. HNO_3 is also served as the major sink of atmospheric NO_x (Dunker et al., 2014).

1.3 Research motivation

This thesis describes an investigation of air pollution at the street canyon scale. In such an atmospheric compartment, natural air ventilation through micro-scale dynamical processes is drastically constrained by surrounding buildings (Cheng et al., 2008). Buildings in urban areas are artificial obstacles to the atmospheric flow (Salim et al., 2011a) and cause insufficient ventilation for street canyons thereby leading to air pollution levels much greater than air quality objectives (Sahm et al., 2002). Emissions from vehicles, such as NO_x, CO and VOCs, are dominant among anthropogenic pollutant sources inside street canyons in urbanised areas. Many such vehicle emissions are reactive, undergoing chemical processing within urban street canyons to generate secondary pollutants such as O_3 and highly reactive radicals (e.g. HO_x). Considering the street canyon scale (short distances from emissions sources to receptors), the pollutant transport time scale is of the order of minutes and therefore chemical transformation processes of significance in street canyons are those which display comparable (or shorter) timescales. Thus, some pollutants (such as CO and many hydrocarbons), which are not significantly influenced by chemical transformation on second-minute timescales, can be regarded as passive scalars (non-reactive scalars) in the street canyon context. However, this is not the case for short-lived pollutants (such as NO_2 and O_3) and highly reactive chemical species (such as OH and HO_2). In those situations, chemical reactions must be taken into account for the prediction of pollutant abundances in street canyons.

It is recognised that the urban street canyon is the place in which the majority of the outdoor activities of the urban populations occur. These are also locations where substantial human exposure occurs, for pedestrians, road-users and occupants of adjacent buildings which may gain their ventilation from the outdoor canyon environment. Exposure to such environments tends to cause adverse public health effects (Solazzo et al., 2011). Since both primary and secondary air pollutants exhibit inhomogeneous distributions in urban street canyons and vary significantly over time, it is not an easy task to assess exposure to such pollutants. The pedestrian level (breathing height) in street canyons is expected to experience particularly high levels of pollutants due to the proximity to vehicle emissions. Pollutant abundance within street canyons frequently far exceeds that in the wider urban background; in 2005, for example, measured data at the London Marylebone Road 'super-site' showed that NO_2 hourly concentrations exceeded the hourly objective for 853 times (Defra, 2008). Those exceedences of air quality objectives normally occur near local hotspots of pollution in street canyons.

Various approaches such as field measurements, physical modelling, numerical modelling and parametric (operational) modelling have been undertaken over recent years to investigate air pollution in street canyons. Field measurements can provide first-hand information on pollutant abundance (subject to the limitations of measurement technologies), air flow and pollutant dispersion, but with several limitations (e.g. challenges to data interpretation, uncontrollable meteorological conditions, low spatial coverage, and typically high expense). Physical modelling (e.g. wind tunnels and water channels) provides insight mainly into dynamics; such approaches are able to fully control testing parameters and sampling points, and provide well-documented dataset for the evaluations of numerical models. Due to scale limitations, it is a challenge for such models

to replicate fully the large-scale atmospheric turbulence of the real world. Numerical modelling can provide high spatial and temporal distributions of flow and pollutant fields in street canyons. Such models can be repeated with controllable test parameters at relatively low economic expense. However, they normally demand a high level of computational resources and may require substantial input information (computational domain, flow characteristics, chemical schemes). Parametric modelling can provide useful time-series information regarding pollutant abundance for regulatory applications, based on semi-empirical parameterisation of street canyons. This approach is relatively simple to use and demands far less computational cost than numerical modelling. However, due to the empirical assumptions, they fail to reproduce the detailed distribution of the flow or pollutant fields in street canyons.

There are relatively few studies considering the coupling between the dynamical and chemical processes involving the pollutant mixing and transformation in street canyons (reviewed in Chapter 2). Understanding both dynamical and chemical processes of reactive pollutants in street canyons is of vital importance to effectively quantify air quality and to help the urban planners develop policies (e.g. for street canyon design and traffic management) to mitigate the adverse impacts of air pollution. This thesis aims to investigate the coupling between dynamics and chemistry in street canyons and attempts to address some key scientific issues of air pollution levels inside the urban canopy that are significantly affected by local traffic, fast photochemical reactions, and wind conditions. Two modelling approaches will be adopted in this thesis, i.e. i) a state-of-the-art numerical methodology called large-eddy simulation (LES) that resolves sub-metre turbulent eddies and sub-second air dynamics AND photochemical reactions, and ii) a box-model methodology (parametric modelling approach) that enables a quantification of the non-

linear contribution of photochemical processes to the oxidants of a controlled box due to segregation effect (chemistry) and the exchange (dynamics) between the street canyon and overlying atmospheric background.

The core research questions of this thesis are stated as follows:

1) *What is the turbulent flow pattern within a (deep) street canyon and how does it influence the turbulent mixing and chemical processes of reactive pollutants?*
2) *What are the differences in pollutant levels between the within-canyon atmosphere and the overlying background, and how are traffic emissions pre-processed by the street canyon dynamics and chemistry before entering into the overlying background atmosphere?*
3) *What is the effect of HO_x chemical processing on pollutants levels within a street canyon?*
4) *What is the human exposure to air pollutants within a street canyon environment?*
5) *What is the segregation effect due to incomplete mixing of reactive pollutants within a street canyon and how may this effect be captured?*
6) *What are the mean pollutant levels within a street canyon (exposure-related) under a variety of emission scenarios and meteorological conditions?*
7) *What are segregation effects of sub-grid heterogeneous emissions in urban air quality models if a grid-averaging parameterisation is adopted?*

In order to address these research questions, the following objectives have been completed:

1) *To develop a LES package coupled with the key chemical mechanisms providing the capability of capturing the micro-scale mixing of street-canyon turbulent flow and fast chemical reactions.*

2) *To investigate the spatial and temporal patterns of reactive pollutants in the canyon environment.*
3) *To develop a conceptual and simplistic framework for the application of the box model in street canyons considering both dynamics and chemistry.*
4) *To examine how the variation of emissions (chemistry) and exchange velocity (dynamics) influence segregation effects on pollutant levels.*
5) *To assess the misrepresentation of reactive pollutants' concentrations in street canyons by box models and to rectify the misrepresentation of emissions profile as input to urban-scale air quality models.*

1.4 Thesis overview

This thesis is structured as follows.

Chapter 2 provides a comprehensive review of the coupling between the dynamics and chemistry. The applications of dynamical modelling and the chemical mechanisms for air pollution modelling are reviewed. Several studies considering the coupling between the dynamics and chemistry are discussed.

Chapter 3 describes the LES model coupled with chemistry in a street canyon. The street canyon configurations, numerical method and model performance are presented. The evaluation of the dynamical model is also conducted.

Chapter 4 investigates the dispersion and transport of air pollutants within a street canyon. The coupling effect of dynamical and chemical processing of emissions within the street canyon is examined. Segregation effect due to incomplete mixing of air pollution within the street canyon is discussed. A two-box model coupled with chemistry is developed to

represent key photo-chemical processes with timescales similar to and smaller than the turbulent mixing timescale. The potential exposure to air pollution is assessed.

Chapter 5 extends the application of the two-box model approach (vertically segregated) in a street canyon. The two-box model provides the capability of efficiently running a series of emission scenarios under a set of meteorological conditions so that the coupling effect between the flow dynamics and chemistry can be investigated.

Chapter 6 investigates segregation effects of heterogeneous emissions in two idealised street canyons within the urban canopy layer by using two independent box models (horizontally segregated). Both dynamical and chemical effects on systematic errors in the model output are investigated.

Chapter 7 summarises the findings of this research. The implications of this research are discussed. The future directions are also proposed.

2 Literature review

Several recent studies have examined different aspects of numerical simulation of urban street canyon dynamics/pollution/chemistry. Ahmad et al. (2005) reviewed wind tunnel experiments on wind flow and pollutant dispersion patterns in street canyons; such experiments do not however examine chemical processes, i.e. only inert tracer gas is considered. Vardoulakis et al. (2003) covered a wide range of approaches of the air quality in street canyons focussing upon measurement and parametric modelling approaches, with little discussion on computational fluid dynamics (CFD) modelling. Subsequently, Li et al. (2006) conducted a separate review on CFD modelling of wind flow and pollutant transport in street canyons. Their study focused mainly on the dynamic processes of pollutant dispersion within street canyons, rather than on the chemical processes. Yazid et al. (2014) reviewed a variety of studies on the flow structure and pollutant dispersion to provide guidelines of urban planning strategies for urban developer. Although they considered the factor of chemical reactions, there were relatively limited discussion on the coupling approach of dynamics and chemistry. The dynamics-chemistry coupling approach has increasingly been applied to in the street-canyon scale (e.g. Kwak and Baik (2014) and Park et al. (2015)) with a range of related, but distinct approaches, and identifying substantial consequences for our understanding of urban street canyon pollutant abundance. It is in this context that the present chapter reviews progress in the development of coupling between dynamics and chemistry, as applied to the street-canyon air pollution modelling.

2.1 Modelling dynamics in street canyons

2.1.1 Numerical modelling

With the recent development and ongoing performance improvements in advanced computer technology, it has become feasible to apply detailed numerical modelling approaches to explore the coupling between dynamical and chemical processes involving pollutant dispersion and transformation in street canyons. Computational fluid dynamics (CFD) is a powerful numerical modelling technique to investigate experimental flow problems, to characterize air pollutant mixing processes, and to provide a detailed distribution of canyon flow and pollutant dispersion with high spatial-temporal resolution (Chang, 2006). CFD includes a series of numerical governing equations for turbulent flow and reactive pollutants dispersion, potentially involving the coupling of both dynamics and chemistry. CFD can be mainly classified into two categories based on the turbulence closure schemes: Reynolds-averaged Navier–Stokes (RANS) and Large-Eddy Simulation (LES). RANS resolves only the mean time-averaged properties with all the turbulence motions to be modelled. Thus, RANS is normally well established and computationally fast. In place of the time-averaging used in RANS, LES adopts a spatial filtering operation, which can resolve large scale eddies directly and calculates small scale eddies with sub-grid scale (SGS) models. LES usually requires more computational cost. The atmospheric turbulent flow in and above street canyons involves turbulent eddies on a variety of scales (McNabola et al., 2009). The sizes of large scale eddies are usually comparable to the characteristic length scales of atmospheric turbulent flow and more dependent on the street canyon geometries and turbulent flow boundary conditions. On the other hand, small scale eddies typically have a universal behaviour throughout the computational domain and are

more dependent on the local energy dissipation. The applications of RANS and LES in street-canyon dynamics will be discussed below.

(1) Reynolds-averaged Navier–Stokes

Reynolds-averaged Navier–Stokes (RANS) can determine the mean turbulent flow in a domain quickly and has been widely used in engineering applications. The most commonly used RANS turbulent models for the investigation of the urban canopy flow include the standard $k-\varepsilon$ (k is the turbulent kinetic energy and ε is the dissipation rate) model, the renormalized-group (RNG) $k-\varepsilon$ model, the realizable $k-\varepsilon$ model and the Reynolds Stress model (RSM). The standard $k-\varepsilon$ model is well documented and can perform well in the general structure for fully turbulent flow (Tsai and Chen, 2004). However, for the street-canyon flow, it does not predict turbulent kinetic energy with good accuracy in the regions close to the wall or to the shear layer at the canyon roof level (Sini et al. (1996); Hassan and Crowther (1998); Baik and Kim (1999)). Baik and Kim (2002) evaluated the standard $k-\varepsilon$ model using a water channel experiment (Baik et al., 2000) and then investigated the effect of inflow turbulence intensities (Kim and Baik, 2003) on the flow dispersion in the street canyon. The turbulent kinetic energy (TKE) was found to increase with an increase in turbulence intensity. Solazzo et al. (2008) employed the standard $k-\varepsilon$ model to investigate the effect of traffic-induced turbulence. Compared to a wind tunnel experiment (Kastner-Klein et al., 2001), the model performed well in terms of predicting the turbulent kinetic energy and mean horizontal velocity but showed limitations in reproducing the mean vertical velocity. The RNG $k-\varepsilon$ model modifies the standard $k-\varepsilon$ model by adding an additional source term for the ε equation in order to determine the effective turbulent dissipation close to the wall boundaries and has been successfully implemented in simulating street canyon transitional flow. Memon et al.

(2010) applied the RNG $k-\varepsilon$ model to 2D isolated street canyons on the heating situations. Compared with a wind tunnel experiment (Uehara et al., 2000), there was a good agreement with the normalized potential temperature. The model underestimated the normalized horizontal velocity at the canyon roof level (by 10%) because the effect of 3D city blocks and roughness elements in the experiment not being fully represented by the 2D model. Kim and Baik (2004) carried out a 3D CFD model coupled with the RNG $k-\varepsilon$ model to examine the wind flow in street canyons. Although their model reproduced the flow separation by buildings and reversed flow, it underestimated the TKE and wind velocity compared with a wind tunnel experiment (Brown et al., 2000). Chan et al. (2002) conducted a series of $k-\varepsilon$ model simulations to study the flow dispersion in a 2D isolated street canyon. Compared to wind tunnel experiments, the RNG $k-\varepsilon$ model was found to be optimal in their simulations. They attributed this to the analytically derived formula of turbulent viscosity in the RNG $k-\varepsilon$ model. The realizable $k-\varepsilon$ model has an improved equation for ε considering the vorticity fluctuation and provides better performance for flows involving separation, rotation, and recirculation. Tian et al. (2009) developed an idealized 3D model based on the realizable $k-\varepsilon$ model to investigate the flow dispersion around arrays of buildings. Their model captured well the secondary oval vorticity around the buildings and the air exchange between the inside and outside streets. Gromke and Blocken (2015) adopted the realizable $k-\varepsilon$ model to simulate the flow and dispersion in and above 3D street canyons with avenue-trees. Their study demonstrated the capability of the realizable $k-\varepsilon$ model to simulate the flow and turbulence involving trees. The RSM explicitly calculates the individual Reynolds stresses (poorly represented by the $k-\varepsilon$ models). Thus in theory the RSM can perform better for complex flows (e.g. street canyon flow) than the $k-\varepsilon$ models. However, the RSM is

more complex involving more terms with more uncertainties to be modelled and greater computational cost. Nazridoust and Ahmadi (2006) applied the RSM, standard and RNG $k-\varepsilon$ models to study the airflow and pollutant dispersion in 2D street canyons. The RSM generally agreed better with wind tunnel experimental data among the turbulence models used in their study. The standard $k-\varepsilon$ model and the RNG $k-\varepsilon$ model predicted similar results, which was in alignment with the findings of Chang and Meroney (2001). Koutsourakis et al. (2012) evaluated the performance of the RSM, standard $k-\varepsilon$ model and RNG $k-\varepsilon$ model in simulating the street canyon flows using six experimental datasets (i.e. Baik et al. (2000), Hoydysh and Dabberdt (1988), Depaul and Sheih (1986), Kovar-Panskus et al. (2002b), Sahm et al. (2002) and Li et al. (2008a). The model with the best performance could be any of the three turbulence models, depending on the experimental dataset. Their study demonstrated that due to the high uncertainties of both models and experiments, it was insufficient to compare only one experimental dataset when assessing the performance of a particular turbulent model.

(2) Large-Eddy Simulation

Although RANS is computationally fast and extensively adopted, there are some limitations such as handling complex geometries involving separation (e.g. building blocks), near-wall treatment and empirical model parameters. The Large Eddy Simulation (LES) approach performs better than RANS in terms of modelling accuracy for flow turbulence but has greater computational cost. With recent advances in computer technology, LES is increasingly affordable by parallel computing with high performance computers equipped with more processors and memory. LES tends to be a promising tool to investigate turbulent mixing processes for research purposes. Salim et al. (2011a)

claimed that LES could potentially serve as an alternative to experiments for prediction of street-canyon flow characteristics in urban planning.

Cui et al. (2004) developed an LES model, based on the Regional Atmospheric Modelling System (RAMS) meteorological code, to investigate turbulent flow in and above a street canyon (AR=1). Their study provided a detailed analysis of the turbulent canyon flow structure as well as the contributions of ejection or sweep events near the roof level to the momentum flux between the canyon and the boundary layer aloft. In comparison with wind-tunnel experimental data, their results showed that the LES model underestimated the momentum flux, indicated by a weaker mean primary vortex inside the canyon than that measured. They attributed this to (i) the limited domain size (which may underestimate the turbulent intensity above the canyon) and (ii) the relatively coarse mesh size near roof level where a strong wind shear and associated instability were present. Cai et al. (2008) adopted the same RAMS model to simulate the transfer characteristics of passive scalars corresponding to the area sources over the road surface, the upstream wall and the downstream wall, respectively, in a 2D street canyon. By comparing with wind-tunnel experimental data (i.e. Meroney et al. (1996) and Kastner-Klein and Plate (1999)), they demonstrated that their LES model captured the main characteristics of canyon flow and scalar dispersion. Cheng and Liu (2011) developed an LES model to investigate the turbulent flow and pollutant removal in and above 2D street canyons (AR=1). The maximum values of standard deviations for wind flow were found close to the windward corners at the roof level. In comparison with the model configuration of Cui et al. (2004) , their grid resolution was slightly coarser (by 30 %) in the streamwise direction, but their domain sizes were larger by a factor of 3, 1.5 and 2.7 in the streamwise, spanwise and vertical directions, respectively. However, the simulated intensity of the mean primary

vortex in the canyon was weaker than that of Cui et al. (2004). Therefore they claimed that increasing an LES domain size cannot fully rectify the underpredicted intensity of mean primary vortex. This comparison indicated that well-resolved shear layers at the canyon roof level with high gradients of velocities may be required and worth a thorough investigation. Liu et al. (2005) employed an LES model to investigate air exchange rate (ACH) and pollutant exchange rate (PCH) in street canyons with different aspect ratios of 0.5, 1.0 and 2.0 based on the detailed LES database by Liu and Barth (2002) and Liu et al. (2004). The ACH (PCH) was the integration of the product of instantaneous fluctuating vertical velocity (and the instantaneous pollutant concentration) over the air exchange area at the canyon roof level. It was found that more pollutants were trapped inside the street canyon near the ground with an increase of the canyon aspect ratio. The transient turbulence properties at the roof level were well represented by the ACH and PCH. Michioka et al. (2011) adopted an LES model to examine the flow and pollutant dispersion mechanism in a 2D street canyon (AR=1). Compared with wind-tunnel experiments, the LES model provided qualitatively-correct predictions of the velocity statistics but with small discrepancies when the computational domain size was smaller. They also found that the accuracy of the LES model would be improved with the increase of the streamwise domain size, i.e. to more than 10 times than the canyon height as suggested by Kanda et al. (2004). Michioka and Sato (2012) further investigated the effect of incoming turbulent structure on the pollutant removal from 2D idealised street canyons using the same LES as Michioka et al. (2011). Their study showed that the turbulence structure of external flow influenced significantly on the turbulent kinetic energy within the canyon and the momentum exchange at the canyon roof level, but less on the mean velocity within the canyon.

(3) Comparison of RANS and LES

Walton et al. (2002) and Walton and Cheng (2002) compared LES and RANS with field measurements and found that the LES model provided the better agreement with the measurements, possibly due to the more accurate prediction in the turbulent intensities of the flow. Cheng et al. (2003) showed that both LES and RANS could predict the main features of the *mean* air flow over an array of urban buildings with reasonable accuracy although LES performed better than RANS in terms of capturing the details of the flow within the urban canopy. They reported that the computational cost of LES was about 100 times that of RANS. Xie and Castro (2006) also found that although LES better captured turbulent flow around buildings, its computational cost was at least an order of magnitude greater than that of RANS. Santiago et al. (2010) and Dejoan et al. (2010) reported that the local mean flow quantities predicted by LES were closer to the Mock Urban Setting Test (MUST) data than that predicted by RANS. Salim et al. (2011a) and Salim et al. (2011b) evaluated the performance of LES and RANS on the prediction of flow dispersion in a street canyon (AR=1) with and without avenue-like trees. They found a similar tendency in performance of LES and RANS. Trees reduced the street-canyon circulation and air exchange between the street canyon and overlying background. Tominaga and Stathopoulos (2011) applied both LES and RANS to simulation of flow dispersion in a street canyon (AR=1). LES was found to give better results than RANS compared with a wind tunnel experiment. The turbulence diffusion was well reproduced by LES, but underestimated by RANS. The performance in modelling turbulence diffusion by LES or RANS played an important role in the accuracy of pollutant dispersion predictions (Tominaga and Stathopoulos, 2010).

2.1.2 Simplified parameterisation

Although numerical modelling is able to capture temporally and spatially detailed information about dynamics in street canyons, it is still very complex and computationally expensive for many practical applications. Parametric modelling based on simple operational parameterisations about the street-canyon flow and dispersion conditions is an alternative tool, which is relatively simple and demands much less computational cost (Murena et al., 2009). Numerical modelling, in turn, can serve to better understand and provide such algorithms for implementation within parametric modelling. Detailed applications of the parametric modelling are reviewed by Vardoulakis et al. (2007) and Kakosimos et al. (2010). Here, focus will be on simplified parameterisations of dynamics in street canyons.

Turbulent exchange (transfer) between the street canyon and the overlying atmospheric boundary layer controls the pollutant abundance in the street canyon (Barlow et al., 2004) and plays an important role in parametric modelling (Murena, 2012). This phenomenon can be represented by a simplified parameter called the 'transfer velocity' (Salizzoni et al., 2009) or 'air ventilation rate' (Liu and Leung, 2008), herein referred to as 'exchange velocity' (Bright et al., 2013), denoted by w_t, which may be defined as the spatially averaged velocity responsible for exchanging mass between the street canyon and the overlying atmospheric boundary layer. A simple parameterisation of the exchange velocity can be derived from the numerical modelling of a specific street-canyon flow (if considering the street canyon as a box), e.g. Liu et al. (2005) and Bright et al. (2013). More practically in the STREET (Johnson et al., 1973) and the Operational Street Pollution Model (OSPM) (Buckland, 1998), it is assumed that the exchange velocity is proportional to the characteristic velocity in the overlying boundary layer. However, the dependence of

the exchange velocity on the street-canyon flow can be very complex and influenced by many parameters. Murena et al. (2011) investigated the effects of the external wind speed on the exchange velocity and a nearly linear relationship between them was found. Salizzoni et al. (2011) found that the turbulent exchange was dependent on the coupling between the turbulence in the shear layer and turbulent eddies in the external atmospheric flow. Caton et al. (2003) showed that under lower external turbulence, the shear layer turbulence governed the exchange processes and the linear assumption between the exchange velocity and the external wind speed can be derived, but under higher external turbulence, the exchange processes depended upon both the turbulent structure of incoming flow and that of the shear layer. Liu et al. (2011) and Solazzo and Britter (2007) investigated the effect of aspect ratio on the exchange velocity and also found a linear relationship but with a varying relationship between the exchange velocity and the external wind speed depending on the flow regimes involved.

This simplified parameterisation of turbulent exchange between the street canyon and the overlying atmospheric boundary layer represents the overall performance of the dynamics in street canyons, but necessarily fails to reproduce the flow field within street canyons. The introduction of 'exchange velocity' enables the application of parametric models (such as the box model approach) into street canyon modelling. A street canyon is considered as a single well-mixed (homogeneous) box, assuming that emissions into the box are mixed instantaneously and uniformly distributed. This simplified dynamical framework permits relatively complex chemistry to be afforded within street canyon modelling.

2.1.3 Field measurements of street canyon flows

Longley et al. (2004) carried out flow field measurements in two street canyons in Manchester, UK. In those studied street canyons (bordered by buildings with varying heights and shapes), mean canyon flow was mainly characterised by a lateral channel flow, with limited evidence of a vortex flow. Their findings indicated that simple assumptions (e.g. a vortex flow) implicit adopted by most modelling studies may not reflect the complexity of airflow and turbulence in real street canyons. There was also evidence of traffic-produced turbulence. This effect was much significant, especially for a lower vertical layer (about 3 m) close to the street ground. Their study suggested that the effect of traffic should be incorporated into street canyon modelling in order to capture realistic conditions. Smalley et al. (2008) measured turbulent flow field in a complex street canyon in York, UK, under different background wind direction conditions. There was evidence of flow channelling (for winds blowing along the street), flow recirculation (for winds blowing across the street) and helical-type flow (for oblique winds). Those findings were similar to those associated with classical 2D canyons. The TKE in the canyon was found to increase with the increase in the background TKE above the canyon. Eliasson et al. (2006) carried out a field measurement campaign to investigate wind fields and turbulence characteristics in an urban street in Göteborg, Sweden. The penetration of the roof-top shear layer was found to significantly disturb established vortex development and circulation within the street canyon, even under low wind conditions. This may be attributed to considerable turbulence caused by the complex building geometry and local topography. Mean flow in the canyon was dependent upon ambient wind directions. A helical vortex was observed in the canyon under some ambient wind directions. Dobre et al. (2005) conducted field measurements of airflow in street canyons with realistic geometries

and at an urban intersection in London, UK, during the 2003 campaign for the DAPPLE (Dispersion of Air Pollution and its Penetration into the Local Environment) project (Arnold et al., 2004). Their study demonstrated that street canyon flow could be a helical flow, which was a combination of the parallel and perpendicular contributions (i.e. a channelling vortex along the street and a recirculating vortex across the street). Each of those two vortices can be linearly dependent upon the relative component of the reference wind at the roof top. At the interaction, they found a switching of wind direction between difference streets, indicating highly complex flow. Barlow et al. (2009) presented results of both street-level and outer flow from the DAPPLE 2004 campaign. They developed a methodology for an evaluation of reference measurements. Their findings indicate that the reference measurement at the upper level (at the height of 9 H, free of local obstruction) was better than the roof-top reference measurement (at the height of H, influenced by local obstruction) to scale street canyon flow. Christen et al. (2007) analysed the dataset from the BUBBLE (Basel urban boundary layer experiment) campaign (Rotach et al., 2005) to investigate the effect of coherent structure on turbulent exchange. Their study indicated that both in-street and outer mean flow may be influenced by ambient wind directions and stability. This effect on turbulent structure was more significant above the canyon than within the canyon. They identified two types of events (i.e. sweeps and ejections), dominating turbulent exchange at the canyon roof level. Schatzmann et al. (2006) carried out the VALIUM (Validation of instruments for environmental policies) campaign in Hannover, Germany. They found wind fields were heterogeneous in real urban streets, thereby influencing long-range and regional flow and pollutant dispersion. The velocity data was affected by ambient wind directions and the building structure.

In a real urban environment, there are a variety of geometrical arrangements of surrounding building blocks around urban streets. Those buildings normally vary in roof shapes, heights and structure. Complex, non-uniform geometries are very different from simple assumptions of idealised geometries, which are usually used in a number of modelling studies. The associated flow field in such a real urban environment could be very complex and uncontrollable (Smalley et al., 2008), influenced by many factors (e.g. complex building geometries, real-time ambient wind directions, atmosphere stability and inflow turbulence). Despite complex flow structures, along-street flow channelling and across-street flow recirculation could still be the dominant flow characteristics under most ambient wind directions conditions (Boddy et al., 2005).

2.2 Chemistry for air pollution modelling

Modelling dynamics in street canyons, which determines the evolution and physical removal of atmospheric pollutants, is only one component of the coupling approach of dynamics and chemistry. The representation of atmospheric chemistry for air pollution modelling also plays an important role for reactive species. A chemical mechanism describes mathematically the chemical processes in the atmosphere by describing a set of chemical reactions for the removal and formation of primary and secondary chemical species (Jimenez et al., 2003) and will be discussed below.

2.2.1 Simple NO_x-O_3 chemistry

Simple NO_x-O_3 chemistry (Carpenter et al., 1998) describes the photochemical reactions between NO, NO_2 and O_3, the interaction of which is discussed in Section 1.2.3. NO_x emitted from vehicles into street canyons is predominantly in form of NO with a small (but in many environments increasing) fraction of NO_2. Within urban environments, the NO_x-

O_3 titration interaction with freshly emitted NO can result in a significant local sink for O_3 in street canyons, providing a reduction of O_3 level compared with surrounding rural areas. This effect is called the "urban decrement" (Munir et al., 2013). Due to its simplicity, the simple daytime NO_x-O_3 system has been adopted in parametric modelling, e.g. OSPM (Berkowicz, 2000) and ADMS (McHugh et al., 1997). The incorporation of such simple NO_x-O_3 chemistry into street canyon dynamics model can also be affordable especially for expensive LES approaches (e.g. Baker et al. (2004)).

2.2.2 Complex chemistry

Simple NO_x-O_3 chemistry only accounts for daytime NO_x-O_3 interactions, without consideration of other NO_y species, nighttime processing, and the oxidation of VOCs. Therefore, more realistic chemistry involving detailed inorganic and VOCs reactions should be also considered for a comprehensive description of the urban atmosphere. Such representations may include the reactions of radical species (HO_2, RO_2) which may result in additional (non-O_3) conversion of NO to NO_2, and hence to net ozone / oxidant production, that cannot be captured by the simple NO_x-O_3 chemistry. There are a wide range of mechanisms (from near-explicit to reduced mechanisms) with varying complexity considering both the NO_x and VOCs chemistry which have been applied in street canyon studies, and which are briefly discussed below.

(1) MCM

The Master Chemical Mechanism (MCM) is a near-explicit chemical mechanism, representing in detail the gas-phase tropospheric degradation of primary VOCs and formation of (gaseous) secondary pollutants (Jenkin et al., 1997). The MCM v1.0 consists of over 2,400 species and 7,100 reactions describing the degradation of 120 VOCs

(Derwent et al., 1998). The MCM v2.0 updates the chemistry of aromatic hydrocarbons and includes 3,487 species and 10,763 reactions (Whitehouse et al., 2004). To improve the chemical degradation of aromatics (Jenkin et al., 2003), the MCM v3.0 was developed, containing 12,691 organic reactions for 4,351 organic species, and 46 inorganic reactions (Saunders et al., 2003). To promote the understanding of aromatic photo-oxidation (Bloss et al., 2005), MCM v3.0 was updated to MCM v3.1, which comprises about 13,500 chemical reactions and 5,900 species (Pinho et al., 2007). The MCM has been evaluated against an extensive experimental database from photochemical reaction chambers and field campaigns. Due to its near-explicit nature, the MCM is principally employed within box models, and is usually considered too expensive for 3D grid-based air pollution models. For such applications, it is necessary to develop reduced chemical mechanisms which are of an appropriate size, and yet which retain a quantitative description of the atmospheric chemistry. The MCM may also be considered as a reference or benchmark mechanism for developing and evaluating such reduced chemical mechanisms. Reduced techniques include lumping, sensitivity analysis and timescale analysis approaches (Neophytou et al., 2004). The lumping technique condenses several unique species into single ones (Makar and Polavarapu, 1997) and has been the most frequently employed approach to the reduction of chemical mechanisms. Three approaches are commonly used (Zaveri and Peters, 1999), i.e. surrogate species, lumped molecule (lumping VOCs into a series of categories according to similarity of oxidation reactivity) and lumped structure (lumping VOCs according to their chemical nature as reflected in their molecular structures). The sensitivity analysis technique, also called ‘‘iterative screening and structure analysis’’, uses chemical reaction and sensitivity analysis to indentify sensitive or key species by calculating concentrations of some species as a function of others

(Mauersberger, 2005). Timescale analysis removes fast-reacting “steady-state” species, replacing these with calculated values, by distinguishing between “fast” and “slow” chemical time scales using the quasi-steady-state approximation (Lovas et al., 2006).

(2) CRI Mechanism

The Common Representative Intermediates (CRI) Mechanism is a reduced chemical mechanism with intermediate complexity. The CRI is derived from the reference benchmark mechanism (MCM v3.1) using a lumped structure technique (Jenkin et al., 2008) based on the assumption that the number of reactive bonds (i.e. C-C and C-H) represent the index of the photochemical ozone production potential of each VOC (Jenkin et al., 2002). Based on this simple index, a set of generic intermediates (each of which is a “common representative”) can be derived. Significantly reduced from MCM v3.1, the resultant mechanism CRI v2 consists of 1,183 chemical reactions and 434 species, but it is still too detailed to incorporate into most chemistry-dispersion models. To further simplify CRI v2, a set of reduced mechanisms (CRI v2-R1, CRI v2-R2,CRI v2-R3,CRI v2-R4 and CRI v2-R5) have been developed (Watson et al., 2008). The final reduced mechanism (CRI v2-R5) contains 555 chemical reactions of 196 species (including 22 VOCs) and is a useful reference mechanism for air quality modelling, focusing upon ozone production. Bright et al. (2013) further reduced the CRI v2-R5 and developed a Reduced Chemical Scheme (RCS), which includes 136 reactions of 51 species, for the application into an LES model at the street canyon scale.

(3) CBM

The Carbon Bond Mechanism (CBM-IV) was developed based on the lumped-structure condensation approach for chemical reactions with similar carbon bonds (C-CHO,C-C,

C=C, etc.) (Gery et al., 1989). The CBM-IV contains 81 reactions of 33 species. These species are classified into four groups: explicit organic species, organic species (carbon surrogates), organic species (molecular surrogates), and inorganic species (no lumping). Several other versions were also developed. Heard et al. (1998) compared the CBM-IV with CBM-EX (including 204 reactions and 90 species) and the reduced CBM-LEEDS (including 59 reactions of 29 species). Based on CBM-IV, Zaveri and Peters (1999) developed an extended mechanism called CBM-Z (including 132 reactions and 52 species). CBM-IV is a popular lumped-structure mechanism but does not contain some of the long-lived species and peroxy radical interactions, and has a relatively crude isoprene mechanism. Due to its compactness, CBM-IV is an attractive chemical mechanism for air quality modelling at the street canyon scale (e.g. Garmory et al. (2009); Kwak and Baik (2012); Kwak et al. (2013); Kwak and Baik (2014)).

(4) GEOS-CHEM

GEOS-CHEM (Eller et al., 2009) is a chemistry-transport model for simulating atmospheric composition in the troposphere at the global scale, using the Goddard Earth Observing System (GEOS) meteorological information (Abad et al., 2011). The chemical mechanism in the GEOS-CHEM model contains over 300 reactions of 80 species with explicit chemical schemes for main anthropogenic hydrocarbons and isoprene (Bey et al., 2001). Ito et al. (2007) developed a GEOS-CHEM Mechanism extension (GEOSito), which includes a 490 reaction scheme of 179 species accounting for a detailed representation of hydroxyl alkyl nitrates. Kim et al. (2012) has successfully applied the GEOS-CHEM photochemical scheme to a street canyon application.

(5) Generalized VOCs and NO_x Mechanism

The Generalized VOCs and NO_x Mechanism (Seinfeld and Pandis, 1998) contains 20 chemical reactions of 23 species. Although this mechanism is far from comprehensive, it maintains the key features of the VOC-NO_x chemistry thereby providing the capablity to qualitatively analyze the formation of O_3 through the conversion of VOCs and NO_x. The simple nature of this VOC-NO_x mechanism allows it to be incorporated into most air pollution models. An early attempt to implement the VOCs and NO_x Mechanism into street canyon modelling was reported by Liu and Leung (2008).

(6) Other chemical mechanisms

There are a number of other chemical mechanisms which have been applied to air pollution modelling; although not widely used in the street canyon simulations, they may have the potential for future development, and they are briefly discussed below.

The MIM (Mainz Isoprene Mechanism) developed by (Pöschl et al., 2000) is a reduced isoprene degradation scheme, using a lumped molecule technique based on the Master Chemical Mechanism. It includes 44 chemical reactions of 16 species, originally constructed for atmospheric modelling at the global scale. As MIM only includes lumped species for many compounds, it has limited capability to represent the nonlinear chemical behaviours of the tropospheric atmosphere across the parameters space, especially in the context of polluted (high NO_x) canyon conditions. Taraborrelli et al. (2009) updated the MIM into MIM2 to represent more intermediates. MIM2 includes 199 chemical reactions of 68 species and is suitable for air quality modelling at both regional and global scales. The SAPRC Mechanism (SAPRC-90) was developed by a research group at the Statewide Air Pollution Research Center (Carter, 1990). SAPRC-90 (158 chemical reactions of 54 species) is a lumped molecule mechanism, in which lumped species and reactions are used

to describe the representation of organic compounds. An updated version (SAPRC-99), which includes 198 reactions and 72 species, was developed by Carter (2000b). The latest version of SAPRC Mechanism (SAPRC-07) has a total of 339 reactions of 119 species (Carter, 2010), giving separate representation for 748 types of VOCs. The SAPRC mechanism can be used to calculate ozone reactivity scales for VOCs and predict impacts of emissions on formation of secondary pollutants. The CACM (Caltech Atmospheric Chemistry Mechanism) is a lumped-structure mechanism including a total of 361 reactions of 191 species (Griffin et al., 2002). The inorganic chemical scheme in the CACM is based on the SAPRC99, while the primary VOCs are reduced by a lumped-structure technique. CACM contains a detailed chemical scheme to characterize ozone formation and formation of semi-volatile products. The RACM (Regional Atmospheric Chemistry Mechanism) (Stockwell et al., 1997) consists of 237 reactions of 77 species revised from the Regional Acid Deposition Model (RADM2) Mechanism (Stockwell et al., 1990). RACM is a lumped-molecule chemistry mechanism to describe atmospheric chemistry on a regional scale. RACM has been coupled online with the RAMS model (Arteta et al., 2006). RACM is capable of simulating both the lower and upper troposphere from rural to urban areas. The EMEP (European Monitoring and Evaluation Programme) mechanism is related to policy studies in Europe including 148 reactions of 79 species (Gross and Stockwell, 2003). The EMEP mechanism applies a lumped molecule technique to give representations of organic compounds with a series of species of similar structure and reactivity. The EMEP mechanism is highly aggregated, and is usually only applied within the atmospheric boundary layer.

2.2.3 Comparison of chemical mechanisms

Table 2.1 shows a comparison of chemical mechanisms varying in complexity from near-explicit to highly simplified. Each of the complex mechanisms contains an "inorganic mechanism" considering O_x-HO_x-NO_x-CO-CH_4 chemistry (Emmerson and Evans, 2009), and an "organic mechanism" mainly considering the degradation of VOCs. In terms of the "inorganic mechanisms", there is not too much variability as these processes are (comparatively) well understood. The very simple NO_x-O_3 chemistry is simply extracted from the "inorganic mechanism". For more complex chemical mechanisms, the main difference depends upon the condensation scheme that reduces the number of VOC species and reactions involved. In principle, any chemical mechanisms originally developed at different scales, from global to urban, could be applied to the study of atmospheric chemistry / air pollution in street canyons (such as RCS, GEOS-CHEM, CBM-IV). However, the chemical processes represented by such mechanisms are inherently non-linear since the chemical timescales of some species are very short and others are rather long. The chemical processing varies rapidly for these species with different timescales. This chemical non-linearity leads to a number of difficulties for efficient coupling of chemistry with dynamic models, which is the focus of the next section of this review.

Table 2.1 Comparison of chemical mechanisms for air quality modelling.

Full name	Reduction type	Reference	Versions	Reaction NO.	Species NO.	Applied scale
Master Chemical Mechanisms	Near-explicit	Derwent et al. (1998)	MCM v1.0	7,100	2,400	Troposphere
		Whitehouse et al. (2004)	MCM v2.0	10,763	3,487	
		Saunders et al. (2003)	MCM v3.0	12,737	>4351	
		Pinho et al. (2007)	MCM v3.1	13,500	5,900	
Common Representative	LM	Jenkin et al. (2008)	CRI v2	1183	434	Troposphere
		Watson et al. (2008)	CRI v2-R1	1012	373	

Intermediates			CRI v2-R2	988	352	
Mechanism			CRI v2-R3	882	296	
			CRI v2-R4	643	219	
			CRI v2-R5	555	196	
		Bright et al. (2013)	RCS	136	51	Urban
Carbon Bond Mechanism	LS	Gery et al. (1989)	CBM-IV	81	33	Urban/Regional
		Heard et al. (1998)	CBM-EX	204	90	
		Heard et al. (1998)	CBM-LEEDS	59	29	
		Zaveri and Peters (1999)	CBM-Z	132	52	
Goddard Earth Observing	/	Eller et al. (2009)	GEOS-CHEM	300	80	Global
System-Chemistry		Ito et al. (2007)	GEOSito	490	179	
Generalized VOCs and NO_x Mechanism	/	Seinfeld and Pandis (1998)	/	20	23	Urban
Mainz Isoprene	LM	Pöschl et al. (2000)	MIM	44	16	Regional/Global
Mechanism		Taraborrelli et al. (2009)	MIM2	199	68	
Statewide Air	LM	Carter (1990)	SAPRC-90	158	54	Urban
Pollution		Carter (2000b)	SAPRC-99	198	72	
Research Center		Carter (2010)	SAPRC-07	339	119	
Caltech Atmospheric Chemistry Mechanism	LS	Griffin et al. (2002)	CACM	361	191	Urban
Regional Atmospheric	LM	Stockwell et al. (1997)	RACM	237	77	Regional
Chemistry Mechanism	LM	Stockwell et al. (1990)	RADM2	158	63	
European Monitoring and Evaluation Programme	LM	Gross and Stockwell (2003)	EMEP	148	79	Regional
NO_x-O_3 chemistry	/	Carpenter et al. (1998)	/	3	5	Urban

Note: LS denotes the lumped structure reduction technique. LM denotes the lumped molecule reduction technique.

2.3 Coupling dynamics and chemistry

The coupling between dynamics and chemistry plays a major role in air pollution modelling within street canyons. Several attempts have been made to deal with the dynamic and chemical complexity. Most long lived traffic-related pollutants (e.g. CO and VOCs) are dependent almost exclusively on canyon dynamical processing, rather than chemical processing, due to the much longer chemical oxidation time scale compared with the canyon dynamical time scale. Those pollutants are normally considered as passive scalar quantities. Therefore, many past studies (e.g. Cai et al. (2008); Solazzo et al. (2011); Madalozzo et al. (2014)) have only taken the transport and dispersion of passive scalars into consideration, a well-established approach avoiding complex chemical processing. More recently, studies have considered increasing chemical reactivity and complexity; those associated with the simple NO_x-O_3 chemistry and then complex chemistry involving the VOCs (shown as Table 2.2) are discussed below.

Table 2.2 Comparison of selected studies: coupling dynamics and chemistry in street canyons.

Reference	Research model	AR (H/W)	Vortex No.	Chemical mechanism	Remarks
Baker et al. (2004)	LES	1	1	NO_x-O_3 chemistry	*Significant spatial variations of NO_x and O_3 *Introduction of the photostationary state defect
Grawe et al. (2007)	LES	1	1	NO_x-O_3 chemistry	*Shading effect *A near-linear relationship between concentration differences and the reduction of the NO_2 photolysis frequency
Baik et al. (2007)	RANS	1	1	NO_x-O_3 chemistry	*Street bottom heating scenario *Budget analysis of the advection, diffusion and chemical reaction term
Kang et al. (2008)	RANS	1	1	NO_x-O_3 chemistry	*Varying the intensities of street bottom heating *Significant change in pattern of the flow and pollutant dispersion
Tong and Leung (2012)	RANS	0.5-8	Varying	NO_x-O_3 chemistry	* Different diurnal heating scenarios * Varying canyon aspect ratios
Kikumoto and Ooka (2012)	LES	1	1	NO_x-O_3 chemistry	*Contrasted transport mechanism for NO_x and O_3 *Correlation of concentration fluctuations
Liu and Leung	Box model	0.5,1,2	Box	Generalized VOCs-	*O_3 sensitivity to the NO_x and VOCs

(2008)				NO_x mechanism	emissions * One-box chemsitry model * Parameteriaed air ventilation rate
Garmory et al. (2009)	RANS	1.2	1	NO_x-O_3 chemistry and CBM-IV	*Field Monte Carlo method for turbulent reacting flow simulation *Segregation effect and micro-mixing
Kim et al. (2012)	RANS	1	1	NO_x-O_3 chemistry and GEOS-Chem	*An online photolysis frequency calculation module *Consideration of dry deposition and PM.
Kwak and Baik (2012)	RANS	1	1	CBM-IV	* Dispersion type of reactive species *O_3 sensitivity to the NO_x and VOCs emissions
Kwak et al. (2013)	RANS	1 - 2	1 - 2	CBM-IV	* Photochemical evolution * O_3 and OH oxidation processes
Bright et al. (2013)	LES, Box model	1	1	NO_x-O_3 chemistry and RCS	* Segregation effect * Comparion with box model * Atmospheric "pre-processing"
Kwak and Baik (2014)	RANS	1	1 or 2	CBM-IV	* Surface heating *Diurnal variation of NO_x and O_3 exchange

2.3.1 Coupling with simple NO_x-O_3 chemistry

For relatively short-lived traffic-related pollutants (e.g. NO_2 and O_3), the assumption of passive scalars is inappropriate because their chemical time scales are comparable to the canyon dynamical time scale. The chemical processing of NO_x and O_3 can play a key role in determining the spatial and temporal variation of these species in street canyons. Therefore, simple NO_x-O_3 chemistry was incorporated into the canyon dynamical model.

The first attempt of this approach can be found in Baker et al. (2004). They introduced simple NO_x-O_3 chemistry into an LES model based on the RAMS numerical code under neutral meteorological conditions and examined the dispersion and transport of reactive pollutants (NO, NO_2 and O_3) inside a regular street canyon (AR=1). The distributions of pollutants exhibited significant spatial variations dominated by a primary vortex in the street canyon, which agreed well with a previous field observation (Xie et al., 2003). The concept of the photostationary state (PSS) defect (See Section 4.2.4 for its definition) was introduced. The results of PSS defect showed that the chemistry was close to equilibrium

within the primary canyon vortex, but far from equilibrium at the canyon roof level and near traffic emissions where two air parcels with distinctively different chemical compositions meet. The PSS defect was shown to be a useful measure of reactive mixing in and above a street canyon. Their study highlighted the impact of chemical processing in the street canyon context, providing the basis of coupling reactive species. However, only a very limited chemistry was considered.

Grawe et al. (2007) extended the overall framework of Baker et al. (2004) to the investigation of the local shading effects of windward and leeward walls on the NO_2 and O_3 concentrations. This study found that kerbside NO_2 and O_3 concentrations had more than 6 ppb difference due to the presence of local shading and that the magnitude of concentration differences exhibited a near-linear relationship with the reduction of the photolysis frequency of NO_2 for shaded regions. The shading geometry was found to influence the spatial pollutant distribution within the canyon, rather than the overall abundance. Their study indicated that such shading effects can be extremely significant in deep street canyons. Only the effect of solar radiation on the chemical reaction rate (i.e. the NO_2 photolysis frequency) was investigated in this study.

Baik et al. (2007) carried out a RANS model (the RNG $k-\varepsilon$ model) coupled with simple NO_x-O_3 chemistry to examine the dispersion of reactive pollutants within a street canyon (AR=1) with bottom heating. The reaction rate constants and photolysis rates were temperature-dependent in this study, while constant values were used in Baker et al. (2004). An oscillation of the primary vortex was found in the street canyon when bottom heating was introduced and this caused significant variations of chemical species. This study found that the averaged temperature, NO and NO_2 concentrations had the same trend of oscillation, but opposite in sign to that of the O_3 concentration. The main features of the

PSS defect was found to be consistent with Baker et al. (2004). A budget analysis showed that the advection or diffusion term was much higher than the chemical reaction term for NO and NO_2, but comparable to each for O_3. This budget analysis provided useful insight into the impact of chemical processing vs. dynamical processing of each species on the overall distributions and the findings indicated that the distribution of O_3 was more affected by the inhomogeneous temperature in street canyons through chemistry. Although this study considered the effect of heating on both the dynamical process (changing the flow pattern) and chemical process (temperature-dependent chemical reaction rates), it was restricted to one typical street bottom heating scenario.

Kang et al. (2008) further investigated the effect of street bottom heating (varying the intensities of street bottom heating) on the flow and reactive pollutant dispersion using the same framework as Baik et al. (2007). They found that the centre of the primary vortex varied with the street-bottom heating intensity and thereby lead to a significant variation of chemical species abundance. The evolution of the canyon-averaged NO concentration under different heating intensities was found to have three types of patterns (i.e. quasi-steady, oscillatory and fluctuating). Canyon-averaged pollutant concentrations tend to decrease with the increase in the street bottom heating intensity. The effect of street bottom heating on the concentration of O_3 through temperature-dependent chemical reaction rates increases with the increase of the street bottom heating intensity, but this influence through chemical processing was small. These findings demonstrated that these canyon-averaged patterns were mainly due to the dynamics influenced by street-bottom heating rather than the chemical processing. However, experimental data were not available for the evaluation of pollutant concentrations in the street-bottom heating canyon.

Tong and Leung (2012) developed a RANS model (the RNG $k-\varepsilon$ turbulence model) coupled with simple NO_x-O_3 photochemistry to examine spatial characteristics of reactive pollutants and level of chemical equilibrium in idealized street canyons with aspect ratios varying from 0.5 to 8 under different ambient wind speeds and diurnal heating scenarios. The performance of this street canyon model under bottom heating on flow and temperature fields was evaluated both experimentally (Uehara et al., 2000) and numerically (i.e. Kim and Baik (2001); Xie et al. (2006) and Memon et al. (2010)), and a satisfactory agreement was found. The entrainment of O_3 from the overlying background into the canyon was found to be highly dependent upon the wind speed and canyon aspect ratios. The PSS defects approached to zero (reaching chemical equilibrium) more easily for the deeper street canyons. They also found that the diurnal heating scenario significantly affected the pollutant exchange between the canyon and overlying background through the vortex circulation and chemical reaction rates influenced by thermal effect. The information about the general principle of the effects of canyon aspect ratios, wind speed and diurnal heating provided by their study could be very useful in guiding future lab / field measurements of air pollutants within street canyons.

Kikumoto and Ooka (2012) investigated the characteristics of reactive pollutants dispersion within a regular street canyon (AR=1) by performing an LES model coupled with a sole bimolecular chemical reaction (O_3 + NO→product) (i.e. basically simple NO_x-O_3 photochemistry). Their study indicated that the chemical reaction rate was dependent on both the product of the reactants' mean concentrations and the correlation of their concentration fluctuations, which can be derived from the LES model. RANS usually considers only the mean term and omits the correlation term. In this aspect, LES can perform better than RANS by providing additional turbulent fluctuations. NO_x and O_3 had

contrasting mechanisms of transport and the correlation between each reactant's concentration fluctuations strongly influenced the rates of chemical reaction between them, especially at the canyon roof level. Their study provided a detailed analysis of turbulent fluctuations of pollutants and the impact on the reaction rate.

2.3.2 Coupling with complex chemistry

For very fast chemical species (e.g. OH, HO_2), although these species are not emitted directly from vehicles, they play an important role in driving the chemical cycle of VOCs degradation (O_3 precursors) leading to the additional conversion of NO to NO_2 (which is not represented by simple NO_x-O_3 chemistry). These species with chemical lifetimes of seconds are highly dependent on the chemical processing and react vary fast within street canyons. The complex chemical mechanisms considering both NO_x and VOCs chemistry were also introduced and incorporated into the canyon dynamic model.

Liu and Leung (2008) attempted to adopt a one-box chemistry model coupled with the generalized VOCs and NO_x mechanism (Seinfeld and Pandis, 1998) for the consideration of coupling the dynamics and chemistry in street canyons (AR=0.5, 1, 2). The values of air ventilation rates were derived from LES models for different ARs (Liu et al., 2005). They found that the O_3 concentration within the street canyon was dependent upon both the VOCs and NO_x emission rates. While the ratio of VOCs to NO_x emission rate was higher than 10, the O_3 concentration could be up to the order of 100 ppb. The emission ratio of VOCs and NO_x could be a useful indicator for controlling O_3 levels in street canyons. Because their study treated the whole canyon as one well-mixed box for all ARs, the model was unable to reproduce significant contrasts of pollutant concentration between the lower and upper canyon, especially for the deep street canyon.

Garmory et al. (2009) employed the Stochastic Field method to characterise the turbulent reacting flow for the investigation of the transport and dispersion of reactive scalars within a street canyon (AR=1.2) adopting both simple NO_x-O_3 chemistry and CBM-IV mechanism. The flow field was based on the standard $k-\varepsilon$ model. The Stochastic Field method can be easily incorporated into the RANS model and capture both the means and variances together with the consideration of segregation effect on reaction rates. This statistical information was not able to be obtained from the traditional RANS models. The variance of reactive pollutants was found to be very high in the order of mean values at the canyon roof level with strong mixing. They found that for both mechanisms, there were similar predictions and no significant segregation effect (the fluctuation from the mean in their study) for most major species (e.g. NO, NO_2 and O_3). However, for some fast chemical species (e.g. OH, HO_2 etc.), there were significant differences.

Kim et al. (2012) adopted the RNG $k-\varepsilon$ turbulence (RANS) model coupled with both simple NO_x-O_3 chemistry and the GEOS-CHEM photochemical scheme to investigate transport and dispersion of reactive pollutants within a street canyon (AR=1). An online photolysis frequency calculation module was applied to account for the surface heating effect of diurnal solar radiation on the photolysis frequency. The NO concentrations predicted from simple NO_x-O_3 chemistry had a difference up to 100 ppb (i.e. the relative error was about 20%~30%) compared to those of Baker et al. (2004). They attributed this discrepancy to the different turbulence models, RANS in this study vs. LES in Baker et al. (2004). Compared with field measurements, the model over-predicted the NO concentration by a factor of 3. This big error in NO concentration was expected to decrease as the NO_x emissions became lower. There was an evidence of a significant difference in O_3 concentration between complex photochemistry and simple NO_x-O_3

chemistry, indicating the importance of additional formation of O_3 through the VOCs oxidation process. This study highlighted the important effect of photochemistry on the concentration of oxidation products (e.g. NO_2 and O_3).

Kwak and Baik (2012) employed the RNG $k-\varepsilon$ turbulence (RANS) model coupled with the CBM-IV mechanism to explore reactive pollutant dispersion within idealized street canyons (AR=1) and to investigate the O_3 sensitivity to the NO_x and VOCs emissions. According to the dispersion characteristics of NO, NO_2 and O_3 in simple NO_x-O_3 chemistry, the dispersion of species in this simulation were identified and classified into three types, i.e. NO-type, NO_2-type and O_3-type with maximum concentrations near the bottom of the street canyon, close to the centre of the street canyon, and above the street canyon. The dispersion type transition of chemical species except the NO-type was found to be highly dependent upon the ratio of VOCs to NO_x emission rates and the reactive species in the O_3-type dispersion was expected to shift into NO_2-type dispersion with the increase of the emission ratio of VOCs to NO_x. Their study showed that the OH concentration increased with an increase in VOCs to NO_x emission ratio, indicating an important role of OH via the chemical reaction cycle. The O_3 concentration was found to be negatively correlated with NO_x, reflecting a negatively NO_x-sensitivity regime for the street canyon. However, this differed from the general finding that a VOC-sensitive regime was identical for broad-scale urban areas (e.g. Lei et al. (2007); Deguillaume et al. (2008) and Song et al. (2010)). This was possibly due to the high NO-to-NO_2 ratio in the street canyon, where the NO titration of O_3 was more pronounced compared to NO_2 photolysis. Their study provided a good understanding of the dispersion type of reactive species and the O_3 sensitivity to a range of NO_x and VOCs emission scenarios for the street canyon.

Kwak et al. (2013) implemented the same RANS model and chemical mechanism as those adopted by Kwak and Baik (2012), but focusing on the photochemical evolution of reactive species within the canyons (AR=1,2). The photochemical ages of NO_x and VOCs (defined as the time-integrated exposures of an air parcel to O_3 and OH respectively) were introduced to represent the O_3 and OH oxidation processes and normalized by their background ages respectively. The normalized photochemical ages ranging from 0 (emission characteristics) to 1 (background characteristics) had the advantage of avoiding the uncertainty of calculating the averaged O_3 and OH concentrations individually. They found that both O_3 and OH oxidation processes were of vital importance for the photochemistry at the canyon-scale. O_3 was chemically reduced for the lower part, but chemically produced for the upper part of the deep street canyon (AR=2). This finding was very interesting and indicated that O_3 was not always chemically reduced in a street canyon. From a sensitivity analysis, the concentration of O_3 was found to be weakly sensitive to the wind speed. An increase of O_3 concentration was found with the increase in the ratio of VOCs to NO_x emission rates, which was consistent with Liu and Leung (2008). This finding implied that the O_3 concentration was more sensitive to the change of emissions rather than the change of dynamics. In terms of characterizing the O_3 and OH chemical processing, the idea of photochemical ages by this study was very useful for the photochemistry at the street-canyon scale and could potentially be extended to the photochemistry at the neighbourhood scale.

Bright et al. (2013) employed an LES coupled with a Reduced Chemcial Scheme (RCS) and simple NO_x-O_3 photochemistry to investigate the effects of mixing and chemical processing on the atmospheric composition in a urban street canyon (AR=1). A one-box chemistry model was also adopted for the comparison with the LES coupled chemistry

model to assess the effect of dynamical and chemcial processing. The LES coupled chemistry model was found to underestimate the concentrations of NO_x, OH and HO_2, but overestimate the concentration of O_3 averaged over the whole canyon compared to the one-box chemistry model. The segregation effect caused by the incomplete mixing was found to reduce the overall canyon-averaged rate and be responsible for the spatial inhomogeneity of reactive species. It was shown that the RCS scheme predicted higher levels of NO_2 and O_3, but a lower level of NO compared with simple NO_x-O_3 photochemistry. This can be explained by the additional NO to NO_2 conversion through VOCs oxidation chemistry. Their study provided a better understanding of the atmospheric "pre-processing" of emissions from the street canyon to the wider overlying background.

Kwak and Baik (2014) adopted the RNG $k-\varepsilon$ turbulence (RANS) model coupled with the CBM-IV mechanism to examine the removal and entrainment of reactive pollutants at the canyon roof level via the diurnal variation of NO_x and O_3 exchange between the 2D street canyon (AR=1) and overlying background. In the morning, there were two conter-rotating vortices found in the street canyon because the heating of downwind wall was relatively stronger than that of upwind wall. Therefore, the NO_x and O_3 exchange was found to be dominant by turbulent flow. However, in the afternoon, only one intensified primary vortex was found because the heating of downwind wall was relatively lower than that of upwind wall. The turbulent flow became comparable to the mean flow in terms of the NO_x and O_3 exchange. Their findings indicated that the exchange velocities were strongly dependent on both the flow pattern induced by surface heating and the photochemistry in the street canyons. This study considered idealised scenerios with constant model parameters and simple representations of shadow, rather than realistic scenerios.

Simple NO_x-O_3 chemistry plays an important role in the street canyon chemistry. The NO_x-O_3 photostationary state defect is a useful measure of reacting mixing in the street canyon environment. Due to its simple nature, Simple NO_x-O_3 chemistry can easily be coupled with either LES or RANS models. Complex chemical mechanisms involve detailed VOCs oxidation reactions driven by fast radicals (e.g. OH and HO_2), leading to additional NO to NO_2 conversion (non-O_3). In this sense, complex chemical mechanisms are more realistic than simple NO_x-O_3 chemistry. However, due to large amounts of chemical reactions and species, more efforts need to be spent when incorporating a complex chemical mechanism into numerical models. LES models perform better in terms of the turbulent mixing of pollutants within street canyons, but require much more computational cost than RANS. LES can be used to investigate the detailed mechanism of pollutant dispersion and transport (e.g. Baker et al. (2004); Bright et al. (2013)), with higher (e.g. for NO_x) or lower (e.g. for O_3, OH and HO_2) concentrations in the canyon than those at the overlying background. RANS provides the capability to run quickly for a few scenarios, such as varying intensities of street heating ambient wind speeds, canyon aspect ratios and emissions (e.g. Kang et al. (2008); Tong and Leung (2012); Kwak and Baik (2012); Kwak et al. (2013)),. With simplified parameterisation of street canyon air ventilation, box models can be run very quickly for a series of wind conditions and emission scenarios (e.g. Liu and Leung (2008)) so that complex chemical mechanisms are affordable for street canyon chemistry modelling.

2.4 Modelling concerns

2.4.1 Street canyon geometry

Street canyon geometry plays an important role in determining flow patterns and pollutant dispersion within street canyons. The AR (aspect ratio) influences the number of primary re-circulations formed inside a street canyon and the higher the AR is, the larger the number of primary re-circulations will be. A single primary vortex is formed within regular street canyons (e.g. Baker et al. (2004)) and multiple primary vortices are formed within deep street canyons (e.g. Li et al. (2009); Murena (2012)). The vortices formed in street canyons influenced pollutant dispersion behaviour and the air ventilation. There was evidence that higher concentrations of pollutants were favourable to the street canyon with higher aspect ratios. Liu et al. (2004) showed that the percentages of pollutants residing inside street canyons (compared to the total pollutants in the computational domain) with aspect ratios of 0.5, 1.0 and 2.0 were about 95%, 97% and 99%, respectively. This implied the effect of canyon aspect ratio on the pollutant removal from the street canyon. Li et al. (2009) found that there was a higher pollutant accumulation at the ground level in the street canyon with AR=5 compared with that with AR=3. This could be reflected by the very small wind speed at the ground level, which slowed down the dispersion of ground-level pollutant. This finding was consistent with field measurements in a deep street canyon with AR=5.7 (Murena and Favale (2007); Murena et al. (2008)), which showed that the concentration at pedestrian level in the deep street canyon could be up to three times compared to that in a regular street canyon with AR=1.

2.4.2 Meteorological conditions

Meteorological conditions including the information about ambient wind, and solar radiation significantly affect the turbulent flow and dispersion of reactive pollutants within street canyons. The ambient wind speed plays an important role in the formation and intensity of primary vortices thereby determining the pollutant retention time (defined as H/w_{t0}, H is the building height and w_{t0} is the exchange velocity defined in Section 2.1.2) for a given street canyon, while its direction influence the number and shape of primary vortices (Baik et al., 2003). Nazridoust and Ahmadi (2006) revealed that the turbulence intensity within the street canyon increased with the increase in the ambient wind speed. As the pollutant dispersion was controlled by the turbulence intensity, higher wind speed would make it effective for pollutants to be removed from the street canyon. This behaviour was also found by Huang et al. (2000). Small secondary vortices were formed at the corner of the street canyon under lower wind speed conditions, but would disappear under higher wind speed conditions. Michioka and Sato (2012) examined the effect of incoming turbulent structure on the flow and pollutant dispersion. The pollutant concentration in the street canyon decreased with the increase in the incoming turbulent intensities. The change of ambient wind direction would affect significantly the recirculation pattern of flow in street canyons (Soulhac et al. (2008); Soulhac and Salizzoni (2010); Blackman et al. (2015)) and thereby influencing the pollutant dispersion. The pollutant dispersion was more effective in the oblique flow than that in the perpendicular flow, as found in a field measurement by Kumar et al. (2008). In the presence of solar radiation, the surfaces of the street ground and buildings are heated, which will influence the atmospheric stability and chemical rate constant (e.g. Baik et al. (2007)). The flow field and pollutant dispersion in street canyons can be significantly

affected by the additional thermally induced vortices. The combination of the mechanically induced vortices by wind and the thermally induced vortices by heating could be more complicated (Xie et al., 2005). Cai (2012a) and Cai (2012b) identified two characteristic heating scenarios in a street canyon: the assisting case (both roof and upwind wall heating) and the opposing case (both roof and downwind wall heating) depending on the direction of the thermal-driven flow in relation to the wind-driven circulation. Li et al. (2012) investigated the effect of ground heating on the flow and pollutant dispersion of in street canyons with AR=0.5,1,2 and found the flow and pollutant patterns had significant changes for AR=0.5 and 2, but no significant change for AR=1. In general, the ground heating enhanced the mixing of pollutants in street canyons and the performance was similar to the assisting case.

2.4.3 Emissions

Traffic is considered to be the major source of emissions in urban street canyons. Vehicle emissions can be derived based on the traffic information and emission factors of each vehicle during a period of time. The major traffic information contains vehicle fleet composition, average speeds and traffic volumes. For the roads equipped with automatic traffic counts, this traffic information can be easily obtained. Emission rates for each emitted pollutants can be served as the input of the air pollution modelling (Boddy et al., 2005). Xie et al. (2009) compared a series of measured data for the CO concentration and traffic volumes under the same wind direction and a linear relationship between them was found. This was because CO emitted from vehicles was a relatively inert chemical species in such an environment. The NO_2/NO_x emission ratio by volume from vehicles was normally applied as 1/11 (e.g. Baker et al. (2004)) or 1/10 (e.g. Bright et al. (2013)), which reflected that the fraction of NO_2 was much lower than that of NO in the street canyon,

making the production of NO_2 through the NO titration reaction more important. However, there is evidence of an increase in NO_2/NO_x emission ratio up to 17 % (Carslaw, 2005). The O_3 concentration within street canyons is dependent upon both the VOCs and NO_x emission rates. O_3 was found to be more sensitive to the change of emissions rather than the change of dynamics.

2.4.4 Chemical transformation of pollutants

Emissions from vehicles at the ground level in the street are normally reactive, changing dramatically the chemical composition of the atmosphere in such an environment. These emissions normally undergo the chemical transformation together with the recirculation driven by the canyon flow before their escaping into the overlying atmosphere. The chemical transformation of pollutants can vary in a wide range of timescale, posing the difficulty for computationally efficiently handling chemistry coupled with dynamics at the canyon scale. The choice of chemical mechanism should be considered depending on the complexity of chemistry involved. For the street canyon modelling, there are several numerical issues because the governing equation systems are highly nonlinear, and extremely stiff especially when a wide range of lifetime scales of reactive species is involved. If the diurnal heat effect (temperature) on the chemistry is included, this will introduce extra difficulties since the reaction rates and photolysis rates are influenced through the change of solar radiation and temperature. Particular attention should be paid to the handling of fast species, e.g. applying a shorter integration time interval. Also, in the regions close to the emisisons and shear layer (which must be well-resolved), negative values of concentrations may occur due to the presence of high concentration gradient, which would affect the stability of the stiff chemical systems.

2.5 Conclusions

This chapter presented a review of air pollution modelling within street canyons focusing on the coupling of dynamics and chemistry. For dynamics, the CFD technique has become a powerful numerical tool mainly including the RANS and LES models. RANS models are, by nature, a steady-state methodology, while LES models can handle the unsteadiness and intermittency of the flow and retrieve the transient structure of turbulence flow within street canyons. The choice between them depends on the computational cost, the accuracy required and hence the application. A parameter (i.e. 'exchange velocity') representing the overall performance of dynamics in street canyons provides the capablity of handling relatively complex chemistry in the practical applications. The representation of chemistry for air pollution modelling is also an important component for this coupling approach. Simple NO_x-O_3 chemistry only accounts for the O_3 chemistry changes driven by NO_x, without consideration of VOCs processing. A wide range of chemical mechanisms with varying complexity considering both NO_x and VOCs chemistry could be potentially adopted in the street canyon chemistry. A variety of factors should be concerned such as street canyon geometry, meteorological conditions, emissions and chemical transformation of pollutants. Modelling air pollution within a street canyon requires state-of-the-art dynamic models coupled with high-quality chemistry mechanisms to simulate the concentrations and spatial patterns of key atmospheric chemical species, providing the reference information of air quality inside street canyons for policy-makers in the decision of the traffic policy and urban planning.

3 The LES-chemistry model

In this chapter, a Large Eddy Simulation (LES) model coupled with chemistry (i.e. the LES-chemistry model) is described in greater detail. The LES is a promising numerical tool to reproduce turbulent flows. The flow equations, sub-grid scale parameterisation and wall treatment in the LES model are presented. Equations for reactive pollutants, chemical mechanism, emissions and code implementation are reported. Numerical method and model configuration and initialisation are presented. The performance of parallel running of the LES-chemistry model, preliminary analysis and model evaluation for the street canyon dynamics are discussed.

3.1 The LES model

The numerical model employed to simulate the turbulent flow within and above a street canyon is based on the LES technique, which computes the larger, grid-resolved eddies explicitly and parameterises the smaller, unresolved eddies. In the LES, a spatial filtering operation is used to decompose a variable ϕ into a resolved-scale value $\bar{\phi}$ with a subgrid-scale (SGS) component $\tilde{\phi}$ superimposed on it, i.e.

$$\phi = \bar{\phi} + \tilde{\phi} \tag{3.1}$$

The mathematical description of the resolved-scale component $\bar{\phi}$ is as follows (Versteeg and Malalasekera, 2007):

$$\bar{\phi}(x_i,t)=\int_{-\infty}^{\infty}\int_{-\infty}^{\infty}\int_{-\infty}^{\infty}G(x_i,x_i^{'},\Delta)\phi(x_i^{'},t)dx_1^{'}dx_2^{'}dx_3^{'} \tag{3.2}$$

where $G(x_i,x_i^{'},\Delta)$ represents the filter function, x_i and $x_i^{'}$ are the spatial coordinates, i means the direction (i =1, 2, 3) representing the streamwise, spanwise and vertical directions respectively, and Δ is the filter cutoff width.

3.1.1 Flow equations

In this model, the incompressible turbulent flow and neutral meteorological conditions are assumed. The governing equations for fluid motion include the filtered momentum equations, i.e.

$$\frac{\partial\bar{u}_i}{\partial t}+\frac{\partial}{\partial x_j}\bar{u}_i\bar{u}_j=-\frac{\partial P}{\partial x}\delta_{i1}-\frac{\partial\bar{p}}{\partial x_i}-\frac{\partial\tau_{ij}}{\partial x_j}+\upsilon\frac{\partial^2\bar{u}_i}{\partial x_j\partial x_j} \tag{3.3}$$

and the filtered continuity equations, i.e.

$$\frac{\partial\bar{u}_i}{\partial x_i}=0 \tag{3.4}$$

where the overbar ($\bar{\bullet}$) represents the filtered quantity, $\bar{u}_i$ (i=1,2,3) are the filtered velocities, $\frac{\partial P}{\partial x}$ is the large-scale kinematic pressure gradient along the x-direction which is aligned with the background wind direction above the street canyon, δ_{ij} is the Kronecker delta, $\bar{p}$ is the filtered kinematic pressure, υ is the kinematic molecular viscosity and τ_{ij} [$=\overline{u_iu_j}-\bar{u}_i\bar{u}_j$] is the sub-grid scale (SGS) stresses. The SGS stresses describe the effect of the filtered fluctuations at the SGS scale, which cannot be resolved directly. The SGS stresses are normally parameterised by a SGS stress model.

3.1.2 Sub-grid scale turbulence model

According to the eddy viscosity model, the SGS stresses can be parameterised as:

$$\tau_{ij} = -2\upsilon_{SGS}S_{ij} + \frac{1}{3}\tau_{kk}\delta_{ij} \tag{3.5}$$

where S_{ij} is the resolved strain rate, i.e.

$$S_{ij} = \frac{1}{2}(\frac{\partial \bar{u}_i}{\partial x_j} + \frac{\partial \bar{u}_j}{\partial x_i}) \tag{3.6}$$

and υ_{SGS} is the SGS kinematic eddy viscosity, which is modelled using the one-equation SGS model as follows:

$$\upsilon_{SGS} = C_k k_{SGS}^{1/2}\Delta \tag{3.7}$$

$$\Delta = (\Delta_1\Delta_2\Delta_3)^{1/3} \tag{3.8}$$

$$\frac{\partial k_{SGS}}{\partial t} + \frac{\partial}{\partial x_i}(k_{SGS}\bar{u}_i) = 2\upsilon_{SGS}S_{ij}S_{ij} + \frac{\partial}{\partial x_i}[(\upsilon + \upsilon_{SGS})\frac{\partial k_{SGS}}{\partial x_i}] - C_\varepsilon \frac{k_{SGS}^{3/2}}{\Delta} \tag{3.9}$$

where k_{SGS} is the SGS turbulent kinetic energy (TKE), Δ_i is the local grid spacing in the i^{th} direction and the modelling constants $C_k = 0.094, C_\varepsilon = 1.048$ (which are OpenFOAM default values (OpenFOAM, 2012)).

3.1.3 Wall treatment

The LES model simulates a high Reynolds number (~10^6) turbulent flow (see Section 3.3) in a street canyon with rough surfaces and the logarithmic law of the rough-wall (Schlichting and Gersten, 2000) is applied for the near-wall treatment:

$$\bar{u}_{\parallel} = \frac{u_\tau}{\kappa} \ln \frac{z_\perp}{z_0} \tag{3.10}$$

where $\bar{u}_{\parallel}$ is the resolved scale velocity component parallel to the wall, u_τ is the wall friction velocity, κ (=0.42) is the von Kármán constant, $z_\perp$ is the distance normal to the wall and z_0 is the aerodynamic surface roughness length, estimated as 0.015 *m* (which represents one tenth of a characteristic physical length (Grimmond et al., 1998) of 0.15 *m*, e.g. window frames). u_τ is calculated by Equation 3.10 and used to derive υ_{SGS} near the wall using

$$\upsilon_{SGS} = \frac{u_\tau^2}{|\nabla \bar{u}_{\parallel} \cdot \hat{n}|} - \upsilon \tag{3.11}$$

where $\hat{n}$ is the unit vector normal to the wall.

3.2 Coupling with chemistry

3.2.1 Equations for reactive pollutants

The filtered transport equations for concentrations of reactive pollutants are:

$$\frac{\partial \overline{c_i}}{\partial t} + \frac{\partial}{\partial x_i}(\bar{u}_i \overline{c_i}) = \frac{\partial}{\partial x_i}([\frac{\upsilon + \upsilon_{SGS}}{Sc}] \cdot \frac{\partial \overline{c_i}}{\partial x_i}) + \Delta S_i + E_i \tag{3.12}$$

Here, $\overline{c_i}$ represents the resolved-scale concentration of the i^{th} chemical species, *Sc* (=0.72) is the Schmidt number (e.g. Liu et al. (2005); Cheng and Liu (2011); Liu et al. (2011)), ΔS_i is the chemical source term of the i^{th} chemical species, and E_i is the emission of the

i^{th} chemical species. The challenge to solve the transport equations for reactive pollutants is to derive the chemical source terms and will be discussed below.

3.2.2 Chemical mechanism and code implementation

A reduced chemical scheme (RCS), developed and validated by Bright et al. (2013), is used as the chemical mechanism for this LES-chemistry model. The RCS includes 51 chemical species and 136 chemical reactions. The chemistry code implementation (Extracts shown as Appendix B) is discussed below.

According to Hertel et al. (1993), the ordinary differential equations of a chemical system can be describes as follows:

$$\frac{dc_i}{dt} = P_i - L_i c_i \qquad i = 1,2,...,nc \tag{3.13}$$

Here, c_i is the concentration of the i^{th} chemical species, nc is the total number of the chemical species, P_i is the chemical production term of the i^{th} chemical species and L_i is the chemical loss rate of the i^{th} chemical species ($L_i c_i$ therefore represents its chemical loss term). Both P_i and L_i are non-negative functions of concentrations of other chemical species, i.e.

$$P_i = P_i(t, c_1, c_2, ..., c_{nc}) \tag{3.14}$$

$$L_i = L_i(t, c_1, c_2, ..., c_{nc}) \tag{3.15}$$

The chemical timescale of the i^{th} chemical species τ_i (Neophytou et al., 2004) is defined as follows:

$$\tau_i = \frac{1}{L_i} \tag{3.16}$$

It is generally known that the chemical system is stiff due to the variability (from very fast to rather slow) of the chemical time scale (Verwer and Simpson, 1995). The QSSA (quasi-steady-state approximation) algorithm has been widely used to handle with the stiff chemical system in air pollution modelling (e.g. Hesstvedt et al. (1978); Verwer and Vanloon (1994)). The QSSA algorithm is described in details below.

It is assumed that c_i^n is the concentration of the i^{th} chemical species at $t = t_n$. Then over a given time step Δt, it can be obtained that

$$t_{n+1} = t_n + \Delta t \tag{3.17}$$

Equation 3.13 can be solved analytically by the following formula:

$$c_i^{n+1} = \frac{P_i^n}{L_i^n} + (c_i^n - \frac{P_i^n}{L_i^n})e^{-L_i^n \Delta t} \tag{3.18}$$

Depending on the chemical timescales and time steps, three categories of formulae are derived (Alexandrov et al., 1997). (i) If $\tau_i < \frac{\Delta t}{10}$, it means that the chemical reaction is very fast over the given time step. The steady state at the end of the time step can be assumed and Equation 3.18 can be expressed by the following approximation,

$$c_i^{n+1} = \frac{P_i^n}{L_i^n} \tag{3.19}$$

(ii) If $\Delta t / 10 \le \tau_i \le 100\Delta t$, it means that the chemical reaction is at a medium rate over the given time step and Equation 3.18 is applied. (iii) If $\tau_i > 100\Delta t$, it means that the chemical

reaction is rather slow over the given time step and the forward Eulerian formula can be employed,

$$c_i^{n+1} = c_i^n + (P_i^n - L_i^n c_i^n)\Delta t \tag{3.20}$$

The QSSA algorithm has simple formulae and can be easily employed in large air pollution models. However, there are also some drawbacks. At each cell for each species, there are three questions related to the formulae to be determined. It demands more computational time for the air pollution model with a huge number of cells. Also, the computational cost to solve the exponential function in Equation 3.18 is expensive. Therefore, the attempt has been conducted (Alexandrov et al., 1997) to improve the performance of the QSSA algorithm. The exponential function can be rationally approximated by the following expression based on the Taylor expansion in the second order:

$$e^{-L_i^n \Delta t} \approx \frac{1}{1 + L_i^n \Delta t + 0.5(L_i^n \Delta t)^2} \tag{3.21}$$

Then Equation 3.18 can be rewritten as:

$$c_i^{n+1} = \frac{c_i^n + (1 + 0.5 L_i^n \Delta t) P_i^n \Delta t}{1 + L_i^n \Delta t + 0.5(L_i^n \Delta t)^2} \tag{3.22}$$

In this study, the chemical species in the RCS chemical mechanism can be separated into two groups, i.e. slower chemical species (e.g. NO_x and O_3) and faster chemical species (e.g. OH and HO_2). For slow chemical species, a time step of 0.03 s is adopted and Equation 3.20 is used. For fast chemical species, a smaller time step of 0.003 s is used and Equation 3.22 is calculated.

3.2.3 Emissions scenarios

Emissions sources are assumed to be two continuous line sources representing two lanes of traffic located at 2.5 m from both sides of the canyon centre at z=1 m with a Gaussian distribution (in which $\delta_x = 3\,\mathrm{m}$ and $\delta_z = 1\,\mathrm{m}$ are the values of standard deviation of the Gaussian distribution in the x- and z-direction, respectively, used to control the shape of the initial spread of the traffic emissions not resolved by the LES) so that the near-vehicle dispersion is approximated. Drawing upon the UK Road Vehicle Emission Factors (Boulter et al., 2009b), emission rates for NO_x, VOCs and CO are determined as 620, 128 and 1356 g km^{-1} hr^{-1}, respectively. This emission scenario represents an urban continuous road traffic of 1500 vehicles h^{-1} with an average speed of 30 mph for a fleet composition representing the year of 2010 (hereafter referred to a 'Typical Real-world Emission Scenario', TRES). The total emissions for NO_x, VOCs and CO applied in the LES-chemistry model are equivalent to 1000, 791 and 3593 ppb s^{-1}, respectively, which are released into a typical LES model grid (i.e. 0.3 m×1 m×0.3 m in the x- , y- and z-directions, respectively). These total emissions are then assumed to be re-distributed based on the Gaussian distribution mentioned above. The ratio of primary NO to NO_2 emission rate is 9:1, while the relative fractional VOCs emission rates are 44% for ethane (C_2H_4), 19% for propene (C_3H_6), 25% for formaldehyde (HCHO) and 12% for acetaldehyde (CH_3CHO) (assumed as mixing ratio by volume).

3.3 Model configuration and initialisation

Figure **3**.1 illustrates schematically the computational domain of an idealised deep street canyon with an aspect ratio of 2 (i.e. the building height $H = 36\,\mathrm{m}$ and the street width $W = 18\,\mathrm{m}$). The building width B is 18 m (equal halves of the buildings at both sides of the

street are included in the computational domain). The domain width L_x (=0.5B+W+0.5B) is 36 m; the domain size in y-direction L_y is 40 m, and in z-direction L_z is 112 m. The grid resolutions in the x- and y-direction are Δx = 0.3 m and Δy = 1.0 m, respectively. In the z-direction, the grid resolution is Δz = 0.3 m up to the canyon roof level at z =36 m and then gradually increases above the canyon roof level up to a maximum value of Δz =5.54 m. The total number of grid cells in the x- , y- and z-directions is 288,000 (i.e. 60×40×120) within the canyon and 192,000 (i.e. 120×40×40) above the canyon, respectively.

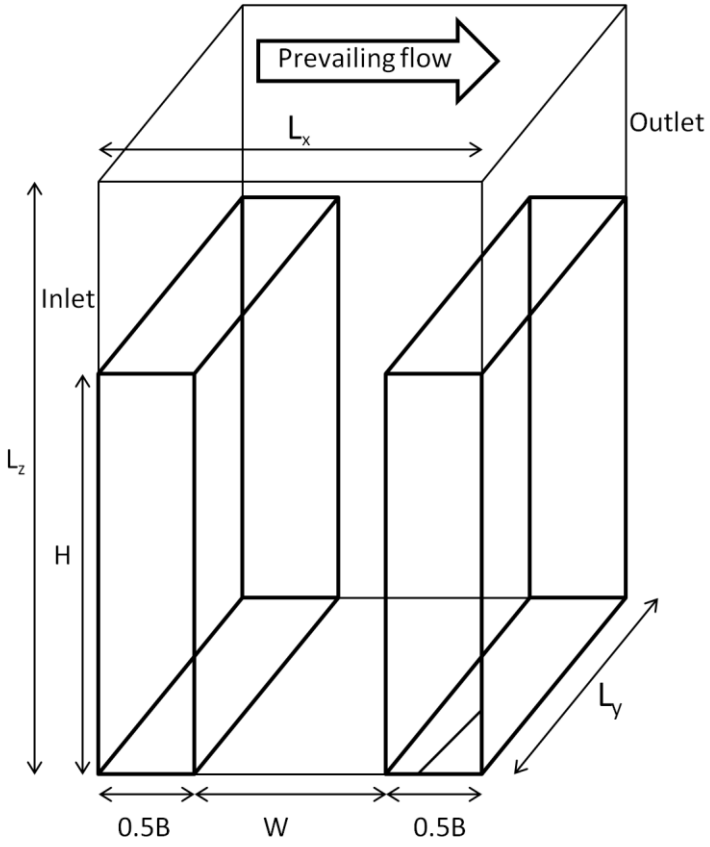

Figure 3.1 Schematic diagram of the computational domain where L_x=36 m, L_y=40 m and L_z=112 m; H (=36 m) is the building height, W (=18 m) is the street width and B (=18 m) is the building width.

A constant pressure gradient across the free surface layer (above the canyon) is imposed in the x-direction to drive the atmospheric flow isothermal conditions (See Equation 3.3), and this pressure force is perpendicular to the street axis, representing the worst-case scenario

for the dispersion of reactive pollutants within a street canyon (Li et al., 2008b). The prevailing wind speed U_f is about 2.2 m s^{-1} at the top domain and the Reynolds number, defined as $\mathrm{Re} = U_f H / \nu$, is the order of 10^6. For velocity components, the wall conditions (See Equations 3.10 and 3.11) are adopted for all the solid boundaries (the surfaces of the buildings and the ground) and the symmetry boundary condition is employed at the domain top. Cyclic boundary conditions are specified in both the *x*- and *y*- directions. Therefore, the model configuration represents an infinite number of idealised street canyons along the *x*-direction and each canyon is infinitely long in the *y*-direction, which is a good approximation of real street canyons relevant to traffic management or urban planning.

Initially, the LES model is run with dynamics for 5 hours in order to generate a statistically steady turbulent flow (Cai et al., 2008). Then the dynamical-equilibrium flow field is taken as the initial condition (i.e. $t = 0$ min) for the dynamical module in this model. At $t = 30$ min, the chemistry scheme and emissions modules are turned on in the presence of canyon dynamics for the next 210 min ($t = 30$ *to* 240 min) with a time step of 0.03 s in order to reach chemical quasi-equilibrium. For chemical species, a simple photochemical box model (including the RCS as the chemical mechanism) is run without emissions for the first 30 minutes ($t = 0$ *to* 30 min) in order to spin up the chemistry module to achieve a photochemical pseudo-equilibrium condition, which allows concentrations of intermediate species (Section 2.2.2) to be calculated. The initial conditions of photochemical box model in this study were taken from those used in Bright et al. (2013) which in turn were based upon atmospheric field data from the Tropospheric Organic CHemistry (TORCH) experiment (Lee et al., 2006). Then the concentrations of all

chemical species at $t = 30$ min (derived from the photochemical box model) are used as the background conditions in the boundary layer for exchange with the inside canyon environment, which are uniformly distributed among the whole domain initially and also employed as inlet boundary conditions, i.e. signifying no emissions from upwind canyons. For the outlet, the advective boundary condition

$$\frac{\partial \overline{c}_i}{\partial t} + \overline{u}\frac{\partial \overline{c}_i}{\partial x} = 0 \tag{3.23}$$

is applied, representing no reflection of pollutants back into the computational domain. For the solid boundaries, zero-gradient boundaries are applied to represent an assumption of no pollutant deposition on them. A typical deposition velocity (V_d) for a chemical species (e.g. O_3) on concrete material is estimated as the order of 0.1 cm s^{-1} (Grontoft and Raychaudhuri, 2004). The timescale for deposition in the street canyon environment can be defined as the ratio of the length scale of the canyon (H=36 m) to the velocity scale of deposition (V_d =0.1 cm s^{-1}) and is calculated as 3.6×10^4 s. The timescale for deposition is much larger than the turbulent mixing timescale or the chemical timescale for key chemical species (See Section 4.3.1). In such a situation, the neglect of deposition processes may be assumed. The symmetry boundary is set on the top of the computational domain and a cyclic boundary condition is adopted in the *y*-direction for the pollutants.

3.4 Implementation of the RCS in OpenFOAM and parallel computation

The LES-chemistry model employed in this research is solved by a free, open source CFD software package, i.e. OpenFOAM (Open Field Operation and Manipulation) v2.1.1 (OpenFOAM, 2012). OpenFOAM is coded in C++, which can be used to generate

executable files (i.e. applications). The applications in OpenFOAM consist of two groups, i.e. solvers and utilities. The solvers are developed to solve particular problems, which are different from case to case and the utilities are normally associated with the data manipulation and visualisation in either pre-processing or post-processing. OpenFOAM involves pre-processing, solving and post-processing (shown as Figure 3.2), associated with solvers, utilities and tools. There are several advantages of OpenFOAM. Users can design their own solvers or utilities according to their specific scenarios based on existing applications in OpenFOAM. The cases in OpenFOAM can be run in parallel, which can make full use of users' computer resources.

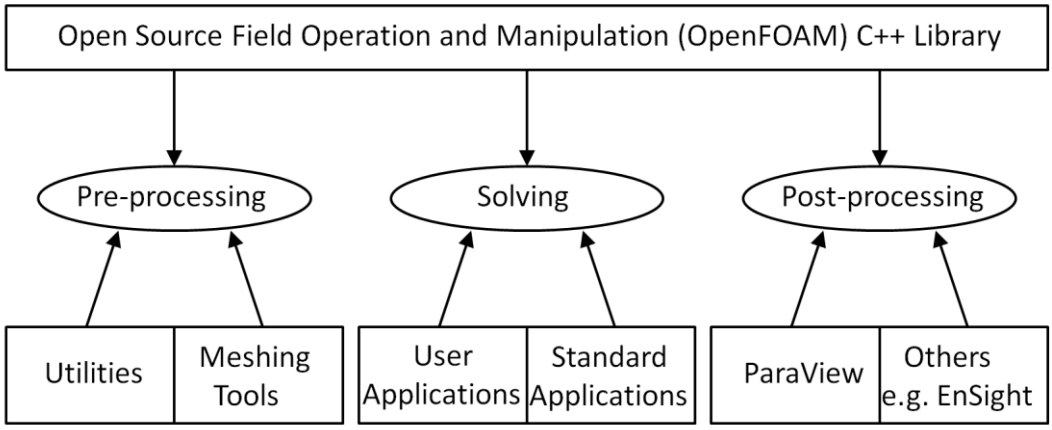

Figure 3.2 OpenFOAM structure (OpenFOAM, 2012).

The OpenFOAM case for the LES-chemistry model consists of three directories, i.e. the *constant* directory, a *system* directory and the '*time*' directory, each of which has its subdirectories (See Figure 3.3 for the detailed structure of the case directories). The associated governing equations for flow and reactive pollutants in the LES-chemistry model are solved by the finite volume method (FVM) with the Pressure Implicit with Splitting of Operators (PISO) algorithm for the pressure-velocity correction. The time and

spatial integration are solved by the second-order-accurate backward and central differencing, respectively. The equation systems for the resolved-scale $\bar{u}_i$, k_{SGS} and $\overline{c_i}$ are solved by the preconditioned bi-conjugate gradient (PBiCG) scheme. For the resolved-scale $\bar{p}$, the preconditioned conjugate gradient (PCG) scheme is used. The computational domain is generated using the *blockMesh* utility. The constant pressure gradient across the free surface layer is specified using the *SetFields* utility. The Gaussian distribution of emission sources are specified using the *funkySetFields* utility. Base on the *pisoFoam* application (i.e. a standard OpenFOAM solver for incompressible transient flow), a user application is developed as the solver for the LES-chemistry model, in which the RCS chemical mechanism (See section 3.2.2) is coupled. The domain decomposition approach (using the *decomposePar* utility) and the Message Passing Interface (MPI) technique are used to carry out the parallel computing.

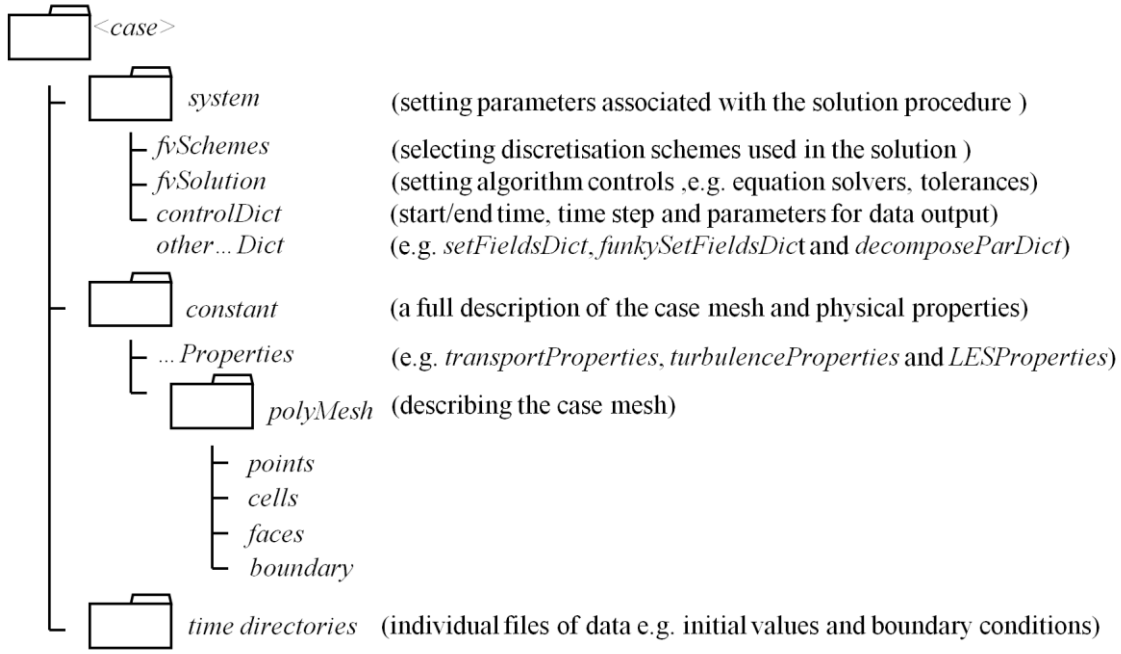

Figure 3.3 Structure of the OpenFOAM case, adopted from OpenFOAM (2012).

The computations of the LES-chemistry model were performed using the University of Birmingham's BlueBEAR (BEAR represents the Birmingham Environment for Academic Research), which is a Linux-based High Performance Computing (HPC) cluster (for more details: http://www.bear.bham.ac.uk). The performance of the parallel running of the LES-chemistry model using OpenFOAM with different number of cores was estimated, in which the running time was normalized by that of 1 core (shown as Figure 3.4). A nonlinear relationship between the normalized running time and the number of cores is evident. While the number of cores increases, the normalized running time is not expected to reduce efficiently. In this research, the total number of cores used was given as 32, i.e. the LES-chemistry model was run in parallel on 2 nodes in the BlueBEAR, each of which consists of 16 cores with 64-bit 2.2 GHz processors and 32 GB of memory. The total wall time for the computation of the LES-chemistry (Section 3.3) was about 10 days.

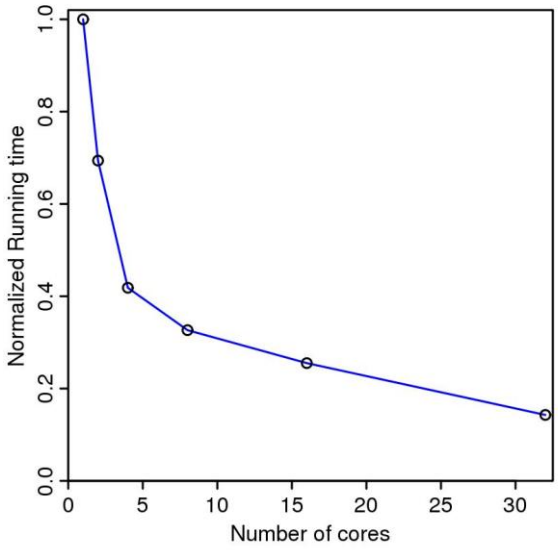

Figure 3.4 Performance of the parallel running using OpenFOAM: Change of number of cores in normalized running time.

3.5 Post-processing of LES output

For the general analysis, the simulation 3-D outputs over the last 60 min period ($t = 180$ *to* 240 min) at a time interval of 3 s are stored and post-processed to derive the resolved-scale turbulent statistics based on the averages over the period and along the *y*-direction (over which there is clear evidence of homogeneous turbulent statistics (Bright et al., 2013)). This temporal average over $t \in [t_1, t_2]$ and spatial average over $y \in [0, L_y]$ of any resolved-scale quantity $\bar{\phi}$ gives $\langle \bar{\phi} \rangle$, which is a 2D function of (*x*,*z*), i.e.

$$\langle \bar{\phi} \rangle (x,z) = \frac{1}{L_y (t_2 - t_1)} \int_{t_1}^{t_2} \int_0^{L_y} \bar{\phi}(x,y,z,t) dy dt \tag{3.24}$$

and $\phi'(x,y,z,t) = \bar{\phi}(x,y,z,t) - \langle \bar{\phi} \rangle (x,z)$ denotes the resolved-scale fluctuation component of $\bar{\phi}$ about $\langle \bar{\phi} \rangle$. Then the second moment of $\bar{\phi}$ (denoted by its auto-variance $\langle \phi' \phi' \rangle$, which captures the turbulent fluctuation intensity) is defined as follows:

$$\langle \phi' \phi' \rangle (x,z) = \frac{1}{L_y (t_2 - t_1)} \int_{t_1}^{t_2} \int_0^{L_y} \phi'(x,y,z,t) \phi'(x,y,z,t) dy dt \,. \tag{3.25}$$

In particular, the resolved-scale turbulent kinetic energy (RS-TKE) (E_{rs}) is defined, i.e.

$$E_{rs}(x,z) = \frac{1}{2} [\langle u' u' \rangle (x,z) + \langle v' v' \rangle (x,z) + \langle w' w' \rangle (x,z)]. \tag{3.26}$$

The resolved-scale fluctuation of $\bar{\phi}$ is characterised by its standard deviation δ_ϕ, i.e.

$$\delta_\phi (x,z) = \sqrt{\langle \phi' \phi' \rangle (x,z)} \,. \tag{3.27}$$

δ_ϕ measures the amount of variation for a distribution and a higher value of δ_ϕ represents a wider distribution of $\bar{\phi}$.

Similarly, the co-variance of two resolved-scale quantities $\bar{\phi}$ and $\bar{\varphi}$ (denoted by $\langle \phi' \varphi' \rangle$) is calculated as follows:

$$\langle \phi' \varphi' \rangle (x,z) = \frac{1}{L_y (t_2 - t_1)} \int_{t_1}^{t_2} \int_0^{L_y} \phi'(x,y,z,t) \varphi'(x,y,z,t) dy dt . \tag{3.28}$$

A positive value of $\langle \phi' \varphi' \rangle$ means that these two resolved-scale quantities exhibit a similar behaviour, while a negative value of $\langle \phi' \varphi' \rangle$ means that these two resolved-scale quantities have opposite behaviours.

The third moment of $\bar{\phi}$ is calculated by

$$\langle \phi'^3 \rangle (x,z) = \frac{1}{L_y (t_2 - t_1)} \int_{t_1}^{t_2} \int_0^{L_y} \phi'^3 (x,y,z,t) dy dt . \tag{3.29}$$

Then the skewness (s_ϕ) is defined as follows:

$$s_\phi (x,z) = \frac{\langle \phi'^3 \rangle (x,z)}{\delta_\phi^{\,3} (x,z)} . \tag{3.30}$$

Skewness measures the degree of asymmetry of the distribution. If skewness is zero, the distribution is symmetric. If skewness is negative, the distribution is left-skewed (i.e. skewed to the left with longer left tail). If skewness is positive, the distribution is right-skewed (i.e. skewed to the right with longer right tail).

Similarly, the fourth moment of $\bar{\phi}$ is calculated by

$$\langle \phi'^4 \rangle (x,z) = \frac{1}{L_y (t_2 - t_1)} \int_{t_1}^{t_2} \int_0^{L_y} \phi'^4 (x,y,z,t) dy dt . \tag{3.31}$$

Then the kurtosis (k_ϕ) is defined as follows:

$$k_{\phi}(x,z) = \frac{\left\langle \phi'^{4} \right\rangle (x,z)}{\delta_{\phi}^{4}(x,z)}. \tag{3.32}$$

Kurtosis measures the peakedness (or flatness in the opposite sense) of the distribution. Kurtosis of a normal distribution is 3 and a value of kurtosis higher or lower than 3 (i.e. positive or excess) represents a 'peaked' or 'flat' distribution with regard to the normal distribution.

3.6 Model dynamics evaluation

A water-channel experiment (Li et al., 2008a) is employed to evaluate the performance of the current LES simulation with respect to the flow field. This water-channel experiment was conducted in a laboratory flume, which was 10 m in length, 0.3 m in width and 0.5 m in height. Several identical building blocks (0.1 m×0.3 m×0.1 m in the *x*-, *y*- and z-directions) were placed perpendicular to the flow with the street width of 0.05 m (i.e. AR=2). The Laser Doppler Anemometer (LDA) technique was applied for the data acquisition of the velocities and turbulent statistics.

Figure 3.5 shows the comparison of vertical profiles of the normalized averaged streamwise and vertical resolved-scale velocities and their standard deviations at the upstream, centre and downstream locations for the deep street canon (AR=2) between the current LES simulation and the water-channel experiment carried out by Li et al. (2008a). The comparisons demonstrate a generally good agreement between the LES output and the experimental data. All of the quantities in Figure 3.5 are normalized by u_{norm} (the averaged value of $\langle \bar{u} \rangle$ at the height $2.0 \leq z/W \leq 2.2$). Figure 3.5a presents the mean

streamwise velocity and there is clear evidence of a shear layer across the canyon roof level, at which strong wind shear strength is observed. It is observed that the streamwise velocity above the street canyon increases gradually with height. But there is a significant decrease of streamwise velocity inside the street canyon, with positive values at the top and bottom canyon, and negative values around the middle canyon. Figure 3.5b shows the vertical mean velocities and there is clear evidence of the complicated flow pattern: the clockwise vortex in the upper part of the canyon (i.e. positive values at the upstream position and negative values at the downstream position) and the weak anti-clockwise vortex in the lower part of the canyon (i.e. negative values at the upstream position and positive values at the downstream position but with a relatively smaller magnitude). The upper recirculation is created by the strong wind shear at the roof level and the lower recirculation is generated by a relatively weaker wind shear induced by the upper recirculation. Figure 3.5c and Figure 3.5d illustrate the standard deviations of the two resolved-scale velocities, which display local maxima at the canyon roof level. These maxima may be caused by the instability of the wind shear-layer at the canyon roof level. This indicates that the normal distribution cannot be applied for the turbulence at the canyon roof level, suggesting that particular caution should be paid when the $k-\varepsilon$ turbulence models are adopted in street canyon flow simulation. As shown in Figure 3.5, there are some small discrepancies between the current LES simulation and the water-channel experiment. In general, the current LES simulation slightly underestimates all the quantities compared with the experiment. There are several possible reasons for this. Firstly, due to the computational cost, a limited computational domain is employed in the current LES simulation, which can only represent eddies with sizes smaller than half of the domain width, which is about W. However, eddies in the experiment are created by the

vortex generators and there may be larger eddies which are not modelled in the LES simulation. Secondly, the grid mesh might not be fine enough across the shear-layer, and therefore some small eddies within the shear-layer and the momentum exchange caused by these small eddies might not be resolved. Finally, these discrepancies may be attributed to different averaging approaches. In the LES simulation, the temporal and spatial averaging approach is adopted to derive the flow quantities. In the experiment, these quantities were only measured on a middle vertical plane in the *y*- direction (Li et al., 2008a).

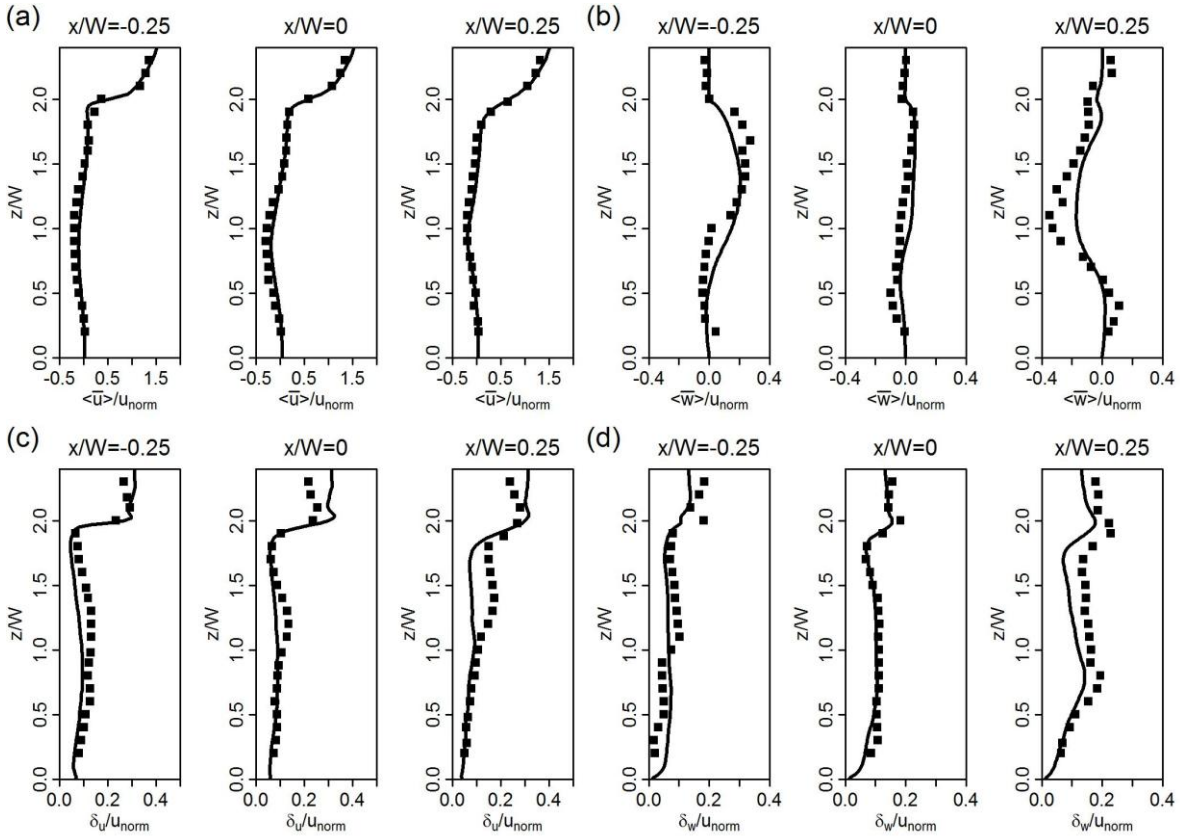

Figure 3.5 Comparison of the vertical profiles of the normalized averaged streamwise and vertical velocities and their fluctuations at the upstream (*x*/W=-0.25), centre (*x*/W=0) and downstream position (*x*/W=0.25) for a deep street canon with an aspect ratio of 2: (a) $\langle \overline{u} \rangle / u_{norm}$, (b) $\langle \overline{w} \rangle / u_{norm}$, (c) δ_u / u_{norm} and (d) δ_w / u_{norm}. Solid lines represent the current LES simulation; Dark squares denote the water-channel experiment carried out by Li et al. (2008a).

Figure 3.6 illustrates the vortex structure in the current LES simulation compared with a wind tunnel experiment carried out by Kovar-Panskus et al. (2002a). Both the model and experiment shows that there are two counter-rotating vortices formed within the deep street canyon (AR=2) and that the upper one is larger than the lower one in the vertical size. This is a major difference from the single-vortex flow for a street canyon with AR=1 (e.g. Bright et al., 2013). The two-vortex mean flow was also found by other studies for AR=2 using RANS, e.g. Kwak et al. (2013), but their RANS model generated a larger lower vortex than the one found in the water tank experiment and in the LES result here. It is also noted that the upper vortex is centred lower within the canyon compared with the experiment. It is also noted that the centre of the lower vortex is shifted downstream closer to the windward wall compared with that of the upper vortex both in the model and experiment.

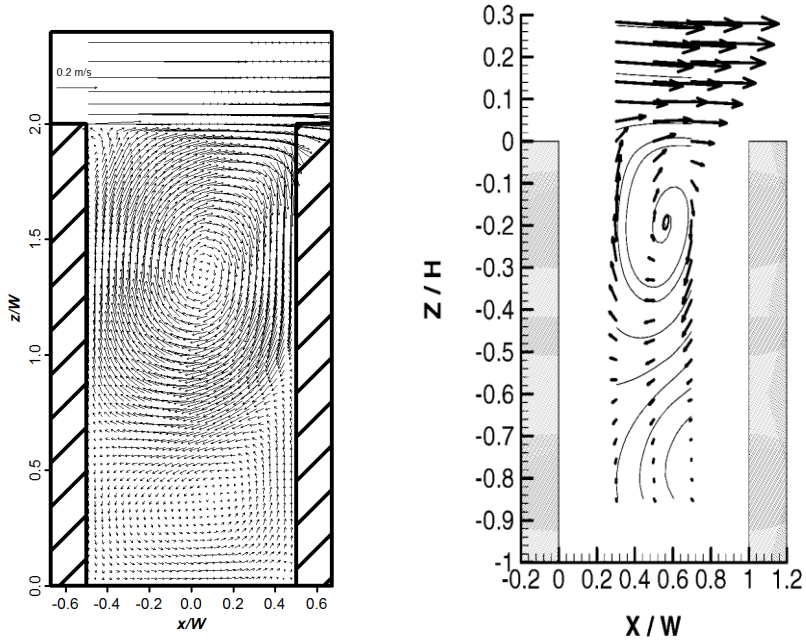

Figure 3.6 Vortex structure in the (a) current LES simulation (b) wind tunnel experiment carried out by Kovar-Panskus et al. (2002a).

Overall, the current LES simulation agrees well with the experiments in terms of the averaged resolved-scale velocities and their standard deviations, and vortex structure, which provides confidence that the simulated dynamics within the canyon is reasonable. However, there are currently no suitable water-channel or wind-tunnel experiments to evaluate the dispersion of reactive species, especially in deep street canyons. Further analysis of other turbulence characteristics in the deep street canyon derived from the current LES simulation is presented in Section 3.7. The dispersion and transport of reactive pollutants within the street canyon using the LES-chemistry model are discussed in details in Chapter 4.

3.7 Further analysis of turbulence in the street canyon

Figure 3.7a illustrates the spatial pattern of the resolved-scale turbulent kinetic energy (RS-TKE), i.e E_{rs}. It is observed that RS-TKE values above the canyon are generally much higher than those inside the canyon. This finding is consistent with Cui et al. (2004) in which AR=1. The maxima of RS-TKE values (around 0.024 m^2 s^{-2}) are found close to the vicinity of the downstream building. It is found that there are secondary local maxima of RS-TKE values (around 0.006 m^2 s^{-2}) slightly below the middle canyon towards the downstream building. These higher values of RS-TKE indicate the unsteady characteristics of the vortices, between which stronger air exchange occurs. There is also evidence of the existence of two primary vortices formed inside the canyon, and the upper one is stronger than the lower one (indicated by Figure 3.7a). Figure 3.7b depicts the spatial pattern of streamwise turbulence intensity $\langle u'u' \rangle$. It is observed that there are broad maxima of $\langle u'u' \rangle$ (around 0.027 m^2 s^{-2}) just above the canyon roof-level towards the downstream building. Secondary local maxima of $\langle u'u' \rangle$ (around 0.003 m^2 s^{-2}) are also found at the

region slightly below the middle canyon along the upstream building. These two local maxima are attributed to the existence of the two unsteady vortices formed inside the canyon (Figure 3.6). Figure 3.7c depicts the spatial pattern of vertical turbulence intensity $\langle w'w' \rangle$. There is clear evidence of two local maxima of $\langle w'w' \rangle$. The first one is around 0.012 m^2 s^{-2} at the roof-level corner towards the downstream building and the second one is around 0.006 m^2 s^{-2} slightly below the middle canyon towards the downstream building, about half of the roof-level maximum value. These observations of turbulence intensity are strongly correlated to the mechanism of the TKE generation and dissipation. At the canyon roof level, the mechanical wind shear at the interface between the atmospheric flow above the canyon and the vortices inside the canyon plays an important role in converting the bulk kinetic energy into the TKE, which is responsible for local maxima of TKE near the roof level. The induced TKE at the canyon roof level then dissipates along the primary vortex near the top of the canyon. The secondary local maximum is caused by relatively smaller mechanical wind shear between the upper and lower vortices within the canyon. Figure 3.7d depicts the spatial pattern of momentum turbulent flux $\langle u'w' \rangle$. It is found that $\langle u'w' \rangle$ exhibits broad peaks of negative values near the canyon roof level towards the downstream building, which is in line with the stronger turbulence in the shear layer bringing momentum downwards into the canyon. Those negative values of $\langle u'w' \rangle$ suggest that the momentum transfer is dominated by either ejection events (i.e. $u' < 0, w' > 0$) or sweep events (i.e. $u' > 0, w' < 0$), which is also found near the canyon roof level by Cui et al. (2004) in which AR=1. Within the canyon, there are two peaks of positive values (indicated by red colour scales in Figure 3.7d). The first one is along the downstream building at the top canyon and the other is slightly below the middle canyon. Those

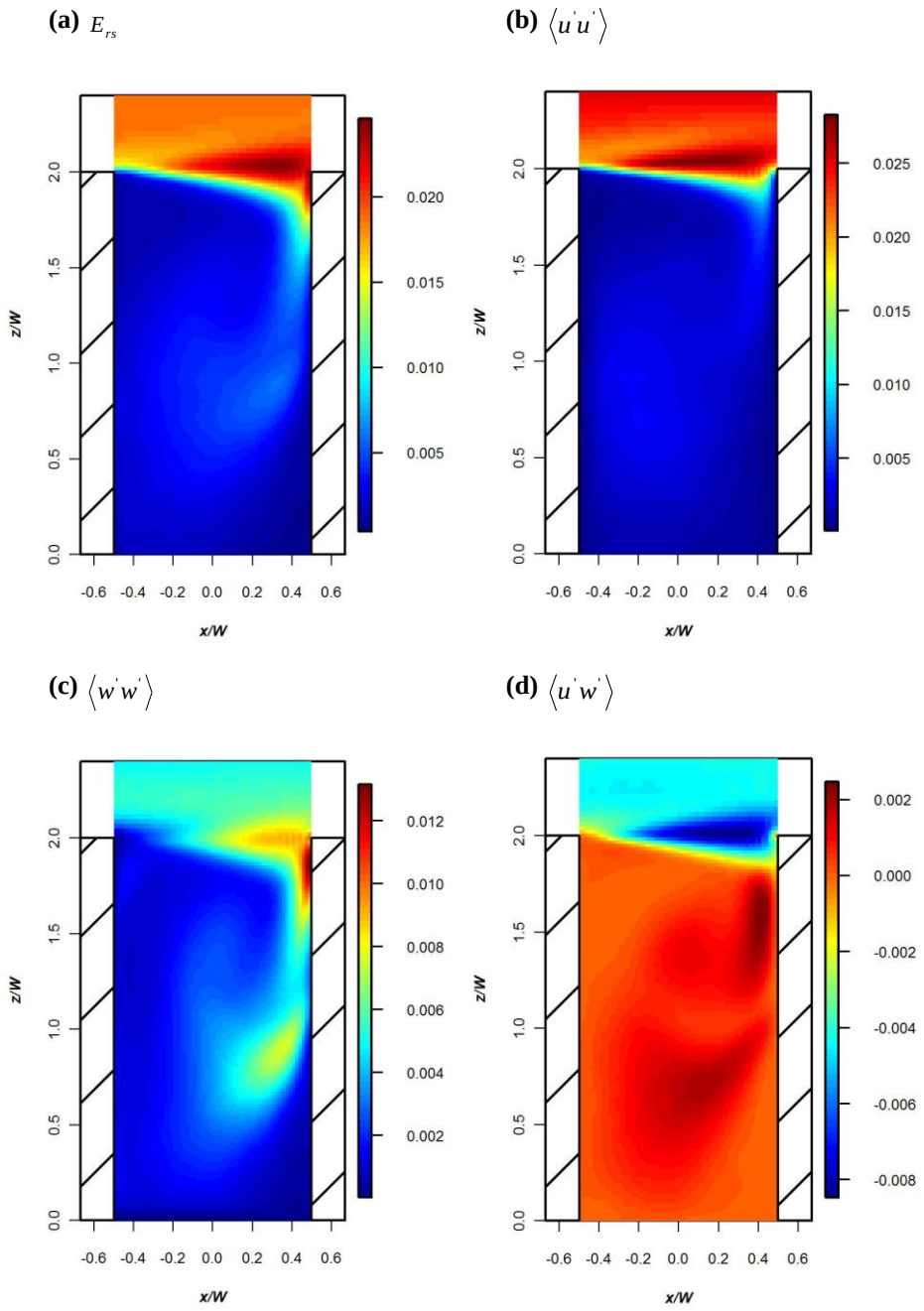

Figure 3.7 Spatial variation of (a) E_{rs} (resolved-scale turbulent kinetic energy), (b) $\langle u'u' \rangle$ (streamwise turbulence intensity), (c) $\langle w'w' \rangle$ (vertical turbulence intensity) and (d) $\langle u'w' \rangle$ (momentum turbulent flux).

positive values of $\langle u'w' \rangle$ are dominated by either $u' < 0, w' < 0$ or $u' > 0, w' > 0$, suggesting a similar behaviour between them. This indicates that the momentum transport inside the

canyon is mainly attributed to inward interaction (i.e $u' < 0$, $w' < 0$) and outward interaction (i.e $u' > 0, w' > 0$). Positive (or negative) sign of the momentum turbulent flux means u-momentum upwards (or downwards). The momentum transfer is also affected by the two unsteady vortices inside the canyon, which is induced by the turbulence generated at the shear layer. Since the momentum transfer is spatially and temporally averaged, Figure 3.7d represents the overall effect of these four possible occurrences of ejection events (i.e. $u' < 0, w' > 0$), sweep events (i.e. $u' > 0, w' < 0$), inward interaction (i.e $u' < 0$, $w' < 0$) and outward interaction (i.e $u' > 0, w' > 0$).

Figure 3.8 illustrates vertical profiles of the (a) *u*-skewness (s_u), (b) *w*-skewness (s_w), (c) *u*-kurtosis (k_u) and (d) *w*-kurtosis (k_w) at the upstream (*x*/W=-0.25), centre (*x*/W=0) and downstream position (*x*/W=0.25). Figure 3.8a shows that there is a peak of positive s_u at the canyon roof level, moving from a sharp one at the upstream position to a broad one at the downstream position. This indicates the asymmetric distribution of *u* due to the strong turbulence at the shear layer. These positive values of s_u demonstrate that the distribution of *u* is right-skewed, i.e. with its mean value higher than its median value and its mode value as well. It means that there are more events for $u < \bar{u}$ (i.e. $u' < 0$) than those for $u > \bar{u}$ (i.e. $u' > 0$). In contrast, Figure 3.8b demonstrates the a peak of negative s_w at the canyon roof level, which means that the distribution of *w* is left-skewed, i.e. with its mean value lower than its median value and its mode value as well. Therefore, there are more events for $w > \bar{w}$ (i.e. $w' > 0$) than those for $w < \bar{w}$ (i.e. $w' > 0$). The characteristics of s_u and s_w are very interesting in terms of relating to quadrant analysis of events. Figure 3.8a and Figure 3.8b indicate that there are likely more ejection events (i.e $u' < 0, w' > 0$) than

sweep events (i.e $u^{'} > 0, w^{'} < 0$) happened at the canyon roof level where strong shear is present. These events are responsible for the TKE generation at the shear layer. There are also relatively fewer events of inward interaction (i.e $u^{'} < 0, w^{'} < 0$) and outward interaction (i.e $u^{'} > 0, w^{'} > 0$), which are responsible for the turbulence consumption at the canyon roof level. Figure 3.8c and Figure 3.8d show that there are peaks of positive excess (greater than 3) of k_u and k_w at the canyon roof level, similar to these of s_u and s_w. It means that there are 'peaked' distributions of *u* and *w*, at which $u < \overline{u}$ (i.e. $u^{'} < 0$) and $w > \overline{w}$ (i.e. $w^{'} > 0$). This also indicates that the turbulence of the atmospheric flow at the

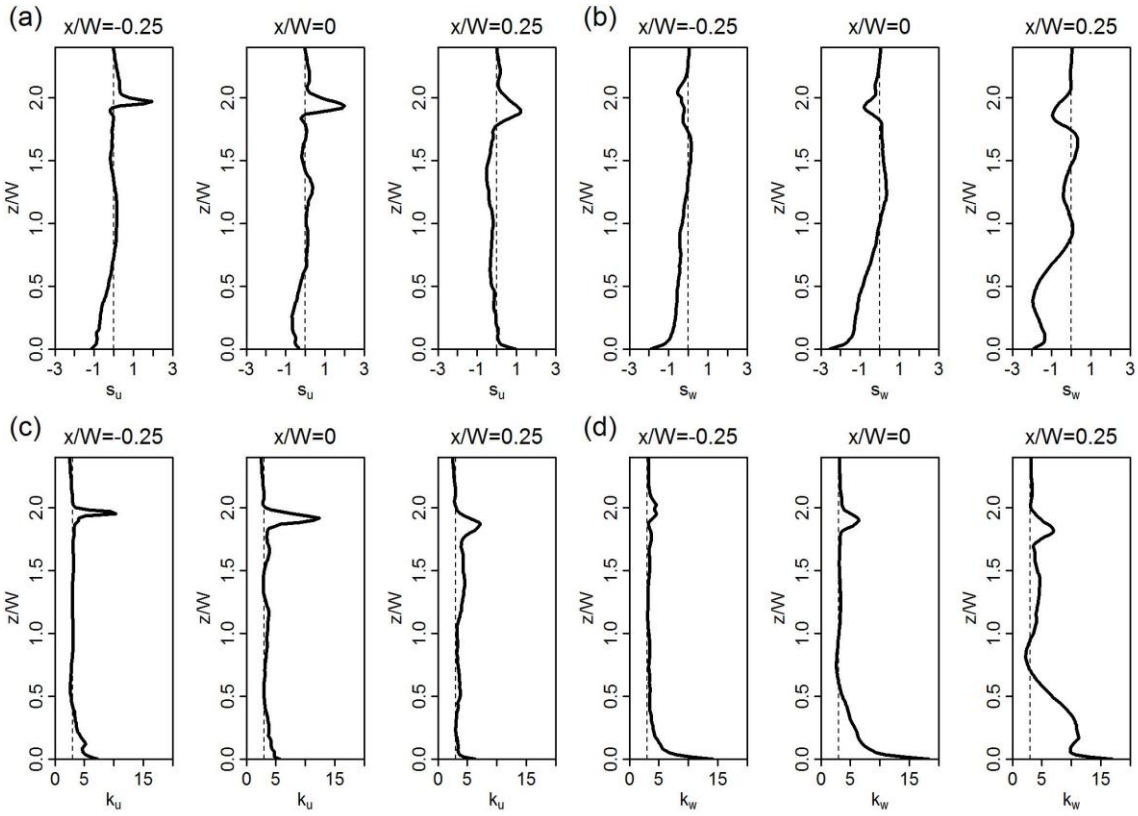

Figure 3.8 Vertical profiles of (a) s_u, (b) s_w, (c) k_u and (d) k_w at the upstream (*x*/W=-0.25), centre (*x*/W=0) and downstream position (*x*/W=0.25).

canyon roof level is likely dominated by the ejection events (i.e $u' < 0, w' > 0$), which is in line with the findings by Cui et al. (2004) and Cheng and Liu (2011) for the AR=1 cases. Figure 3.8 also shows that at the upper canyon, s_u and s_w change slightly around 0, and k_u and k_w changes around 3. It is also observed that there are relatively larger perturbations at the bottom canyon than the upper canyon. It is also interesting to note that there are very sharp gradient of these quantities close to the street ground. These similar features are also found by Cui et al. (2004) and Cheng and Liu (2011) for the AR=1 cases, but with relatively flat gradient than the present LES model. This may be attributed to the relatively smaller size of the lower vortex (which is dragged by the street ground) than that of the upper vortex (Figure 3.6).

4 Dispersion and transport of reactive pollutants within a street canyon: Using the LES-chemistry model

4.1 Introduction

This chapter will present and discuss the results of the dispersion and transport of reactive pollutants within a street canyon derived from the LES-chemistry model, which was introduced and described in Chapter 3. In this chapter, the spatial patterns of several key reactive pollutants and their chemistry-induced concentrations within the street canyon will be presented. The coupling effect of dynamical and chemical pre-processing of emissions within the street canyon will be investigated in detail. Effects of HO_x chemistry will be examined by comparing the results with and without VOCs chemistry. Segregation effects due to incomplete mixing of atmospheric pollutants within the street canyon will be discussed. A two-box model is developed for the comparison of the results from the LES-chemistry model. The potential exposure to air pollution is assessed by investigating short-term time series air pollution data and air pollution statistics within the simulated street canyon.

4.2 Analysis

4.2.1 Decomposition of contributions from emission and chemistry

For a passive scalar (i.e. a non-reactive scalar), its abundance within a street canyon is affected by the emission rate of the passive scalar once the street canyon turbulent flow is determined. For a reactive scalar, the contribution from chemistry also plays an important

role in determining its level within the street canyon. If the mean concentration for any chemical species inside an idealised 2D street canyon derived from LES is denoted by $C(x,z)$, it is assumed that $C(x,z)$ can be decomposed by two contributions from emission and chemistry, i.e.

$$C(x,z) = C_{ps}(x,z) + C_{chem}(x,z) \tag{4.1}$$

The assumption implies a linear decomposition. 'ps' denotes 'passive' and 'chem' is chemical contribution. Further,

$$C_{ps}(x,z) = C_b(x,z) + C_{emn}(x,z) \tag{4.2}$$

Here, 'b' is for 'background' and 'emn' is for 'emission'. $C_{emn}(x,z)$ is the field of the passive scalar induced by the given emission and corresponding to 'zero background'. $C_b(x,z)$ is the spatial distribution induced by an upwind background concentration of C_0. It is assumed that

$$C_b(x,z) = C_0 = const \tag{4.3}$$

This assumption is true if the system is allowed to achieve a steady state; air inside the canyon will be in balance with above roof concentration and it should be constant. Thus,

$$C_{ps}(x,z) = C_0 + C_{emn}(x,z) \tag{4.4}$$

It is assumed that $C_{emn}(x,z)$ is linearly scaled with the emission rate. In other words, with doubled emission rate, $C_{emn}(x,z)$ will be simply doubled. It is further defined that

$C_{emn,1}(x,z)$ is the concentration for a unit emission rate and $C_{emn,1}(x,z)$ can be derived from the LES simulation for a passive scalar (with zero background). Therefore,

$$C_{emn}(x,z) = E * C_{emn,1}(x,z) \tag{4.5}$$

where E is the emission rate for this species. In such a way, a spatial pattern of a passive scalar can be used to reconstruct the pattern for any other passive scalars, or the emission-induced component of a non-passive scalar.

Therefore, the contribution from chemistry to any non-passive scalar can be diagnosed by following equation:

$$C_{chem}(x,z) = C(x,z) - E * C_{emn,1}(x,z) - C_0 \tag{4.6}$$

in which both $C(x,z)$ and $C_{emn,1}(x,z)$ are derived from LES with prescribed E and C_0. This formula can be applied for all emitted species (e.g. NO, NO_2, NO_x and O_x). In particular, for any non-emitted species (e.g. O_3, OH and HO_2), the contribution from emission is effectively ignored and therefore the contribution from chemistry is simply obtained:

$$C_{chem}(x,z) = C(x,z) - C_0 \tag{4.7}$$

A negative value of C_{chem} means the chemical consumption and a positive value of C_{chem} means the chemical production. A zero value of C_{chem} means no chemical consumption or production. In other words, the chemistry is in the quasi-equilibrium state. The assumption of a linear decomposition has some limitations for higher-order reactions, in which the chemical contribution may be dependent upon the passive-scalar type abundance.

4.2.2 Vertical advective and turbulent fluxes of pollutants

Following Equation 3.24 and 3.28, the vertical advective flux of any species at the resolved-scale is defined:

$$F_{adv}(x,z) = \left\langle \overline{w} \right\rangle (x,z) \left\langle \overline{\phi} \right\rangle (x,z) \tag{4.8}$$

and the vertical turbulent flux is defined:

$$F_{turb}(x,z) = \left\langle w' \phi' \right\rangle (x,z) \tag{4.9}$$

Thus the vertical total flux is obtained as follows:

$$F_{total}(x,z) = F_{turb}(x,z) + F_{adv}(x,z) \tag{4.10}$$

These quantities of fluxes represent the 2D spatial variation. For the purpose of discussion, these quantities are further averaged horizontally and vertical profiles are derived:

$$F(z) = \frac{1}{W} \int_{-0.5W}^{0.5W} F\ (x,z) dx \tag{4.11}$$

4.2.3 Ozone production rate

The local ozone production rate (PO_3) associated with the VOCs chemistry under the perfect mixing condition can be defined as follows. According to Volz-Thomas et al. (2003), the local ozone production rate (PO_3) can be approximated to the rate, at which hydro- and organic-peroxy radicals (RO_2 and HO_2) react with NO to generate NO_2 through Reactions 1.14 and 1.16 (i.e. the effect of minor reactions is assumed to be negligible). Considering a chemical equilibrium system with perfect mixing comprising Reactions 1.1-1.3, 1.14 and 1.16, we can derive

$$j_{NO_2}[NO_2] - k_{NO+O_3}[O_3][NO] = k_3[NO][HO_2] + \sum_i k_{4,i}[NO][RO_2]_i \qquad (4.12)$$

where the value of j_{NO_2} in Reaction 1.1 is 0.0092 s^{-1} and the value of k_{NO+O_3} in Reaction 1.3 is 0.0004 ppb^{-1} s^{-1} under the simulation conditions (Bright et al., 2013); k_3 and $k_{4,i}$ are the rate constants for Reactions 1.14 and 1.16, respectively; i is the i^{th} organic-peroxy radical. The terms $k_3[NO][HO_2] + \sum_i k_{4,i}[NO][RO_2]_i$ represent the rate of conversion of NO to NO_2 (through VOCs chemistry-derived peroxy radicals); NO_2 is subsequently photolysed leading to O_3 production. Thus the local ozone production rate (PO_3) is defined (Volz-Thomas et al., 2003), i.e.

$$PO_3 = k_3[NO][HO_2] + \sum_i k_{4,i}[NO][RO_2]_i \qquad (4.13)$$

Due to the difficulties of evaluating HO_2 and RO_2 from simultaneous measurements, Equation 4.12 may be used as an *indirect approach* to infer PO_3 (defined as Equation 4.13) from the NO_x and O_3 measurements:

$$PO_{3[pss]} = j_{NO_2}[\overline{NO_2}] - k_{NO+O_3}[\overline{O_3}][\overline{NO}] \qquad (4.14)$$

This is referred to as the *NO_x-O_3-steady-state-defect* approach. In this approach, it is implicitly assumed that deviations from the photostationary state (PSS) of NO_x and O_3 arising from imperfect mixing are negligible (Volz-Thomas et al., 2003). However, this assumption of perfect mixing is often not achieved in the real atmosphere (Belcher, 2005), especially for the canopy layer where reactive pollutants exhibit the spatial and temporal variability due to incomplete mixing. The accuracy of this assumption within the street canyon environment is evaluated in Section 4.3.3.

4.2.4 Photostationary state defect

For a further analysis of the combined effect on chemical equilibrium, the photostationary state (PSS) defect $de_{[pss]}$ (in percentage) of NO_x and O_3 (Baker et al., 2004) is defined as follows:

$$de_{[pss]} = \left(\frac{k_{NO+O_3}[\overline{O_3}][\overline{NO}]}{j_{NO_2}[\overline{NO_2}]} - 1\right) \times 100 \tag{4.15}$$

The term $de_{[pss]}$ is a widely-used measure to describe the deviation from the state of chemical equilibrium. The larger is the magnitude of $de_{[pss]}$, the higher is the deviation from the chemical equilibrium. $de_{[pss]} = 0$ means that the chemistry is at the equilibrium state.

For a chemical system involving VOCs chemistry (based on Equation 4.12), Equation 4.15 may be modified as follows:

$$de = \left(\frac{k_{NO+O_3}[\overline{O_3}][\overline{NO}] + k_3[NO][HO_2] + \sum_i k_{4,i}[NO][RO_2]_i}{j_{NO_2}[\overline{NO_2}]} - 1\right) \times 100 \tag{4.16}$$

4.2.5 Intensity of segregation

In order to characterise the segregation effect due to incomplete mixing of chemical species, a widely used dimensionless number, the *intensity of segregation* (Krol et al., 2000) between two chemical species A and B, $I_{S(A+B)}$, is introduced and defined as:

$$I_{S(A+B)} = \frac{\langle A'B' \rangle}{\langle A \rangle \langle B \rangle} \tag{4.17}$$

where the angle brackets represent the volume average, the prime denotes the local deviation from the volume-averaged concentration, and $A'B'$ stands for the spatial covariance between A and B.

The intensity of segregation is a proper measure of the effect of segregation on nonlinear chemical processes (Hilst, 1998) and represents the deviation from a well-mixed environment due to the coupling between dynamics and chemistry. For a second-order reaction A+B $\rightarrow$ C in a heterogeneous system, the rate of formation of C (Vinuesa and de Arellano, 2005) can be described as follows,

$$\frac{d\langle C\rangle}{dt} = \langle k_{eff\,(A+B)}\rangle\langle A\rangle\langle B\rangle \tag{4.18}$$

where $\langle k_{eff\,(A+B)}\rangle$ is the effective second-order rate constant for formation of C in the heterogeneous system due to incomplete mixing which can be represented by

$$\left\langle k_{eff\,(A+B)}\right\rangle = k_{(A+B)}(1+I_{S(A+B)}) \tag{4.19}$$

where $k_{(A+B)}$ is the original rate constant of the reaction in a well-mixed system (spatially homogenous). Such a constant is normally obtained from laboratory experiments in a well-mixed chamber. If $I_{S(A+B)} = 0$, it means that species A and B can be regarded as well-mixed (i.e. spatially homogeneous); If $I_{S(A+B)} > 0$ or $I_{S(A+B)} < 0$, it implies that $\langle k_{eff\,(A+B)}\rangle$ in the heterogeneous system is larger or smaller than $k_{(A+B)}$ in the well-mixed system due to the effect of segregation. In this study, $k_{(A+B)}$ is adopted homogeneous among the canyon. $I_{S(A+B)}$ is calculated based on the 2D data for the canyon (Equation 3.24). Thus positive or negative values of $I_{S(A+B)}$ represent segregation effect for the street canyon environment.

4.3 Results and discussion

4.3.1 Spatial variation of reactive pollutants

Figure 4.1 depicts the spatial variation of (a) $\langle \overline{NO} \rangle$, (b) $\langle \overline{NO_2} \rangle$, (c) $\langle \overline{O_3} \rangle$, (d) $\langle \overline{NO_x} \rangle$, (e) $\langle \overline{O_x} \rangle$, (f) $\langle \overline{NO} \rangle / \langle \overline{NO_2} \rangle$, (g) $\langle \overline{OH} \rangle$ and (h) $\langle \overline{HO_2} \rangle$ (See Equation 3.24). The plots apparently show the influence of two primary vortices, which span the deep street canyon, i.e. the upper clockwise vortex, and the lower anti-clockwise vortex. For the upper (or lower) vortex, the vicinity of the leeward building is higher (or lower) in the mixing ratios of NO and NO_2, but lower (or higher) in the mixing ratio of O_3 compared with in the vicinity of the windward building. This influence was also found by Kwak et al. (2013) for the street canyon with AR=2 using a RANS model. In general, the spatial patterns of the quantities for the upper vortex resemble those for the single vortex in a street canyon with AR=1 (e.g. Baker et al. (2004), Baik et al. (2007), Bright et al., 2013, Garmory et al. (2009), Tong and Leung (2012), and Kwak and Baik (2012)). There also exist two shear layers. A shear layer can be defined as a region of high shear with approximately linear segment of the mean velocity profile (Huq et al., 2007), which separates the layers with different mean flow and turbulent characteristics (e.g. the external boundary layer above the canyon and the cavity in the canyon). The shear layer plays an important role in the transfer of mass and momentum (Salizzoni et al., 2011). The shear layer dynamics are significantly affected by the characteristics of its separation points of building and the structure / intensity of the external flow (Perret and Savory, 2013). Pitched roofs are expected to have a deeper and stronger shear layer and more turbulent exchange at the shear layer than flat roofs (Louka et al., 2000). The increase of the external flow intensity poses a direct influence on the shear layer dynamics and hence on the overall turbulent

exchange of pollutants at the shear layer. Due to the high computational cost, limited sizes of the computational domain are used in the current LES simulation. Therefore some unsteady larger scale structures of the external flow are inevitably not captured (Coceal et al., 2006), which may reduce the turbulent exchange of pollutants. The first is at the canyon roof level with increasing turbulence and amplitude from the leeward building to the windward building, which traps emitted pollutants (e.g. NO and NO_2) near the leeward building, allows more exchange near the windward building and entrains ambient atmosphere (e.g O_3) into the canyon toward the windward building. The other is near the interface between the two vortices, which allows emissions released from the ground level inside the lower vortex to transfer into the upper vortex and the ambient atmosphere inside the upper vortex to be entrained into the lower vortex. The atmospheric chemical species mix and react with each other inside the two vortices in the presence of the two shear layers where exchanges take place. It is noted that at the ground level towards the windward building, there are accumulations of traffic emissions (with maximum values of about 800 ppb for NO and 200 for NO_2) and low levels of O_3, OH and HO_2 (with minimum values of about 6 ppb, 0.09 ppt and 0.22 ppt, respectively). This is attributed to a high level of NO_x emitted into the very weak lower vortex reacting with the limited O_3 entrained along the windward wall from above (a direct result of reduced mixing and chemical processing). This result for the O_3 mixing ratio is very different from (i.e. much lower than) that by Kwak et al. (2013) shown in their Figure 2(d), which gives a local maximum of about 30 ppb near the centre of the lower vortex. One explanation is that their emission rate of NO_x is much lower than that in this work (20 vs. 90 ppb s^{-1} released into 1 m^3 of air), giving a less significant titration effect to convert NO to NO_2 with the consumption of O_3. It is known that NO_x plays a key role in the street-canyon atmospheric

chemistry, which determines NO_2 levels through the chemical processing of NO with other species (e.g. O_3). Therefore, both $NO_x = (NO + NO_2)$ and the total oxidant $O_x = (O_3 + NO_2)$ are useful measures of the street-canyon atmospheric chemistry. It is noted that both NO_x and O_x (shown as Figure 4.1d and Figure 4.1e) exhibit a similar spatial distribution to each other driven by the two primary vortices and much higher mixing ratios within the street canyon are observed compared with the overlying background. For simple NO_x-O_3 chemistry, NO_x and O_x are conserved with respect to addition (emission) of NO and can be considered as effectively passive scalars. But for the complex chemistry, there are additional sinks of NO_x and sources of O_x due to the VOC oxidation chemistry (discussed in Section 4.3.3). The ratio of NO/NO_2 (Figure 4.1f) is another useful indicator of chemical interactions within the street canyon. The NO/NO_2 ratio also shows a similar pattern across the two vortices ranging from about 3.6 at the right corner towards the windward building to about 1.4 at the canyon roof level, which clearly indicates the conversion of NO to NO_2 by the within-canyon pre-processing. The NO/NO_2 ratio within the street canyon is much lower compared to the raw emission ratio of NO/NO_2 (assumed as a value of 9). This also reflects that both the directly emitted NO_2 and the chemical oxidation of emitted NO contribute to increased levels of NO_2. The fast reacting chemical species (OH and HO_2) also play an important role in the conversion of NO to NO_2 through the chemical interaction. The spatial distributions of OH and HO_2 (Figure 4.1g) have similar patterns to that of O_3, in which their background mixing ratios are much higher than those inside the canyon (by a factor of about 2 for OH, 5 for HO_2 and 3 for O_3 compared with their canyon-averaged abundances).

(a) NO

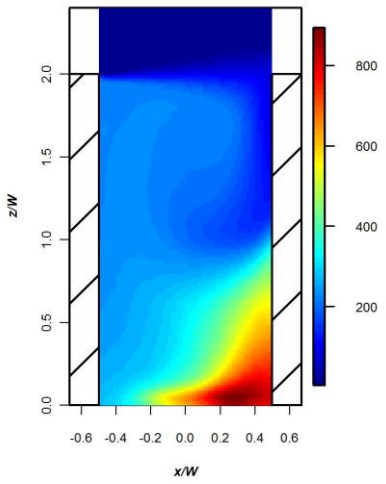

(b) NO_2

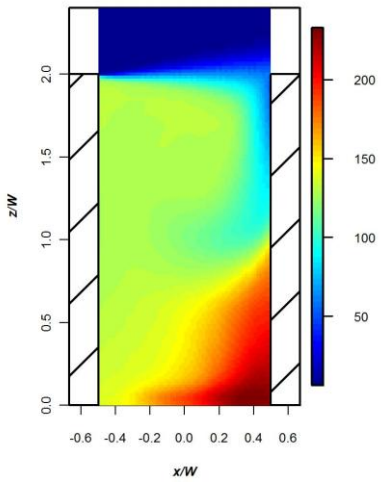

(b) O_3

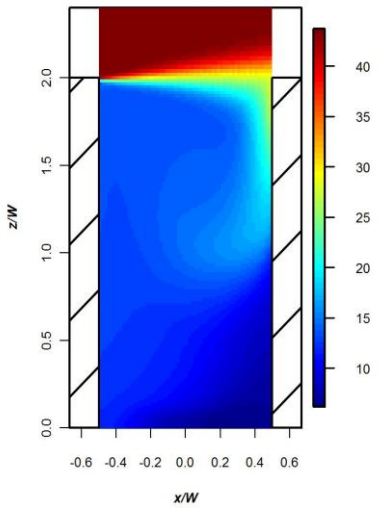

(d) NO_x

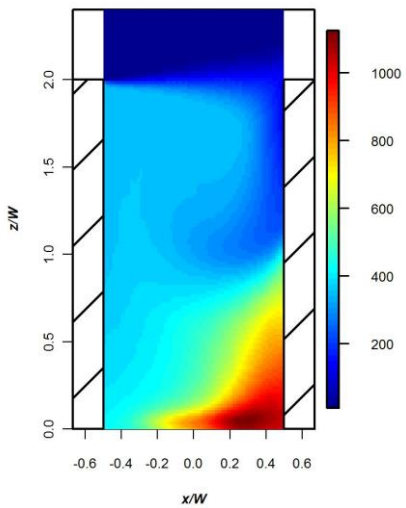

(e) O_x

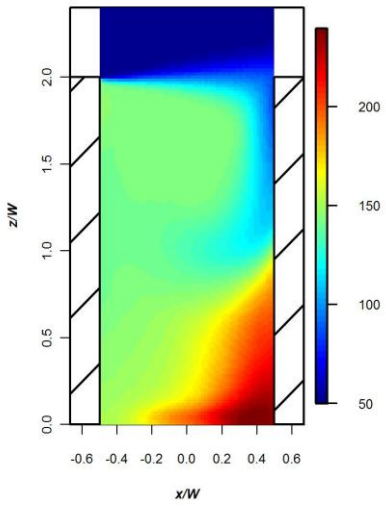

(f) NO/ NO_2

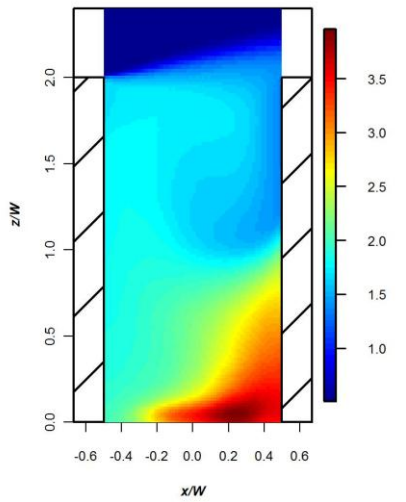

(g) OH **(h) HO_2**

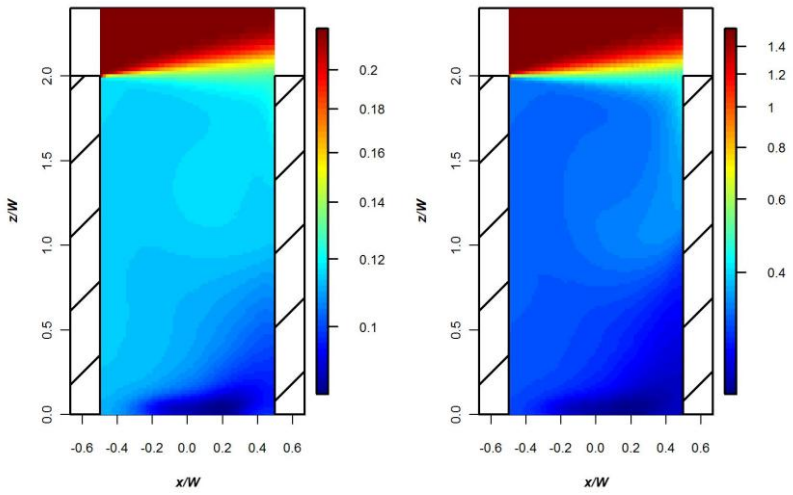

Figure 4.1 Spatial variation of (a) $\langle\overline{NO}\rangle$ (ppb), (b) $\langle\overline{NO_2}\rangle$ (ppb), (c) $\langle\overline{O_3}\rangle$ (ppb), (d) $\langle\overline{NO_x}\rangle$ (ppb), (e) $\langle\overline{O_x}\rangle$ (ppb), and (f) $\langle\overline{NO}\rangle/\langle\overline{NO_2}\rangle$, (g) $\langle\overline{OH}\rangle$ (ppt) and (h) $\langle\overline{HO_2}\rangle$ (ppt). Logarithmic colour scales are applied for $\langle\overline{OH}\rangle$ and $\langle\overline{HO_2}\rangle$.

Figure 4.2 illustrates vertical profiles of (a) $\langle\overline{NO}\rangle$, (b) $\langle\overline{NO_2}\rangle$, (c) $\langle\overline{NO_x}\rangle$, (d) $\langle\overline{O_x}\rangle$, (e) $\langle\overline{NO}\rangle/\langle\overline{NO_2}\rangle$, (f) $\langle\overline{C}\rangle/C_b$ (for O_3, OH and HO_2 normalised by their background levels) along the leeward and windward walls, respectively. These quantities are averaged within the nearest three cells adjacent to the leeward and windward walls, respectively. It is noted that NO, NO_2, NO_x, O_x and NO/NO_2 on the leeward wall are generally higher than those on the windward wall within the upper part of the canyon, but lower within the lower part. This indicates that traffic emissions are mainly trapped within the anti-clockwise lower vortex. But for O_3, the situation is reversed with much lower values on the leeward wall compared to those on the windward wall within the upper part of the canyon, but with slightly higher values within the lower part. This is attributed to ambient O_3 being brought from the background atmosphere into the upper part of canyon along the windward wall. It is also noted that the concentration reduces with height along both leeward and windward walls for NO, NO_2, NO_x, O_x and NO/NO_2, but increases with height for O_3. For the

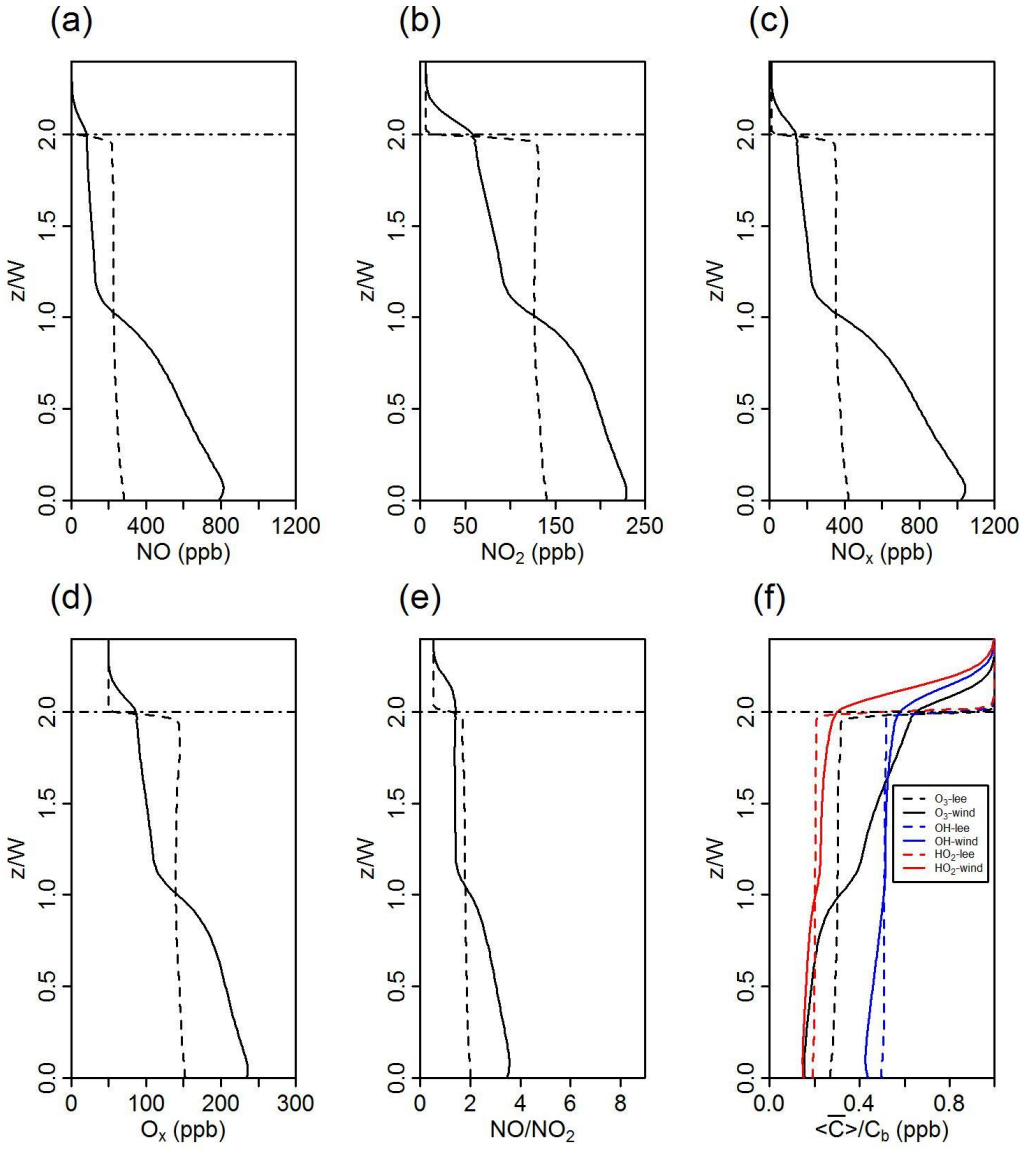

Figure 4.2 Vertical profiles of (a) $\langle \overline{NO} \rangle$, (b) $\langle \overline{NO_2} \rangle$, (c) $\langle \overline{NO_x} \rangle$, (d) $\langle \overline{O_x} \rangle$, (e) $\langle \overline{NO} \rangle / \langle \overline{NO_2} \rangle$, and (f) $\langle \overline{C} \rangle / C_b$ (for O_3, OH and HO_2 normalised by their background levels) along the leeward and windward walls, represented by the dash and solid lines respectively.

leeward wall, there is a sharp transition at the canyon roof level where each species rapidly approaches its background level, and a small gradient in concentration within the canyon. For the windward wall, there are two gradual transitions near the roof level and close to the middle level of the canyon, respectively. These results for the upper part of the canyon match those of the field measurements by Xie et al. (2003), in which there was only one primary vortex inside the street canyon. For the AR=1 case, there are higher

concentrations of pollutants towards the leeward building at the pedestrian level. However, for the AR=2 case, higher concentrations of pollutants are observed towards the windward building at the pedestrian level (due to the opposite direction between the upper vortex and lower vortex). This indicates that these findings for the AR=1 case may be unreliable for the assessment of pollutant exposure towards the leeward or windward building at the pedestrian level in a deep street canyon with AR=2. It is also interesting to note that just above the canyon roof level (z/W=2), there are much higher levels of pollutants (e.g. NO_x) at the windward side (i.e. the canyon outlet) than those at the leeward side (i.e. the canyon inlet). This reflects increased levels of pollutants transferred from the canyon to the wider ambient environment, which indicates the importance of the coupling effect of emissions, mixing and chemical pre-processing within the street canyon. The windward side is the main location of this street canyon ventilation system, potentially taking ambient air into buildings. This pre-processing of air pollution within the street canyon will be further investigated in Section 4.3.2. The vertical profiles of OH and HO_2 have similar patterns to that of O_3, in which their levels along both the leeward and windward walls increase with the increase of the vertical height and approach to their corresponding background concentrations at approximately z/W=2.4. In the upper (or lower) part of the canyon, the mixing ratios of OH and HO_2 along the windward wall are slightly higher (or lower) than those along the leeward wall. For comparison, levels of O_3, OH and HO_2 are normalised by their background concentrations. It is observed that HO_2 has the sharpest drop near the canyon roof level while O_3 has flattest drop. This indicates that either HO_2 or OH is more rapidly consumed than O_3 at the canyon roof level. Within the canyon, there is a similar consumption rate for OH and HO_2 (reflected by the similar slopes for the curves), but much slower than that for O_3. The rapid O_3 consumption inside the canyon can be

explained by NO_x (NO) emissions from the street level, which has a significant titration effect thereby leading to the rapid consumption of O_3 within the canyon.

Figure 4.3 illustrates the spatial variation of (a) $C_{emn,1}$ and C_{chem} of (b) NO, (c) NO_2, (d) NO_x, (e) O_x, (f) O_3, (g) OH and (h) HO_2 (See Equations 4.5, 4.6 and 4.7). The spatial pattern of a passive scalar with a unit emission rate (equivalent to 1 ppb s^{-1} released into a typical LES model grid, i.e. 0.3 m×1 m×0.3 m in the *x*- , *y*- and *z*-directions, respectively) is depicted in Figure 4.3a. It is observed that the distribution of the passive scalar is characterised by the two unsteady vortices formed inside the street canyon. The emission of the passive scalar is mainly trapped inside the lower vortex closer to the windward wall. This unit emission rate scenario is used to reconstruct the spatial pattern based on Equation 4.6 for the chemistry-induced component of a non-passive scalar in Figure 4.3 b-e. It is found that NO, NO_x, O_3, OH and HO_2 are chemically consumed, indicated by negative values of C_{chem}. For NO_2 and O_x, however, chemical production occurs inside the street canyon, indicated by positive values of C_{chem}. The chemical consumption of NO and O_3 is largely caused by the titration effect, thereby leading to the chemical production of NO_2. The concentration contributed from the chemical consumption for NO_x is about 3% of that for NO. The slight chemical consumption NO_x indicates that there is a sink of NO_x in the chemical processing (Section 1.2.3), but this rate is rather slow on the canyon timescale. The concentration contributed from the chemical production for O_x is about 67% of that for NO_2. This is partially attributed to the chemical consumption of O_3 in the canyon. The chemical production of O_x is due to the VOCs oxidation processes through the chemistry associated with fast radicals (e.g. HO_x) which convert NO to NO_2. During these processes, these fast radicals are chemically consumed. Therefore, it is observed that C_{chem} for OH

and HO_2 are negative. The spatial patterns for these C_{chem} are dependent upon the vortex structure inside the street canyon. There are also sharp gradient at the canyon roof level and a clear separation at the interface between the lower and upper vortices. It is also interesting to note that the magnitudes of either positive or negative values are greatest close to the windward wall in the lower vortex. These may be explained by the trapped emissions due to the anti-clockwise vortex in the lower canyon and the relatively longer retention time than that in a canyon with AR=1. These magnitudes for the upper canyon are slightly lower than those for the lower canyon. It is also noted that in the background atmosphere above the canyon, there is neither chemical production nor consumption (indicated by the values close to zero). This is due to that the background atmosphere (a simple photochemical box model was used to spin up the chemistry in Section 3.3) is already in the quasi-equilibrium state. It indicates that the chemical production or consumption inside the street canyon is caused by the emissions perturbing the chemical equilibrium, under the incomplete mixing environment. The turbulent mixing timescale (T_{mix}) can be defined as the length scale of the canyon divided by its velocity scale. The length scale of the canyon is H (=36 m) and the velocity scale of turbulent mixing is estimated as 0.058 m s^{-1}, i.e. the square root of the mean resolved-scale turbulent kinetic energy (Salizzoni et al., 2009). So the turbulent mixing timescale is estimated as 621 s. The chemical timescales (T_{chem}) within the canyon (calculated based on Equation 3.16 using the canyon averaged quantities over the last 60 min period) are estimated as 185 s for NO, 108 s for NO_2, 9 s for O_3, 0.0043 s for OH and 0.014 s for HO_2. The Damköhler number (Da), defined as the ratio of the turbulent mixing timescale (T_{mix}) to the chemical timescale (T_{chem}), can be used to investigate the combined effect between dynamics and chemistry (Auger and Legras, 2007). When Da << 1, chemical processes are relatively

slow compared to dynamical processes and chemical species may be regarded as well-mixed scalars with minimal segregation effects. When Da >> 1, chemistry is very fast and can achieve a chemical equilibrium before the flow mixes together chemical species. In such situations, the interaction between dynamics and chemistry is very important with significant segregation effects. The Damköhler number (Da) is calculated as 3.4 for NO, 5.8 for NO_2, 69 for O_3, 1.44×10^5 for OH, and 4.44×10^4 for HO_2. This indicates that the chemical production or consumption for these species is significantly limited by dynamical processes in the street canyon environment (Figure 4.3 b-h).

(a) $C_{emn,1}$ **(b)** C_{chem} **for NO**

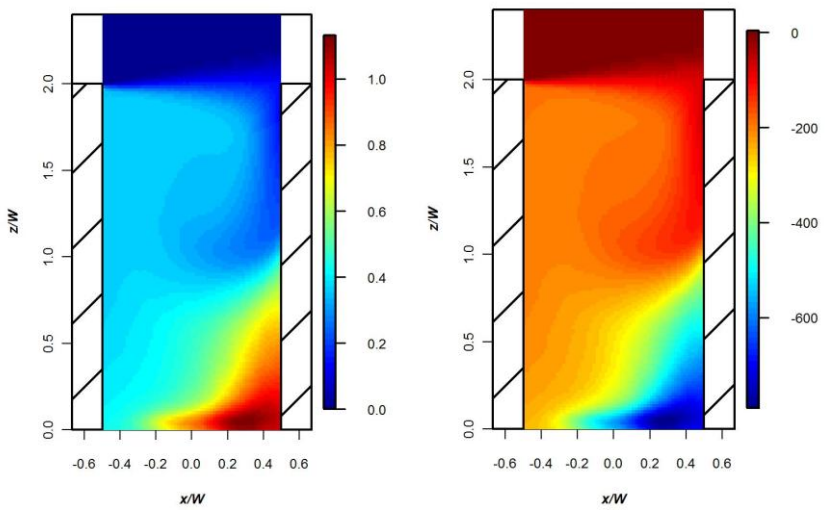

(c) C_{chem} **for** NO_2 **(d)** C_{chem} **for** NO_x

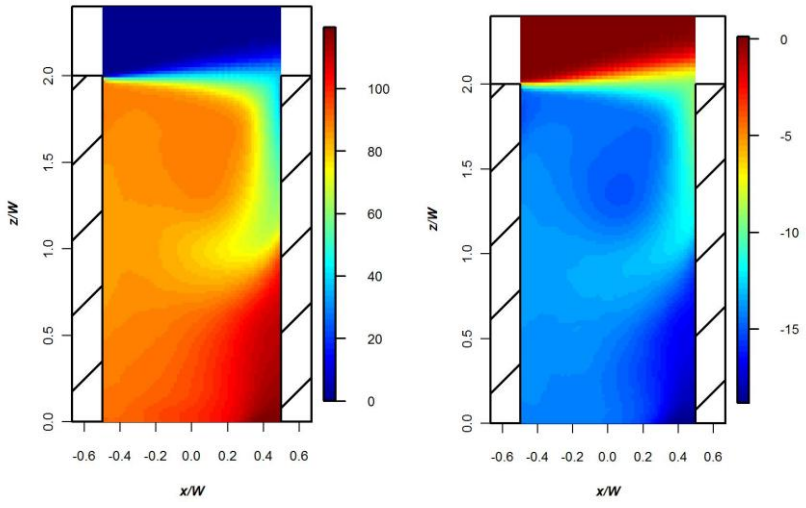

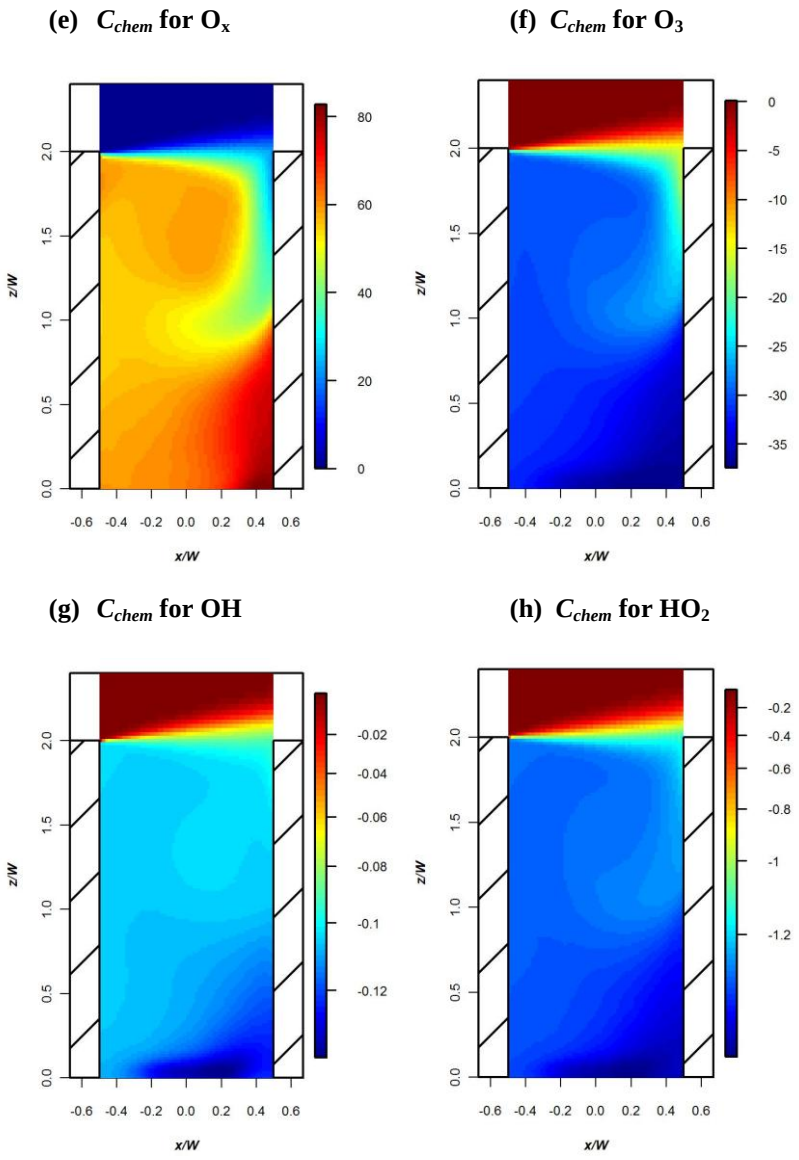

Figure 4.3 Spatial variation of (a) $C_{emn,1}$ (ppb) and C_{chem} of (b) NO (ppb), (c) NO_2 (ppb), (d) NO_x (ppb), (e) O_x (ppb), (f) O_3 (ppb), (g) OH (ppt) and (h) HO_2 (ppt). Logarithmic colour scales are applied for OH and HO_2.

4.3.2 Pre-processing of emitted pollutants

Figure 4.4 illustrates vertical profiles of the horizontally averaged total, turbulent and advective fluxes (See Equation 4.8-11), for (a) NO, (b) NO_2, (c) O_3, (d) NO_x, (e) O_x and (f) NO/NO_2. The total, turbulent and advective fluxes for each quantity are represented by the black solid, dash and dotted lines, respectively. The relative total fluxes for non-passive scalars reconstructed based on a passive scalar with a unit emission rate (Figure 4.3a) are

denoted by the red solid lines. The departure of the total fluxes (black solid lines) away from the red solid lines represents chemically induced fluxes. Negative (or positive) values of fluxes mean that pollutants are entrained downward (or upward) to the street canyon. It is interesting to note that advective fluxes are dominant for both the upper vortex and the lower vortex while turbulent fluxes are dominant for shear layer, which indicates that advective fluxes act as a dominant role for the transport of pollutant within a vortex while turbulent fluxes play an important role for the exchange of pollutant within the zone

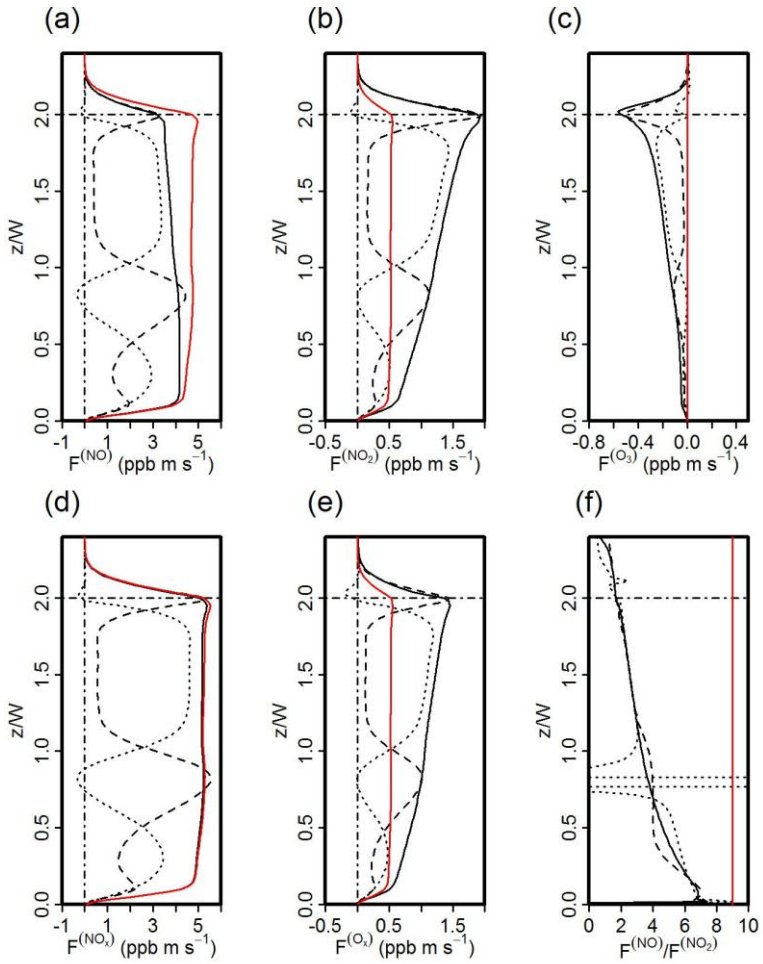

Figure 4.4 Vertical profiles of the horizontally averaged total, turbulent and advective fluxes for (a) NO, (b) NO_2, (c) O_3, (d) NO_x, (e) O_x and (f) NO/NO_2. The total, turbulent and advective fluxes for each quantity are represented by the black solid, dash and dotted lines, respectively. The relative total fluxes for non-passive scalars reconstructed based on a passive scalar with a unit emission rate are denoted by red solid lines.

between the vortices. There is also clear evidence that both advective fluxes (becoming negative values) and turbulent fluxes (even higher than the total fluxes) changes rapidly close to the canyon roof level and the level where two vortices formed in the deep street canyon interact. This sensitivity to the vertical height at the canyon roof level was also found by Cheng and Liu (2011), in which LES simulations of a passive scalar in the street canyon with AR=1 were conducted. It is also noted that advective fluxes in the lower vortex are generally lower than those in the upper vortex while turbulent fluxes in the lower vortex are generally higher than those in the upper vortex. It is observed that there is a positive (upward) total flux for NO and NO_2 from the canyon roof level into the background atmosphere aloft, and a negative (downward) total flux for O_3 indicating that O_3 is brought into the canyon from the overlying background atmosphere. A rapid increase in the total flux of NO and NO_2 is observed from the ground to the level at z/W=0.1. This is due to the elevation of traffic emissions from the ground level. The total flux generally decreases with height for NO, but increases for NO_2 indicating the conversion of NO to NO_2 within the canyon chemical processing before they escape to the wider background environment. This conversion is also indicated as the ratios of total fluxes of NO to NO_2 decrease with height. The NO/NO_2 ratio of total fluxes is about 1.7 at the canyon roof level, which is significantly lower than the raw emission ratio of NO/NO_2 (assumed as a value of 9). Therefore, the within-canyon processing results in increased levels of NO_2 through the chemical conversion of NO to NO_2 and changes the partition of total NO_x emissions at the canyon roof level. This indicates that apart from the emitted NO_2, the chemical processing within the canyon has a significant contribution to the high level of NO_2 (even in breach of its air quality limit). The fluxes at the canyon roof level represent the interface between the canyon and wider background atmosphere. For NO_x, the total flux remains almost constant

with height (about 5 ppb m s^{-1}) except a rapid increase near the ground level, which is attributed that the near-vehicle dispersion is assumed to exhibit a Gaussian distribution. But for O_x, the total flux increases significantly with an increase in the vertical height up to about 1.4 ppb m s^{-1} at the canyon roof level, which is about 2.8 times its raw emission flux (about 0.5 ppb m s^{-1}). This ratio is significantly higher (about 1.3 times) than that found by Bright et al. (2013) for the AR=1 case. This is attributed to the HO_x chemistry, which converts NO to NO_2 resulting in an increase of total O_x flux. Without the HO_x chemistry, O_x flux would be nearly a constant in the canyon environment because titration will not contribute anything to O_x. It is the longer retention time of pollutants in the deep street canyon (AR=2) that allows the accumulation of O_x generated from the HO_x chemistry. This is very different for the AR=1 case (Bright et al., 2013) with the short retention time of pollutants. The fluxes increase further with an increase in the vertical height for the deep street canyon (AR=2) in this study. These findings indicate that the within-canyon pre-processing results in an increase in the oxidant flux and this effect is more significant for the deeper street canyon.

4.3.3 Effect of the HO_x chemistry

Figure 4.5 shows spatial variations of (a) $PO_{3[pss]}$, (b) PO_3, (c) $de_{[pss]}$ and (d) de (See Equations 4.13-16). The magnitudes of those quantities are smaller in the lower vortex than that in the upper vortex indicating that there is greater mixing for the chemistry system to approach chemical equilibrium in the lower vortex compared to that in the upper vortex. This can be explained by the weaker vortex in the lower part of the canyon, where time scale is adequate to approach chemical equilibrium. Local maxima of those quantities are observed across the canyon roof level in the presence of the strong turbulence. It is also observed that there are significantly larger values of those quantities along the upper part

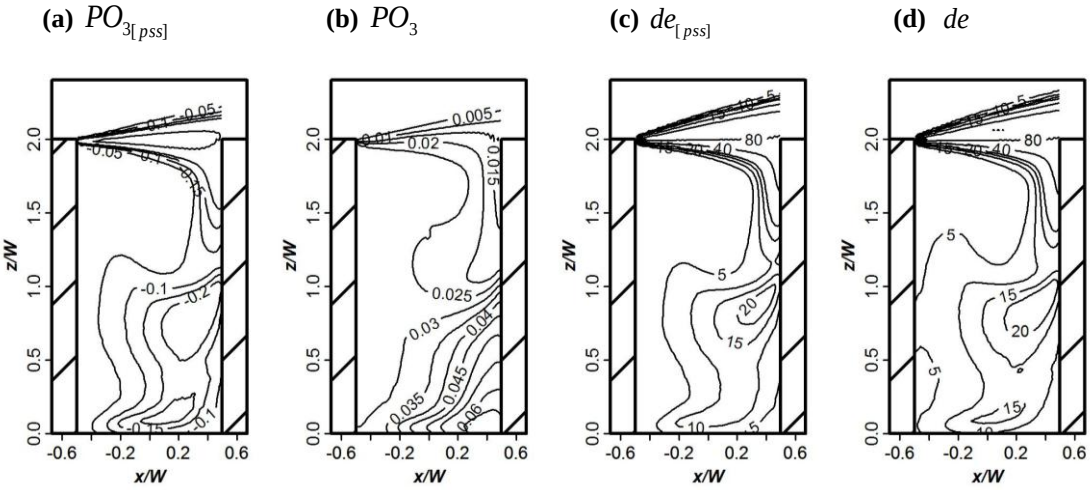

Figure 4.5 Spatial variations of (a) $PO_{3[pss]}$ (ppb s^{-1}), (b) PO_3 (ppb s^{-1}), (c) $de_{[pss]}$ (%) and (d) de (%).

of the windward building, indicating larger deviation from photochemical equilibrium in the region where two air parcels with very different chemical compositions interact. If no peroxy radical reactions are considered in the model scheme, *net* chemical ozone production cannot occur. Non-zero values for the PSS defect, $de_{[pss]}$ and de (in the same order indicated by Figure 4.5c and Figure 4.5d), therefore reflect the impact of imperfect mixing (heterogeneity) within the canyon, rather than ozone production chemistry. The values of $PO_{3[pss]}$ obtained here may therefore be regarded as measures of a systematic error in the NO_x-O_3-steady-state-defect approach to assess ozone production rates (via NO_x/O_3 measurements in the real atmosphere), i.e. indicating the magnitude of the imperfect-mixing-generated deviation from steady-state. The canyon averaged $PO_{3[pss]}$ = -0.102 ppb s^{-1} (i.e. -367 ppb h^{-1}) inferred base on the PSS (Figure 4.5a) indicates a negative bias in results nearly at all locations, which is large compared with measured free boundary layer / free troposphere ozone production rates [typically a few ppb h^{-1}, up to 50 ppb h^{-1} in the most polluted regions, e.g. Mexico City (Wood et al., 2009)]. This reflects

the fact that the $PO_{3[pss]}$ term effectively represents a small difference between two large quantities, such that the impact of mixing may be very substantial. In fact, this effect (imperfect mixing in the vicinity of NO_x emission sources) is entirely general, and so a systematic negative contribution to NO_x-O_3-steady-state derived ozone production rates will recur throughout the urban atmosphere, to an extent dependent upon the local heterogeneity. However, the canyon averaged PO_3 = 0.031 ppb s^{-1} (i.e. 110 ppb h^{-1}) (Figure 4.5b) calculated directly from the NO and peroxy radicals (assumed to be obtained by measurements), is relatively large compared with measured free boundary layer / free troposphere ozone production rates. These findings demonstrate that the indirect approach to estimate ozone production rate based on the PSS gives the wrong results in street canyon environment, as a consequence of the segregation effect due to incomplete mixing.

Figure 4.6 illustrates spatial variations of the overestimation of the spatially and temporally averaged concentrations (%) by simple NO_x-O_3 chemistry compared with the RCS chemical mechanism for (a) $\langle\overline{NO}\rangle$, (b) $\langle\overline{NO_2}\rangle$, (c) $\langle\overline{O_3}\rangle$, (d) $\langle\overline{NO_x}\rangle$, (e) $\langle\overline{O_x}\rangle$ and (f) $\langle\overline{NO}\rangle/\langle\overline{NO_2}\rangle$. Generally, simple NO_x-O_3 chemistry would overestimate (indicated by positive values) levels of NO, NO_x and NO/NO_2, but underestimate (indicated by negative values) levels of NO_2, O_3 and O_x. Such findings suggest that using simple NO_x-O_3 chemistry may provide optimistic prediction of air pollution in street canyon (for NO2 - i.e. predicted levels are biased low) while in reality the NO_2 level (i.e. a current air pollution issue of the UK) has exceeded the air quality standards, which may mislead the policy-maker to make an inappropriate decision with respect to air quality management. There are some common features for these overestimations (biases) in Figure 4.6. At the canyon roof level, a sharp decrease of the magnitudes of those biases is observed and those values approach to zero for the wider background (both simple NO_x-O_3 and RCS chemistry adopted same

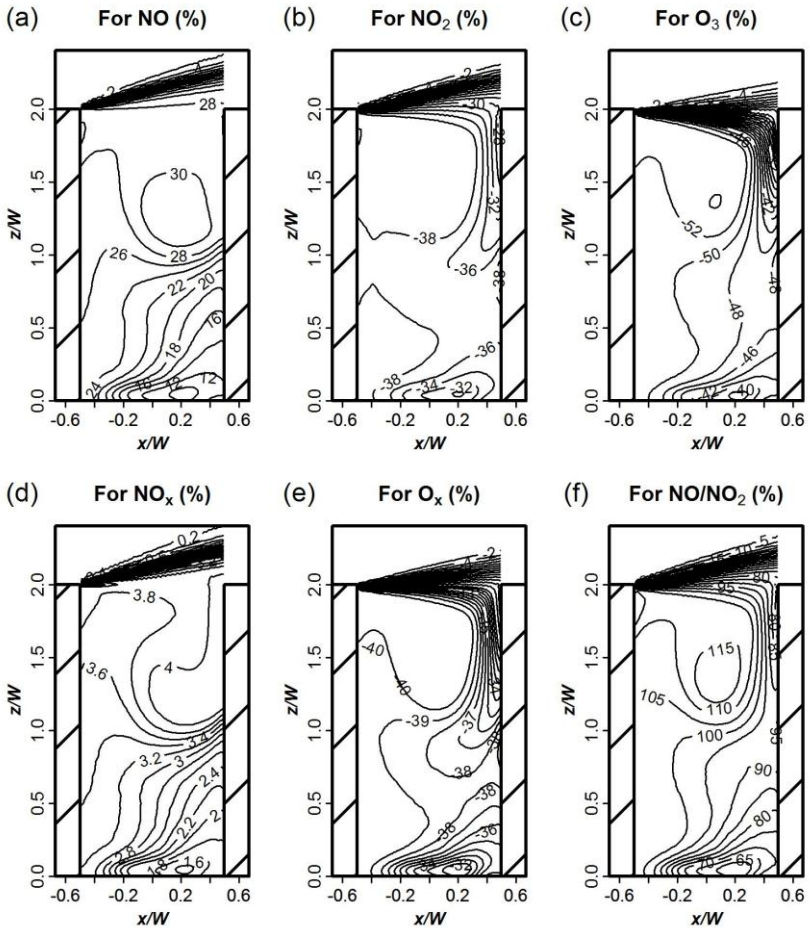

Figure 4.6 Spatial variations of the overestimation of the spatially and temporally averaged concentrations (%) by simple NO_x-O_3 chemistry compared with the RCS chemical mechanism for (a) $\langle\overline{NO}\rangle$, (b) $\langle\overline{NO_2}\rangle$, (c) $\langle\overline{O_3}\rangle$, (d) $\langle\overline{NO_x}\rangle$, (e) $\langle\overline{O_x}\rangle$ and (f) $\langle\overline{NO}\rangle/\langle\overline{NO_2}\rangle$.

background concentrations for NO_x and O_3). The largest value of the magnitudes of those overestimations (about 30 % for NO, about -38% for NO_2, about -52% for O_3, about 4% for NO_x, about -40% for O_x and about 115% for NO/NO_2) is found close to the centre of the upper vortex. For the current UK air pollution problem related to higher levels of NO_2 in urban areas an underestimate of NO_2 by 40% could be a substantial issue. In the lower part of the canyon, the magnitudes of those overestimations are comparatively low and generally decrease down to the street ground. It is noted that there is a slight overestimation for NO_x by the simple chemistry and this is due to the extra sink of NO_x to

other N-contained species (such as HNO_3 and HONO). It is interesting that there is a large underestimation for the oxidants (NO_2, O_3 and O_x) by the simple chemistry. This is attributed to the additional conversion of NO to NO_2 by the VOC chemistry in the RCS chemical mechanism.

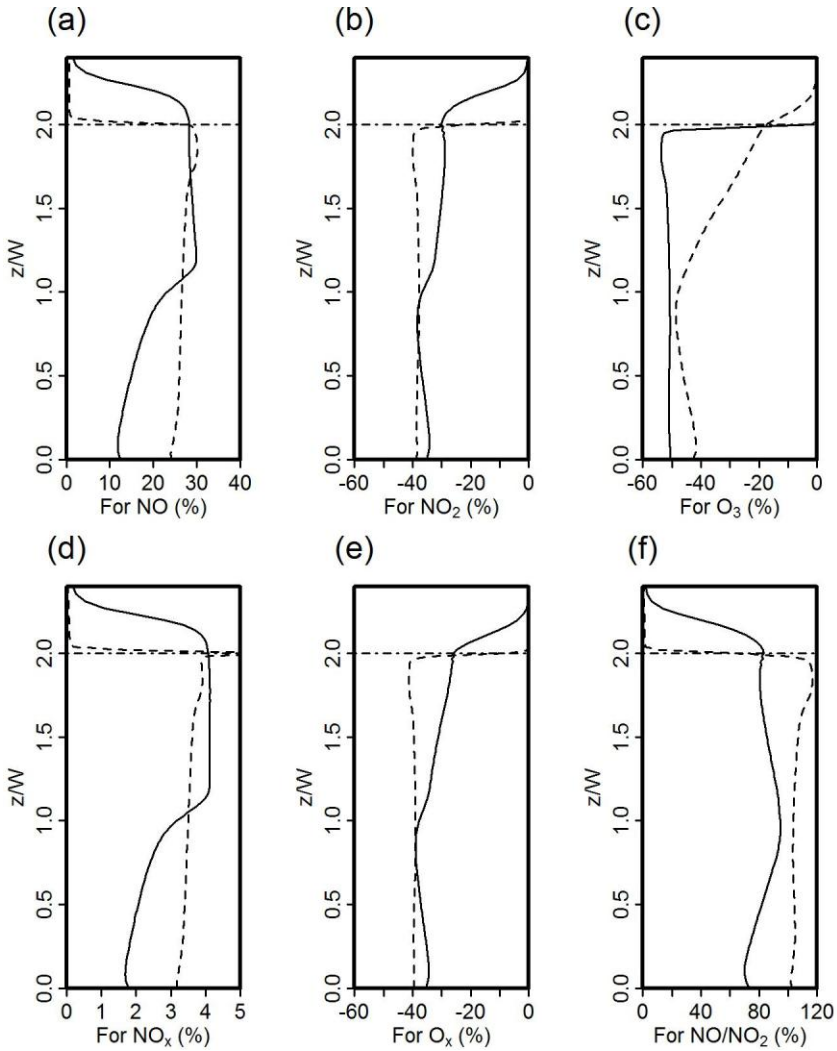

Figure 4.7 Vertical profiles of the overestimation of the spatially and temporally averaged concentrations (%) by the simple chemistry compared with the RCS chemical mechanism for (a) $\langle\overline{NO}\rangle$, (b) $\langle\overline{NO_2}\rangle$, (c) $\langle\overline{O_3}\rangle$, (d) $\langle\overline{NO_x}\rangle$, (e) $\langle\overline{O_x}\rangle$ and (f) $\langle\overline{NO}\rangle/\langle\overline{NO_2}\rangle$ along the leeward wall represented by the dash lines, and along the windward wall represented by the solid lines.

Figure 4.7 shows the vertical profiles of the overestimation of the spatially and temporally averaged concentrations (%) by the simple chemistry compared with the RCS chemical

mechanism for (a) $\langle\overline{NO}\rangle$, (b) $\langle\overline{NO_2}\rangle$, (c) $\langle\overline{O_3}\rangle$, (d) $\langle\overline{NO_x}\rangle$, (e) $\langle\overline{O_x}\rangle$ and (f) $\langle\overline{NO}\rangle/\langle\overline{NO_2}\rangle$ along the leeward and windward wall. For the leeward wall, there are no significant changes of the overestimations within the canyon except for O_3 (with a rapid change in the upper part of the canyon), i.e. around 25% for NO, around -40% for NO_2, around 3% for NO_x, around -40% for O_x, and around 100% for NO/NO_2. For the windward wall, there are significant contrasts for the lower and upper part of the canyon except for O_3 (nearly constant values of around 50% inside the canyon). The magnitudes of overestimation of NO and NO_x along the windward wall in the lower part of the canyon are lower (by a factor of about 0.5) than those in the upper part of the canyon. The magnitudes of overestimation of NO_2 and O_x along the windward wall in the lower part of the canyon are higher (by a factor of about 1.5) than those in the upper part of the canyon.

Figure 4.8 illustrates vertical profiles of the overestimation of the spatially and temporally averaged total, turbulent and advective fluxes (%) by the simple chemistry compared with the RCS chemical mechanism for (a) NO, (b) NO_2, (c) O_3, (d) NO_x, (e) O_x and (f) NO/NO_2 averaged across the canyon. The overestimations of the total, turbulent and advective fluxes follow similar patterns. It is also noted that there are some peaks for the advective fluxes at the mixing region between the lower and upper parts of the canyon for all the quantities and that the magnitude of the overestimation of the total flux for O_x is much lower than those of the turbulent and advective fluxes. The magnitudes of those overestimation generally increase with the increase of the vertical height except that the overestimation of O_3 gradually crosses the zero line from negative values to positive values. This also indicates the importance of VOCs chemistry in the street canyon context.

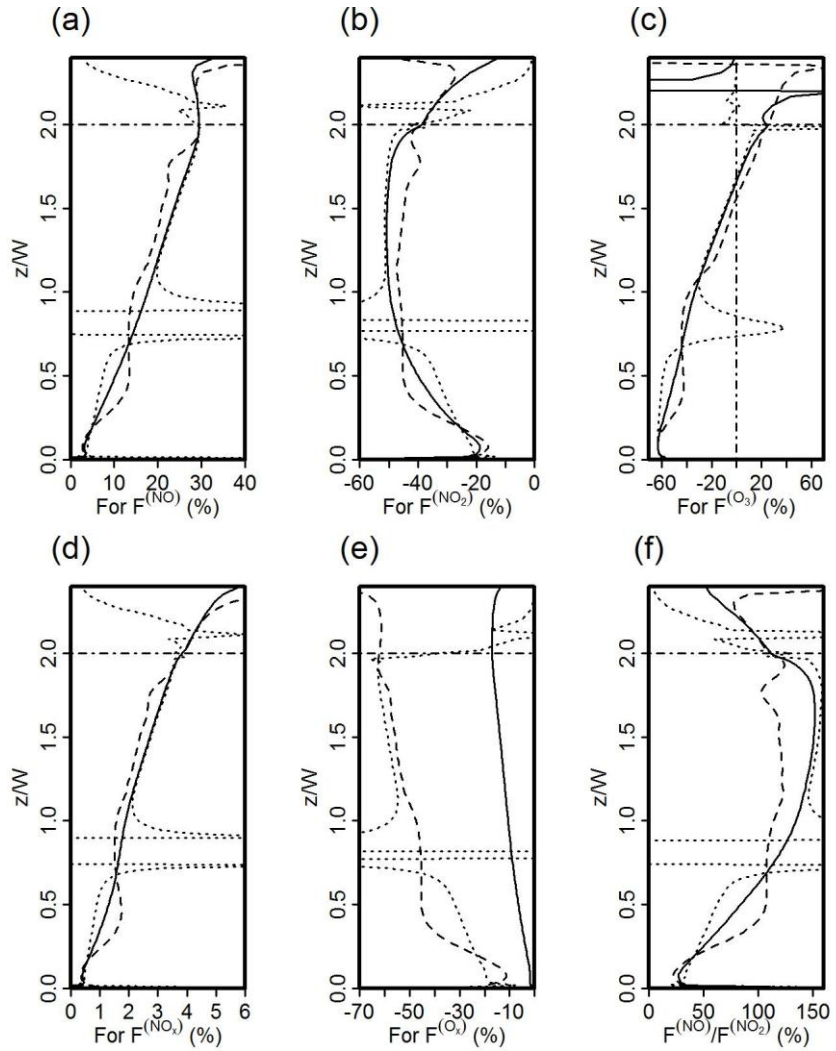

Figure 4.8 Vertical profiles of the overestimation of the spatially and temporally averaged total, turbulent and advective fluxes (%) by the simple chemistry compared with the RCS chemical mechanism for (a) NO, (b) NO_2 , (c) O_3, (d) NO_x, (e) O_x and (f) NO/NO_2 averaged across the canyon. The total, turbulent and advective fluxes for each quantity are represented by the solid, dash and dotted lines, respectively.

4.3.4 Segregation effects

Table 4.1 lists intensities of segregation (in percentage) between selected pairs of chemical species averaged across the canyon and over the period of 180 to 240 min. It is interesting to note that intensities of segregation between A and B (where A=B) (as shown along the diagonal line in Table 4.1) are positive, with the largest value of 28.49 % between NO and NO, and the smallest value of 0.36 % between OH and OH. This is attributed to the fact

that the auto-covariance of any chemical species is always positive if the chemical species is not homogenously distributed within the canyon. Intensities of segregation between A and B (where A=B) may reflect the spatial variability of the chemical species within the canyon relative to its mean concentration.

It is found that there are positive values for intensities of segregation between NO, NO_2 and VOCs, indicating that 'emitted chemical species' have similar correlations and are driven by the dynamical processes acting upon emissions. The highest value is found to be 22.32 %, which is the intensity of segregation between NO and VOCs. These emitted chemical species are carried by the canyon vortices and removed from the canyon roof level to the background atmosphere. Positive values of intensities of segregation between O_3, OH and HO_2 are also clearly observed, but the magnitudes are lower around 3% (e.g. 2.87 % for the intensity of segregation between O_3 and HO_2). This can be explained by considering that O_3, OH and HO_2 are 'entrained chemical species' with higher levels in the background environment than those inside the street canyon and thereby exhibiting similar behaviour. This indicates that segregation effect would enhance the rate of a reaction between pairs of species with similar origins (either 'emitted chemical species' or 'entrained chemical species').

It is also noted that negative values are found for intensities of segregation between emitted chemical species (i.e. NO, NO_2 and VOCs) and entrained chemical species (O_3, OH and HO_2). This is attributed to the opposite origin of those chemical species, i.e. one is emitted from the street canyon while the other is entrained from the background environment. Negative correlations between those species are therefore expected, giving the negative values for intensities of segregation between them. As shown in Table 4.1, these pairs of both emitted and entrained chemical species generally undergo the chemical

reactions within the canyon. The average chemical reaction rates across the canyon domain are expected to be reduced due to the incomplete mixing in such an environment, which plays a key role in determining the net chemical processing in the street canyon. Segregation effects are relatively larger between O_3 and emitted species (i.e. -11.09 % for NO, -5.10 % for NO_2, -8.91 % for VOCs) than those between OH (or HO_2) and emitted species. It is expected that the NO and O_3 titration to generate NO_2 within the street canyon is reduced by 11.09 % due to the segregation effect compared with a well-mixed system. It is also noted that intensity of segregation between VOCs and OH is -2.37 %, indicating that the canyon-averaged reaction rate between VOCs and OH will be retarded by -2.37 % due to incomplete mixing, thereby leading to a reduction in the additional conversion rate of NO to NO_2 by the VOCs oxidation chemistry. This negative intensity of segregation between VOCs and OH (about -3.4 %, slightly higher than -2.37% in this study) was also found by (Krol et al., 2000) in which a LES model in a convective atmospheric boundary layer was conducted. Auger and Legras (2007) suggested that due to the nonlinear nature of chemical processes, even a small value for intensity of segregation (e.g. 1 %) may lead to significant effects on the mean concentrations, especially while the pollutant residence time is short. This further indicates that segregation effects are very important and should be highlighted for any incomplete mixing environment (e.g. the street canyon), in which the interactions between the dynamics and nonlinear chemistry take place.

Table 4.1 Intensities of segregation (in percentage) between pairs of chemical species averaged among the canyon and over the period of 180 to 240 min. Values shown in parentheses and bold denote those pairs of chemical species that react directly with each other.

	O_3	NO	NO_2	VOCs	HO_2	OH
O_3	6.34	–	–	–	–	–
NO	**(-11.09)**	**(28.49)**	–	–	–	–
NO_2	**(-5.10)**	11.18	4.73	–	–	–
VOCs	**(-8.91)**	22.32	8.86	17.51	–	–
HO_2	**(2.87)**	**(-5.67)**	**(-2.44)**	**(-4.51)**	**(1.39)**	–
OH	**(1.25)**	**(-3.03)**	**(-1.17)**	**(-2.37)**	**(0.66)**	0.36

Figure 4.9 depicts spatial variations of intensities of segregation (in percentage) between (a) O_3 and NO, and (b) OH and VOCs within the street canyon ($z/W \leq 2$). It is found that there are very large negative segregation effects close to the emission source towards the windward wall at the street level. The highest negative values of intensities of segregation could be about -90 % between O_3 and NO and about -20 % between OH and VOCs. This can be explained by the large spatial variability in these regions which are directly determined by emitted species. These large negative values indicate that the associated chemical reactions near emissions are significantly reduced due to the non-uniform emissions. Large negative segregation effects were also observed at the canyon roof level towards the windward wall, i.e. about -60 % between O_3 and NO and about -8 % between OH and VOCs. This is attributed to that these regions are places where the background atmosphere (e.g. O_3 and OH) is entrained into the street canyon and then interact with the emitted species from the street canyon. The large spatial variability in these species is also expected. Towards the leeward wall near the canyon roof level, there is a rapid decrease in

the intensities of segregation for both pair of chemical species, indicating that there are much greater mixing for emitted species in these regions. It is also noted that intensities of segregation are separated by the two vortices formed in the street canyon and then increase both upwards to the canyon roof level and downwards to the street ground.

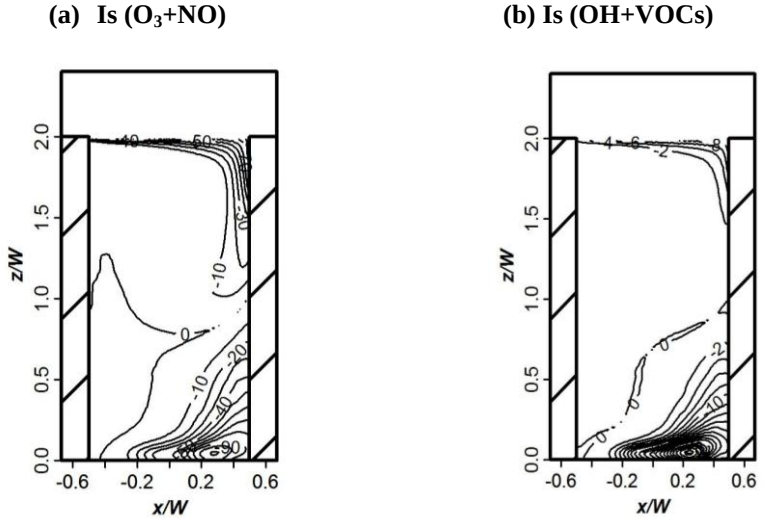

Figure 4.9 Spatial variations of intensities of segregation (in percentage) between (a) O_3 and NO; (b) OH and VOCs.

4.3.5 Development of a two-box model

The preliminary results from the LES model show the formation of two primary counter-rotating vortices (Figure 3.6) and the associated spatial variation of air pollution (Figure 4.1) in the deep street canyon (AR=2), providing the motivation to develop an alternative simplified two-box model. The averaged pollutant concentration in the lower box could be up to about 2 times than that in the upper box, which reflects the potential segregation effect by the counter-rotating vortices. In order to capture this significant concentration contrast, the deep street canyon is divided into two boxes with the corresponding vortex inside each box (Figure 3.6 and Figure 4.10) by using a plane at the level of $z/H = \alpha$ (where α is the box height ratio determined by the flow structure with the street canyon;

here $\alpha = 0.25$). It is assumed that each vortex has sufficient intensity for the chemical species to be well-mixed within the corresponding box (Murena et al., 2011). The mass transfer between two adjacent boxes is expressed by the introduction of an 'exchange velocity'. A one-box chemistry model has been previously adopted by Liu and Leung (2008) to study reactive pollutant dispersion in street canyons (AR=0.5, 1, 2), using the values of exchange velocities derived from LESs for different ARs. Because they treated the whole canyon as one well-mixed box for all ARs, their model was unable to reproduce the substantial contrasts of pollutant concentration between the lower and upper canyon as shown in Figure 4.1. In this study, a more complex box model (i.e. a two-box model) is adopted. The mathematical description of the two-box model (Figure 4.10) is as follows:

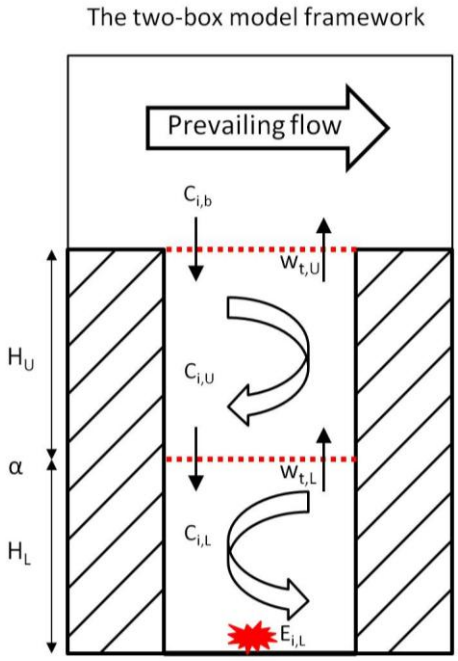

Figure 4.10 Sketch of the two-box model framework. $C_{i,L}$ **and** $C_{i,U}$ **are the concentrations of ith species in the lower and upper boxes, respectively;** H_L **and** H_U **are the height of the lower and upper boxes, respectively;** $w_{t,L}$ **is the exchange velocity between the lower and upper boxes, and** $w_{t,U}$ **is the exchange velocity between the upper box and the overlying background atmosphere; and** $E_{i,L}$ **is the emission rates of ith species.**

$$\frac{dC_{i,L}}{dt} = -\frac{w_{t,L}}{H_L}(C_{i,L} - C_{i,U}) + E_{i,L} + \Delta S_{i,L} \quad (4.20)$$

$$\frac{dC_{i,U}}{dt} = \frac{w_{t,L}}{H_U}(C_{i,L} - C_{i,U}) - \frac{w_{t,U}}{H_U}(C_{i,U} - C_{i,b}) + \Delta S_{i,U} \quad (4.21)$$

where $C_{i,L}$ (ppb) and $C_{i,U}$ (ppb) are concentrations of i^{th} species in the lower and upper boxes, respectively; t (s) is the time; H_L (m) and H_U (m) are heights of the lower and upper boxes, respectively; $w_{t,L}$ (m s^{-1}) is the exchange velocity between the lower and upper boxes, and $w_{t,U}$ (m s^{-1}) is the exchange velocity between the upper box and the overlying background atmosphere; $\Delta S_{i,L}$ (ppb s^{-1}) and $\Delta S_{i,U}$ (ppb s^{-1}) are chemical sources of i^{th} species in the lower and upper boxes, respectively; and $E_{i,L}$ (ppb s^{-1}) is emission rates of i^{th} species.

Exchange velocities implemented into the two-box model are determined from the current LES model by calculating the ventilation of a passive scalar, i.e. $w_{t,L} = \frac{F_{ps,L}}{C_{ps,L} - C_{ps,U}}$ and $w_{t,U} = \frac{F_{ps,U}}{C_{ps,U} - C_{ps,b}}$, where $F_{ps,L}$ is the flux between the lower and upper boxes, $F_{ps,U}$ is the flux between the upper box and the overlying background atmosphere and 'ps' denotes the passive scalar. The resulting values applied into the two-box model are 0.018 m s^{-1} for $w_{t,L}$ and 0.014 m s^{-1} for $w_{t,U}$.

Figure 4.11 shows the time evolution of the volume averaged mixing ratios of NO, NO_2, O_3, NO_x, O_x, OH and HO_2 calculated by the LES-chemistry model and the two-box model, respectively. Volume- and time-averaged (over the period of 180-240 min) mixing ratios

in the lower and upper boxes derived from the LES-chemistry model and the two-box model are also listed in Table 4.2. In Figure 4.11, it is interesting that there are apparent fluctuations in the mixing ratios of chemical species (especially for NO and NO_2) inherent in the LES approach due to dynamically-driven variability of large scale eddies and unsteady ventilation caused by the two primary vortices in the canyon. It is observed that there are rapid changes in mixing ratios when the emissions are released into the street canyon at 30 min. Compared with the LES-chemistry model over the period of 180-240 min, the two-box model underestimates NO levels by about 5.25 % and 5.8 % for the lower and upper boxes respectively, but overestimates NO_2 levels by about 8.47 % and 5.94 % for the lower and upper boxes respectively. Levels of O_3 derived from the two-box model are about 1.97 % and 1.83 % lower for the lower and upper boxes respectively than those derived from the LES-chemistry model. These differences are small, suggesting that the two-box approach performs pretty well compared with the "ture" LES-chemistry model. These results also indicate that *segregation effects caused by incomplete mixing (i.e. spatial inhomogeneity represented by the LES-chemistry model) reduce the conversion rate of NO to NO_2 through chemistry* (dominated by NO and O_3 titration with an additional pathway through VOCs chemistry), which is consistent with negative values of intensities of segregation between NO and O_3, and between OH and VOCs (shown in Table 4.1). It is also observed that NO_2/NO ratios in the two-box model are generally higher than those in the LES-chemistry model, i.e. about 14.47 % for the lower box and about 12.50 % for the upper box. Therefore, there are higher levels of O_3 and NO, but lower levels of NO_2 in the LES-chemistry model than those in the two-box model for both lower and upper boxes. The LES-chemistry model has slightly higher levels of NO_x (about 1.59 % for the lower box and 1.69 % for the upper box) compared with the two-box model, which suggests that

segregation effects slightly reduce the NO_x loss rate to other species (e.g. HNO_3 and HONO). This is also consistent with negative values of intensities of segregation between OH and NO_2, and between OH and NO (shown in Table 4.1). Lower levels of O_x are observed in the LES-chemistry model compared with the two-box model, i.e. about 7.89 % for the lower box and 5.15 % for the upper box. This indicates that *segregation effects generally reduce the rate of oxidation chemistry* for both the lower and upper boxes. It is observed that the two-box model slightly underestimates levels of both OH and HO_2 (generally around 1%) compared with the LES-chemistry model. This may be explained as levels of OH and HO_2 are rather lower within street canyons and their reactions with other chemical species are very fast. Segregation effects can reduce the rate for some of these chemical reactions, but increase the rate for others of these chemical reactions (indicated in Table 4.1). The total segregation effect may be slightly balanced by each other. In terms of general performance, the two-box model generally matches the LES approach in the mixing ratios for both the lower and upper boxes.

Table 4.2 Volume- and time-averaged (over the period of 180-240 min) mixing ratios in the lower and upper boxes derived from the LES-chemistry model (LES-RCS) and the two-box model (BOX-RCS), respectively.

	Mixing ratio (ppb) for Lower Box				Mixing ratio (ppb) for Upper Box			
180-237m	(A) LES-RCS	(B) Box-RCS	(B)-(A)	[(B)-(A)]/(A) %	(C) LES-RCS	(D) Box-RCS	(D)-(C)	[(D)-(C)]/(C) %
O_3	9.7858	9.59	-0.1930	-1.9722	14.25	13.9900	-0.2618	-1.8367
NO	462.4665	438.18	-24.2825	-5.2507	231.31	217.8370	-13.4744	-5.8252
NO_2	168.1708	182.41	14.2362	8.4653	125.36	132.8130	7.4497	5.9425
OH(ppt)	0.103619	0.1023	-0.0013	-1.2482	0.1115	0.1111	-0.0005	-0.4080
HO_2(ppt)	0.265364	0.2640	-0.0013	-0.4991	0.3210	0.3186	-0.0024	-0.7387
NO_x	630.6373	620.5910	-10.0463	-1.5930	356.6747	350.6500	-6.0247	-1.6891
O_x	177.9566	191.9999	14.0432	7.8914	139.6151	146.8030	7.1879	5.1484
HO_x	0.3690	0.3664	-0.0026	-0.7095	0.4325	0.4297	-0.0028	-0.6534
NO_2/NO	0.3636	0.4163	0.0526	14.4761	0.5420	0.6097	0.0677	12.4956

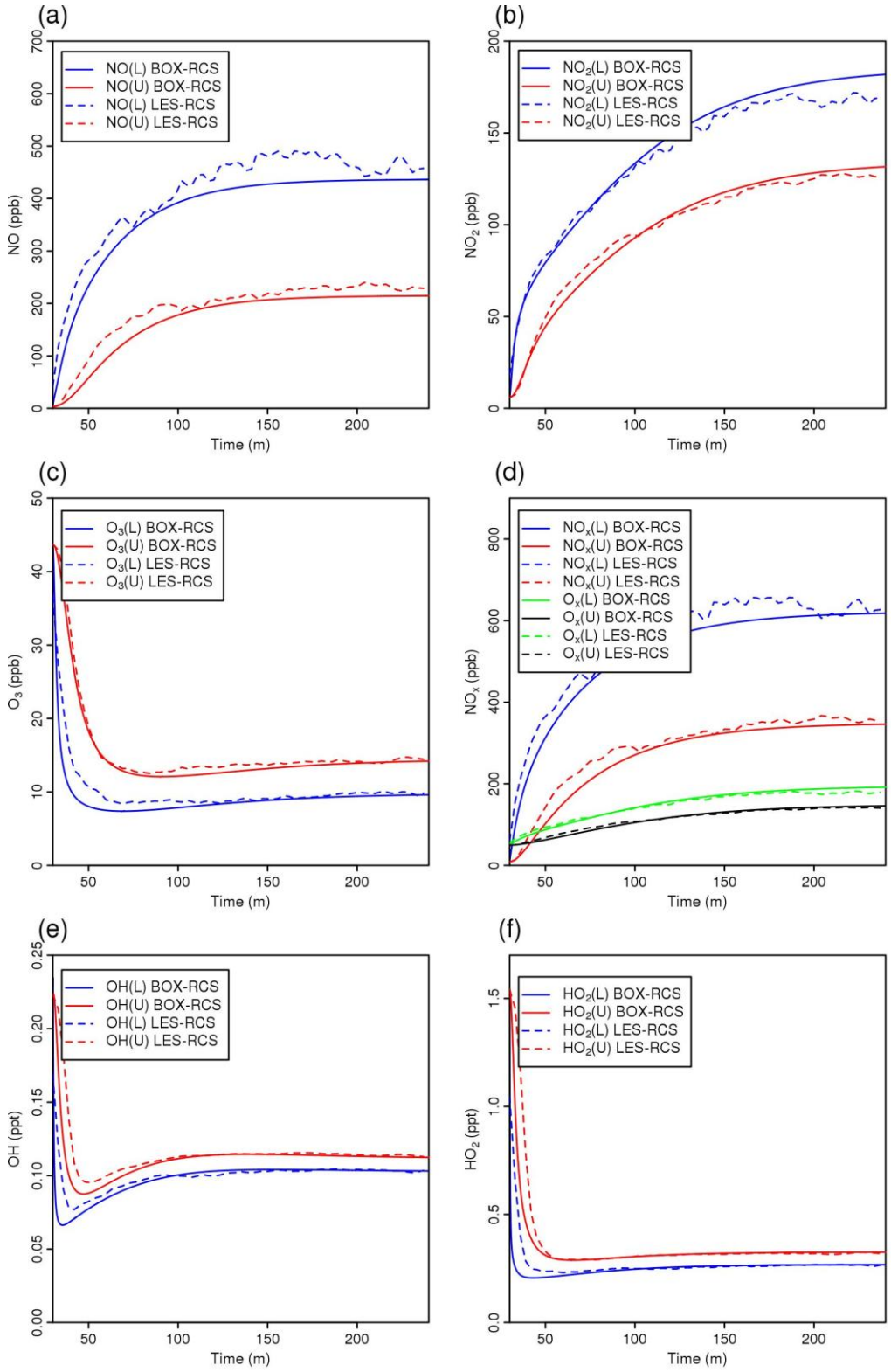

Figure 4.11 Time evolution of the volume averaged mixing ratios of (a) NO, (b) NO_2, (c) O_3, (d) NO_x and O_x, (e) OH and (f) HO_2 derived from the LES-chemistry model (LES-RCS) and the two-box model (BOX-RCS), respectively. 'L' represents the lower box while 'U' represents the upper box.

4.3.6 Temporal variation of air pollution: exposure assessment

Figures 4.12 a-c show time series of concentrations for (a) NO, (b) NO_2 and (c) O_3 (indicated by solid lines) and their averaged concentration (indicated by dashed lines) over the period of 180 to 240 min with an interval of 3 second at the left (L) and right (R) of the lower (L) and upper (U) parts of the canyon in the middle vertical plane (i.e. y=0). 'LL' and 'LR' represent the left and right of the lower part of the canyon, i.e. (x/W=-0.4, z/W=0.1) and (x/W=0.4, z/W=0.1) respectively. 'UL' and 'UR' represent the left and right of the upper part of the canyon, i.e. (x/W=-0.4, z/W=1.1) and (x/W=0.4, z/W=1.1) respectively. The LES outputs are stored in every 3 second over that period. It is noted that there are significant short-term concentration fluctuations for NO, NO_2 and O_3 and those concentration fluctuations in the lower part of the canyon are less pronounced than those in the upper part of the canyon, which is related to the air pollution measurement procedures and sampling frequency. This is attributed to that those concentration fluctuations are strongly dependent upon the fluctuations of the flow turbulence inside the street canyon, the location of emissions (from ground level) and the nonlinear photochemistry. The upper part of the canyon is mainly influenced by the background above the canyon, while the lower part of the canyon is mainly influenced by the emissions at the ground level. The turbulence in the upper canyon is stronger than that in the lower canyon (indicated by the velocities in Figure 3.5), which is consistent with the highly frequent concentration fluctuations for the upper part of the canyon. The globally defined Reynolds number (See Section 3.3) can serve as a good indicator of flow characteristics (such as laminar vs turbulent flows) as a whole and is estimated as the order of 10^6 in the current simulation (See Section 3.3), which is much higher than the critical Reynolds number of 10^4 for the whole region in a large variety of flows (Cui et al., 2014). The Reynolds number locally

for the upper canyon ($\mathrm{Re}_U = U_U W/\nu$, where U_U is the velocity scale in the upper canyon) is estimated as the order of 10^5 and the Reynolds number locally for the lower canyon ($\mathrm{Re}_L = U_L W/\nu$, where U_L is the velocity scale in the lower canyon) is estimated as the order of 10^4. This indicates that the turbulent intensity of flow in the lower canyon is relatively smaller than that in the upper canyon. For the lower part of the canyon, the atmospheric composition is changed mainly through the effect of the nonlinear photochemistry with emissions rather than the effect of the weak flow turbulence. Also, since emissions in the LES-chemistry model are assumed as constant values, the temporal concentration fluctuations are expected to be underestimated compared with those in the real world. Concentrations of NO and NO_2 in the lower canyon are significantly higher than those in the upper canyon, which reflects that the emissions of NO and NO_2 are more trapped by the lower vortex. Concentrations of NO and NO_2 on the left side are considerably lower than those on the right side for the lower canyon, but considerably higher for the upper canyon. Therefore, for NO and NO_2, the highest concentrations are at the right side of the lower canyon and lowest concentrations are at the left side of the upper canyon. This can be explained by the two aligned vortices with opposite circulation direction (i.e. the clockwise vortex in the upper canyon and the anti-clockwise vortex in the lower canyon). But for O_3, the situation is reversed since O_3 is not emitted from the street canyon, but titrated by the emitted NO at the lower canyon. Also, O_3 is entrained from the background above the canyon into the street canyon. For O_3, the lowest concentrations are at the right side of the lower canyon and highest concentrations are at the left side of the upper canyon. For the left and right side in the lower and upper canyon (i.e. the order is LL, LR, UL and UR), mean concentrations (indicated by dashed lines) and standard deviations (the variability of mixing ratios) are 278.58±55.13, 844.28±254.53,

233.38±48.49 and 142.25±52.84 ppb for NO, 139.21±12.46, 228.31±41.76, 127.99±13.14 and 96.82±21.09 ppb for NO_2 and 11.74±1.37, 6.48±1.05, 12.87±1.39, 16.96±2.99 ppb for O_3 respectively (shown as Table 4.3). The ratio of standard deviations to mean concentrations (expressed as percentages in Table 4.3) for NO, NO_2 and O_3 at the right side are up to about 2 times higher than those at the left side for both the lower and upper canyon. The ranges of percentages are (19.80 %, 37.15%) for NO, (8.95%, 21.78%) for NO_2, (10.81%, 17.63%) for O_3, indicating that those percentages are generally slightly higher for the species with higher mean concentrations (such as NO). Figure 4.12d illustrates spectral turbulent kinetic energy distributions (frequency spectrum) in the log-linear coordinates. Fast Fourier Transformation (FFT) was applied for all three components of velocity fluctuations in order to obtain the spectra for the turbulent kinetic energy (i.e. $E(f)$, where f is the frequency) (Dobre et al., 2005). The spectra are normalised by E_{norm}/f, where E_{norm} is the turbulent kinetic energy at the canyon roof level. The frequency (f) is normalised by T_s^{-1}, where T_s (=3 s) is the time interval of data output. It is interesting to note that there are broad maxima in spectral energy and the magnitude of these maxima in the upper canyon is generally higher (about 2~3 times) than those in the lower canyon. Corresponding time scales for these spectral maxima are around 60-150 s (i.e. values of $f*T_s$ from 0.02 to 0.05) for the upper canyon and around 300-1000 s (i.e. values of $f*T_s$ from 0.003 to 0.01) in the lower canyon. These findings indicate that the turbulent flow in the upper canyon is generally more energetic with shorter timescales than that in the lower canyon.

(a) Time series of NO concentrations **(b) Time series of NO_2 concentrations**

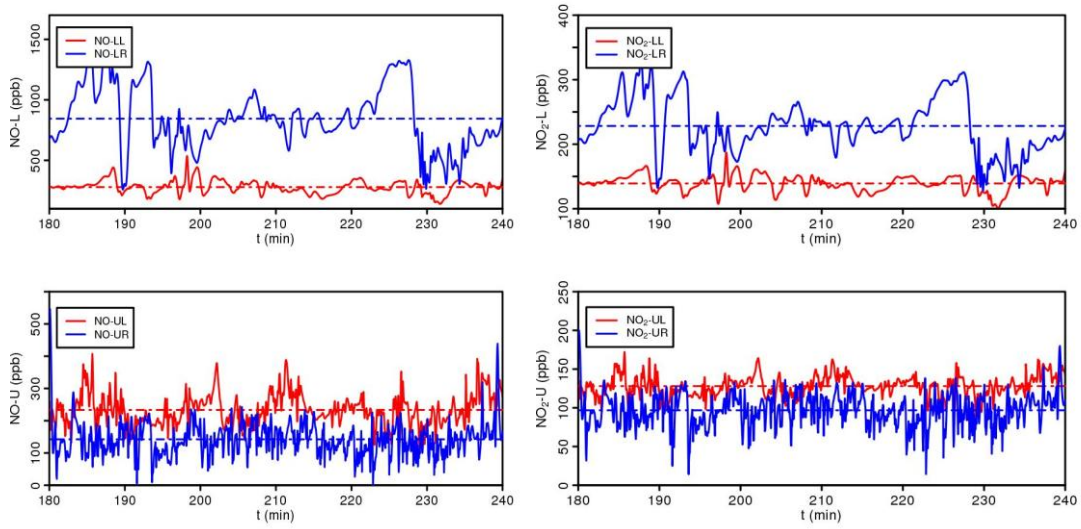

(c) Time series of O_3 concentrations **(d) Spectral turbulent kinetic energy distributions**

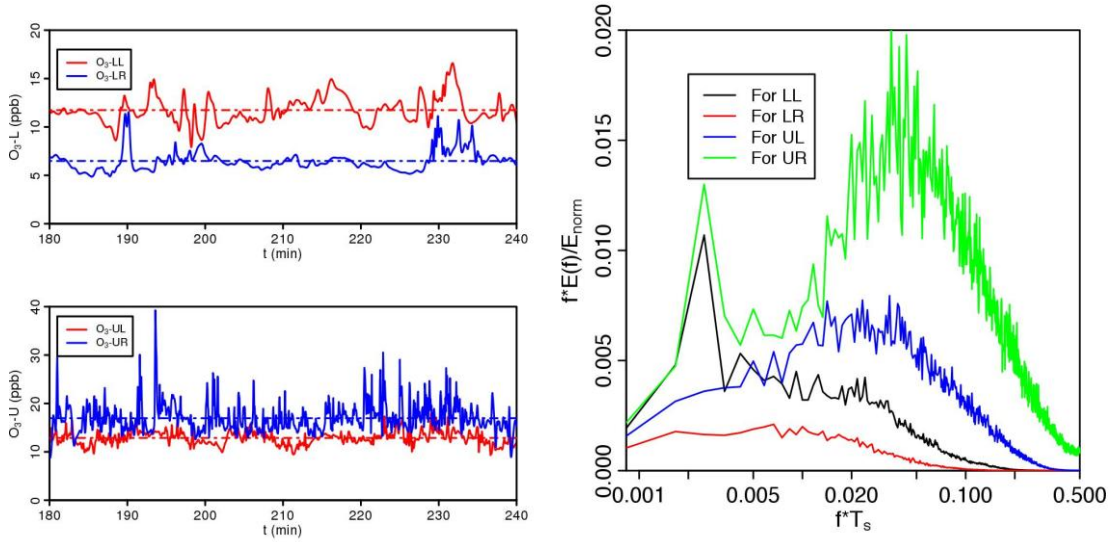

Figure 4.12 Time series of concentrations for (a) NO, (b) NO_2, and (c) O_3 over the period of 180 to 240 min with an interval of 3 second (averaged concentrations indicated by dashed lines) and (d) Spectral turbulent kinetic energy distributions at the left (L) and right (R) of the lower (L) and upper (U) parts of the canyon.

Table 4.3 Overview of statistics for time series data-sets of NO, NO_2 and O_3 over the period of 180 to 240 min at the left (L) and right of the lower (L) and upper (U) parts of the canyon.

	NO			
	LL	LR	UL	UR
Mean (ppb)	278.58	844.28	233.38	142.25
Median (ppb)	279.32	816.67	228.43	138.11
SD (ppb)	55.13	254.53	48.49	52.84
SD/Mean (%)	19.80	30.15	20.78	37.15
Skewness	0.408	0.283	0.579	1.81
	Right-skewed	Right-skewed	Right-skewed	Right-skewed
kurtosis	4.210	2.763	3.536	13.352
	Peaked	Flat	Peaked	Peaked
	NO_2			
	LL	LR	UL	UR
Mean (ppb)	139.21	228.31	127.99	96.82
Median (ppb)	140.64	225.39	127.5	96.72
SD (ppb)	12.46	41.76	13.14	21.09
SD/Mean (%)	8.95	18.29	10.27	21.78
Skewness	-0.332	0.183	0.134	0.122
	Left-skewed	Right-skewed	Right-skewed	Right-skewed
kurtosis	3.576	2.685	3.226	4.83
	Peaked	Flat	Peaked	Peaked
	O_3			
	LL	LR	UL	UR
Mean (ppb)	11.74	6.48	12.87	16.96
Median (ppb)	11.53	6.31	12.84	16.46
SD (ppb)	1.37	1.05	1.39	2.99
SD/Mean (%)	11.69	16.15	10.81	17.63
Skewness	0.613	1.79	0.298	1.54
	Right-skewed	Right-skewed	Right-skewed	Right-skewed
kurtosis	3.826	7.707	3.387	8.902
	Peaked	Peaked	Peaked	Peaked

Figure 4.13 illustrates percentiles for NO, NO_2 and O_3 over the period of 180 to 240 min at the left (L) and right (R) of the lower (L) and upper (U) parts of the canyon. The 5^{th}, 25^{th}, 50^{th}, 75^{th} and 95^{th} percentiles of NO, NO_2 and O_3 are highlighted by round points. There is a clear shift for different locations within the canyon. As expected, concentrations for a given percentile generally increase with the increase in percentiles. A nearly linear relationship between them is observed while the percentile ranges from 25^{th} to 75^{th}. It is also noted that there is a sharp gradient below 5^{th} and above 95^{th} percentiles. The greatest spread between 5^{th} and 95^{th} percentiles of NO and NO_2 are on the right side in the lower part, i.e. (439, 1303) ppb for NO, (160, 303) ppb for NO_2. But for O_3, it is on the right side in the upper part, i.e. (13, 22) ppb. The concentrations for a given percentile at the left side

of both lower and upper canyon are relatively close to each other, but higher than those at the right side of the upper canyon and lower than those at the right side of the lower canyon for NO and NO_2. The situation is reversed for O_3. The concentrations at the 50^{th} percentile, also called the median, are generally close to the mean concentrations (shown as Table 4.3).

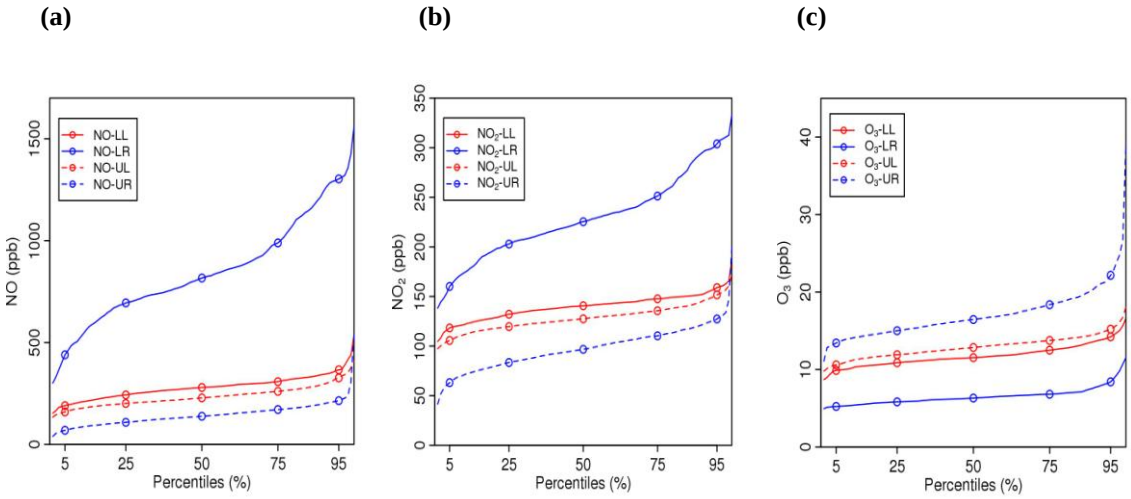

Figure 4.13 Percentiles for NO, NO_2 and O_3 over the period of 180 to 240 min at the left (L) and right (R) of the lower (L) and upper (U) parts of the canyon. The points indicated represent the 5^{th}, 25^{th}, 50^{th}, 75^{th} and 95^{th} percentiles of NO, NO_2 and O_3.

Figure 4.14 illustrates frequency histograms of NO, NO_2 and O_3 over the period of 180 to 240 min at the left (L) and right (R) of the lower (L) and upper (U) parts of the canyon. The dash and dotted red lines denote the canyon-averaged values from the LES and box models, respectively (Section 4.3.5). It is noted that these statistics in Figure 4.14 are not reflected by the box model output. There is clear evidence that multiple peaks are observed in the frequency histogram of NO and NO_2 for the right side in the lower part. The lower part is the place where emissions take place. These peaks can be expressed by the combined effect of primary emissions, chemical processing and mixing. The peak with highest frequency is about 720 ppb for NO and about 200 ppb for NO_2. The peaks at a

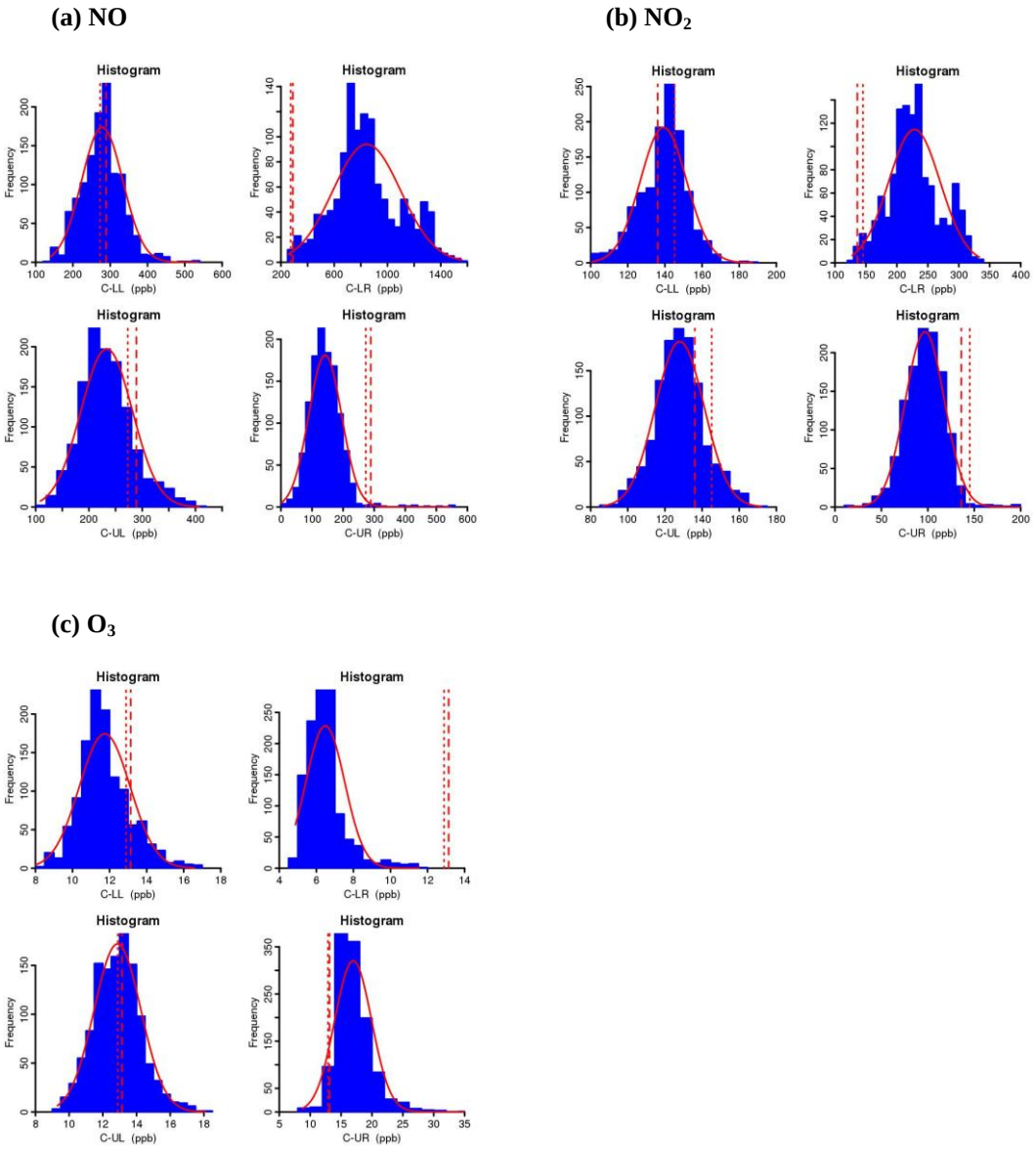

Figure 4.14 Frequency histograms of (a) NO, (b) NO_2 and (c) O_3 over the period of 180 to 240 min at the left (L) and right (R) of the lower (L) and upper (U) parts of the canyon. The dash and dotted red lines denote the canyon-averaged values from the LES and box models, respectively.

higher concentration (but with lower frequency) are attributed to the direct effect of primary emissions of NO (around 1200 ppb) and NO_2 (about 300 ppb) from the (simulated) ground-level traffic. These emissions are carried towards the right side at the lower part and periodically contribute to higher concentrations at the corresponding receptor location. It is also observed that there are peaks at lower concentration with very low frequency for

NO_2. This may be explained by that the chemical processing (i.e. the titration effect) periodically converts the primary emitted NO to NO_2. For the left side in the lower part, there are relatively longer tails of higher concentrations for NO and NO_2, which may be due to the re-circulation of the emissions of NO and NO_2 in the lower vortex, occasionally giving extremely high concentrations (about 500 for NO and about 190 for NO_2). This phenomenon is also found at the right in the upper part of the canyon. This may be attributed to the mixing zone between the unsteady lower vortex and upper vortex, which can occasionally carry an air parcel with high concentrations from the lower part to upper part at the right side. The highest concentrations could be about 550 ppb for NO and about 200 ppb for NO_2, which are slightly higher than those at the left side in the lower part. This indicates that the air parcels with higher concentrations at the right side in the lower part are dispersed relatively quickly to the right side in the upper part (short vertical distance) through the mixing processes than to the left side in the lower part through the re-circulation of the lower vortex. Generally, there is no clear evidence of multiple peaks for the upper part of the canyon, indicating that the upper canyon is more influenced by the mixing and chemical processing.

There are also multiple peaks (to some extent) observed in the frequency histogram of O_3 for the right side and lower part of the canyon. As O_3 is not emitted directly, but titrated by the primary NO emitted from the street ground. The distribution of O_3 can be solely influenced by the combined effect of the mixing and chemical processing. The right side of the lower part is expected to be more affected by the emissions thereby leading to significant titration effect. The first peak with higher frequency is relatively low (about 6.5 ppb) and most of the observations fall into the region around the peak. There are also small peaks at higher concentrations. This may correspond to occasional lower levels of NO or

high levels of NO_2 which reduce the titration effect. The concentration on the left side of lower canyon is generally higher than that at the right of the street canyon, which indicated the anti-clockwise re-circulation of emissions. For the upper canyon, the distribution is more affected by the higher background abundance of O_3 from the canyon above. As the vortex is clockwise, levels on the right side are more strongly dependent upon the background. Therefore, there is a longer tail of high concentrations of O_3 for the right of the upper canyon due to the mixing of background air.

4.4 Conclusions

The dispersion and transport of air pollution in a deep urban street canyon (AR=2) has been examined using the LES-chemistry model, which is capable of simulating the coupling effect of emissions, mixing and chemical pre-processing within the street canyon. It is observed that two vertically aligned unsteady vortices determine the dispersion and transport of reactive pollutants within the street canyon. Reactive pollutants exhibit significant spatial and temporal variations caused by the two vortices. Due to the simple assumption of the idealised street canyon geometry under perpendicular ambient wind, flow field within the canyon is dominated by flow recirculation (i.e. two vortices). However, the current LES model of idealised scenarios does not capture lateral channelling flow (e.g. Longley et al., 2004) or even helical flow (e.g. Dobre et al. (2005); Barlow et al. (2009)) present in real, complex urban street canyons (Smalley et al. (2008)). Pollutant levels (e.g. NO_x) on the leeward wall are generally higher (around 1.5 to 2 times) than those on the windward wall in the upper part of the canyon, but lower (around 50% to 70%) than the windward levels in the lower part of the canyon. Ground-level sourced pollutants (e.g. NO_x) are found to be largely trapped within the anti-clockwise lower vortex. Such findings are very useful in the assessment of air pollution in deep street

canyons. At the pedestrian level, higher concentrations of pollutants are found towards the windward than leeward buildings in the deep street canyon (AR=2), which is opposite to the results for the case of AR=1 as investigated by previous studies. This suggests that the findings for the AR=1 case may not be appropriate for the assessment of pollutant exposure at the pedestrian level in a deep street canyon.

The pre-processing of air pollution within the street canyon is also influenced by the two unsteady vortices. It is found that advective fluxes are dominant for both the upper vortex and the lower vortex while turbulent fluxes are dominant for the shear layer at the roof level. This finding indicates that advective fluxes play a dominant role for the transport of pollutant within a vortex while turbulent fluxes play an important role for the exchange of pollutant within the zone between the vortices. Pre-processing within the canyon results in significant conversion of NO to NO_2, indicated by the NO/NO_2 ratio of total fluxes at the canyon roof level being much lower than the raw emission ratio of NO/NO_2 (i.e. 1.7 vs 9). Such findings can be of importance in guiding the development of atmospheric pollutant flux parameterisation schemes for larger scale (e.g. city or regional scale) models.

The effect of HO_x oxidation chemistry is evident. Imperfect mixing (reflected in non-zero values of the PSS defect) results in negative apparent chemical ozone production, representing a systematic error if such a NO_x-O_3-steady-state-defect approach is applied to obtain ozone production rates within a poorly-mixed environment close to NO_x emissions sources. The substantial magnitude of the apparent ozone loss rate, relative to those encountered in the wider boundary layer / free troposphere, further suggests that even at some distance from fresh emissions, mixing-derived PSS defects may limit this approach to inferring chemical ozone production. The indirect approach to estimate ozone production rate based on the PSS gives the wrong results in a street canyon environment,

and instead reflects the effect of incomplete mixing. Compared with the RCS chemical mechanism, simple NO_x-O_3 chemistry would overestimate the NO level (by about 30 %), but underestimate levels of NO_2 and O_3 (by about -38% and -52% respectively), indicating the additional conversion of NO to NO_2 through VOCs oxidation chemistry, which was previously thought to be unimportant for small (temporal and spatial) scale processes. Such findings suggest that using simple NO_x-O_3 chemistry may provide an overly optimistic prediction of air pollution in street canyon from the perspective of NO_2 levels, which already exceed the air quality standards in many places in a city, with consequences for air quality management if such predictions are adopted.

Segregation effects due to incomplete mixing within the street canyon are investigated using intensity of segregation between pairs of chemical species. There is clear evidence of two distinctive behaviours for emitted chemical species and entrained chemical species. Positive (or negative) values of intensities of segregation are found between the pair of species with a similar (or opposite) behaviour. It is expected that segregation effects within the street canyon reduce the NO and O_3 titration rate (by 11.09 %), and the VOCs-OH oxidation rate (by 2.37 %). Therefore the conversion of NO to NO_2 within street canyon will be reduced compared with that in a well-mixed system. Large segregation effects are observed in the regions close to the emission source and near the canyon roof level, where the spatial variability can be extremely significant. Segregation effects are separated by the two vortices formed in the street canyon. Such findings indicate that segregation effects are of importance in the incomplete mixing environment (e.g. the street canyon) with chemical processing involved.

The formation of two primary counter-rotating vortices and the associated spatial variation of air pollution in the deep street canyon provide a potential to develop an alternative

simplified two-box model. The significant concentration contrast between the lower and upper box is well reproduced by the two-box model. The two-box model underestimates NO and O_3 levels, but overestimates NO_2 levels for both the lower and upper boxes compared with the LES-chemistry model. NO_2/NO ratios in the two-box model are found to be much higher than those in the LES-chemistry model, i.e. about 14.47 % for the lower box and about 12.50 % for the upper box. It is suggested that segregation effects due to incomplete mixing (i.e. spatial inhomogeneity represented by the LES-chemistry model) reduce the conversion rate of NO to NO_2 through chemistry. The two-box model could potentially support traffic management and urban planning strategy or personal exposure assessment.

The potential exposure to air pollution is assessed by investigating the short-term time series data within the street canyon. More significant concentration fluctuations are observed in the upper part of the canyon than that in the lower part of the canyon. Concentration fluctuations within the street canyon are strongly dependent upon the fluctuations of the flow turbulence, the location of emissions and the nonlinear photochemistry. NO_2 level at the windward side of the lower canyon is found to be about 89 ppb higher than that at the leeward side of the lower canyon, which suggests personal exposure at the windward side of the lower canyon is more significant. The assumption of homogenous assumption in air pollution levels within a street canyon employed in most exposure models may not allow exposure to be accurately calculated. The spatial and temporal variation in pollutant abundance within the street canyon should be considered in exposure assessments.

5 Modelling photochemical pollutants in a street canyon: Application of a two-box model

5.1 Introduction

High levels of air pollutants were found at the pedestrian level in urban areas, especially for deep street canyons in the modelling study by Li et al. (2009). This is consistent with the field measurements in deep street canyons (Murena and Favale (2007); Murena et al. (2008)), which indicated that the pollutant concentration at pedestrian level in a deep street canyon could be up to three times that in regular street canyons. Murena (2012) attempted to implement a simplified two-box model with regard to the prediction of carbon monoxide (CO) concentration in deep street canyons. Their study provided useful guidance for the improving the performance of the street-canyon operational models, e.g. Operational Street Pollution Model (OSPM) (Buckland, 1998), which might be unreliable when applied to deep street canyons since they were developed for street canyons with unity aspect ratio. CO in their two-box model was considered as a passive scalar and therefore no chemical processing was taken into account.

A two-box model coupled with a chemical scheme (i.e. the RCS) has been developed and evaluated against the LES-chemistry model in Chapter 4. This two-box model has sucessfully captured the contrast between the bulk concentration in the lower street box and that in the upper street box. The lower street canyon is the place of interest for the assessment of human health effect (i.e. where exposure occurs). This chapter will extend the application of the two-box model approach into deep street canyons and consider both

NO_x and VOCs chemical processing under a variety of wind conditions for a wide range of emission scenarios. The performance of the one-box model considering the whole canyon as a well-mixed box will be evaluated compared with the two-box model. Several factors affecting the two-box model will be also investigated and discussed.

5.2 Application of the two-box model

5.2.1 Overestimation by the one-box model

In the box model approach, a well-mixed hypothesis is adopted, i.e. the air inside the box is assumed to be well-mixed. The box model is a particularly simple approach to describe the evolution of air pollutants, which requires low computational cost. For deep street canyons, the presence of two primary counter-rotating vortices, which separates the street-canyon flow layers with contrast features so that pollutants exhibit a significant reduction with building height, is also observed in the literature (Murena and Favale, 2007). In such situations, the well-mixed hypothesis for a whole deep street canyon tends to fail (Murena et al., 2011). Therefore, a more complex box model (i.e. a two-box model) set in series (vertically segregated), which can characterize the communication between vortices in the deep street canyon, should be developed (See 4.3.5 for the detailed mathematical description of the two-box model). Then the performance of the one-box model (with the well-mixed hypothesis for the whole deep street canyon) compared with the two-box model, shown as Figure 5.1, is evaluated below.

If the whole deep street canyon is taken as one well-mixed box, the one-box model can be described as follows:

$$\frac{d}{dt}C_{i,0}(t) = E_{i,0} - \frac{w_{t,0}}{H_0}(C_{i,0} - C_{i,b}) + \Delta S_{i,0} \tag{5.1}$$

where, $C_{i,0}$ (ppb) is the concentration of i^{th} species within the whole canyon; $E_{i,0}$ (ppb s^{-1}) is the emission rate of i^{th} species within the whole canyon; $w_{t,0}$ (m s^{-1}) is the exchange velocity between the whole canyon and background; H_0 (m) is the height of the whole; $\Delta S_{i,0}$ (ppb s^{-1}) is the net production rate of i^{th} species due to chemical reactions within the whole canyon.

(a) **(b)**

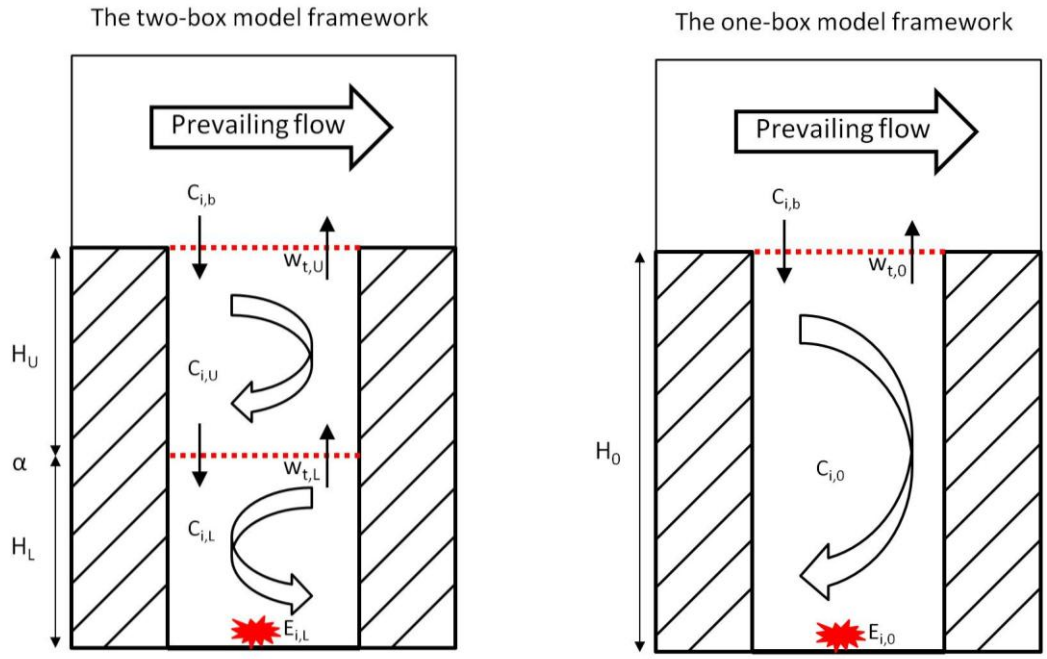

Figure 5.1 Framework of the two-box model (see Section 4.3.5 for details) and the one-box model (see text for details).

There will be an error for the "one-box" model due to the well-mixed assumption, compared with the concentration in the lower box (i.e. the interest area of potential exposure assessment) by the "two-box" model. This error can be expressed by the concentration difference due to segregation as follows:

$$\Delta C_{i,L} = C_{i,0} - C_{i,L} \tag{5.2}$$

Then we can define the percentage of overestimation by the "one-box" model compared with the concentration in the lower box by the "two-box" model due to segregation effect:

$$\phi_{i,L}(t) = \frac{\Delta C_{i,L}(t)}{C_{i,L}(t)} \times 100\% \tag{5.3}$$

5.2.2 Exchange velocities in the two-box model

Exchange velocities implemented into the two-box model can be determined from the numerical models by calculating the ventilation of a passive scalar. According to Fick's law, the flux of a passive scalar (denoted as "ps"), F_{ps} (ppb m s^{-1}), for the lower and upper box under the steady state (the "two-box" model approach) can be written as follows,

$$F_{ps} = w_{t,L}(C_{ps,L} - C_{ps,U}) \tag{5.4}$$

$$F_{ps} = w_{t,U}(C_{ps,U} - C_{ps,b}) \tag{5.5}$$

If the whole street canyon is considered as one box (the quantities associated are denoted as "0" rather than the "U" and "L" in the two box model approach), the flux of a passive scalar for the whole box under the steady state (one-box model approach) is derived as:

$$F_{ps} = w_{t,0}(C_{ps,0} - C_{ps,b}) \tag{5.6}$$

$$C_{ps,0} = \alpha C_{ps,L} + (1-\alpha) C_{ps,U} \tag{5.7}$$

Equation 5.7 can be rewritten as:

$$C_{ps,0} = C_{ps,U} + \alpha(C_{ps,L} - C_{ps,U}) \tag{5.8}$$

Here, α is the ratio of the lower box's volume to the volume of the whole canyon. When an idealised street canyon is considered, α becomes the box height ratio, H_L/H_0. H_L can be determined by the flow structure within the street canyon, namely, the height of the lower vortex.

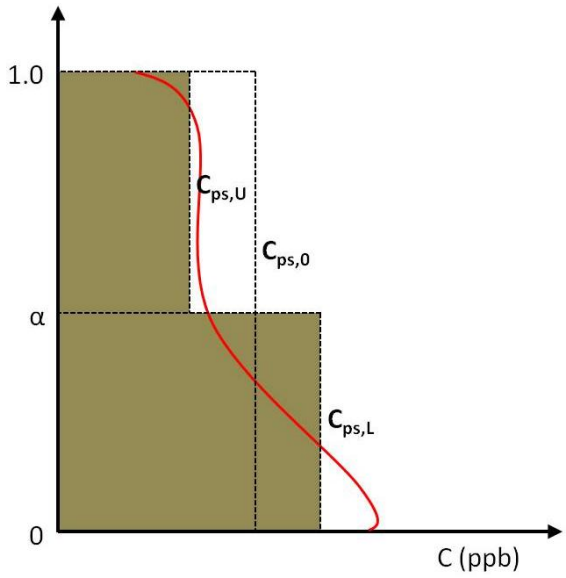

Figure 5.2 Schematic diagram of vertical concentration profile and bulk concentrations in the lower and upper boxes, and in the whole street canyon of passive scalar.

It is assumed that $C_{ps,L} \geq C_{ps,U}$ is the case for passive scalars emitted from street canyons near ground level (Figure 5.2). According to Equation 5.5, 5.6 and 5.8, $C_{ps,0} \geq C_{ps,U}$ and $w_{t,0} \leq w_{t,U}$ can be derived. Then we may also define a non-dimensional parameter to represent the heterogeneity coefficient (or spatial variation) across the two boxes, i.e.

$$\eta = 1 - \frac{w_{t,0}}{w_{t,U}} \tag{5.9}$$

where $\eta \in [0,1]$. If $\eta = 0$, then $w_{t,0} = w_{t,U}$ from Equation 5.9 and it yields $C_{ps,0} = C_{ps,U}$ according to Equation 5.5 and 5.6 and $C_{ps,U} = C_{ps,L}$ based on Equation 5.8. Thus the two

boxes are homogenous. Higher (or lower) values of η represent that the two boxes are more (or less) segregated, i.e. it possesses more (or less) significant heterogeneity.

In this study, it is assumed that $C_{ps,b} = 0$. According to Equations 5.4-5.7, it can be derived that:

$$\frac{1}{w_{t,0}} = \frac{\alpha}{w_{t,L}} + \frac{1}{w_{t,U}} \tag{5.10}$$

Based on Equations 5.4-5.10, exchange velocities for the two-box model are obtained as follows:

$$w_{t,U} = \frac{w_{t,0}}{(1-\eta)} \tag{5.11}$$

$$w_{t,L} = \frac{\alpha w_{t,0}}{\eta} \tag{5.12}$$

The physical mechanisms that determine the value of the heterogeneity coefficient (η) are explained below. For a given α ,the heterogeneity coefficient may be determined by the spatial pattern of turbulence, which could be in turn affected by the building geometry, local wind conditions, local turbulence generated by moving vehicles or thermal forcing, and damped turbulence by tree leaves or stable atmosphere, etc.. For example, the more significant local vehicle generated turbulence (or other factors) transfers more pollutants from the lower box into the upper box, giving a higher value of $C_{ps,U}$. Based on Equation 5.5, a lower value of $w_{t,U}$ is derived. Then a lower value of η is obtained based on Equation 5.9, i.e. the two-box system possesses less significant heterogeneity. If only the wind speed above the canyon is concerned, η will remain unchanged because the turbulence pattern is unaffected, although the wind speed inside the canyon will be scaled with the wind speed above the canyon (Equation 5.9).

5.2.3 Street canyon shading

The access of solar radiation into a street canyon is often highly obstructed by the surrounding buildings of the street and varies significantly over the typical daytime period (Bourbia and Awbi, 2004a). Some regions of a street canyon are shaded, while others are not. This shading effect can significantly reduce the solar radiation into the street canyon (Hwang et al., 2011) and is of vital importance in the urban environment (Bourbia and Awbi, 2004b). Photolysis reaction rates are expected to exhibit a high spatial variation in the street canyon, thereby influencing the chemical processing of reactive pollutants (Grawe et al., 2007). This shading effect can be reflected by the significant reduction of photolysis reaction rates for shaded regions in street canyons (Koepke et al., 2010) and may be considered in the urban air quality studies. For the practical application of the shading effect, parameterisations are normally adopted in the chemical models (Koepke et al., 2010). In this study, a parameter, i.e. shading ratio coefficient (RJ), is introduced as follows:

$$RJ = \frac{J_i^{shaded}}{J_i^{unshaded}} \tag{5.13}$$

where J_i^{shaded} denotes the photolysis frequency within shaded areas of the street canyon; $J_i^{unshaded}$ is the photolysis frequency within the unshaded areas of the street canyon (undisturbed conditions); i represents the i^{th} species involving the photolysis reaction. It is assumed that RJ is determined by the street properties, solar angles, and atmospheric conditions. For the general consideration of the shading effect in a street canyon, a constant value between 0 and 1 can be given for RJ . In this study, it is assumed that only the lower box in the street canyon is shaded and parameterized with the shading ratio coefficient (RJ), shown as Figure 5.3.

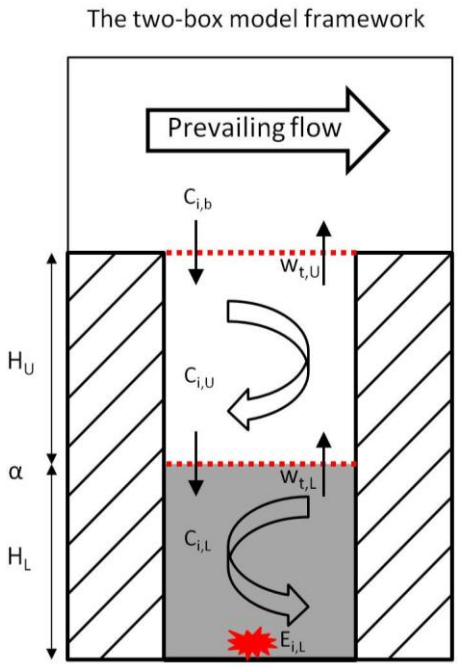

Figure 5.3 Framework of the two-box model (see Section 4.3.5 for details) considering the shading effect of the lower box.

5.2.4 Model scenarios in the two-box model

Initial and background conditions of chemistry used in the two-box model are set the same as those adopted in the LES-chemistry model (see Section 3.3 for details). In order to characterize a wide range of real scenarios, the representative E_{NOx} and E_{VOCs} are scaled by different factors of between 0.1 and 2 applied to those of the TRES values (i.e. the 'Typical Real-world Emission Scenario' defined in 3.2.3).

This chapter focuses on the effects of η (i.e. heterogeneity of concentration) and $w_{t,0}$ (i.e. exchange velocity), α (i.e. box height ratio) and RJ (shading ratio coefficient) on the NO_2 characteristics in the lower box. Table 5.1 gives an overview of the case settings. For the case BASE, these parameters are set as: $\eta = 0.5$, $w_{t,0} = 0.02$ m s^{-1}, $\alpha = 0.5$, and $RJ = 1$. The value of $\eta = 0.5$ represent a median level of heterogeneity, i.e. the pollutant

concentration in the lower (or upper) box is 50% higher (or lower) than the mean concentration averaged over the whole canyon for a given $\alpha = 0.5$. In other words, the concentration in the lower box is 3 times that in the upper box, which could be the case for deep street canyons. The value for $w_{t,0} = 0.02$ m s^{-1} is used in the same order as those derived from large-eddy simulations in street canyons. As discussed in Section 5.2.2, $w_{t,0}$ could be scaled with the wind speed above the street canyon while keeping the same turbulence pattern. The value of $\alpha = 0.5$ represents the same size of vortices for both lower and upper boxes, which could be also the case for deep street canyons. The value of $RJ = 1$ denotes the case without considering the street canyon shading effect. To investigate the effect of η, the values of other parameters are kept the same as those used in the Case BASE and test a series of values of η, i.e. Case HC-LL ($\eta = 0.1$), Case HC-L ($\eta = 0.3$), Case HC-H ($\eta = 0.7$) and Case HC-HH ($\eta = 0.9$). Likewise, a series of other cases together with their parameters are also indicated in Table 5.1, i.e. the effect of $w_{t,0}$ with Case EX-LL ($w_{t,0}$ =0.012 m s^{-1}), Case EX-L ($w_{t,0}$ =0.016 m s^{-1}), Case EX-H ($w_{t,0}$ =0.024 m s^{-1}) and Case EX-HH ($w_{t,0}$ =0.028 m s^{-1}); the effect of α with Case HB-LL (α =0.1), Case HB-L (α =0.3), Case HB-H (α =0.7), and Case HB-HH (α =0.9); the effect of RJ with Case RJ-LL (RJ=0.1), Case RJ-L (RJ=0.3), d Case RJ-H (RJ=0.7), and Case RJ-HH (RJ=0.9). For each case, the corresponding 'one-box' model and the 'two-box' model were run (Figure 5.1). Figure 5.4 illustrates the exchange velocities (based on Equations 5.11-5.12) implemented in the 'two-box' model for the scenarios in Table 5.1, considering the effect of η, $w_{t,0}$ and α, respectively. Figure 5.4a shows that, for a given $\alpha = 0.5$ and $w_{t,0} = 0.02$ m s^{-1}, as η increases, $w_{t,L}$ decreases, but $w_{t,U}$ increases. Figure

5.4b shows that, for a given $\alpha = 0.5$ and $\eta = 0.5$, as $w_{t,0}$ increases, both $w_{t,L}$ and $w_{t,U}$ increases linearly. This linear relationship is also found in the literature (Murena et al., 2011). Figure 5.4c shows that, for a given $\eta = 0.5$ and $w_{t,0} = 0.02$ (m s^{-1}), as α increases, $w_{t,L}$ remains the same level, but $w_{t,U}$ increases linearly. For street canyon shading cases, both $w_{t,L}$ and $w_{t,U}$ are the same as those used in Case BASE.

Table 5.1 Overview of the model scenarios

Case	Box heterogeneity coefficient (η)	Exchange velocity $w_{t,0}$ (m s^{-1})	Box height ratio (α)	Shading ratio coefficient (RJ)
BASE	0.5	0.02	0.5	1
HC-LL	0.1	0.02	0.5	1
HC-L	0.3	0.02	0.5	1
HC-H	0.7	0.02	0.5	1
HC-HH	0.9	0.02	0.5	1
EX-LL	0.5	0.012	0.5	1
EX-L	0.5	0.016	0.5	1
EX-H	0.5	0.024	0.5	1
EX-HH	0.5	0.028	0.5	1
BH-LL	0.5	0.02	0.1	1
BH-L	0.5	0.02	0.3	1
BH-H	0.5	0.02	0.7	1
BH-H	0.5	0.02	0.9	1
RJ-LL	0.5	0.02	0.5	0.1
RJ-L	0.5	0.02	0.5	0.3
RJ-M	0.5	0.02	0.5	0.5
RJ-H	0.5	0.02	0.5	0.7
RJ-HH	0.5	0.02	0.5	0.9

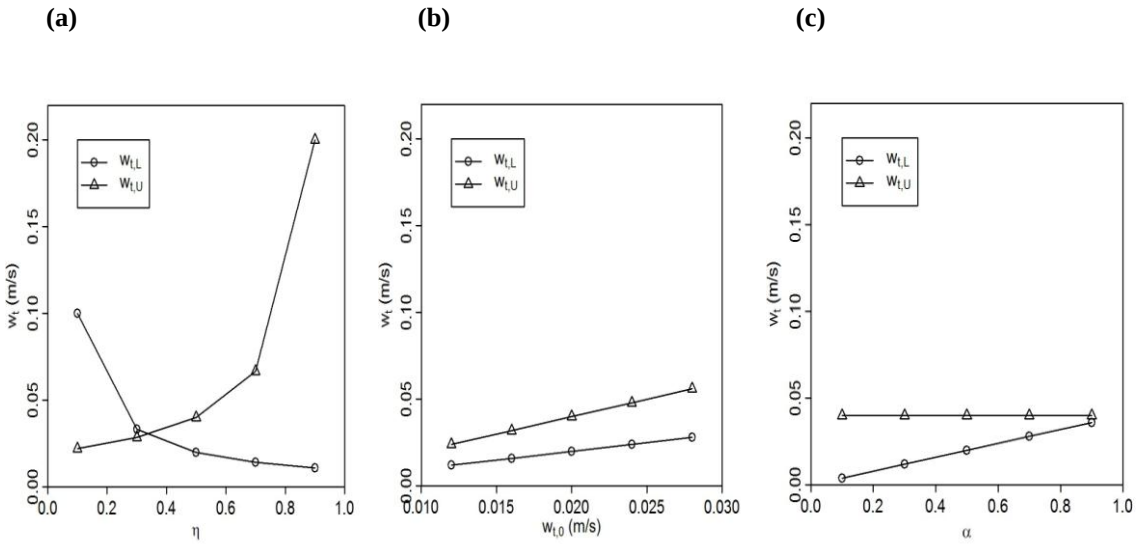

Figure 5.4 The relationship between exchange velocities for the two-box model against (a) η, (b) $w_{t,0}$ and (c) α. See Equations 5.11-5.12.

5.3 Results and discussion

5.3.1 Effect of the heterogeneity coefficient

Figure 5.5 illustrates the effect of the heterogeneity coefficient (η) on $C_{NO_2,L}$ (ppb), i.e. the NO_2 concentration in the lower box, for (a) Case HC-LL (η =0.1), (b) Case HC-L (η =0.3), (c) Case BASE (η =0.5), (d) Case HC-H (η =0.7), (e) Case HC-HH (η =0.9) and (f) Selected lines for analysis. These hypothetical cases could be related to realistic conditions. η can vary with the AR of the canyon, i.e. a larger AR will give a higher value of η due to the worse ventilation conditions. Also, lower turbulence caused by a stable atmosphere (Ramamurthy et al., 2007) and decoupling caused by an elevated tree-leaf canopy (Gromke and Ruck, 2012) will give higher values of η. In Figure 5.5, E_{VOCs} and E_{NOx} are normalised by those of the Typical Real-world Emission Scenario (TRES, represented by △), for the year of 2010. Trajectory 2005-2020 represents the changing emission scenarios

(a) $C_{NO_2,L}$ **(ppb) for Case HC-LL** **(b)** $C_{NO_2,L}$ **(ppb) for Case HC-L**

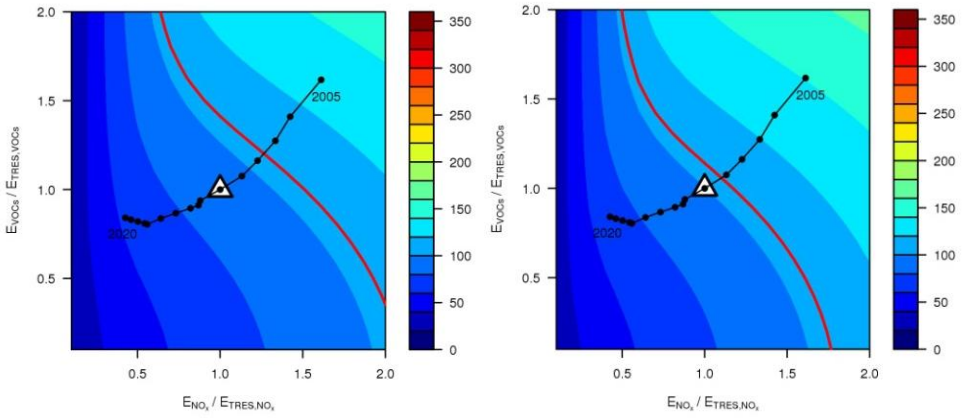

(c) $C_{NO_2,L}$ **(ppb) for Case BASE** **(d)** $C_{NO_2,L}$ **(ppb) for Case HC-H**

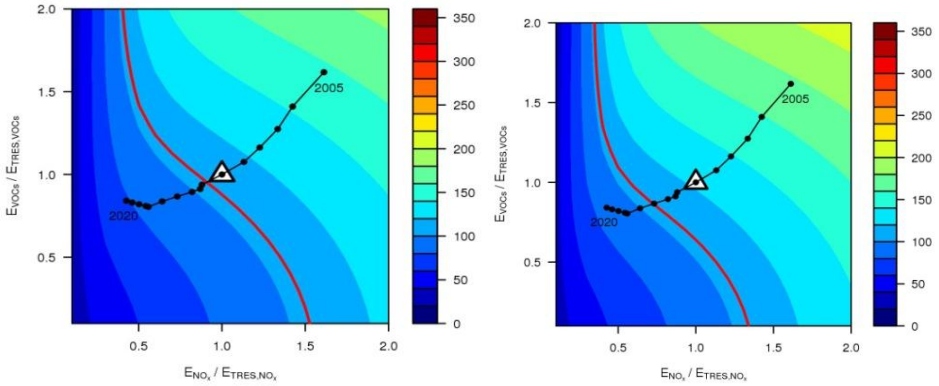

(e) $C_{NO_2,L}$ **(ppb) for Case HC-HH** **(f) Selected lines for analysis**

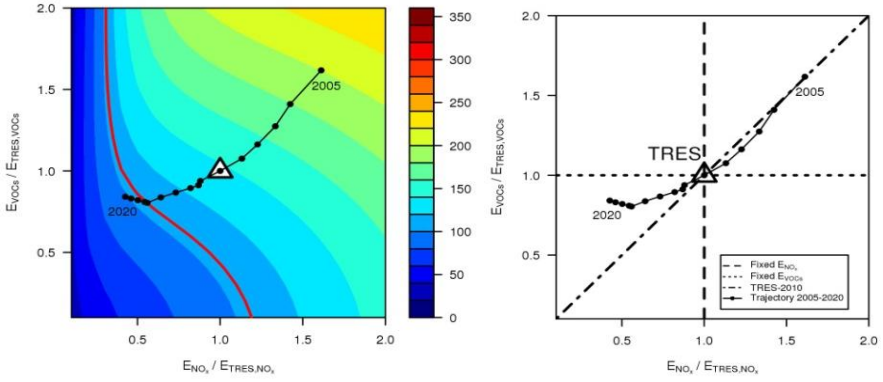

Figure 5.5 $C_{NO_2,L}$ **(ppb), i.e. the concentration in the lower box derived from the "two-box" model, in the (a) Case HC-LL (**η **=0.1), (b) Case HC-L (**η **=0.3), (c) Case BASE (**η **=0.5), (d) Case HC-H (**η **=0.7), (e) Case HC-HH (**η **=0.9) and (f) Selected lines for analysis.** E_{VOCs} **and** E_{NOx} **are normalised by those of the Typical Real-world Emission Scenario (TRES, represented by△), for the year of 2010. Trajectory 2005-2020 represents the emission scenarios for 2005 to 2020, assuming constant traffic volume and speed. The solid red curves denote the UK air quality standard of hourly NO_2 (105 ppb).**

for 2005 to 2020, which are derived from the UK fleet composition projections (NAEI, 2003) and the UK Road Vehicle Emission Factors (Boulter et al., 2009) assuming constant traffic volumes and speeds equal to those in the 'TRES' scenario for 2010 - i.e. only the emission change with vehicle technology and fleet composition is considered, rather than traffic growth. The solid red curves denote the UK air quality standard of hourly NO_2 (105 ppb). It is interesting to note that $C_{NO_2,L}$ generally has a similar pattern for the cases and increases with the heterogeneity coefficient from 0.1 (Figure 5.5a) to 0.9 (Figure 5.5e). This can be explained by the poor exchange between the lower and upper box (indicated by a lower value of $w_{t,L}$ in Figure 5.4) so that the heterogeneity coefficient is high. The higher heterogeneity coefficient may also reflect the less local traffic produced turbulence in the lower box, which reduces the air ventilation from the lower box to the upper box. This is consistent with the finding by Murena et al. (2011) that there would be a lower exchange velocity between the lower and upper box and a higher level of pollutant concentration in the lower box for the case without considering the local traffic produced turbulence. Many previous studies (e.g. Kastner-Klein et al. (2000); Jicha et al. (2000); Kastner-Klein et al. (2001); Vachon et al. (2002)) were also in support of that the traffic produced turbulence can enhance the street-level mixing. This indicates that the heterogeneity in the street canyon significantly influences pollutant concentrations in the lower box. Therefore, it is not surprising that the solid red curve shifts from the higher emission region to the lower emission region as the heterogeneity coefficient increases (Figure 5.5a-e). It is also noted that emissions at the TRES level are expected to lead to exceedance of the UK air quality standard of hourly NO_2 while the heterogeneity coefficient is larger than 0.5 (Figure 5.5c-e). It is observed that trajectory 2005-2020 cuts across the solid red curve. This indicates the importance of future technology in the

reduction of NO_2 levels thereby meeting the UK NO_2 air quality standards over years. For the heterogeneity coefficient of 0.9, the UK air quality standard of hourly NO_2 is exceeded for most of the years. This indicates that it is important to improve the air ventilation between the boxes in the street canyon, thereby decreasing the heterogeneity coefficient leading to better air quality.

Figure 5.6 shows the transects of $C_{NO_2,L}$ (ppb) for Case HC-LL, Case HC-L, Case BASE, Case HC-H and Case HC-HH through the selected lines for analysis in Figure 5.5f. The rationale behind the choices is explained as follows. The dashed line ("Fixed E_{NOx}"), the dotted line ("Fixed E_{VOCs}"), the dot-dash line ("TRES-2010") and the trajectory line ("Trajectory 2005-2020") all pass through the point for the TRES, as marked in Figure 5.5f. The emission profile along this dashed line at the fixed E_{NOx} of TRES represents a technology of targeting only E_{VOCs} from vehicles, or the roads with a varying coverage of vegetation which may emit further VOCs into the urban canopy (Loughner et al., 2012). The emission profile along this dotted line at the fixed E_{VOCs} of TRES represents a technology of targeting only E_{NOx}. The emission profile along the dot-dash line represents a technology of both E_{VOCs} and E_{NOx} ("TRES-2010") with the proportional traffic-emitting rate of both VOCs and NO_x as specified for the TRES. This dot-dashed line may also represent control of the number of vehicles in streets or scenarios for different areas (busier or less busy roads) with the same fleet composition as the TRES. The trajectory line indicates emission scenarios for the years 2005 to 2020 with the same traffic volume and speed as the TRES. The corresponding results along selected lines are analysed below.

Figure 5.6a shows that $C_{NO_2,L}$ gradually increases with the increase of E_{VOCs} at a fixed E_{NOx} (same as that of TRES). This can be explained as VOCs can play a key role in the

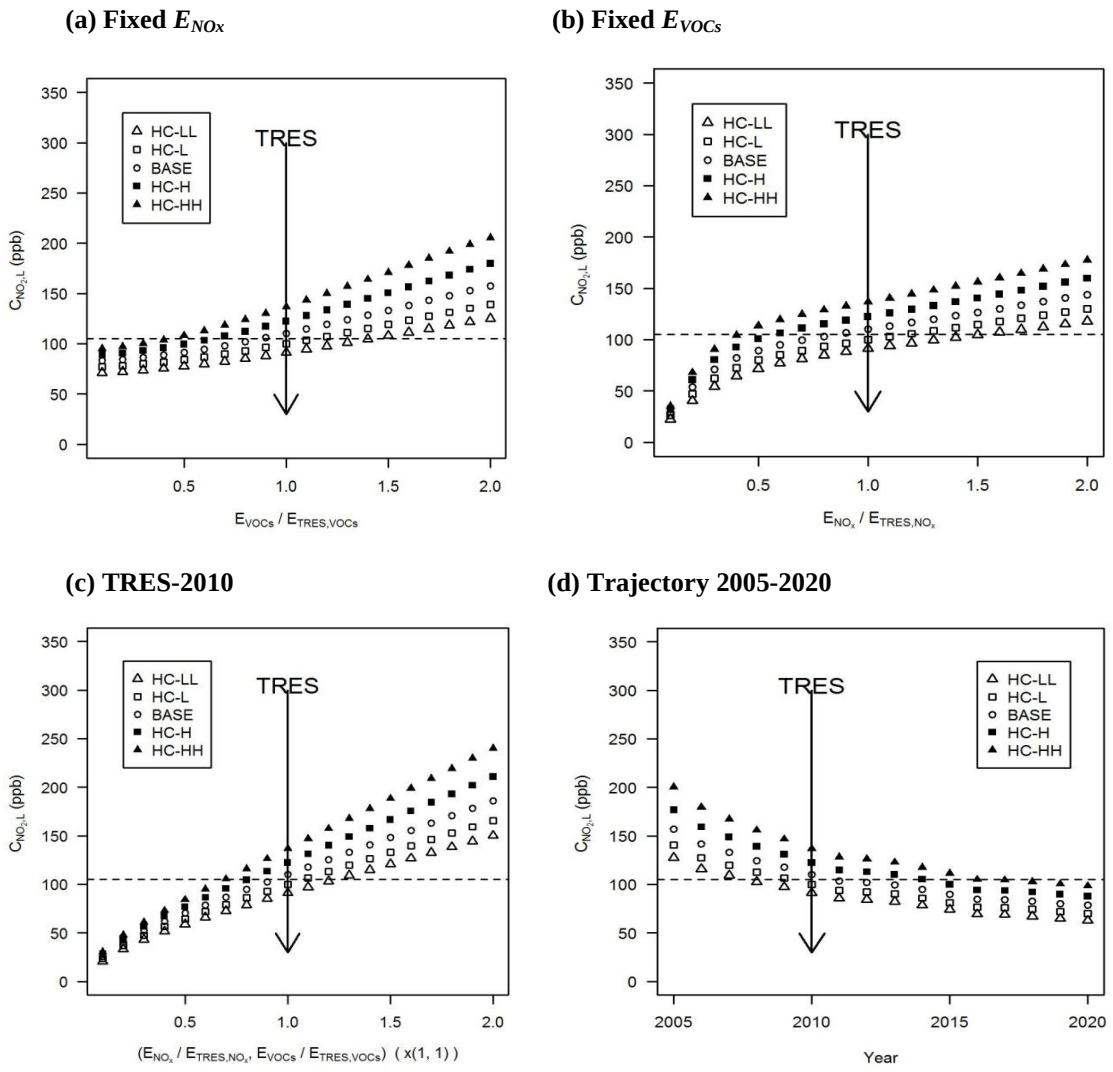

Figure 5.6 $C_{NO_2,L}$ (ppb), i.e. the concentration in the lower box derived from the "two-box" model, for (a) "Fixed E_{NOx}" at a fixed NO_x emissions of TRES, (b) "Fixed E_{VOCs}" at a fixed VOCs emissions of TRES, (c) "TRES-2010" varying the total traffic volume only and (d) "Trajectory 2005-2020" assuming constant traffic volume and speed varying η. E_{VOCs} and E_{NOx} are normalised by those of the Typical Real-world Emission Scenario (TRES, represented by△), for the year of 2010. The dashed line indicates the UK air quality standard of hourly NO_2 (105 ppb).

conversion of NO to NO_2 through chemistry. At the fixed E_{NOx}, the increase of $C_{NO_2,L}$ is mainly due to the chemical processing through VOCs. This indicates that there are higher levels of NO_2 for more green (i.e. vegetated) areas producing extra E_{VOCs} (with biogenic VOC emissions, assuming such emissions were not incorporated in the model scenario / conditions). The main biogenic VOC emissions are isoprene, monoterpenes,

sesquiterpenes and oxygenated VOC compounds (Oderbolz et al., 2013) , which may be released from a variety of vegetation types in an urban tree canopy (Owen et al., 2003). Biogenic VOC emissions are strongly dependent upon temperature (Kesselmeier and Staudt, 1999). These iogenic VOC emissions may have a considerable impact on street canyon chemical processing. It is noted that the concentration difference of $C_{NO_2,L}$ between Case HC-HH (η=0.9) and Case HC-LL (η=0.1) gradually increases with the increase of E_{VOCs}, from 23 ppb (at $E_{VOCs} / E_{TRES,VOCs}$ =0.1) to 80 ppb (at $E_{VOCs} / E_{TRES,VOCs}$ =2). This finding indicates that the effect of the heterogeneity coefficient is less significant for lower E_{VOCs} when keeping E_{NOx} unchanged. Figure 5.6b also shows that $C_{NO_2,L}$ generally increases with the increase of E_{NOx} at a fixed E_{VOCs} (same as that of TRES), with a rapid increase while $E_{NO_x} / E_{TRES,NO_x}$ ranges from 0.1 to 0.5. This is mainly attributed to that emitted NO_x contributes directly to the increase of $C_{NO_2,L}$. This indicates that adoption of technology controlling NO_x will have a significant effect in reducing NO_2 levels. There is also clear evidence of the less significant effect of the heterogeneity coefficient for lower E_{NOx}. The concentration difference of $C_{NO_2,L}$ between Case HC-HH and Case HC-LL gradually increases with the increase of E_{NOx}, from 13 ppb (at $E_{NO_x} / E_{TRES,NO_x}$ =0.1) to 60 ppb (at $E_{NO_x} / E_{TRES,NO_x}$ =2). Figure 5.6c illustrates the change of $C_{NO_2,L}$ in for TRES-2010 with changing both E_{VOCs} and E_{NOx} assuming constant traffic volume and speed. The pattern of $C_{NO_2,L}$ is a combination of those in Figure 5.6a and Figure 5.6b, and a nearly linear relationship is observed. This indicates that controlling the number of vehicles in street canyons with the same fleet composition as the TRES will have an approximately linear effect on the NO_2 levels. Figure 5.6d shows the results of $C_{NO_2,L}$ from the year 2005 to 2020. It is observed that $C_{NO_2,L}$ decreases with year. This is mainly attributed to the

control technologies applied, which achieve lower E_{VOCs} and E_{NOx}. $C_{NO_2,L}$ begins to attain the air quality standard from the year 2007 for Case HC-LL (η =0.1), 2009 for Case HC-L (η =0.3), 2011 for Case BASE (η =0.5), 2014 for Case HC-H (η =0.7) and 2017 for Case HC-HH (η =0.9).

Figure 5.7 shows the effect of the heterogeneity coefficient (η) on $\phi_{NO_2,L}$ (%), i.e. the percentage of overestimation for NO_2 in the lower canyon by the 'one-box' model. Negative values of $\phi_{NO_2,L}$ are observed for all the cases, which means that the *'one-box' model underestimates NO_2 concentrations* compared with those in the *lower box by the 'two-box' model*. It is interesting to notice that the magnitude of $\phi_{NO_2,L}$ gradually increases with the increase in the heterogeneity coefficient (η), i.e. the range of (-9.54 %, -4.13 %) among all tested emission scenarios for Case HC-LL with η =0.1 (Figure 5.7a), (-23.94 %, -11.36 %) for Case HC-L with η =0.3 (Figure 5.7b), (-33.49 %, -17.07 %) for Case BASE with η =0.5 (Figure 5.7c), (-40.74 %, -21.94 %) for Case HC-H with η =0.7 (Figure 5.7d) and (-46.73 %, -26.22 %) for Case HC-HH with η =0.9 (Figure 5.7e). It is also noted that $\phi_{NO_2,L}$ changes nonlinearly with the change of emissions of NO_x and VOCs. This is mainly attributed to nonlinear photochemical reactions. For a passive scalar, the percentage of overestimation is -9.09 %, -23.08 %, -33.33 %, -41.18 % and -47.37 % for η =0.1, η =0.3, η =0.5, η =0.7 and η =0.9 respectively. This indicates that for higher VOCs emission rate scenarios (Figure 5.7), the nonlinear photochemistry plays a key role in reducing the percentage of overestimation for NO_2 by the 'one-box' model compared with that for a passive scalar.

(a) $\phi_{NO_2,L}$ for Case HC-LL **(b) $\phi_{NO_2,L}$ for Case HC-L**

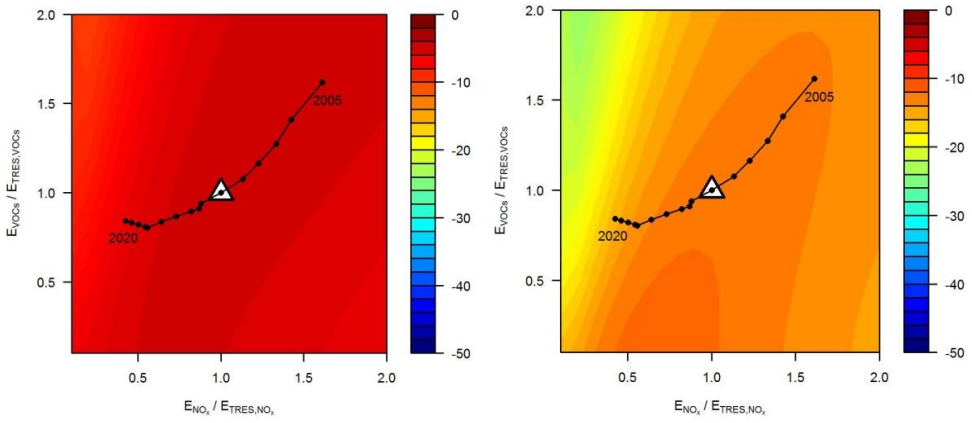

(c) $\phi_{NO_2,L}$ for Case BASE **(d) $\phi_{NO_2,L}$ for Case HC-H**

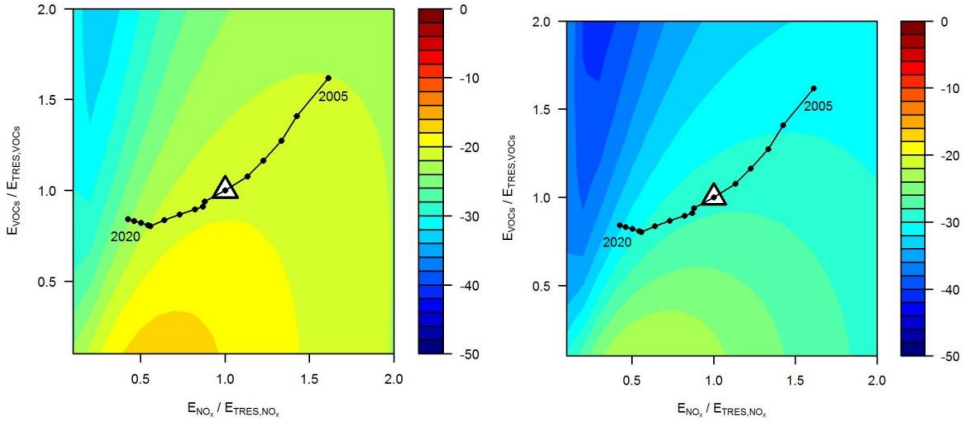

(e) $\phi_{NO_2,L}$ for Case HC-HH

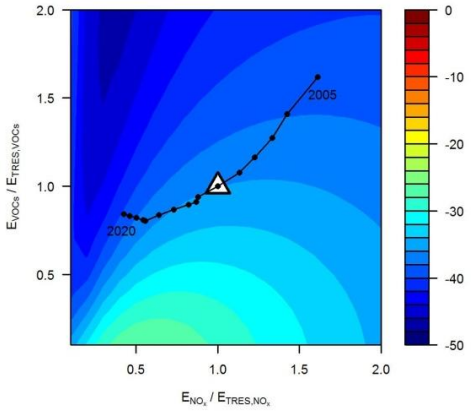

Figure 5.7 $\phi_{NO_2,L}$ (%), i.e. the percentage of overestimation for NO_2 in the lower canyon by the 'one-box' model compared with that by the "two-box" model, in the (a) Case HC-LL (η =0.1), (b) Case HC-L (η =0.3), (c) Case BASE (η =0.5), (d) Case HC-H (η =0.7), (e) Case HC-HH (η =0.9). E_{VOCs} and E_{NOx} are normalised by those of the Typical Real-world Emission Scenario (TRES, represented by△), for the year of 2010. Trajectory 2005-2020 represents the emission scenarios for 2005 to 2020, assuming constant traffic volume and speed.

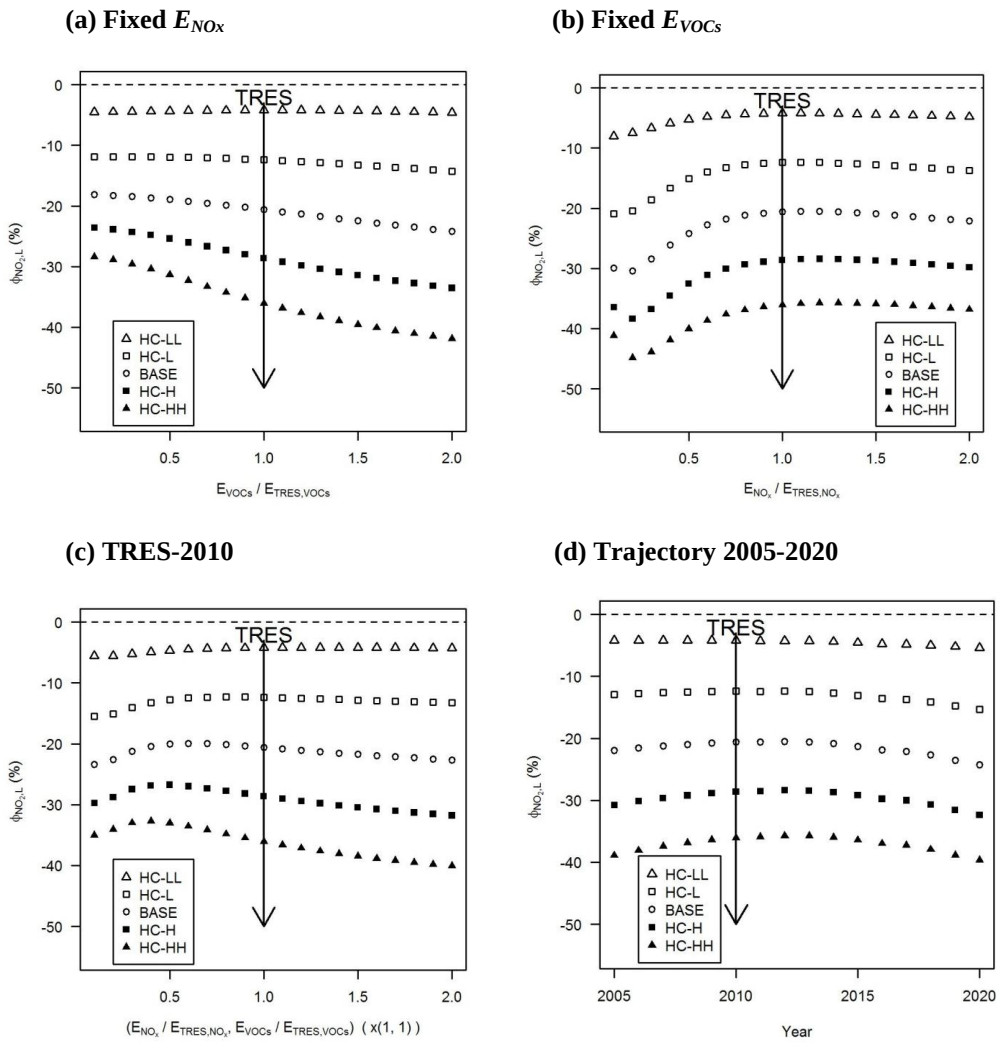

Figure 5.8 $\phi_{NO_2,L}$ (%), i.e. the percentage of overestimation for NO_2 in the lower canyon by the 'one-box' model compared with that by the "two-box" model, for (a) "Fixed E_{NOx}" at a fixed NO_x emissions of TRES, (b) "Fixed E_{VOCs}" at a fixed VOCs emissions of TRES, (c) "TRES-2010" varying the total traffic volume only and (d) "Trajectory 2005-2020" assuming constant traffic volume and speed varying η. E_{VOCs} and E_{NOx} are normalised by those of the Typical Real-world Emission Scenario (TRES, represented by△), for the year of 2010.

Figure 5.8 illustrates the transects of $\phi_{NO_2,L}$ (ppb) for Case HC-LL, Case HC-L, Case BASE, Case HC-H and Case HC-HH through the selected lines for analysis in Figure 5.5f. Figure 5.8a shows that the magnitude of $\phi_{NO_2,L}$ slightly increases with the increase of E_{VOCs}, i.e. from -4.48 % to -4.59 % for η =0.1, from -11.88 % to -14.26 % for η =0.3, from -18.14 % to -24.16 % for η =0.5, from -23.57 % to -33.54 % for η =0.7 and from

-28.37 % to -41.88 % for η =0.9. It is noted that the higher the value of heterogeneity coefficient is, the larger the magnitude of $\phi_{NO_2,L}$ will be. This indicates that the one box model performance is better for the case with lower heterogeneity coefficients or for less "green" (lower VOCs emission) areas. Figure 5.8b shows that the magnitude of $\phi_{NO_2,L}$ generally decreases with the increase of E_{NOx}, except a slight increase at $E_{NO_x} / E_{TRES,NO_x}$ =0.2 for the cases with η =0.5, η =0.7 and η =0.9. Figure 5.8c also shows that there is no significant change in the $\phi_{NO_2,L}$ when changing both E_{VOCs} and E_{NOx} and that the values of $\phi_{NO_2,L}$ are mainly affected by the heterogeneity coefficient (η). This finding is also indicated by Figure 5.8d, in which the values of $\phi_{NO_2,L}$ do not change significantly over the year 2005 to 2020 (the maximum difference is within 5 %) and there is significant contrast between the cases with different heterogeneity coefficient (the contrast is around 10 % with the interval of η =0.2).

5.3.2 Effect of the exchange velocity

Figure 5.9 illustrates the effect of the exchange velocity ($w_{t,0}$) on $C_{NO_2,L}$ (ppb), i.e. the concentration in the lower box for (a) Case EX-LL ($w_{t,0}$ =0.012 m s^{-1}), (b) Case EX-L ($w_{t,0}$ =0.016 m s^{-1}), (c) Case BASE ($w_{t,0}$ =0.02 m s^{-1}), (d) Case EX-H ($w_{t,0}$ =0.024 m s^{-1}) and (e) Case EX-HH ($w_{t,0}$ =0.028 m s^{-1}). $w_{t,0}$ can vary with the external wind turbulence above the street canyon, the street canyon geometry and the stability of the atmosphere. It is observed that $C_{NO_2,L}$ is significantly influenced by $w_{t,0}$. For Case EX-LL, levels of $C_{NO_2,L}$ are extremely high (the maximum value could be up to 350 ppb). This is attributed to the lowest $w_{t,0}$ adopted in Case EX-LL, which gives the worst (lowest) exchange between the lower and upper box (indicated by a lower value of $w_{t,L}$ in Figure 5.4). Therefore, it is not effective for pollutants to be carried from the lower box to the overlying street canyon. It is interesting to notice that the solid red curve (i.e. representing the UK air quality standard of hourly NO_2) shifts from the region with lower emissions to that with higher emissions as $w_{t,0}$ increases. It means that even lower emissions under the worst dispersion conditions can result in very poor air quality inside street canyons. It is also observed that trajectory 2005-2020 falls entirely into the region exceeding the UK air quality standard of hourly NO_2 for Case EX-LL with the lowest $w_{t,0}$. With the increase of the exchange velocity, the solid red curve moves from the year 2020 towards the year 2005. This also indicates that the ventilation conditions should be improved to achieve better air quality for future years. It is also noted that TRES exceed the UK air quality standard of hourly NO_2 for Case EX-LL, Case EX-L and Case BASE, but is within the air quality limit for Case EX-H and Case EX-HH. The detailed results along the selected lines for analysis, shown as Figure 5.5f, are presented below.

(a) $C_{NO_2,L}$ **(ppb) for Case EX-LL** **(b)** $C_{NO_2,L}$ **(ppb) for Case EX-L**

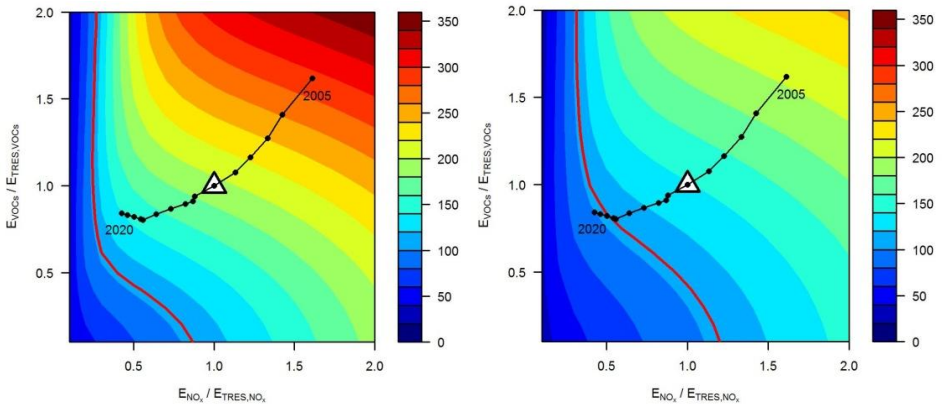

(c) $C_{NO_2,L}$ **(ppb) for Case BASE** **(d)** $C_{NO_2,L}$ **(ppb) for Case EX-H**

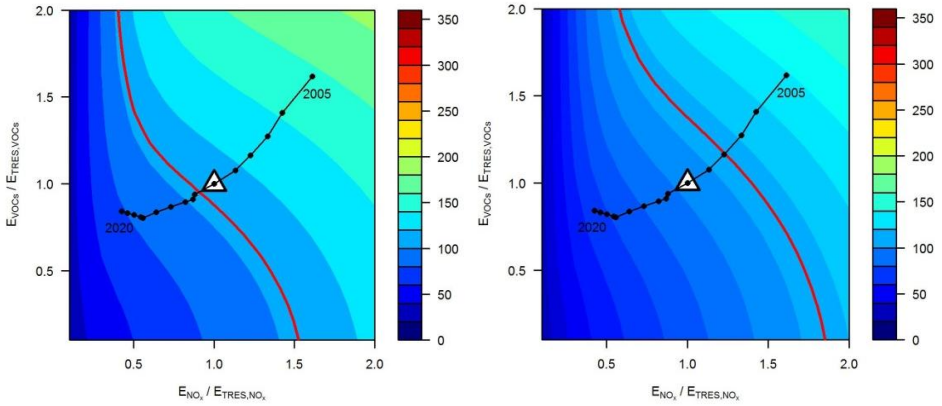

(e) $C_{NO_2,L}$ **(ppb) for Case EX-HH**

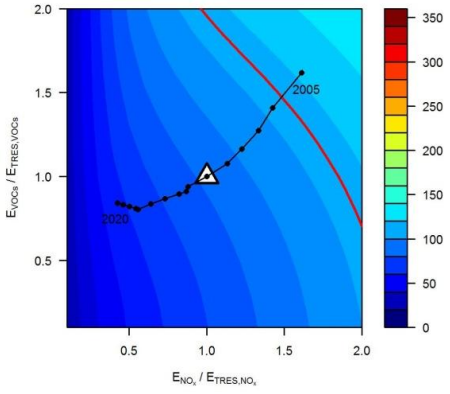

Figure 5.9 $C_{NO_2,L}$ **(ppb), i.e. the concentration in the lower box derived from the "two-box" model, in the (a) Case EX-LL (** $w_{t,0}$ **=0.012 m s^{-1}), (b) Case EX-L (** $w_{t,0}$ **=0.016 m s^{-1}), (c) Case BASE (** $w_{t,0}$ **=0.02 m s^{-1}), (d) Case EX-H (** $w_{t,0}$ **=0.024 m s^{-1}) and (e) Case EX-HH (** $w_{t,0}$ **=0.028 m s^{-1}).** E_{VOCs} **and** E_{NOx} **are normalised by those of the Typical Real-world Emission Scenario (TRES, represented by△), for the year of 2010. Trajectory 2005-2020 represents the emission scenarios for 2005 to 2020, assuming constant traffic volume and speed. The solid red curves denote the UK air quality standard of hourly NO_2 (105 ppb).**

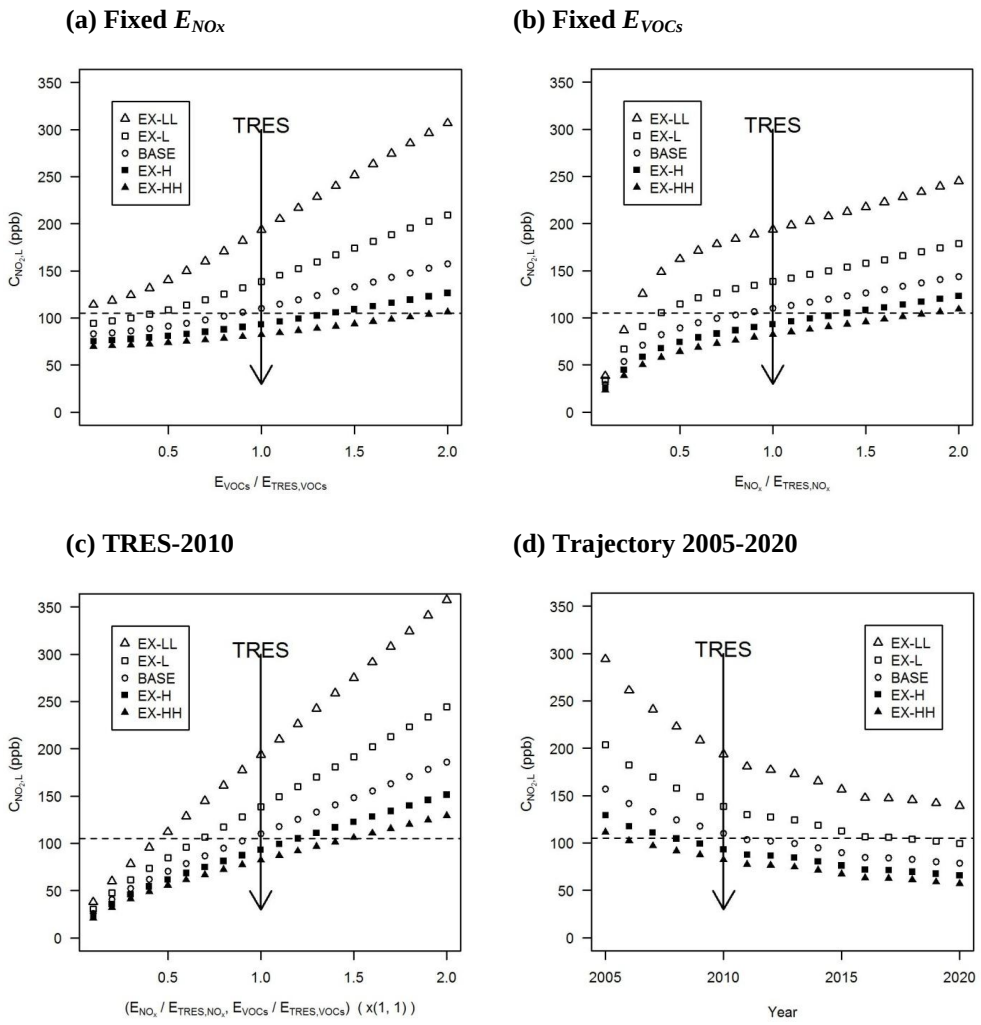

Figure 5.10 $C_{NO_2,L}$ (ppb), i.e. the concentration in the lower box derived from the "two-box" model, for (a) "Fixed E_{NOx}" at a fixed NO_x emissions of TRES, (b) "Fixed E_{VOCs}" at a fixed VOCs emissions of TRES, (c) "TRES-2010" varying the total traffic volume only and (d) "Trajectory 2005-2020" assuming constant traffic volume and speed varying $w_{t,0}$. E_{VOCs} and E_{NOx} are normalised by those of the Typical Real-world Emission Scenario (TRES, represented by△), for the year of 2010. The dashed line indicates the UK air quality standard of hourly NO_2 (105 ppb).

Figure 5.10 shows the transects of $C_{NO_2,L}$ (ppb) for Case EX -LL, Case EX-L, Case BASE, Case EX-H and Case EX-HH through the selected lines for analysis in Figure 5.5f. It is also observed that $C_{NO_2,L}$ increases with increase of E_{VOCs} and E_{NOx}, shown as Figure 5.10a-c. This indicates that the control of either E_{VOCs} or E_{NOx} is effective to reduce the NO_2 levels. It is also interesting to notice that there is not significant change of $C_{NO_2,L}$

while the E_{VOCs} and E_{NOx} are lower. The minimum and maximum differences of $C_{NO_2,L}$ between Case EX-LL with $w_{t,0}$ =0.012 m s^{-1} and Case EX -HH with $w_{t,0}$ =0.028 m s^{-1} are 44 ppb and 201 ppb for Figure 5.10a, 15 ppb and 136 ppb for Figure 5.10b , and 17 ppb and 228 ppb for Figure 5.10c. This indicates the importance of controlling ventilation conditions of street canyons especially for highly polluted scenarios. Figure 5.10d shows that $C_{NO_2,L}$ decreases significantly with year due to the control technologies of both E_{VOCs} and E_{NOx}. This indicates that the air quality will be improved in future years. However, for the worst ventilation condition (e.g. Case EX-LL), $C_{NO_2,L}$ still exceeds the UK air quality standard over the year 2005 to 2020. This indicates that control of air ventilation together with control of vehicle emissions is also important in improving air quality within street canyons. Air ventilation is strongly influenced by the urban street design and deep street canyons could lead to poor ventilation.

Figure 5.11 shows the effect of the exchange velocity ($w_{t,0}$) on $\phi_{NO_2,L}$ (%), i.e. the percentage of overestimation for NO_2 in the lower canyon by the 'one-box' model, compared with the two-box system. It is found that $\phi_{NO_2,L}$ decreases slightly with increasing exchange velocity ($w_{t,0}$), i.e. the range of (-37.49 %, -17.64 %) among all tested emission scenarios for Case EX-LL (-35.26 %, -17.22 %) for Case EX-L, (-33.49 %, -17.07 %) for Case BASE, (-31.89 %, -17.02 %) for Case EX-H and (-30.52 %, -17.01 %) for Case EX-HH. As η =0.5 is adopted for all cases in Figure 10, the nonlinear patterns reflect the characteristics of scenarios with heterogeneity coefficient (η =0.5). This indicates that there is an underestimation of NO_2 concentrations by the 'one-box' model and this underestimation changes significantly with the heterogeneity coefficient (Figure 5.5), to a much greater extent than the change with the exchange velocity (Figure 5.11).

(a) $\phi_{NO_2,L}$ (%) for Case EX-LL

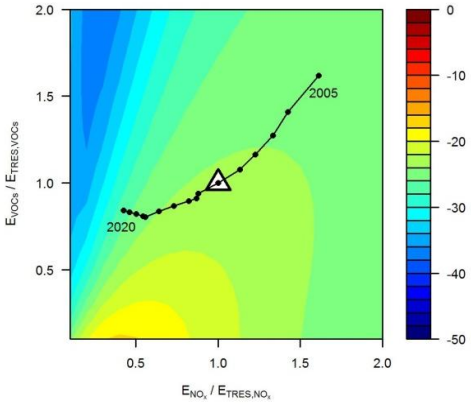

(b) $\phi_{NO_2,L}$ (%) for Case EX-L

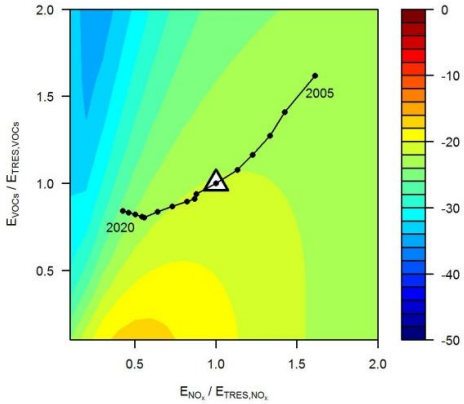

(c) $\phi_{NO_2,L}$ (%) for Case BASE

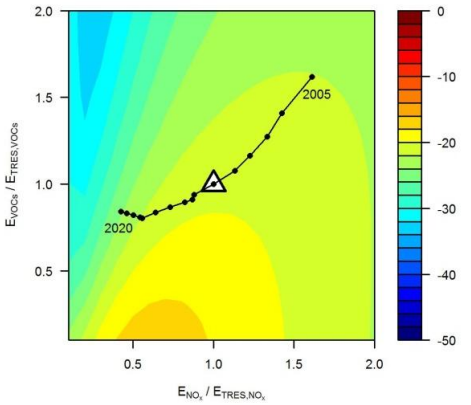

(d) $\phi_{NO_2,L}$ (%) for Case EX-H

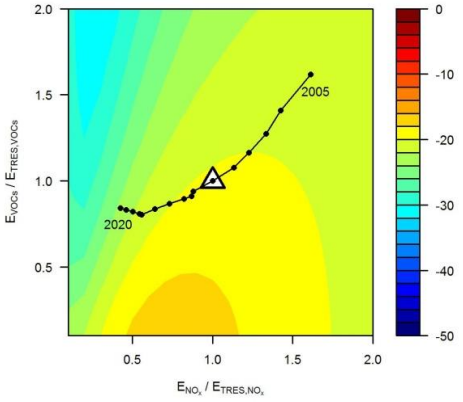

(e) $\phi_{NO_2,L}$ (%) for Case EX-HH

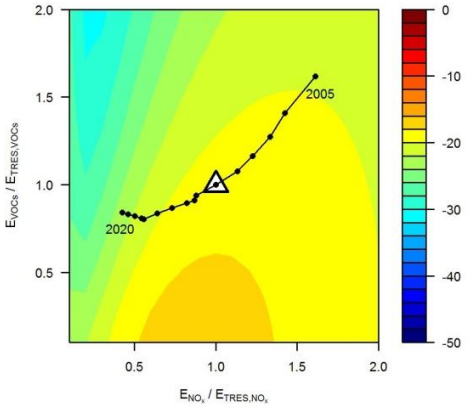

Figure 5.11 $\phi_{NO_2,L}$ (%), i.e. the percentage of overestimation for NO_2 in the lower canyon by the 'one-box' model compared with that by the "two-box" model, in the (a) Case EX-LL ($w_{t,0}$ =0.012 m s^{-1}), (b) Case EX-L ($w_{t,0}$ =0.016 m s^{-1}), (c) Case BASE ($w_{t,0}$ =0.02 m s^{-1}), (d) Case EX-H ($w_{t,0}$ =0.024 m s^{-1}) and (e) Case EX-HH ($w_{t,0}$ =0.028 m s^{-1}). E_{VOCs} and E_{NOx} are normalised by those of the Typical Real-world Emission Scenario (TRES, represented by△), for the year of 2010. Trajectory 2005-2020 represents the emission scenarios for 2005 to 2020, assuming constant traffic volume and speed.

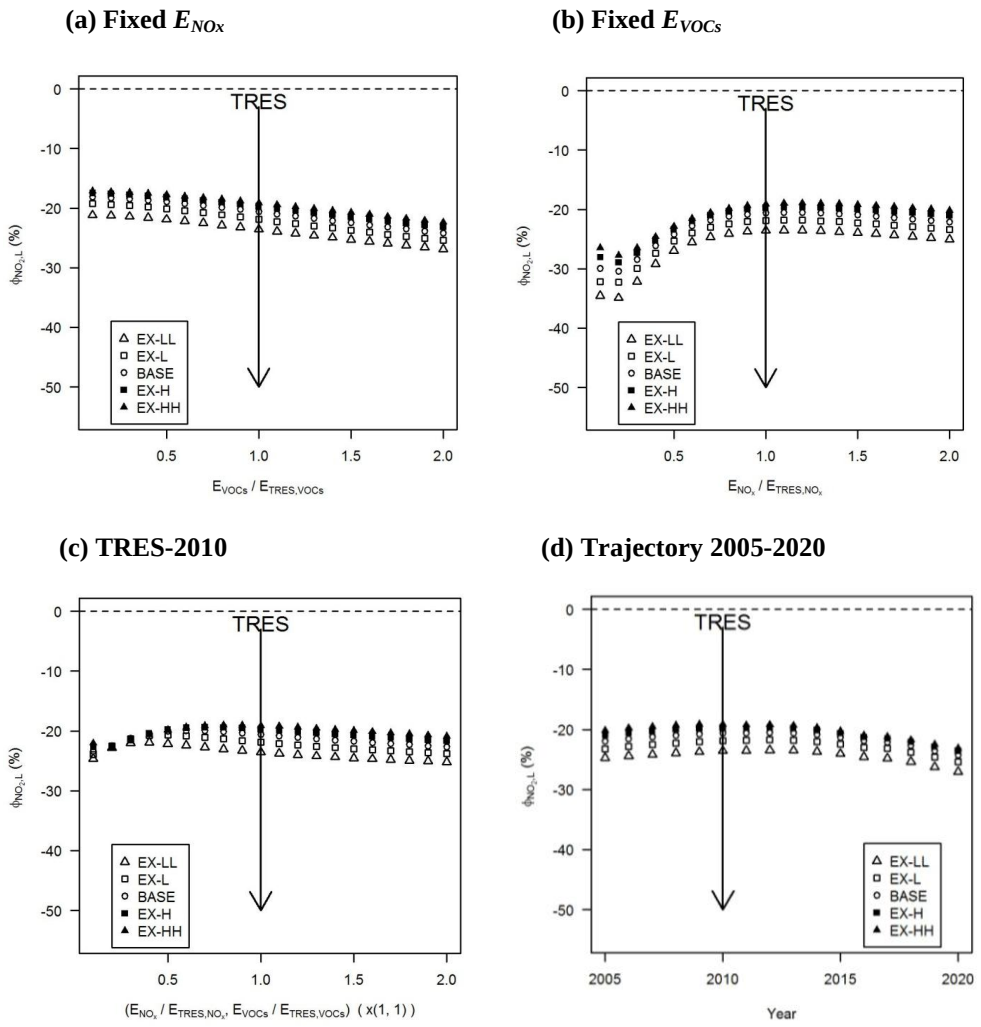

Figure 5.12 $\phi_{NO_2,L}$ (%), i.e. the percentage of overestimation for NO_2 in the lower canyon by the 'one-box' model compared with that by the "two-box" model, for (a) "Fixed E_{NOx}" at a fixed NO_x emissions of TRES, (b) "Fixed E_{VOCs}" at a fixed VOCs emissions of TRES, (c) "TRES-2010" varying the total traffic volume only and (d) "Trajectory 2005-2020" assuming constant traffic volume and speed varying $w_{t,0}$. E_{VOCs} and E_{NOx} are normalised by those of the Typical Real-world Emission Scenario (TRES, represented by△), for the year of 2010.

Figure 5.12 illustrates the transects of $\phi_{NO_2,L}$ (ppb) for Case EX -LL, Case EX-L, Case BASE, Case EX-H and Case EX-HH through the selected lines for analysis in Figure 5.5f. Figure 5.12a shows that $\phi_{NO_2,L}$ slightly decreases with the increase of E_{VOCs}, i.e. from -21.15 % to -26.86 % for Case EX-LL, from -19.26 % to -25.37 % for Case EX-L, from -18.14 % to -24.16 % for Case BASE, from -17.48 % to -23.16 % for Case EX-H and from

-17.15 % to -22.36 % for Case EX-HH. Figure 5.12b shows that $\phi_{NO_2,L}$ generally increases with the increase of E_{NOx}, except a slight decrease at $E_{NO_x} / E_{TRES,NO_x}$ =0.2. Figure 5.12c shows that there is no significant difference between the cases with different exchange velocities (within 5 % difference) while both E_{VOCs} and E_{NOx} are below half of those for TRES. For the year 2005 to 2020 shown as Figure 5.12d, there is also not significant change of $\phi_{NO_2,L}$ (within 5 % difference).

5.3.3 Effect of the box height ratio

Figure 5.13 illustrates the effect of the box height ratio (α) on $C_{NO_2,L}$ (ppb), i.e. the concentration in the lower box for Case HB-LL (α =0.1), (b) Case HB-L (α =0.3), (c) Case BASE (α =0.5), (d) Case HB-H (α =0.7), and (e) Case HB-HH (α =0.9). α can vary with the flow structure in a street canyon, which may be significantly influenced by the building geometry. A high-level circulation induced by pitched roof of the building will give a relatively smaller size of the upper vortex (Louka et al., 2000), suggesting an extremely higher value of α (possibly equivalent to 0.9). There is clear evidence that $C_{NO_2,L}$ is significantly affected by the box height ratio. There is extremely high levels of $C_{NO_2,L}$ for smaller box height ratio, e.g. with a maximum value of about 520 ppb for Case HB-LL with α =0.1. This small box height ratio represents the case that pollutants are highly trapped in the small lower part of the street canyon under poor ventilation conditions. This is similar to the secondary smaller eddies near the street corner, where levels of pollutants can extremely high. The exchange velocity between lower and upper box (indicated by a lower value of $w_{t,L}$ in Figure 5.4) is the lowest for Case HB-LL. It is observed that almost all the scenarios (including trajectory 2005-2020) in Case HB-LL are expected to exceed the UK air quality standard of hourly NO_2 except for scenarios with

extremely lower emissions, shown as Figure 5.13a. As the box height ratio increases, the solid red curve in Figure 5.13 shifts towards scenarios with higher emissions across trajectory 2005-2020. For Case HB-H and Case HB-HH, TRES is observed in the region below the UK air quality standard for NO_2. The box height ratio is mainly determined by the flow structure in the street canyon. Therefore, understanding the flow characteristics in a street canyon is of vital importance and the numerical modelling approach can provide flow patterns in high spatial and temporal resolution within the street canyon.

(a) $C_{NO_2,L}$ **(ppb) for Case HB-LL**

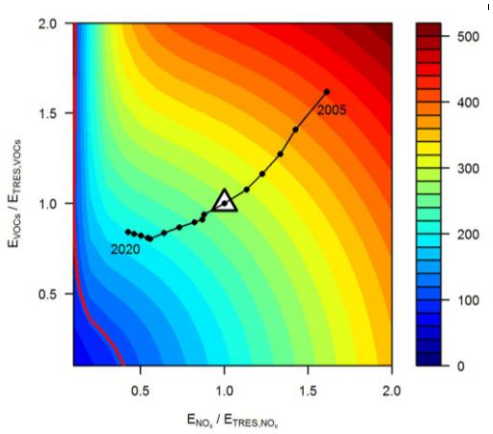

(b) $C_{NO_2,L}$ **(ppb) for Case HB-L**

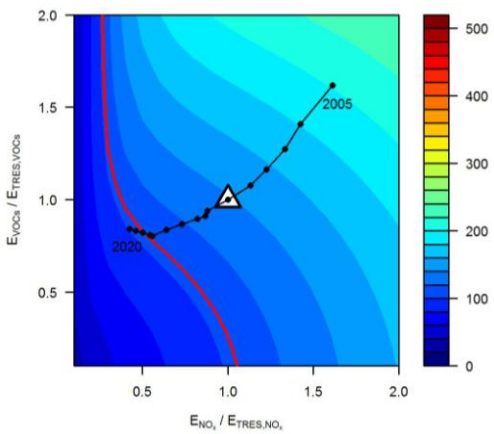

(c) $C_{NO_2,L}$ **(ppb) for Case BASE**

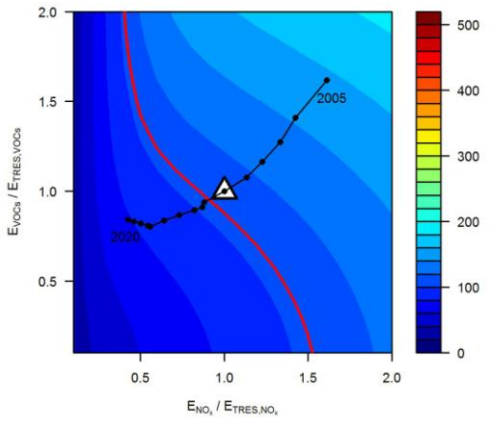

(d) $C_{NO_2,L}$ **(ppb) for Case HB-H**

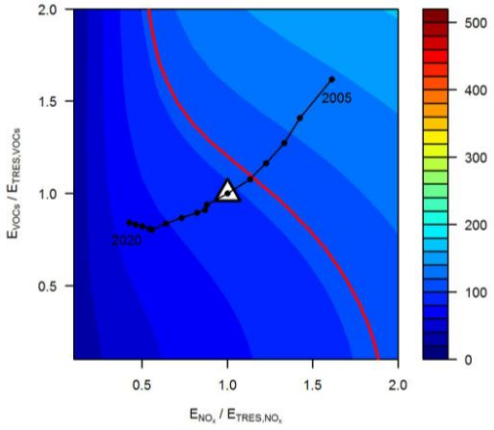

(e) $C_{NO_2,L}$ **(ppb) for Case HB-HH**

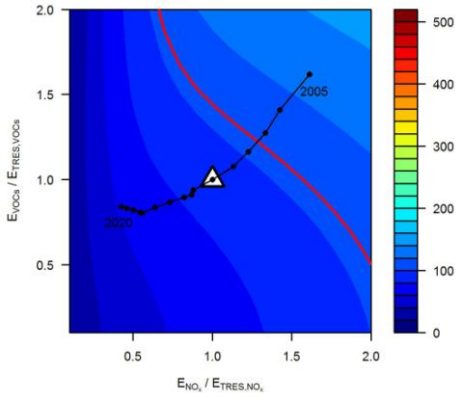

Figure 5.13 $C_{NO_2,L}$ **(ppb), i.e. the concentration in the lower box derived from the "two-box" model, in the (a) Case HB-LL (**α **=0.1), (b) Case HB-L (**α **=0.3), (c) Case BASE (**α **=0.5), (d) Case HB-H (**α **=0.7), and (e) Case HB-HH (**α **=0.9).** E_{VOCs} **and** E_{NOx} **are normalised by those of the Typical Real-world Emission Scenario (TRES, represented by△), for the year of 2010. Trajectory 2005-2020 represents the emission scenarios for 2005 to 2020, assuming constant traffic volume and speed. The solid red curves denote the UK air quality standard of hourly NO_2 (105 ppb).**

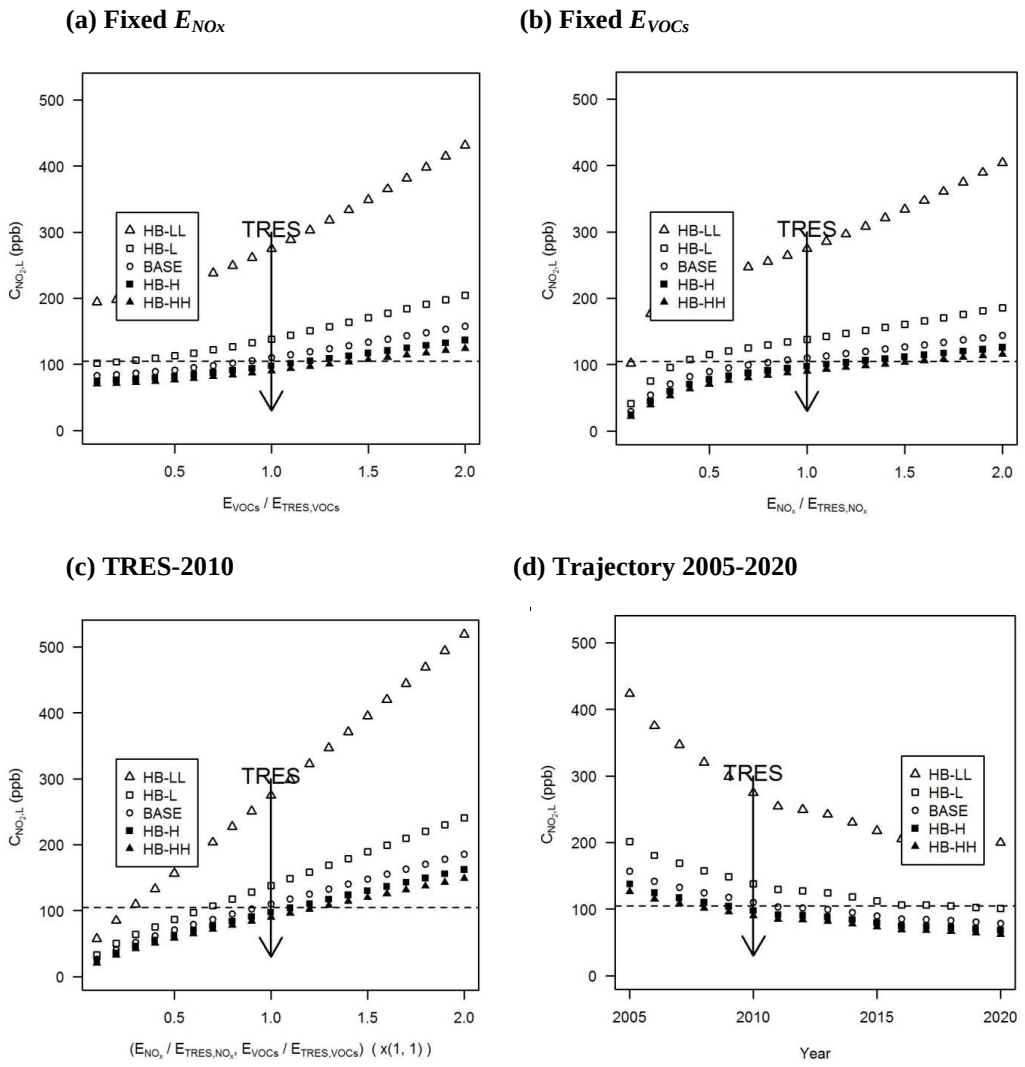

Figure 5.14 $C_{NO_2,L}$ (ppb), i.e. the concentration in the lower box derived from the "two-box" model, for (a) "Fixed E_{NOx}" at a fixed NO_x emissions of TRES, (b) "Fixed E_{VOCs}" at a fixed VOCs emissions of TRES, (c) "TRES-2010" varying the total traffic volume only and (d) "Trajectory 2005-2020" assuming constant traffic volume and speed varying α. E_{VOCs} and E_{NOx} are normalised by those of the Typical Real-world Emission Scenario (TRES, represented by△), for the year of 2010. The dashed line indicates the UK air quality standard of hourly NO_2 (105 ppb).

Figure 5.14 shows the transects of $C_{NO_2,L}$ (ppb) for Case HB-LL, Case HB-L, Case BASE, Case HB-H and Case HB-HH through the selected lines for analysis in Figure 5.5f. It can be seen that there is an increase of $C_{NO_2,L}$ with the increase with increase of E_{VOCs} and E_{NOx}. This increasing tendency is extremely significant for Case HB-LL with the lowest box height ratio (α =0.1), i.e. 207 ppb difference for Figure 5.14a, 302 ppb difference for

Figure 5.14b and 461 ppb difference for Figure 5.14c. For other box height ratios in Figure 5.14a-c, the concentration difference is around 100 ppb, much lower than that for Case HB-LL. Figure 5.14d shows that there is a decrease of $C_{NO_2,L}$ with years. However, the air quality is still worse for Case HB-LL and Case HB-L, i.e. about 4 times and 2 times of the UK air quality standard of hourly NO_2 for the year 2005.

Figure 5.15 shows the effect of the box height ratio (α) on $\phi_{NO_2,L}$ (%), i.e. the percentage of overestimation for NO_2 in the lower canyon by the 'one-box' model. There are significant changes of $\phi_{NO_2,L}$ with the changes of the box height ratio, i.e. (-82.22 %, -57.37 %) for Case HB-LL with α=0.1, (-54.15 %, -30.26 %) for Case HB-L with α=0.3, (-33.49 %, -17.07 %) for Case BASE with α=0.5, (-17.71 %, -8.63 %) for Case HB-H with α=0.7 and (-5.27 %, -2.59 %) for Case HB-HH with α=0.9. This indicates that for higher box height ratio, the 'one-box' model predicts more accurate NO_2 concentrations. It is also noted that $\phi_{NO_2,L}$ is less sensitive to emissions of NO_x and VOCs while the box height ratio is higher. For the extremely high box height ratio, the upper box plays a similar role as shear layer, where frequent exchange takes place. In such a situation, the two-box model can approximate to the one-box model.

(a) $\phi_{NO_2,L}$ (%) for Case HB-LL

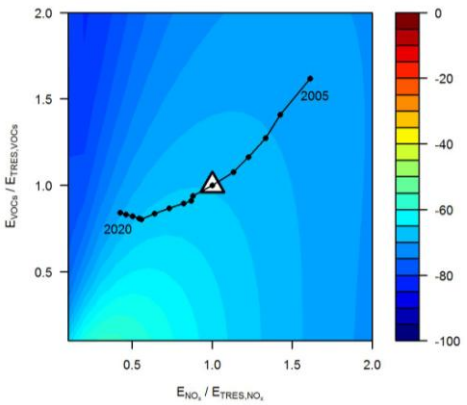

(b) $\phi_{NO_2,L}$ (%) for Case HB-L

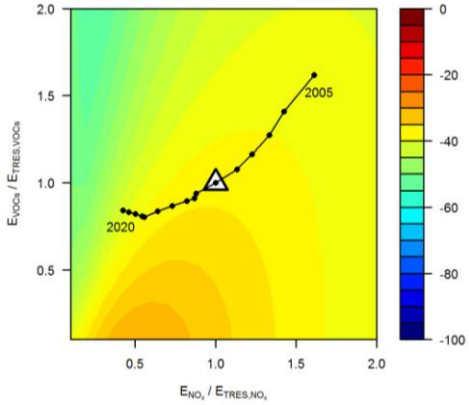

(c) $\phi_{NO_2,L}$ (%) for Case BASE

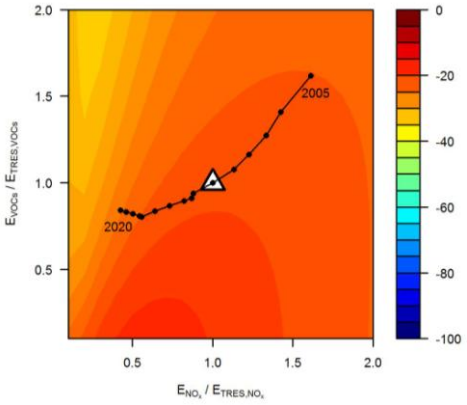

(d) $\phi_{NO_2,L}$ (%) for Case HB-H

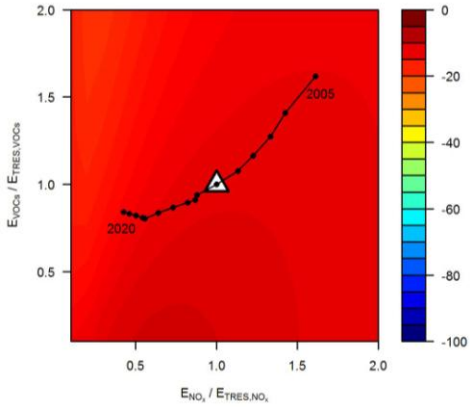

(e) $\phi_{NO_2,L}$ (%) for Case HB-HH

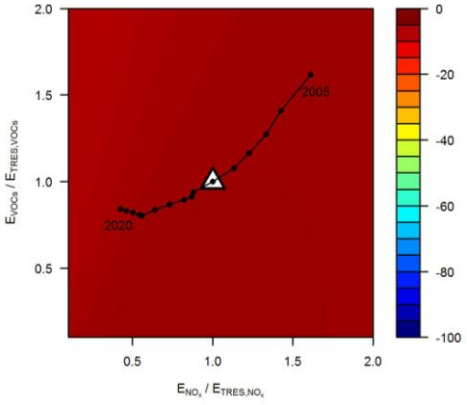

Figure 5.15 $\phi_{NO_2,L}$ (%), i.e. the percentage of overestimation for NO_2 in the lower canyon by the 'one-box' model compared with that by the "two-box" model, in the (a) Case HB-LL (α =0.1), (b) Case HB-L (α =0.3), (c) Case BASE (α =0.5), (d) Case HB-H (α =0.7), and (e) Case HB-HH (α =0.9). E_{VOCs} and E_{NOx} are normalised by those of the Typical Real-world Emission Scenario (TRES, represented by△), for the year of 2010. Trajectory 2005-2020 represents the emission scenarios for 2005 to 2020, assuming constant traffic volume and speed. The solid red curves denote the UK air quality standard of hourly NO_2 (105 ppb).

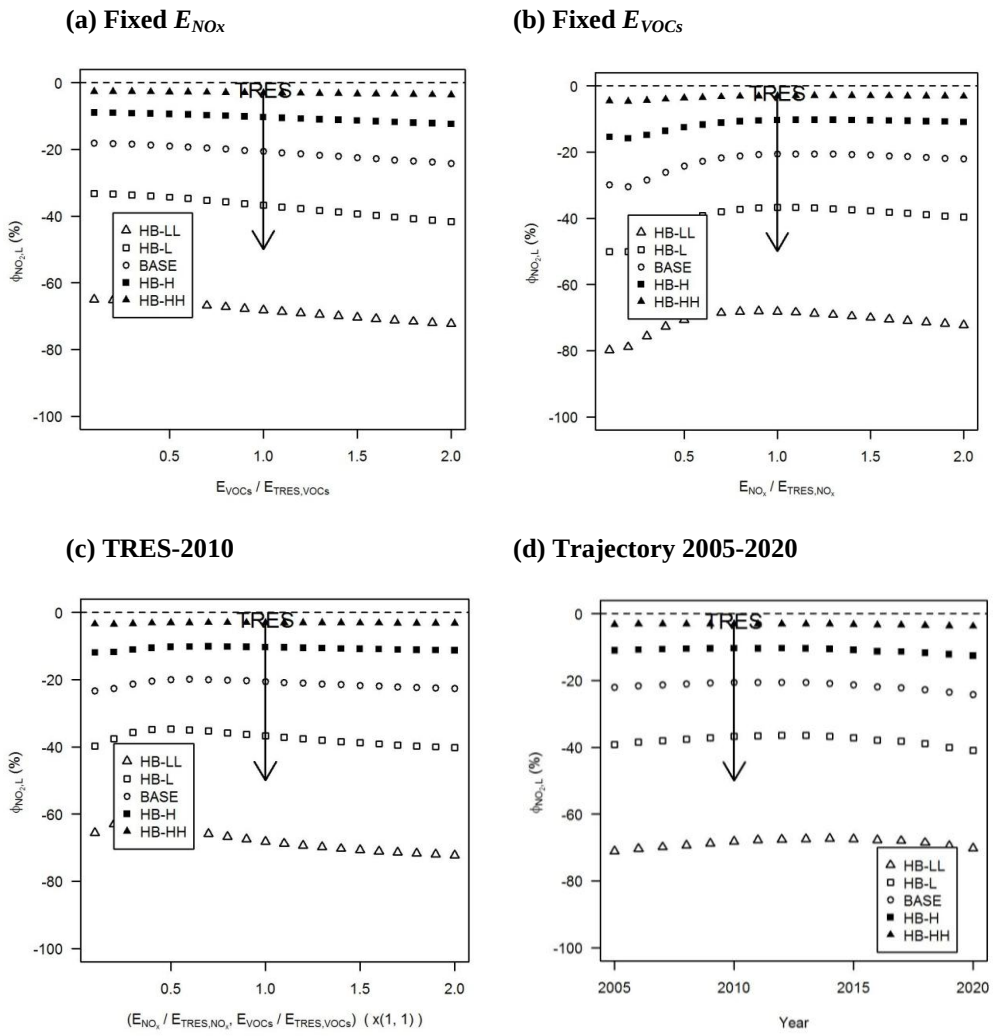

Figure 5.16 $\phi_{NO_2,L}$ (%), i.e. the percentage of overestimation for NO_2 in the lower canyon by the 'one-box' model compared with that by the "two-box" model, for (a) "Fixed E_{NOx}" at a fixed NO_x emissions of TRES, (b) "Fixed E_{VOCs}" at a fixed VOCs emissions of TRES, (c) "TRES-2010" varying the total traffic volume only and (d) "Trajectory 2005-2020" assuming constant traffic volume and speed varying α. E_{VOCs} and E_{NOx} are normalised by those of the Typical Real-world Emission Scenario (TRES, represented by△), for the year of 2010.

Figure 5.16 illustrates the transects of $\phi_{NO_2,L}$ (ppb) for Case HB-LL, Case HB-L, Case BASE, Case HB-H and Case HB-HH through the selected lines for analysis in Figure 5.5f. Figure 5.16a shows that the magnitude of $\phi_{NO_2,L}$ slightly increases with the increase of E_{VOCs}, i.e. from -64.94% to -72.29% for α=0.1, from -33.18% to -41.62% for α=0.3, from -18.14% to -24.16% for α=0.5, from -8.98% to -12.37% for α=0.7 and from -2.65%

to -3.65% for α =0.9. This indicates that the difference of $\phi_{NO_2,L}$ decreases with the increase of the box height ratio and the one box model performs better for the case with higher box height ratio. This finding is also indicated by Figure 5.16b, but the magnitude of $\phi_{NO_2,L}$ slightly decreases with the increase of E_{NOx}, especially for $E_{NO_x} / E_{TRES,NO_x}$ up to 0.5. Figure 5.16c also shows that there is not significant change in the $\phi_{NO_2,L}$ when changing both E_{VOCs} and E_{NOx} and that $\phi_{NO_2,L}$ is mainly influenced by the box height ratio (α). Figure 5.16d also shows that $\phi_{NO_2,L}$ do not change significantly over the year 2005 to 2020, but significant contrasts are found for the cases with different box height ratio.

5.3.4 Effect of shading

Figure 5.17 illustrates the effect of the shading ratio coefficient (RJ) on $C_{NO_2,L}$ (ppb), i.e. the concentration in the lower box for Case RJ-LL (RJ=0.1), (b) Case RJ-L (RJ=0.3), (c) Case RJ-M (RJ=0.5), (d) Case RJ-H (RJ=0.7), and (e) Case RJ-HH (RJ=0.9). RJ may vary with street properties and weather conditions. Koepke et al. (2010) suggest a general value of RJ=0.5 to parameterise street canyon shading effects, for a simple adoption in street canyon chemistry models. For typical street canyons, the value of RJ could be about 0.4~0.7 on a sunny day and about 0.2~0.3 on an overcast day. For skyscraper streets (i.e. deep street canyons), this shading effect will be stronger, with the value of RJ about 0.2~0.55 on a sunny day and about 0.15 on an overcast day. On the contrary, for wider street canyons, this shading effect is less significant, with the value of RJ about 0.85 in a sunny day and about 0.5~0.7 in an overcast day. Therefore, the tested range of RJ (0.1~0.9) is not unrealistic. In Figure 5.17, it is interesting to note that there is a considerable effect of the shading ratio coefficient (RJ) on $C_{NO_2,L}$. This could be indicated by the varying solid red curve. For higher emissions of VOCs, the solid red curve is found to shift dramatically

towards the region with lower emissions of NO_x as the shading ratio coefficient increase. However, for lower emissions of VOCs, the solid red curve is found to shift slightly towards the region with higher emissions of NO_x as the shading ratio coefficient increase. These can be explained as the increase of the shading ratio coefficient increases the conversion rate of NO to NO_2 through the VOCs oxidation driven by the photolysis production of OH, but decreases levels of NO_2 through the corresponding NO_2 photolysis reaction. The overall effect is the combination of those two processes. Those further indicate that for higher emissions of VOCs, the VOCs oxidation effect is dominant, which results in an increase of NO_2 with an increase of the shading ratio coefficient and that for lower emissions of VOCs, the effect of the NO_2 photolysis reaction is relatively more important. It is also noted that the solid red curves are found to cut across the trajectory 2005-2020 and TRES is observed in the region below the UK air quality standard for NO_2 only for Case RJ-LL, Case RJ-L and Case RJ-M. This indicates that the shading effect will affect the air quality in street canyons and that for TRES, NO_2 may exceed its air quality standard with the increase of the shading ratio coefficient.

(a) $C_{NO_2,L}$ **(ppb) for Case RJ-LL** **(b)** $C_{NO_2,L}$ **(ppb) for Case RJ-L**

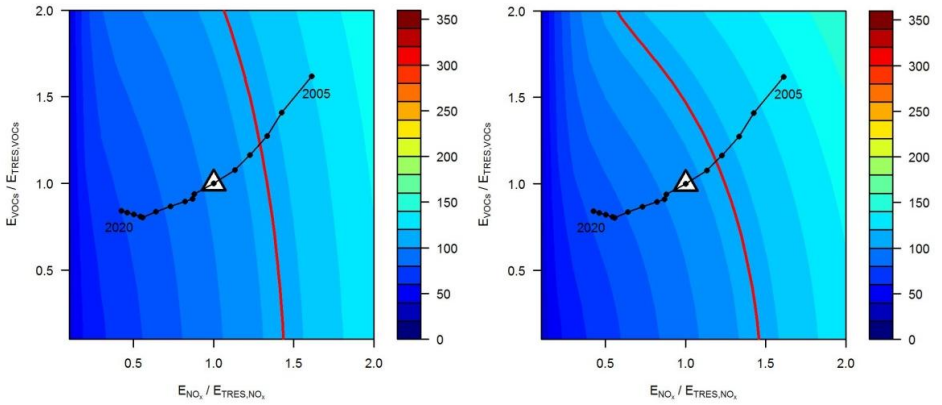

(c) $C_{NO_2,L}$ **(ppb) for Case BASE** **(d)** $C_{NO_2,L}$ **(ppb) for Case RJ-H**

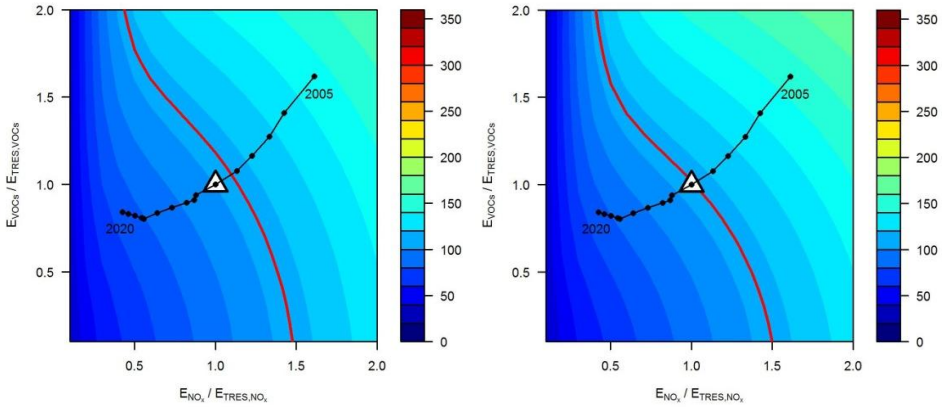

(e) $C_{NO_2,L}$ **(ppb) for Case RJ-HH**

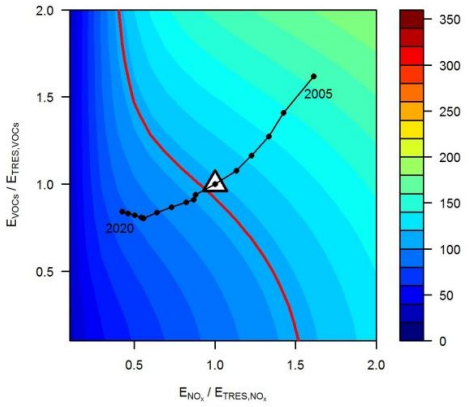

Figure 5.17 $C_{NO_2,L}$ **(ppb), i.e. the concentration in the lower box derived from the "two-box" model, in the (a) Case RJ-LL (RJ=0.1), (b) Case RJ-L (RJ=0.3), (c) Case RJ-M (RJ=0.5), (d) Case RJ-H (RJ=0.7), and (e) Case RJ-HH (RJ=0.9).** E_{VOCs} **and** E_{NOx} **are normalised by those of the Typical Real-world Emission Scenario (TRES, represented by△), for the year of 2010. Trajectory 2005-2020 represents the emission scenarios for 2005 to 2020, assuming constant traffic volume and speed. The solid red curves denote the UK air quality standard of hourly NO_2 (105 ppb).**

Figure 5.18 shows the transects of $C_{NO_2,L}$ (ppb) for Case RJ-LL, Case RJ-L, Case RJ-M, Case RJ-H and Case RJ-HH through the selected lines for analysis in Figure 5.5f. It is observed that $C_{NO_2,L}$ generally increases with the increase of E_{VOCs} and E_{NOx}. There is also evidence of the effect of the shading ratio coefficient on $C_{NO_2,L}$. Figure 5.18a shows that there is a significant difference between Case RJ-HH (RJ=0.9) and Case RJ-LL (RJ=0.1) with a maximum value of 50 ppb while the VOCs emission increase at the fixed NO_x emission. It is also interesting to note that $C_{NO_2,L}$ for Case RJ-LL slightly increases with the increase of VOCs emission at the fixed NO_x emission. This reflects that $C_{NO_2,L}$ is determined mainly by the NO_x emission rather than the photochemistry while the shading ratio coefficient is 0.1. Figure 5.18b shows that there is not significant changes (around 10 ppb) in the difference between Case RJ-HH (RJ=0.9) and Case RJ-LL (RJ=0.1) with the increase of NO_x emission at the fixed VOCs emission, except that negative values are found while NO_x emission is below 0.3 of that for TRES. This difference reflects the conversion extent of NO to NO_2 through VOCs oxidation at the various shading conditions. Figure 5.18c shows the combined effect of varying both VOCs and NO_x emissions. It is also interesting to note that $C_{NO_2,L}$ is significantly influenced by the shading ratio coefficient (RJ) for higher emissions of VOCs and NO_x with a minimum and maximum difference between Case RJ-HH (RJ=0.9) and Case RJ-LL (RJ=0.1) of -11 ppb and 42 ppb. Figure 5.18d shows that both $C_{NO_2,L}$ and the shading effect on $C_{NO_2,L}$ decrease with year. It indicates that less emissions due to the control technology result in lower levels of NO_2 and less significant impacts arising from shading effects.

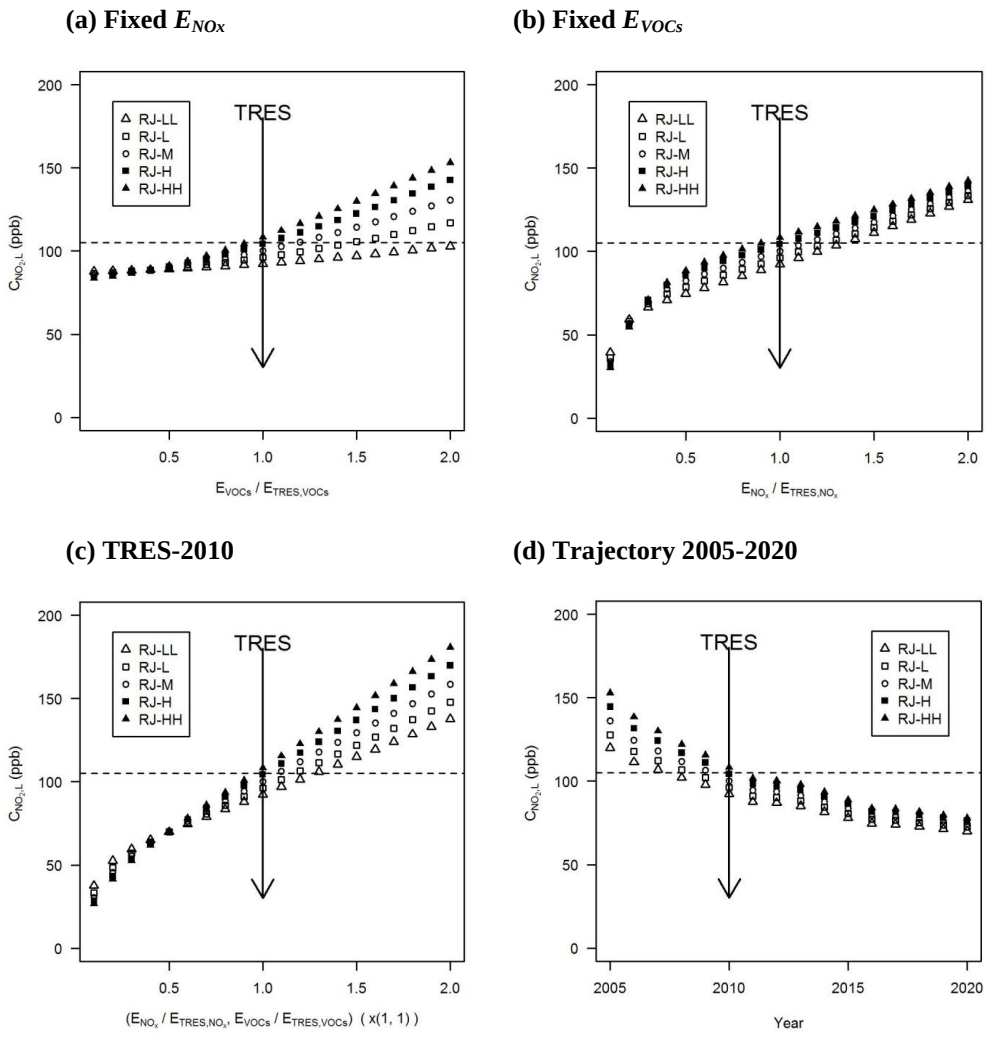

Figure 5.18 $C_{NO_2,L}$ (ppb), i.e. the concentration in the lower box derived from the "two-box" model, for (a) "Fixed E_{NOx}" at a fixed NO_x emissions of TRES, (b) "Fixed E_{VOCs}" at a fixed VOCs emissions of TRES, (c) "TRES-2010" varying the total traffic volume only and (d) "Trajectory 2005-2020" assuming constant traffic volume and speed varying RJ. E_{VOCs} and E_{NOx} are normalised by those of the Typical Real-world Emission Scenario (TRES, represented by△), for the year of 2010. The dashed line indicates the UK air quality standard of hourly NO_2 (105 ppb).

Figure 5.19 shows the effect of the shading ratio coefficient (RJ) on $\phi_{NO_2,L}$ (%), i.e. the percentage of overestimation for NO_2 in the lower canyon by the 'one-box' model without considering shading effect. It is observed that $\phi_{NO_2,L}$ changes significantly with the change of the shading ratio coefficient (RJ), i.e. (-53.16 %, 16.04 %) for Case RJ-LL with RJ=0.1, (-48.19 %, 2.88 %) for Case RJ-L with RJ=0.3, (-43.27 %, -7.01 %) for Case RJ-M with

(a) $\phi_{NO_2,L}$ (%) for Case RJ-LL

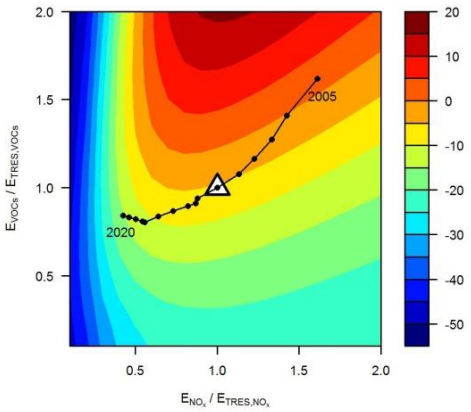

(b) $\phi_{NO_2,L}$ (%) for Case RJ-L

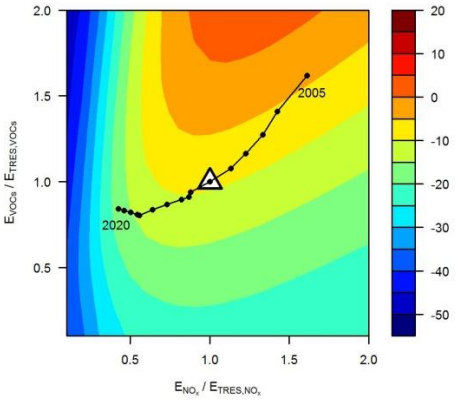

(c) $\phi_{NO_2,L}$ (%) for Case BASE

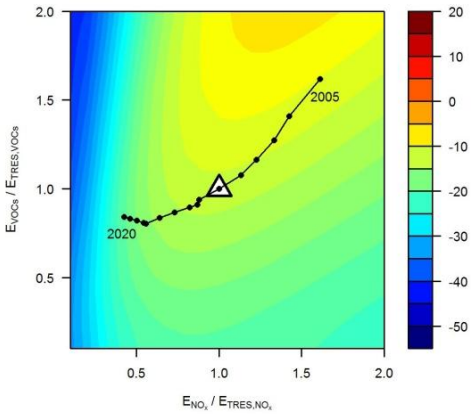

(d) $\phi_{NO_2,L}$ (%) for Case RJ-H

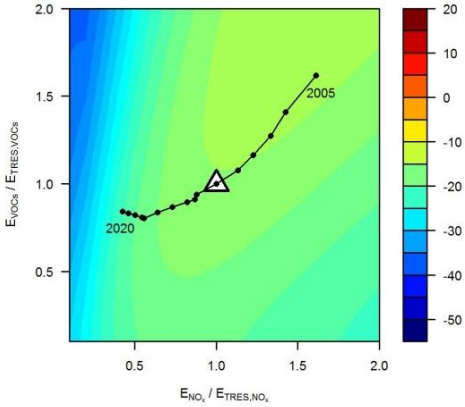

(e) $\phi_{NO_2,L}$ (%) for Case RJ-HH

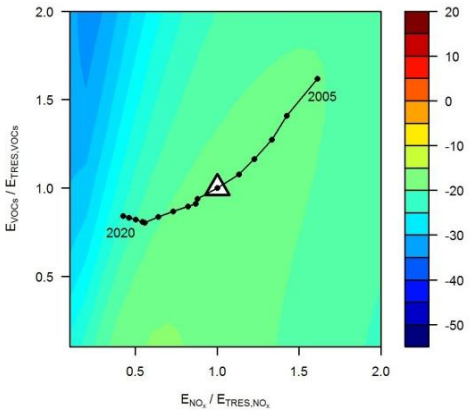

Figure 5.19 $\phi_{NO_2,L}$ (%), i.e. the percentage of overestimation for NO_2 in the lower canyon by the 'one-box' model compared with that by the "two-box" model, in the (a) Case RJ-LL (RJ=0.1), (b) Case RJ-L (RJ=0.3), (c) Case RJ-M (RJ=0.5), (d) Case RJ-H (RJ=0.7), and (e) Case RJ-HH (RJ=0.9). E_{VOCs} and E_{NOx} are normalised by those of the Typical Real-world Emission Scenario (TRES, represented by△), for the year of 2010. Trajectory 2005-2020 represents the emission scenarios for 2005 to 2020, assuming constant traffic volume and speed. The solid red curves denote the UK air quality standard of hourly NO_2 (105 ppb).

RJ=0.5, (-38.84 %, -14.42 %) for Case RJ-H with RJ=0.7 and (-35.37 %, -17.84 %) for Case RJ-HH with RJ=0.9. It is interesting to note that positive values are observed near the region with higher VOCs emissions and NO_x emissions for Case RJ-LL and Case RJ-L. It also indicates that the effect of shading is more significant for higher emissions scenarios. The smaller values of RJ reflect the less effective conversion of NO to NO_2, which is dominant and results in less NO_2. The one-box model generally underestimates NO_2 levels for the lower canyon compared with the two-box model, except for the higher emission scenarios with smaller RJ (e.g. RJ=0.1 and RJ=0.3).

Figure 5.20 illustrates the transects of $\phi_{NO_2,L}$ (ppb) for Case RJ-LL, Case RJ-L, Case RJ-M, Case RJ-H and Case RJ-HH through the selected lines for analysis in Figure 5.5f. Figure 5.20a shows that at the fixed NO_x emission, there are more rapid increase of $\phi_{NO_2,L}$ with the increase of VOCs emission for smaller shading ratio coefficient (e.g. positive values could occur for cases with RJ=0.1 and RJ=0.3). The maximum difference between Case RJ-LL and RJ-HH is up to 37.97 %. This also indicates the importance of shading effect while the VOCs emission is higher. Figure 5.20b shows that at the fixed VOCs emission, $\phi_{NO_2,L}$ increase rapidly while the NO_x emission is below 0.7 of that for TRES and then decreases slightly while the NO_x emission is over 0.7 of that for TRES. Figure 5.20c shows that changes of $\phi_{NO_2,L}$ with both VOCs and NO_x emission exhibit similar patterns as that in Figure 5.20a. This indicates that the effect of changing VOCs emissions is more significant for the scenarios. Figure 5.20d shows that $\phi_{NO_2,L}$ and the effect of the shading ratio coefficient decreases with year. This is due to the control of future emissions. The change for Case LL is the most significant.

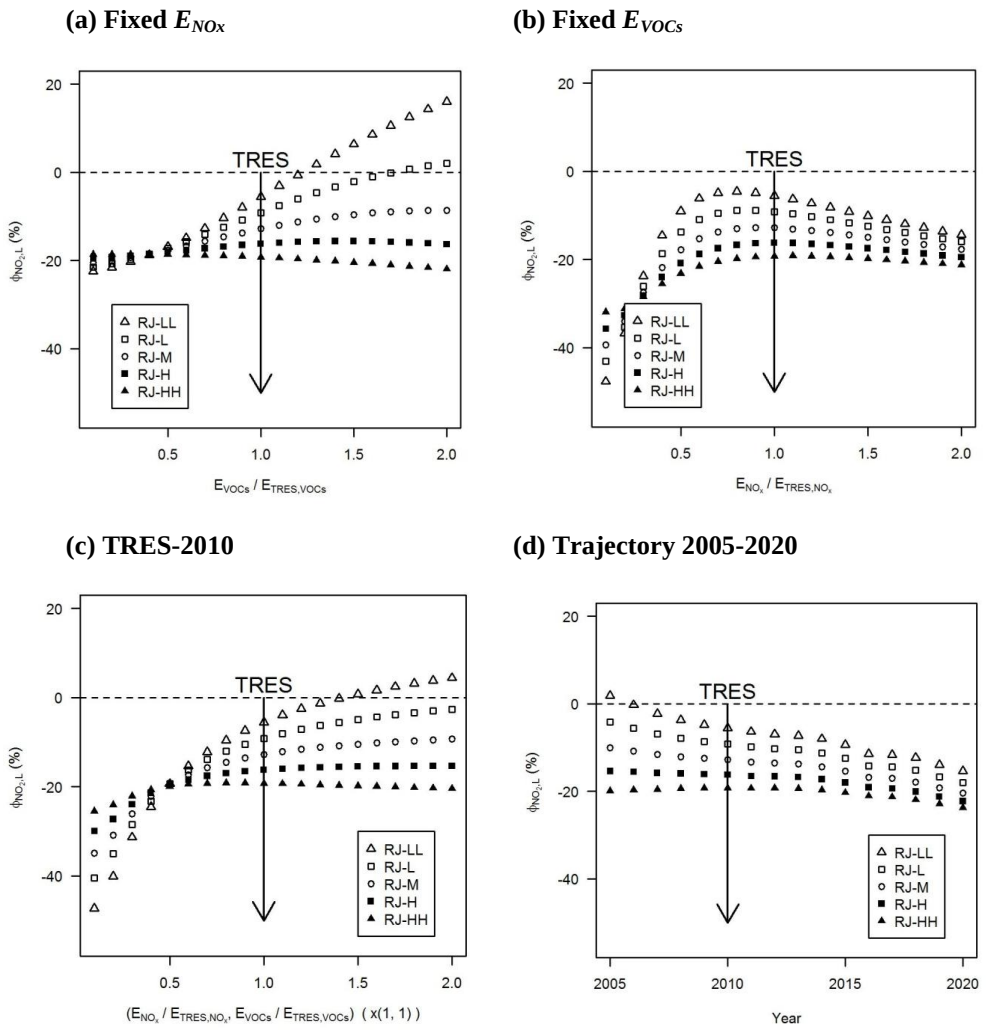

Figure 5.20 $\phi_{NO_2,L}$ (%), i.e. the percentage of overestimation for NO_2 in the lower canyon by the 'one-box' model compared with that by the "two-box" model, for (a) "Fixed E_{NOx}" at a fixed NO_x emissions of TRES, (b) "Fixed E_{VOCs}" at a fixed VOCs emissions of TRES, (c) "TRES-2010" varying the total traffic volume only and (d) "Trajectory 2005-2020" assuming constant traffic volume and speed varying RJ. E_{VOCs} and E_{NOx} are normalised by those of the Typical Real-world Emission Scenario (TRES, represented by△), for the year of 2010.

5.4 Conclusions

The bulk levels of air pollution within a street canyon focusing on the lower vertical levels where pedestrian / human exposure takes place) were investigated using the two-box model approach, which enables a wide range of emission scenarios to be considered. However, the two-box model is not able to capture the complex flow structures (e.g.

channelling flow, recirculating vortex, and helical flow) present in a real urban environment (Longley et al. (2004); Dobre et al. (2005); Barlow et al. (2009); Smalley et al. (2008)). The effect of real time wind speed and direction and stability on turbulent exchange at the shear layer (e.g. Eliasson et al. (2006); Christen et al. (2007); Schatzmann et al (2006)) is also absent by the two-box model. The performance of the one-box model approach (assuming the whole street canyon as a well-mixed box) was examined compared with the two-box model approach in terms of bulk concentrations in the lower canyon. Several important factors in the two-box model approach were also investigated.

The heterogeneity coefficient has a significant effect on NO_2 levels in the lower box (lower canyon) in the two-box model. Higher bulk NO_2 levels in the lower box were observed for cases with higher heterogeneity coefficient. Higher heterogeneity coefficient may be due to a larger AR, less local traffic induced turbulence in the lower box or the presence of more trees in the canyon, which results in less exchange between the lower and upper box. The NO_2 level is more likely to exceed its UK air quality standard for scenarios with higher heterogeneity coefficients. The control of local air ventilation between the lower and upper canyon is of vital importance in the improvement of air quality in the street canyon, through controlling the heterogeneity coefficient. Also, NO_2 levels were found to decrease with year for all heterogeneity coefficients, due to the reduction in emissions. The 'one-box' model was found to underestimate NO_2 levels (up to about 47% while the heterogeneity coefficient is 0.9) compared with those in the lower box by the 'two-box' model. It is also found that the performance of the one-box model tends to be close to the two-box model for cases with lower heterogeneity coefficients, which may reflect that the two boxes are less segregated or more mixed with each other.

The exchange velocity was found to significantly influence NO_2 levels in the lower box in the two-box model. The lower the exchange velocity is, the higher NO_2 levels in the lower box will be. It is not effective for pollutants to be carried from the lower box to the overlying street canyon for the case with lower exchange velocities. Even lower emissions under the worst dispersion conditions can result in very poor air quality inside street canyons. Emissions cases corresponding to a trajectory from 2005 - 2020 were found to completely fall into the region exceeding the UK air quality standard of NO_2 for Case EX-LL with the lowest exchange velocity. It is observed that $C_{NO_2,L}$ increases with increase of E_{VOCs} and E_{NOx}. Air ventilation was found to be of vital importance to control air quality in street canyons. It was found that the underestimation by the one-box model at a certain heterogeneity coefficient (η =0.5) was not significantly influenced by the exchange velocity.

The box height ratio has a significant influence on NO_2 levels in the lower box for the two-box model. It was found that there are extremely high levels of NO_2 for smaller box height ratio, i.e. a maximum value of about 520 ppb for Case HB-LL with α =0.1. This small box height ratio represents the case that pollutants are highly trapped in the small lower part of the street canyon under poor ventilation conditions, e.g. secondary smaller eddies near the street corner (where levels of pollutants are extremely high). The box height ratio is mainly dependent upon flow patterns in the street canyon, which can be reproduced by numerical modelling approach in high spatial and temporal resolution. The one-box model performance was found to be significantly influenced by the box height ratio. For higher box height ratios, the ‘one-box’ model predicts more accurate NO_2 concentrations, closer to the two-box model.

The shading ratio coefficient has a considerable effect on NO_2 levels in the lower box for the two-box model. The increase of the shading ratio coefficient increases the conversion rate of NO to NO_2 through the VOCs chemistry driven by the photolytic production of OH, but decreases levels of NO_2 through the corresponding NO_2 photolysis reaction. The overall effect is the combination of those two processes. NO_2 levels are determined mainly by the NO_x emission rather than the photochemistry when the shading ratio coefficient is very small (e.g RJ=0.1). The one-box model generally underestimates NO_2 levels for the lower canyon compared with the two-box model, except for the higher emission scenarios with smaller RJ (e.g. RJ=0.1 and RJ=0.3). The effect of shading is found to be more significant for higher emissions scenarios.

6 Modelling segregation effects of heterogeneous emissions in street canyons: Application of independent box models

6.1 Introduction

Atmospheric chemical and physical processes are tightly coupled in air quality simulations (Karamchandani et al., 2012). A general operating hypothesis of most urban air quality grid-based models is that primary air pollutants emitted are instantaneously well-mixed or distributed within the entire model grid-cell which contains the emissions (Auger and Legras, 2007). The grid-averaged emission rates of primary air pollutants are normally used as an input representing the mean gridded emissions (Denby et al., 2011) in atmospheric chemical models and the concentration in the canopy layer is modelled as one box representing the canopy layer for the entire grid cell. However, in reality these surface emissions vary, and exhibit a high temporal and spatial heterogeneous distribution at the sub-grid scale, referred to as surface sub-grid emission heterogeneity (Galmarini et al., 2008). This leads to segregation effects due to incomplete mixing. A major issue in urban air quality grid-based models is the parameterisation of surface sub-grid emission heterogeneity. In the grid-averaging procedure, all sub-grid scale processes and features (Ching et al., 2006) are lost and secondary pollutants (especially for O_3) may therefore be systematically under- or over-estimated. Grid-average parameterisation of heterogeneous emissions may result in significant uncertainty, and systematic biases in the urban air quality model output.

Several model approaches have been suggested to account for the impacts of sub-grid emission heterogeneity. Nested-grid or high-resolution modelling is a simple approach to resolve sub-grid scale variability. Examples of such approach can be seen from the Community Multi-scale Air Quality (CMAQ) model (e.g. Sokhi et al. (2006); Shrestha et al. (2009)), the Weather Research and Forecasting/Chemistry (WRF/Chem) model (Grell et al., 2005), and the Comprehensive Air Quality Model with extensions (CAMx) (Shen et al., 2011). A limitation of this approach is that it is only effective locally to a fixed area where the finer resolution grid is located. In order to overcome the limitation, adaptive grid modelling (e.g. Srivastava et al. (2000); Constantinescu et al. (2008); Garcia-Menendez et al. (2010)) was developed to allow dynamic change of the grid system during a simulation. Garcia-Menendez and Odman (2011) discussed the details and reviewed the advances of the adaptive grid modelling. Another approach to incorporate sub-grid emission heterogeneity is hybrid modelling, which combines a regional grid-based model with a local Gaussian dispersion model, e.g. ADMS (Arciszewska and McClatchey, 2001) and AERMOD (Zou et al., 2010). This approach has been extensively implemented, such as the CMAQ-ADMS model (e.g. Chemel et al. (2011); Beevers et al. (2012); Stocker et al. (2012)), the CMAQ-AERMOD model (e.g. Stein et al. (2007); Isakov et al. (2009); Johnson et al. (2010)) and the WRF-AERMOD model (Kesarkar et al., 2007). A more promising approach is the plume-in-grid (PinG) modelling (Karamchandani et al., 2002), which imbeds a non-steady-state plume model inside the grid. Vijayaraghavan et al. (2006) implemented the plume-in-grid (PinG) modelling approach in the CMAQ-APT model to reduce sub-grid scale variability in a simulation of central California. They found that the sub-grid treatment can lead to up to 10 ppb less O_3 under the condition of O_3 formation and up to 6 ppb more O_3 under other conditions, compared with a base simulation without

the PinG treatment. The approach offers a more realistic representation of the elevated point emission sources and their atmospheric fate. Galmarini et al. (2008) developed a Reynolds-averaged model to parameterize sub-grid emission heterogeneity in the meso- and global scale. Their study built upon the assumption that concentrations can be divided into a mean part, depending upon the average emissions, and a fluctuation component which depends on the variability of emissions, respectively. Alternatively, Cassiani et al. (2010) developed a stochastic fields method to address surface sub-grid emission heterogeneity in a mesoscale dispersion model. The advantage of this method is that the sub-grid scale emission variability is well-represented by the probability density functions. Some of the above approaches to address sub-grid scale errors are also reviewed and discussed in detail by Touma et al. (2006) and Karamchandani et al. (2011). Currently, strategies to address sub-grid emission heterogeneity are mostly focussed upon large scale grid-based models. However, for the small scale, there is little research focusing on the effects of sub-grid emission heterogeneity.

This chapter will extend consideration of emissions heterogeneity to the small scale, i.e. the canyon scale. The canopy layer is a major source for emissions into the overlying atmosphere / boundary layer and is normally within the lowest grid-cell of a grid-based model. From the canopy layer perspective, urban street canyons are typical sub-grid scale features separated by rows of buildings. These emissions into the canyon layer may be pre-processed within urban street canyons before they enter to the entire grid-cell in the lowest part of the grid-based model (Fisher et al., 2006). Urban street canyons, where human exposure takes place, are the area of interest in this chapter. The additional information between the grid-averaging implementation and the sub-grid calculation taking the emission heterogeneity into consideration may be of importance in terms of accurately

calculating air pollutant abundance and their associated adverse health effects. This chapter aims to investigate segregation effects of heterogeneous emissions on O_3 levels in idealised urban street canyons, and to identify how segregation effects are influenced by the balance between chemistry and dynamics. The methodology based on independent photochemical box models is described in detail. The results for prediction of O_3 levels and the intensity of segregation are also discussed.

6.2 Methodology

There are a large number of possible arrangements of street canyons in the urban canopy layer. In this chapter, two typical idealised urban street canyons are selected as a representation. One large photochemical box model (hereafter referred to as the 'one-box' model) with averaged emissions of the two street canyons is used to represent the deterministic calculation based on the grid-average process; alternatively two small independent photochemical boxes (hereafter referred to as the 'two-box' model set in parallel) are combined to represent two segregated street canyons with their own respective emissions. The photochemical box models can be simply applied and computationally inexpensive simulated (Curtis and Sweetenham, 1987). The reduced chemical scheme (RCS), developed by Bright et al. (2013), is used as the chemical mechanism within both configurations of the photochemical box models. The detailed model configuration is described as follows.

6.2.1 Model setup

Figure 6.1 illustrates the overview of the box model configuration adopted in this chapter. It is assumed that in a cell of an urban air quality model, there are two street canyons with heterogeneous emissions represented by Box 1 and Box 2 with the same volume of air as

indicated in the right panel (i.e. the 'two-box' model, which is horizontally segregated) of Figure 6.1. There is no exchange between the two boxes, i.e. total segregation is assumed; only the exchange between the within-canyon air and the background air above the canopy layer is taken into account. It is also assumed that the 'two-box' model represents the reality and the mean concentration,

$$C_{i,1+2} = (C_{i,1} + C_{i,2}) / 2 \tag{6.1}$$

represents the 'true' concentration of the i^{th} species in the canopy layer corresponding to this cell, with the concentrations in the 'one-box' model departing from this truth due to segregation effects. If a simplified approach of one single box (Box 0 indicated in the left panel of Figure 6.1) is adopted in which the volume of Box 0 is the sum of the volumes of Box 1 and Box 2 (indicated in the right panel of Figure 6.1) and $C_{i,0}$ is the modelled concentration from the 'one-box' model (Box 0 in Figure 6.1), there would be an error for $C_{i,0}$ (either an overestimation or an underestimation) in comparison with the 'true' mean concentration $C_{i,1+2}$ derived from the 'two-box' model (Box 1 and Box 2 in Figure 6.1).

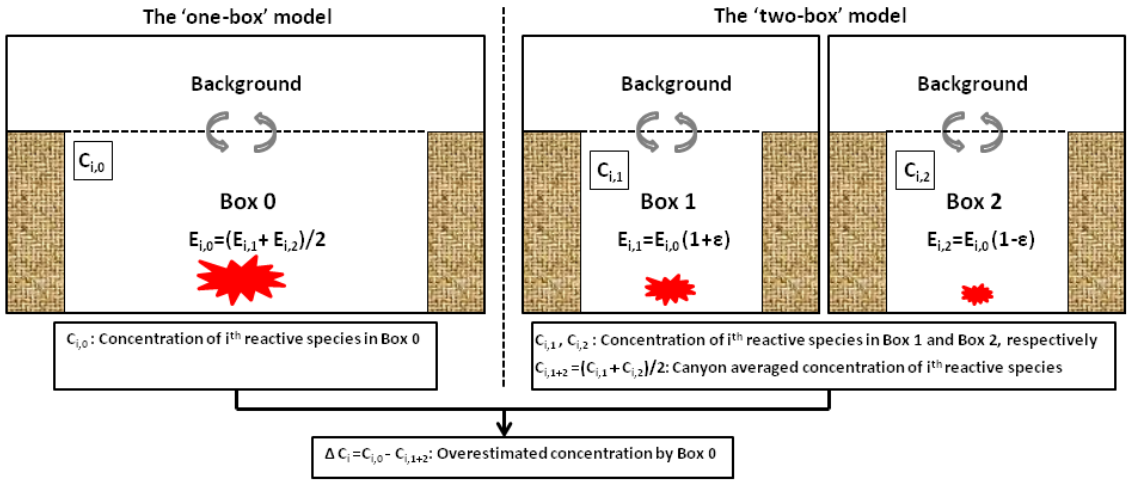

Figure 6.1 Overview of the model setup. $E_{i,m}$ means the emission rate of i^{th} species in Box m (m=0,1,2); ε is the heterogeneity of emissions.

This error can be expressed as

$$\Delta C_i = C_{i,0} - C_{i,1+2} \tag{6.2}$$

The value of ΔC_i may be also interpreted as the concentration difference due to heterogeneity of emissions, or the overestimated concentration by Box 0. For individual reactive species in the 'one-box' model (Box 0), the mass transport can be described as the following equation (Liu and Leung, 2008):

$$\frac{d}{dt} C_{i,0}(t) = E_{i,0} - \frac{w_{t,0}}{H_0}(C_{i,0} - C_{bi,0}) + \Delta S_{i,0} \tag{6.3}$$

where, $C_{i,0}$ (ppb) is the concentration of i^{th} species by volume in Box 0, t (s) is the time, $E_{i,0}$ (ppb s^{-1}) is the emission rate of i^{th} species by volume in Box 0, $w_{t,0}$ (m s^{-1}) is the exchange velocity between the street canyon and background for Box 0, H_0 (m) is the height of the street canyon of Box 0, $C_{bi,0}$ (ppb) is the background concentration of i^{th} species of Box 0 and $\Delta S_{i,0}$ (ppb s^{-1}) is the net production rate of i^{th} species due to chemical reactions in Box 0. Similarly, the system of equations in the 'two-box' model (Box 1 and Box 2) can be expressed as follows:

$$\frac{d}{dt} C_{i,1}(t) = E_{i,1} - \frac{w_{t,1}}{H_1}(C_{i,1} - C_{bi,1}) + \Delta S_{i,1} \tag{6.4}$$

$$\frac{d}{dt} C_{i,2}(t) = E_{i,2} - \frac{w_{t,2}}{H_2}(C_{i,2} - C_{bi,2}) + \Delta S_{i,2} \tag{6.5}$$

In Equations 6.4 and 6.5, all symbols are as those in the Equation 6.3 but for Box 1 and Box 2, respectively. In this model framework, it is assumed that $w_{t,0} = w_{t,1} = w_{t,2}$, $C_{bt,0} = C_{bt,1} = C_{bt,2}$, $E_{i,1} = E_{i,0}(1+\varepsilon)$ and $E_{i,2} = E_{i,0}(1-\varepsilon)$, where ε is the heterogeneity

of emissions for the two-box model (e.g. $\varepsilon = 0$: homogeneous emissions for the two boxes; $\varepsilon = 1$: all emissions into Box 1 and no emissions into Box 2). When the systems reach the steady state (or a quasi-steady state) as $t \to t_s$, then $\frac{d}{dt} C_{i,m}(t) \to 0$ (m=0,1,2), and Equations 6.3-6.5 yield:

$$C_{i,0}(t_s) = \frac{H_0}{w_{t,0}}[E_{i,0} + \Delta S_{i,0}(t_s)] + C_{bi,0} \tag{6.6}$$

$$C_{i,1}(t_s) = \frac{H_1}{w_{t,1}}[E_{i,1} + \Delta S_{i,1}(t_s)] + C_{bi,1} \tag{6.7}$$

$$C_{i,2}(t_s) = \frac{H_2}{w_{t,2}}[E_{i,2} + \Delta S_{i,2}(t_s)] + C_{bi,2} \tag{6.8}$$

$$C_{i,1+2}(t_s) = [C_{i,1}(t_s) + C_{i,2}(t_s)]/2 \tag{6.9}$$

Thus the concentrations $C_{i,m}$ and the chemical production rate $\Delta S_{i,m}$, for m=0,1,2, are related by above respective equations. The relationships are a function of the corresponding emission rates and background conditions, respectively. It is noted that, from Equations 6.2,6.6-6.9, it can be derived that

$$\Delta C_i(t_s) = \frac{H_0}{w_{t,0}}[\Delta S_{i,0}(t_s) - \frac{\Delta S_{i,1}(t_s) + \Delta S_{i,2}(t_s)}{2}] \tag{6.10}$$

If the emission is a passive scalar (i.e. a species which does not undergo chemical reaction), then the difference $\Delta C_i(t_s)$ is zero. For reactive species, the differences depend on the heterogeneity of emissions and the nonlinear nature of photochemical reactions, together with the exchange velocity caused by dynamic effects. Therefore the characteristics of $\Delta C_i(t_s)$ can be complex and will be examined in depth in the following sections.

Finally, the *percentage of overestimation* by the 'one-box' model (Box 0) for the i^{th} species is defined as:

$$\phi_{i,1+2}(t) = \frac{\Delta C_i(t)}{C_{i,1+2}(t)} \times 100\% \tag{6.11}$$

$\phi_{i,1+2}(t)$ may be also interpreted as the overestimated concentration by the 'one-box' model relative to the 'true' concentration by the 'two-box' model. If $\phi_{i,1+2}(t) = 0\%$, it means that the 'one-box' model provides the true answer; if $\phi_{i,1+2}(t) = 10\%$ or -10%, it means that the 'one-box' model over- or under-estimates the concentration by 10%, respectively.

6.2.3 Model scenarios

This chapter focuses on the effects of two parameters, ε (heterogeneity of emissions) and $w_{t,0}$ (exchange velocity), on $\phi_{O_3,1+2}$ and other characteristics. Table 6.1 gives an overview of the two parameters for all cases. For each case, the corresponding one photochemical box model (i.e. the 'one-box' model, Box 0) and two segregated photochemical box models (i.e. the 'two-box' model, Box 1 and Box 2) were run. The heterogeneity of emissions (ε) is set at a value of 0.5 and the exchange velocity ($w_{t,0}$) is set as 0.02 m s^{-1} in the base case, 'BASE'. The value of ε=0.5 implies that the emissions into Box 1 (or Box 2) is 50% higher (or lower) than the averaged emissions parameterized into Box 0. In reality, this is often the case; within an Eulerian cell of an urban air quality model, some streets are likely to have a much higher level of traffic than others. The value of $w_{t,0}$=0.02 m s^{-1} is adopted based on the result from a large-eddy simulation for a street canyon with a 18 m× 18 m cross-section under a neutral condition if the reference wind speed is about 2 m s^{-1}

(Cai, 2012a). In order to account for the segregation effect due to variations of ε and $w_{t,0}$, we examine in detail the cases in which only either ε or $w_{t,0}$ is changed while keeping other parameters unchanged. To consider the effect of ε, Case HE-LL, HE-L, HE-H and HE-HH have been configured with ε =0.1, ε =0.3, ε =0.7, ε =0.9 respectively, while keeping the same $w_{t,0}$ as that of Case BASE (ε =0.5). To consider the effect of $w_{t,0}$, Case EX-LL, EX-L, EX-H and EX-HH have been set up with $w_{t,0}$ =0.012 m s^{-1}, $w_{t,0}$ =0.016 m s^{-1}, $w_{t,0}$ =0.024 m s^{-1}, $w_{t,0}$ =0.028 m s^{-1} respectively, while keeping the same ε as that of Case BASE ($w_{t,0}$ =0.020 m s^{-1}). The range of values of w_t from 0.012 m s^{-1} to 0.028 m s^{-1} is justified based on previous findings that $w_{t,0}$ varies when the canyon aspect ratio is altered from 1 to a higher or lower value (e.g. Chung and Liu (2013)) and that urban surface heating may enhance $w_{t,0}$ significantly (e.g. Cai (2012a)).

Table 6.1 Overview of model scenarios

Case	Heterogeneity of emissions (ε)	Exchange velocity $w_{t,0}$ (m.s^{-1})
BASE	0.5	0.02
HE-LL	0.1	0.02
HE-L	0.3	0.02
HE-H	0.7	0.02
HE-HH	0.9	0.02
EX-LL	0.5	0.012
EX-L	0.5	0.016
EX-H	0.5	0.024
EX-HH	0.5	0.028

Note: 'BASE' is the base case. 'HE' denotes the heterogeneity of emissions, while 'EX' means the exchange velocity. 'L' or 'H' represents a lower or higher value than the corresponding component in the base Case BASE. 'LL' or 'HH' means a even lower value than that for 'L' or 'H'.

6.3 Results and discussion

6.3.1 Effect of the heterogeneity of emissions

Figure 6.2 depicts the effect of the heterogeneity of emissions (ε) on $C_{O_3,1+2}$ (ppb), i.e. the 'true' concentration derived from the 'two-box' model for (a) Case HE-LL (ε =0.1), (b) Case HE-L (ε =0.3), (c) Case BASE (ε =0.5), (d) Case HE-H (ε =0.7) and (e) Case HE-HH (ε =0.9). In this model, the background O_3 concentration is approximately 43.61 ppb and by using a Region Partition Line (RPL), the plot area can be divided into 2 regions, i.e. Region I for which $C_{O_3,1+2}$ is lower than the background O_3 concentration and Region II for which $C_{O_3,1+2}$ is higher than the background O_3 concentration. In Region I, the titration effect of O_3 by NO (indicated by relatively more NO_x emissions in Figure 6.2) is dominant and therefore leads to the net destruction of O_3 (i.e. lower than the background levels). However, in Region II, OH oxidation processes are dominant and sufficient VOCs (indicated by relatively more VOCs emissions in Figure 6.2) are present to promote the conversion of NO to NO_2 by peroxy radicals, thereby causing net ozone formation. It is therefore not surprising that $C_{O_3,1+2}$ is higher than its background level in Region II. The RPL for the cases is marked in Figure 6.2. It is noted that the change of ε has no effect on the position of the RPL, but has a considerable effect on the pattern in Region I and Region II. The TRES is also marked in the plots with triangle symbol; this emission scenario falls into Region I for the cases in Figure 6.2. This represents the typical situation in an urban area, namely that the ozone concentration inside a street canyon is lower than that in the overlying background atmosphere. It is also observed that the trajectory from 2005 to 2020 falls into Region I and is approaching to the RPL with the reduction of

(a) $C_{O_3,1+2}$ (ppb) for Case HE-LL **(b) $C_{O_3,1+2}$ (ppb) for Case HE-L**

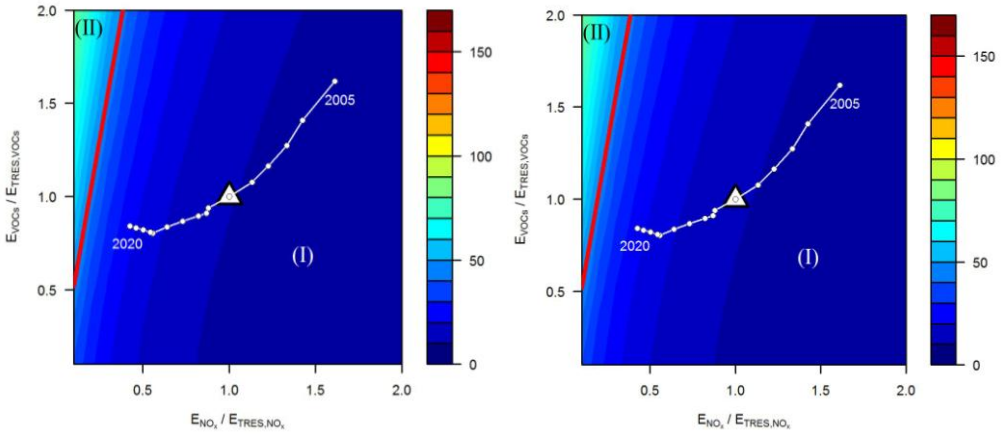

(c) $C_{O_3,1+2}$ (ppb) for Case BASE **(d) $C_{O_3,1+2}$ (ppb) for Case HE-H**

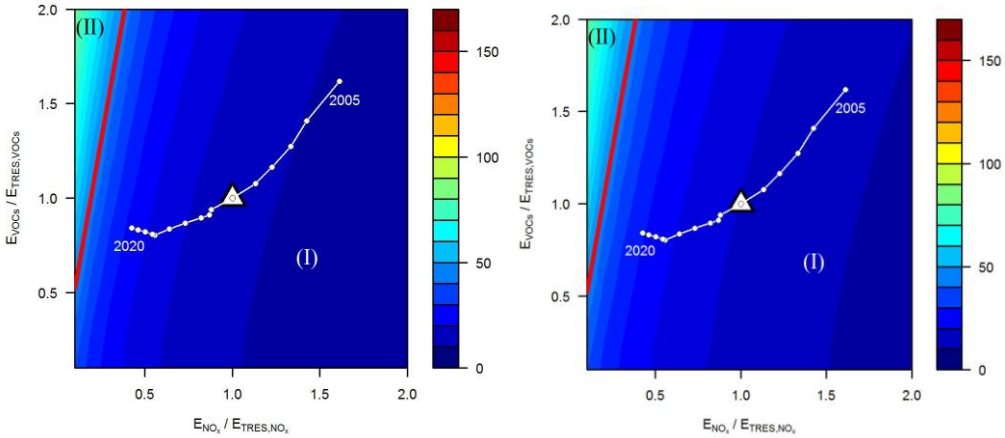

(e) $C_{O_3,1+2}$ (ppb) for Case HE-HH

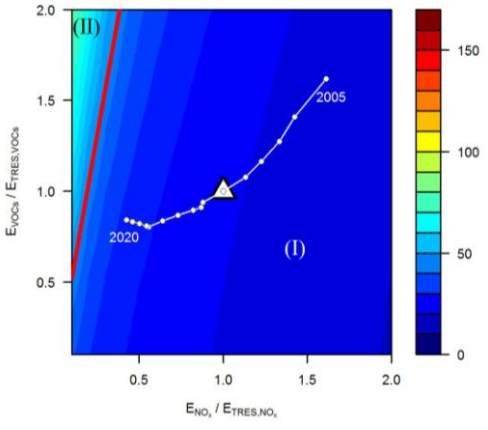

Figure 6.2 $C_{O_3,1+2}$ (ppb), the 'true' concentration of O_3 derived from the 'two-box' model, in (a) Case HE-LL (ε =0.1), (b) Case HE-L (ε =0.3), (c) Case BASE (ε =0.5), (d) Case HE-H (ε =0.7) and (e) Case HE-HH (ε =0.9). E_{VOCs} and E_{NOx} are normalised by those of the Typical Real-world Emission Scenario (TRES, represented by △), for the year of 2010. The Region Partition Line (RPL) is represented by the solid red line; Trajectory 2005-2020 represents the emission scenarios for 2005 to 2020, assuming constant traffic volume and speed.

VOCs and NO_x emissions due to current and future control technologies, assuming constant activity (i.e. traffic) levels.

Figure 6.3 illustrates the transects of $C_{O_3,1+2}$ (ppb) through selected lines for analysis (shown as Figure 5.5f). Figure 6.3a and Figure 6.3b demonstrate that $C_{O_3,1+2}$ increases with E_{VOCs} for the "Fixed E_{NOx}"scenario, but decreases with E_{NOx} for the "Fixed E_{VOCs}" scenario. Figure 6.3c suggests that for less busier roads than the TRES, $C_{O_3,1+2}$ is higher, and vice versa. Figure 6.3d shows that as control technologies are applied, $C_{O_3,1+2}$ increases. By 2020 it will be closer to the background level, particularly for Case HE-HH. The results indicate a nonlinear relationship between the O_3 concentration and E_{VOCs} and/or E_{NOx}, which is in line with many previous studies (e.g. Liu and Leung (2008)). It is also observed that the highest ozone concentration occurs to Case HE-HH with the largest the heterogeneity of emissions (ε =0.9). The segregation of emissions can lead to around 10 ppb difference between Case HE-HH and Case HE-LL and this effect is less significant when E_{NOx} is at a very low value (Figure 6.3b and Figure 6.3c). The TRES is indicated by a solid arrow line in Figure 6.3a-d and while ε is less than 0.5, the effect of segregation on $C_{O_3,1+2}$ for the TRES are less significant with a small variation across those scenarios tested. However, the analysis below demonstrates that these concentrations as determined by the 'two-box' model will be significantly underestimated by the 'one-box' model.

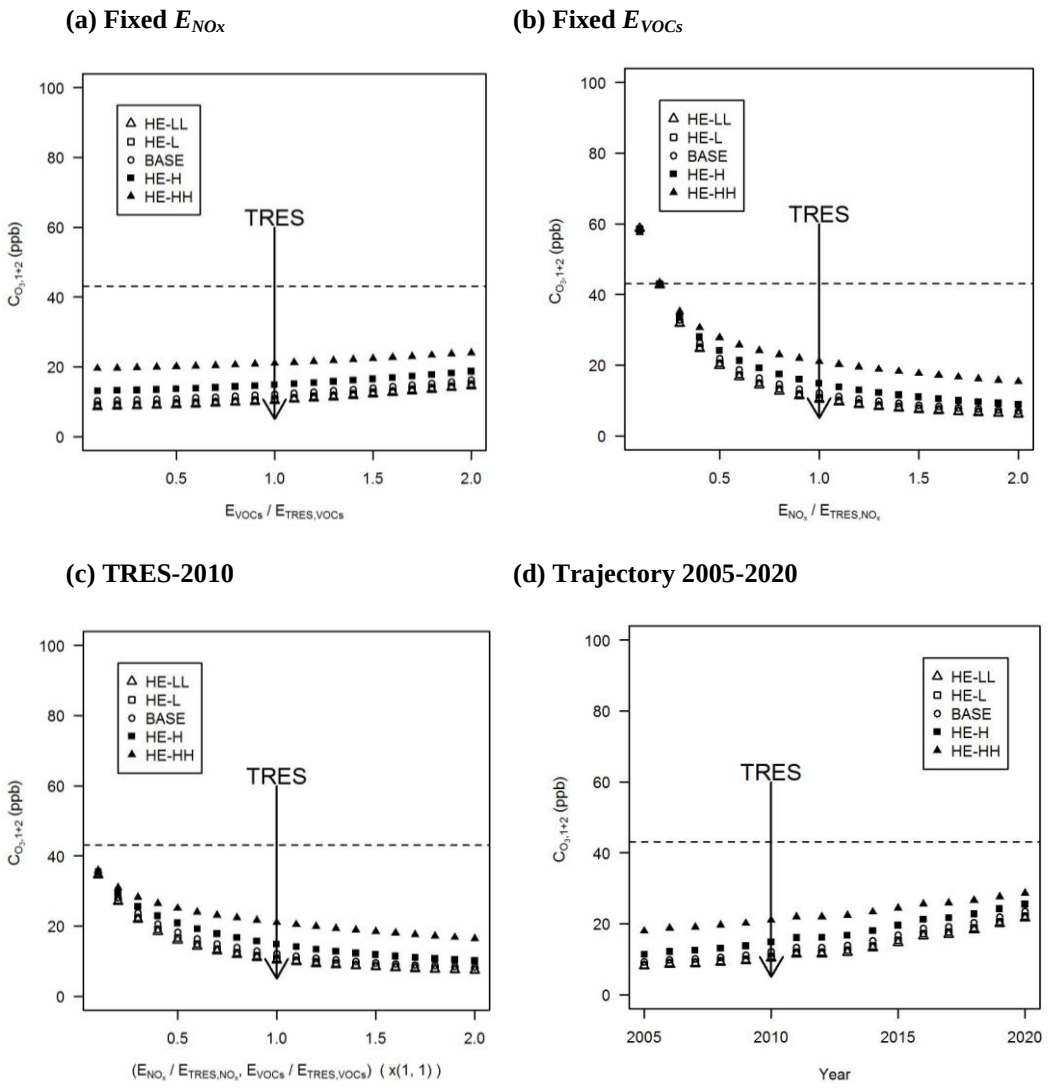

Figure 6.3 $C_{O_3,1+2}$ (ppb), the 'true' concentration of O_3 derived from the 'two-box' model, for (a) "Fixed E_{NOx}" at a fixed NO_x emission of TRES, (b) "Fixed E_{VOCs}" at a fixed VOCs emission of TRES, (c) "TRES-2010" varying the total traffic volume only and (d) "Trajectory 2005-2020" assuming constant traffic volume and speed varying ε. E_{VOCs} and E_{NOx} are normalised by those of the Typical Real-world Emission Scenario (TRES, represented by the solid arrow lines), for the year of 2010; The dashed line indicates the background O_3 level.

Figure 6.4 shows the effect of the heterogeneity of emissions (ε) on the values for $\phi_{O_3,1+2}$ (the percentage of overestimation for O_3 by the 'one-box' model) (a) Case HE-LL (ε=0.1), (b) Case HE-L (ε=0.3), (c) Case BASE (ε=0.5), (d) Case HE-H (ε=0.7) and (e) Case HE-HH (ε =0.9). It is interesting to notice that the RPL (defined above) of each case

approximately splits the plot area into two regions, i.e. Region I where $\phi_{O_3,1+2}$ is negative and Region II where $\phi_{O_3,1+2}$ is positive. In Region I, $\phi_{O_3,1+2}$ is negative, which means the modelled O_3 concentration by the 'one-box' model is lower than the 'true' value by the 'two-box' model (i.e. the 'one-box' model will underestimate O_3 levels). It is further shown that there is a rapid change in $\phi_{O_3,1+2}$ while only ε is changed from 0.1 to 0.9 (Figure 6.4a-e). The larger ε is, the higher the maximum level of $\phi_{O_3,1+2}$ will be. The maximum underestimation could be up to -62.32 % for Case HE-HH (Figure 6.4e), and the minimum underestimation could be -0.67 % for Case HE-LL (Figure 6.4a). The very small underestimation suggests that the performance of the 'one-box' model is very close to that of the 'two-box' model, while the heterogeneity of emissions is very small (ε =0.1). The trajectory from 2005 to 2020 falls into the underestimation area (i.e. Region I), and is marked in the plot (Figure 6.4a-e). In Region II for all the cases, the O_3 levels will be slightly over-estimated up to 4.45 % obtained for Case HE-HH with ε =0.9 (Figure 6.4e). In the procedure of photochemical model evaluations, recommended values (EPA, 1991) for generic systematic biases in the model output are ± 5-15%. Changes in parameterisation of sub-grid heterogeneous emissions are necessary when values of $\phi_{O_3,1+2}$ are above the recommended range of ± 5-15%. Figures 6.4a-e indicate that the effect of emission parameterisation on the model output becomes significant while ε is larger than 0.3. Karamchandani et al. (2012) showed a sub-grid scale error of 5% in predicting O_3 levels by their CMAQ regional modelling with the plume-in-grid (PinG) approach. Vijayaraghavan et al. (2006) showed that there were significant negative biases ranging from -15% to 39% for O_3 in their box models with Advanced Plume Treatment (APT) of sub-grid emissions.

(a) $\phi_{O_3,1+2}$ (%) for Case HE-LL **(b) $\phi_{O_3,1+2}$ (%) for Case HE-L**

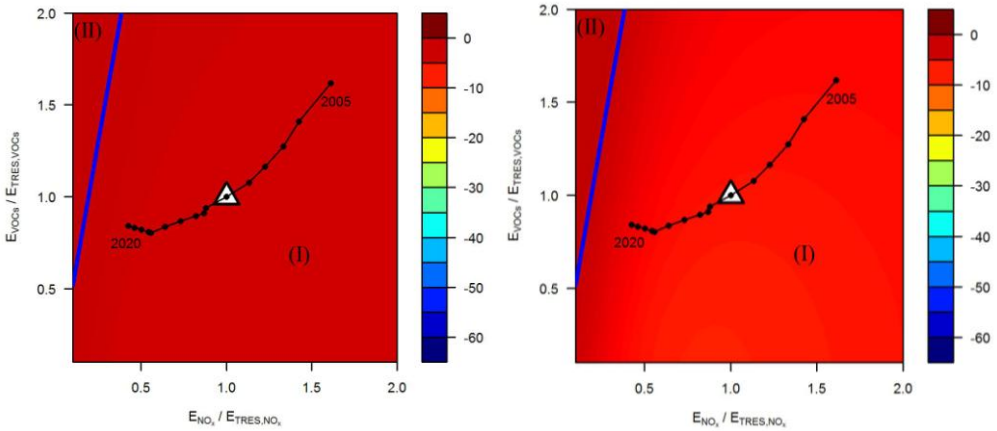

(c) $\phi_{O_3,1+2}$ (%) for Case BASE **(d) $\phi_{O_3,1+2}$ (%) for Case HE-H**

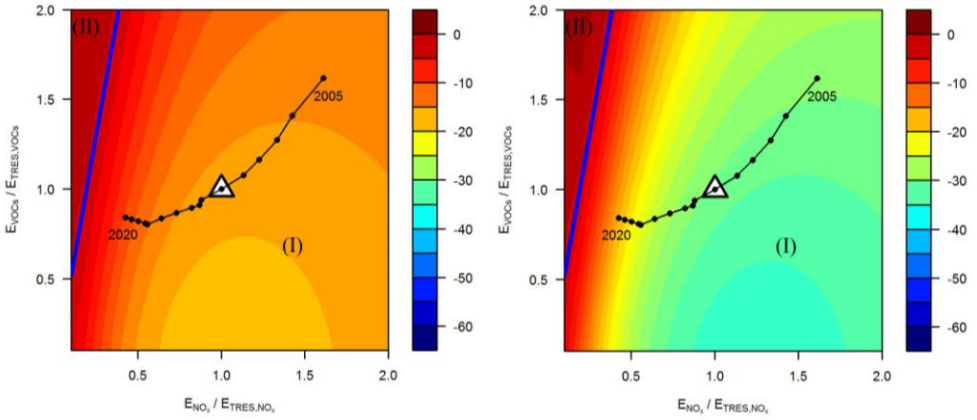

(e) $\phi_{O_3,1+2}$ (%) for Case HE-HH

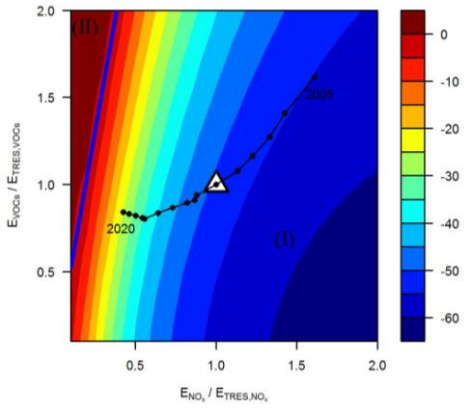

Figure 6.4 $\phi_{O_3,1+2}$ (%), the percentage of overestimation for O_3 by the 'one-box' model, in (a) Case HE-LL (ε =0.1), (b) Case HE-L (ε =0.3), (c) Case BASE (ε =0.5), (d) Case HE-H (ε =0.7) and (e) Case HE-HH (ε =0.9). E_{VOCs} and E_{NOx} are normalised by those of the Typical Real-world Emission Scenario (TRES, represented by △), for the year of 2010. The **Region Partition Line (RPL) is represented by the solid red line; Trajectory 2005-2020 represents the emission scenarios for 2005 to 2020, assuming constant traffic volume and speed.**

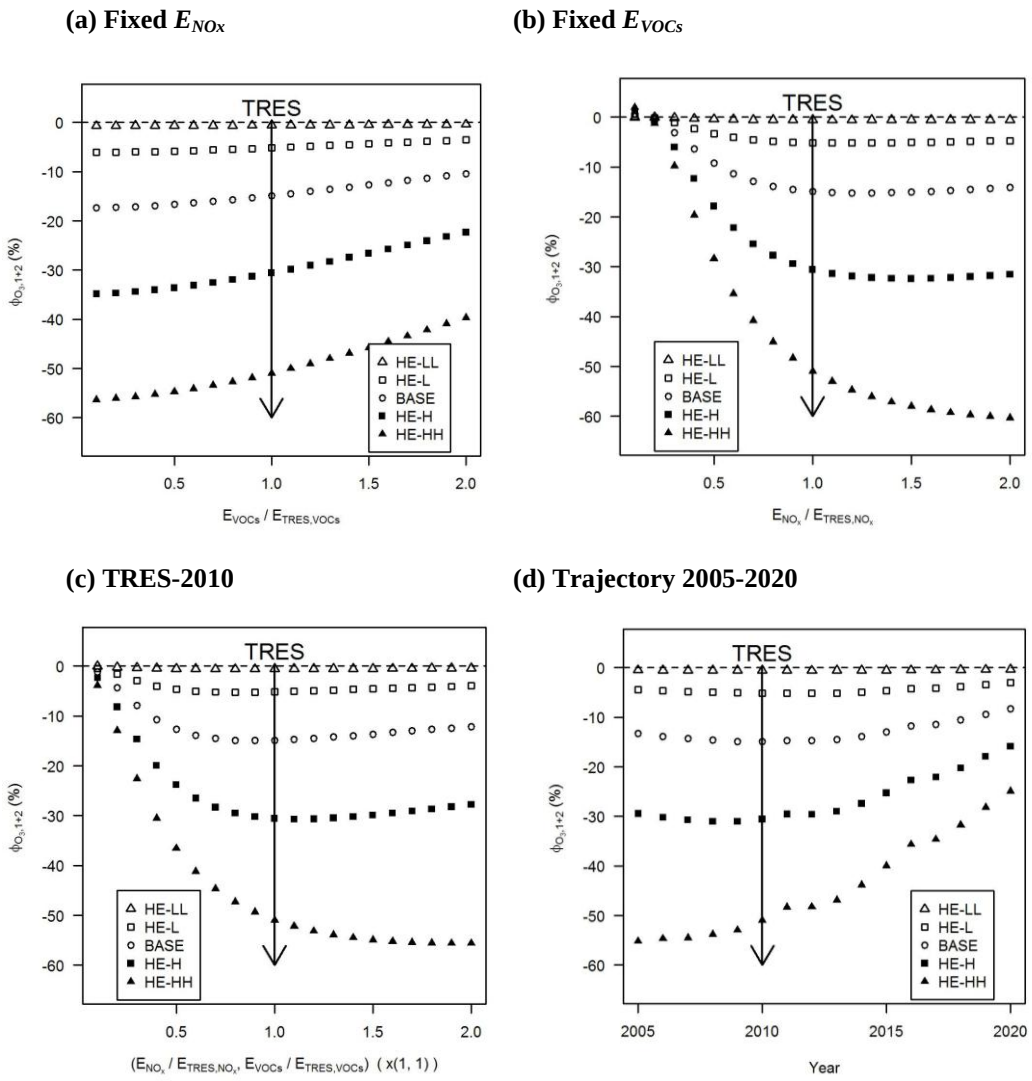

Figure 6.5 ϕ_{O_3} (%), the percentage of overestimation for O_3 by the 'one-box' model, for (a) "Fixed E_{NOx}" at a fixed NO_x emission of TRES, (b) "Fixed E_{VOCs}" at a fixed VOCs emission of TRES, (c) "TRES-2010" varying the total traffic volume only and (d) "Trajectory 2005-2020" assuming constant traffic volume and speed varying ε. E_{VOCs} and E_{NOx} are normalised by those of the Typical Real-world Emission Scenario (TRES, represented by the solid arrow lines), for the year of 2010; The dashed line indicates the background O_3 level.

Figure 6.5 shows the transects of $\phi_{O_3,1+2}$ through the selected lines, which also shows the significant effect of ε on $\phi_{O_3,1+2}$. Figure 6.5a shows that as E_{VOCs} increases at the fixed E_{NOx} of TRES, the modelled O_3 concentrations by the 'one-box' model are underestimated compared with the 'true' values, indicated by the negative $\phi_{O_3,1+2}$. The lower E_{VOCs} is, the

larger the extent of underestimation will be. This indicates that by keeping traffic-emission rate E_{NOx} unchanged, extra E_{VOCs} (e.g. from vegetation or anthropogenic activities) will reduce $\phi_{O_3,1+2}$, resulting in the improved performance (closer approach to reality) of the 'one-box' model. However, future reduction in vehicle-related E_{VOCs}, anticipated to arise from renewal of the vehicle fleet and implementation of more stringent emissions reduction technologies, will lead to an increase in the magnitude of $\phi_{O_3,1+2}$. This also suggests that the performance of the 'one-box' model for O_3 concentration might be expected to be better for a more 'green' area, with biogenic VOC emissions, assuming such emissions were not incorporated in the model scenario / conditions. Figure 6.5b shows that the magnitude of $\phi_{O_3,1+2}$ increases while E_{NOx} increases at the fixed E_{VOCs} of TRES. The modelled O_3 concentrations by the 'one-box' model largely underestimate the 'true' values, indicated by the negative $\phi_{O_3,1+2}$ (within Region I), with small positive values for $\phi_{O_3,1+2}$ only obtained at the lowest E_{NOx} (within Region II). The rapid increase of $\phi_{O_3,1+2}$ for the case with the higher heterogeneity of emissions suggests that reductions in vehicle NO_x emissions anticipated to arise from renewal of the vehicle fleet and implementation of more stringent emissions reduction technologies, will lead to a reduction in the magnitude of $\phi_{O_3,1+2}$, i.e. an improvement in model performance overall. Figure 6.5c shows the results of $\phi_{O_3,1+2}$ along the TRES-2010 line, i.e. varying E_{VOCs} and E_{NOx} with the same emission ratio for the TRES (e.g. less or more trafficked areas). It is noted that the performance of the 'one-box' model for a less trafficked area/scenario (e.g. Birmingham) is generally better than that for a more trafficked area/scenario (e.g. London). Figure 6.5d shows the results of $\phi_{O_3,1+2}$ along the trajectory from the year of 2005 to 2020. It is noted that the level of extent of underestimation generally deceases with year, which

indicates that in the future the performance of the 'one-box' model will be better. The underestimates of O_3 concentrations by the 'one-box' model for the year 2020 could be about -25 % for Case HE-HH with ε=0.9.

Figure 6.6 illustrates the effect of the heterogeneity of emissions (ε) on $I_{S(O_3+NO)}$, i.e. the intensity of segregation between O_3 and NO. It is also interesting to notice that the RPL of each case approximately divides the plot area into two regions, i.e. Region I where $I_{S(O_3+NO)}$ is negative and Region II where $I_{S(O_3+NO)}$ is positive as indicated in Figure 6.6a-e. The trajectory from the year of 2005 to 2020 falls into the negative region (i.e. Region I), and is marked in the plot for each case. It can be shown that $I_{S(O_3+NO)}$ changes significantly with the change of ε (Figure 6.6a-e). The minimum and maximum range of $I_{S(O_3+NO)}$ could be (-0.87 %, 0.17 %) for Case HE-HH with ε=0.9 (Figure 6.6a), (-67.10 %, 17.19 %) for Case HE-HH with ε=0.9 (Figure 6.6e). It is noted that the plots of $I_{S(O_3+NO)}$ (Figure 6.6) are strongly correlated with those of $\phi_{O_3,1+2}$ (Figure 6.4). In Region I, the heterogeneity of emissions will lead to negative values of $I_{S(O_3+NO)}$, which means that the effective rate constant of the titration reaction (NO + O_3 $\rightarrow$ NO_2 + O_2) to consume O_3, $\left\langle k_{eff\,(O_3+NO)} \right\rangle = k_{(O_3+NO)}(1+I_{S(O_3+NO)})$, in the 'two-box' model is lower than the original rate constant, $k_{(O_3+NO)}$, in the 'one-box' model. In other words, adopting the classical rate constant $k_{(O_3+NO)}$ in the 'one-box' model results in too much titration. As a result, the ozone level in the 'two-box' model (i.e. the 'true' value) is higher than the modelled ozone level from the 'one-box' model, which agrees well with a negative value of $\phi_{O_3,1+2}$, i.e. the modelled ozone level from the 'one-box' model is underestimated. In Region II, a positive value of $I_{S(O_3+NO)}$ is observed, which indicates that $\left\langle k_{eff\,(O_3+NO)} \right\rangle$ is larger than $k_{(O_3+NO)}$ and

the ‘true’ value of O_3 is less than the modelled value of O_3 by the the ‘one-box’ model (i.e. a positive value of $\phi_{O_3,1+2}$ is also observed in Region II). Those findings indicate that increasing ε will enhance the effect of segregation and therefore promote sub-grid scale variability and potentially systematic error in modelled O_3 abundance.

(a) $I_{S(O_3+NO)}$ **(%) for Case HE-LL** **(b)** $I_{S(O_3+NO)}$ **(%) for Case HE-L**

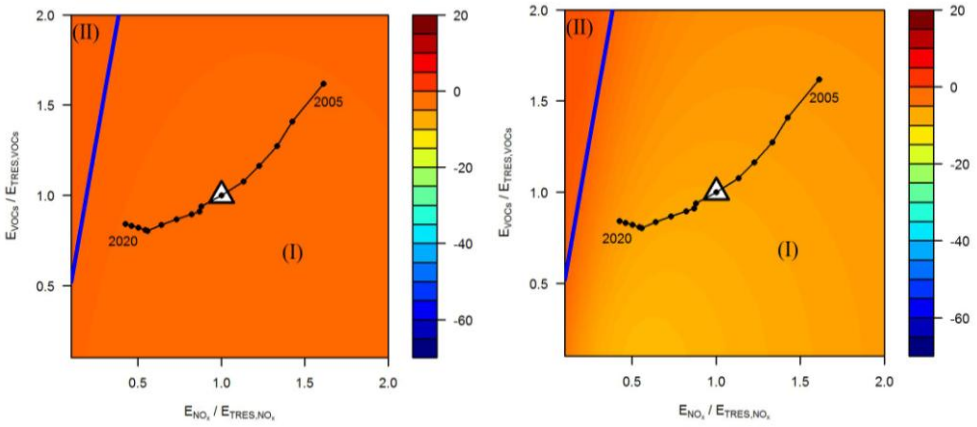

(c) $I_{S(O_3+NO)}$ **(%) for Case BASE** **(d)** $I_{S(O_3+NO)}$ **(%) for Case HE-H**

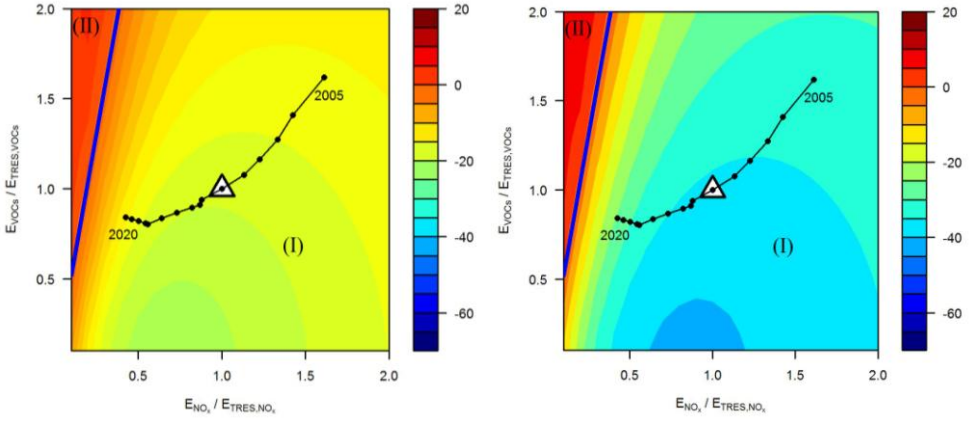

(e) $I_{S(O_3+NO)}$ **(%) for Case HE-HH**

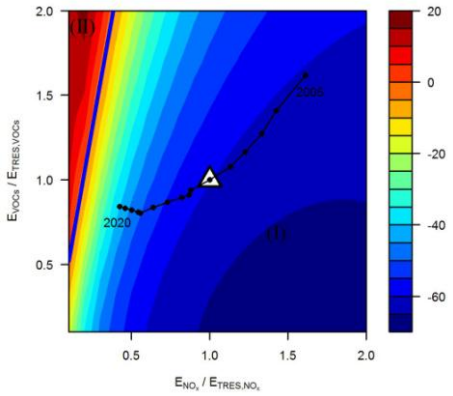

Figure 6.6 $I_{S(O_3+NO)}$ **(%), the intensity of segregation between O_3 and NO, in (a) Case HE-LL (ε =0.1), (b) Case HE-L (ε =0.3), (c) Case BASE (ε =0.5), (d) Case HE-H (ε =0.7) and (e) Case HE-HH (ε =0.9). E_{VOCs} and E_{NOx} are normalised by those of the Typical Real-world Emission Scenario (TRES, represented by △), for the year of 2010. The Region Partition Line (RPL) is represented by the solid red line; Trajectory 2005-2020 represents the emission scenarios for 2005 to 2020, assuming constant traffic volume and speed.**

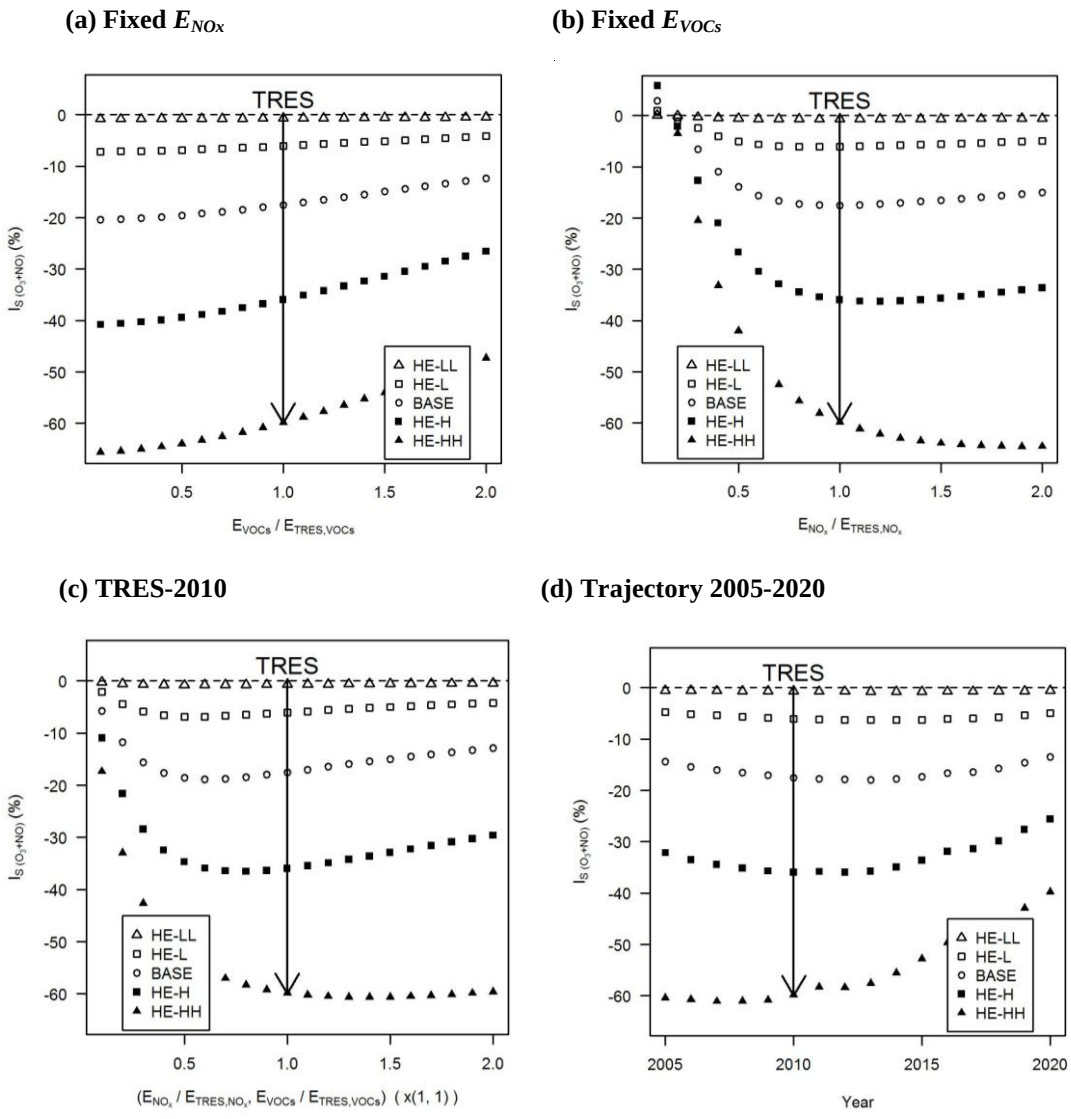

Figure 6.7 $I_{S(O_3+NO)}$ (%), the intensity of segregation between O_3 and NO, for (a) "Fixed E_{NOx}" at a fixed NO_x emission of TRES, (b) "Fixed E_{VOCs}" at a fixed VOCs emission of TRES, (c) "TRES-2010" varying the total traffic volume only and (d) "Trajectory 2005-2020" assuming constant traffic volume and speed varying ε. E_{VOCs} and E_{NOx} are normalised by those of the Typical Real-world Emission Scenario (TRES, represented by the solid arrow lines), for the year of 2010.

Figure 6.7 shows the cross-sectional analyses of $I_{S(O_3+NO)}$ (%). It is also interesting that the smaller the value of ε is, the smaller the magnitude of $I_{S(O_3+NO)}$ will be. Figure 6.7a shows that the magnitude of $I_{S(O_3+NO)}$ for all cases decreases (becomes more negative) with reduced E_{VOCs} at the fixed NO_x emission. However, at the fixed E_{VOCs} (Figure 6.7b), the value of $I_{S(O_3+NO)}$ for each case decreases from positive to exclusively negative values with

increased E_{NOx} in Region II and then becomes increasingly negative as E_{NOx} continues to increase in Region I. It can be seen from Figure 6.7c that $I_{S(O_3+NO)}$ becomes less negative for a less trafficked area/scenario and seems to be stable for the more polluted area/scenario. Figure 6.7d shows that the magnitudes of $I_{S(O_3+NO)}$ decrease with year, suggesting that in the future the segregation effect on ozone levels would be less significant. The comparison between the plots in Figure 6.7 with their equivalents in Figure 6.5 also indicates a strong relationship between $I_{S(O_3+NO)}$ and $\phi_{O_3,1+2}$.

6.3.2 Effect of the exchange velocity

Figure 6.8 depicts the effect of the exchange velocity ($w_{t,0}$) on $C_{O_3,1+2}$ (ppb), i.e. the 'true' concentration derived from the 'two-box' model, for (a) Case EX-LL ($w_{t,0}$ =0.012 m s^{-1}), (b) Case EX-L ($w_{t,0}$ =0.016 m s^{-1}), (c) Case BASE ($w_{t,0}$ =0.02 m s^{-1}), (d) Case EX-H ($w_{t,0}$ =0.024 m s^{-1}) and (e) Case EX-HH ($w_{t,0}$ =0.028 m s^{-1}). It is interesting to note that there is a significant effect of the change of $w_{t,0}$ on the RPL and the higher $w_{t,0}$, the higher the slope of the RPL. However, in Figure 6.2 where only ε is changed at a certain value of $w_{t,0}$, the RPL remains same. Therefore, it may be concluded that the slope of the RPL depends on $w_{t,0}$ but not significantly on ε. It is also noted that the trajectory from 2005 to 2020 (including the TRES) falls into Region I and is relatively closer to the RPL for Case EX-LL, in which the exchange velocity between the canyon and the boundary layer aloft, $w_{t,0}$ =0.012 m s^{-1}, is the lowest among the tested cases. A low $w_{t,0}$ might be caused by a calm, stable meteorological condition, by less traffic-induced turbulence or by a high canyon aspect ratio. There is a relatively more significant effect of $w_{t,0}$ on $C_{O_3,1+2}$ for Region II, where a high level of O_3 would occur (Figure 6.8a).

(a) $C_{O_3,1+2}$ **(ppb) for Case EX-LL**

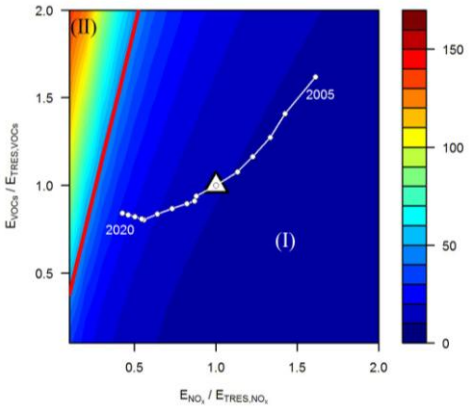

(b) $C_{O_3,1+2}$ **(ppb) for Case EX-L**

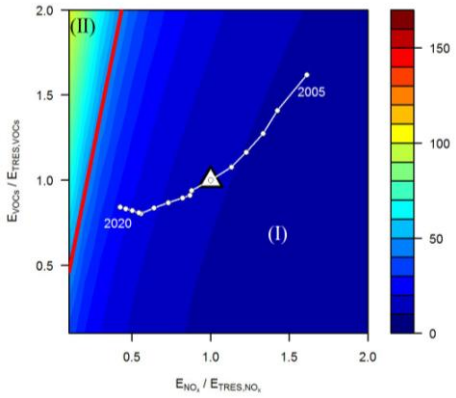

(c) $C_{O_3,1+2}$ **(ppb) for Case BASE**

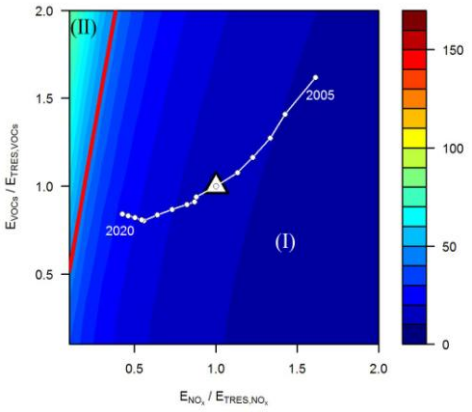

(d) $C_{O_3,1+2}$ **(ppb) for Case EX-H**

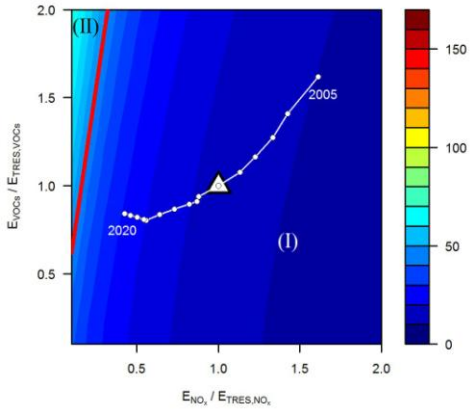

(e) $C_{O_3,1+2}$ **(ppb) for Case EX-HH**

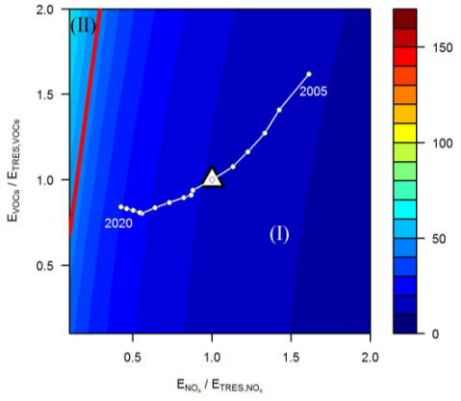

Figure 6.8 $C_{O_3,1+2}$ **(ppb), the 'true' concentration of O_3 derived from the 'two-box' model, in (a) Case EX-LL (** $w_{t,0}$ **=0.012 m s^{-1}), (b) Case EX-L (** $w_{t,0}$ **=0.016 m s^{-1}), (c) Case BASE (** $w_{t,0}$ **=0.02 m s^{-1}), (d) Case EX-H (** $w_{t,0}$ **=0.024 m s^{-1}) and (e) Case EX-HH (** $w_{t,0}$ **=0.028 m s^{-1}).** E_{VOCs} **and** E_{NOx} **are normalised by those of the Typical Real-world Emission Scenario (TRES, represented by △), for the year of 2010. The Region Partition Line (RPL) is represented by the solid red line; Trajectory 2005-2020 represents the emission scenarios for 2005 to 2020, assuming constant traffic volume and speed.**

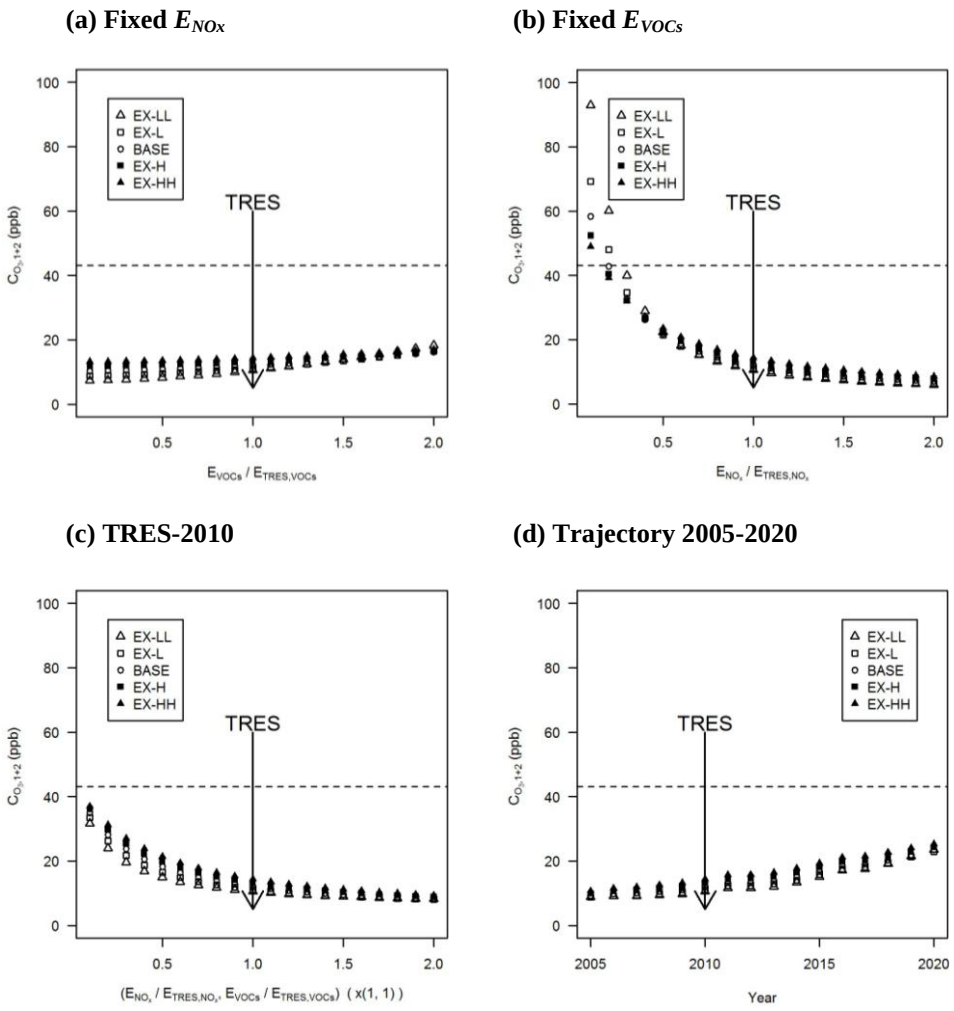

Figure 6.9 $C_{O_3,1+2}$ (ppb), the 'true' concentration of O_3 derived from the 'two-box' model, for (a) "Fixed E_{NOx}" at a fixed NO_x emission of TRES, (b) "Fixed E_{VOCs}" at a fixed VOCs emission of TRES, (c) "TRES-2010" varying the total traffic volume only and (d) "Trajectory 2005-2020" assuming constant traffic volume and speed varying $w_{t,0}$. E_{VOCs} and E_{NOx} are normalised by those of the Typical Real-world Emission Scenario (TRES, represented by the solid arrow lines), for the year of 2010; The dashed line indicates the background O_3 level.

Figure 6.9 illustrates the transects of $C_{O_3,1+2}$ (ppb) through the emission scenarios for cases a variety of $w_{t,0}$. The general tendency of $C_{O_3,1+2}$ with the change of emissions in Figure 6.9 is similar to that in Figure 6.3. However, the effect of $w_{t,0}$ on $C_{O_3,1+2}$ is more complex. For E_{VOCs} lower (or higher) than 1.8 of that for TRES at the "Fixed E_{NOx}" (Figure 6.9a), increasing $w_{t,0}$ will lead to the difference of $C_{O_3,1+2}$ between Case EX-HH and Case EX-

LL up to 6 ppb (or -1 ppb). For E_{NOx} lower (or higher) than 0.5 of that for TRES at the "Fixed E_{VOCs}" (Figure 6.9b), increasing $w_{t,0}$ will lead to the difference of $C_{O_3,1+2}$ between Case EX-HH and Case EX-LL up to -49 ppb (or 3 ppb). Figure 6.9c indicates that for more busier roads than the TRES, the effect of $w_{t,0}$ on $C_{O_3,1+2}$ is less significant. Figure 6.9d shows that $C_{O_3,1+2}$ increases with years, during which the increase of $w_{t,0}$ could lead to around 4 ppb difference of $C_{O_3,1+2}$ between Case EX-HH and Case EX-LL.

Figure 6.10 shows the effect of the exchange velocity ($w_{t,0}$) on $\phi_{O_3,1+2}$ (the percentage of overestimation for O_3 by the 'one-box' model). It is noted that there is a less significant change in the maximum level of $\phi_{O_3,1+2}$ with the change of $w_{t,0}$ from 0.012 m s^{-1} to 0.028 m s^{-1} (Figure 6.10). However, there are noticeable shifts of the RPL (discussed above) and the isopleths patterns in Region I (negative values of $\phi_{O_3,1+2}$) and Region II (positive values of $\phi_{O_3,1+2}$) associated with the variation of $w_{t,0}$. The detailed analysis of the change of $w_{t,0}$ on $\phi_{O_3,1+2}$ is further analysis below.

Figure 6.11 shows the transects of $\phi_{O_3,1+2}$ through the selected lines, which shows a slight change of $\phi_{O_3,1+2}$ with the change of $w_{t,0}$. Figure 6.11a and Figure 6.11b shows that for higher E_{VOCs} at the fixed E_{NOx} of TRES and for higher E_{NOx} at the fixed E_{VOCs} of TRES, the effect of $w_{t,0}$ (up to 10% difference) will be more significant. The higher $w_{t,0}$ is, the larger the extent of underestimation by the 'one-box' model will be. Figure 6.11c also shows that the effect of w_t on $\phi_{O_3,1+2}$ is relatively small for all cases. However it is worth mentioning some secondary features that are counter intuititive, and thus not easily interpreted. Firstly, there exists a threshold of (E_{NOx}, E_{VOCs}) below which, and another

(a) ϕ_{O_3} (%) for Case EX-LL

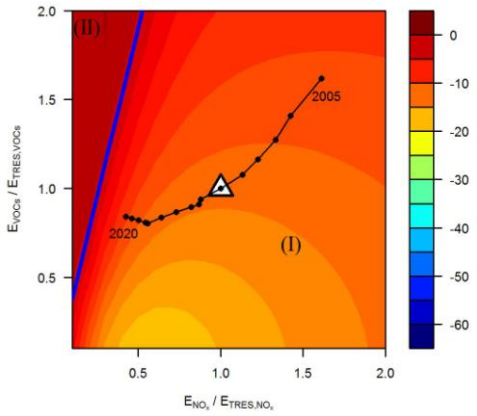

(b) ϕ_{O_3} (%) for Case EX-L

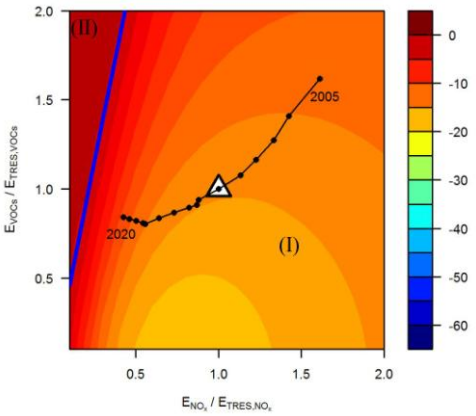

(c) ϕ_{O_3} (%) for Case BASE

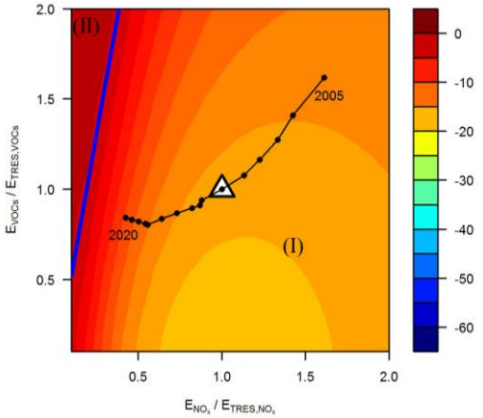

(d) ϕ_{O_3} (%) for Case EX-H

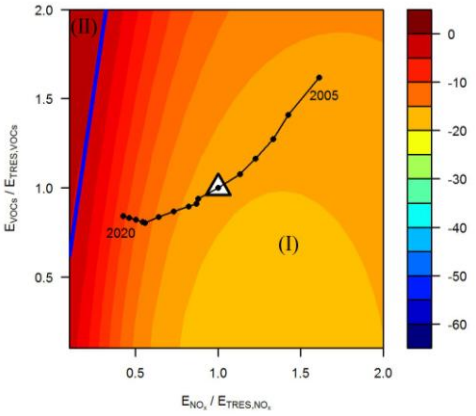

(e) ϕ_{O_3} (%) for Case EX-HH

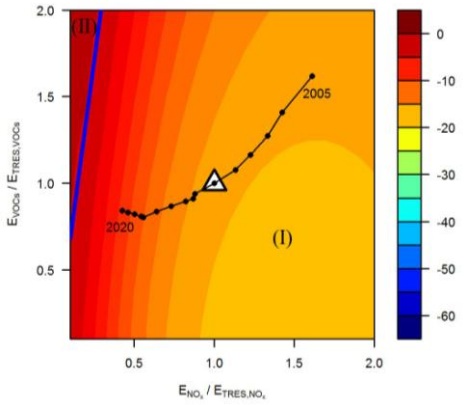

Figure 6.10 ϕ_{O_3} (%), the percentage of overestimation for O_3 by the 'one-box' model, in (a) Case EX-LL ($w_{t,0}$ =0.012 m s^{-1}), (b) Case EX-L ($w_{t,0}$ =0.016 m s^{-1}), (c) Case BASE ($w_{t,0}$ =0.02 m s^{-1}), (d) Case EX-H ($w_{t,0}$ =0.024 m s^{-1}) and (e) Case EX-HH ($w_{t,0}$ =0.028 m s^{-1}). E_{VOCs} and E_{NOx} are normalised by those of the Typical Real-world Emission Scenario (TRES, represented by △), for the year of 2010. Region Partition Line (RPL) is represented by the solid red line; Trajectory 2005-2020 represents the emission scenarios for 2005 to 2020, assuming constant traffic volume and speed.

threshold of (E_{NOx}, E_{VOCs}) above which, $\phi_{O_3,1+2}$ for Case EX-LL and Case EX-L and $\phi_{O_3,1+2}$ for Case EX-H and Case EX-HH are on the opposing sides of $\phi_{O_3,1+2}$ for the Case BASE with a sequence order of $w_{t,0}$; the first threshold of (E_{NOx}, E_{VOCs}) is around 0.6 of that for TRES and the second threshold of (E_{NOx}, E_{VOCs}) is around 1.0 of that for TRES. The transition zone for the values of $\phi_{O_3,1+2}$ is between the two thresholds. Secondly, according to intuition and linear reasoning, a higher $w_{t,0}$ implies a better ventilation of the two street canyons with the background and in consequence a smaller difference between the two canyons; this effect would be similar to a smaller ε that implies a smaller difference between the two canyons. Therefore the points for the case with a higher (or lower) $w_{t,0}$ and for the case with a smaller (or larger) ε should appear on the same side of Case BASE. However, the results for O_3 concentration in Figure 6.3 (the change of ε) and Figure 6.9 (the change of $w_{t,0}$) do not always support the reasoning, neither do the results for $\phi_{O_3,1+2}$ in Figure 6.5 (the change of ε) and Figure 6.11 (the change of $w_{t,0}$). These all indicate the complexity of the nonlinear chemical system and suggest the necessity of in-depth analysis for specific scenarios. Figure 6.11d shows that the underestimate of O_3 concentration by the 'one-box' model generally decrease with years. There is a less significant effect of $w_{t,0}$ on $\phi_{O_3,1+2}$ in the future scenarios.

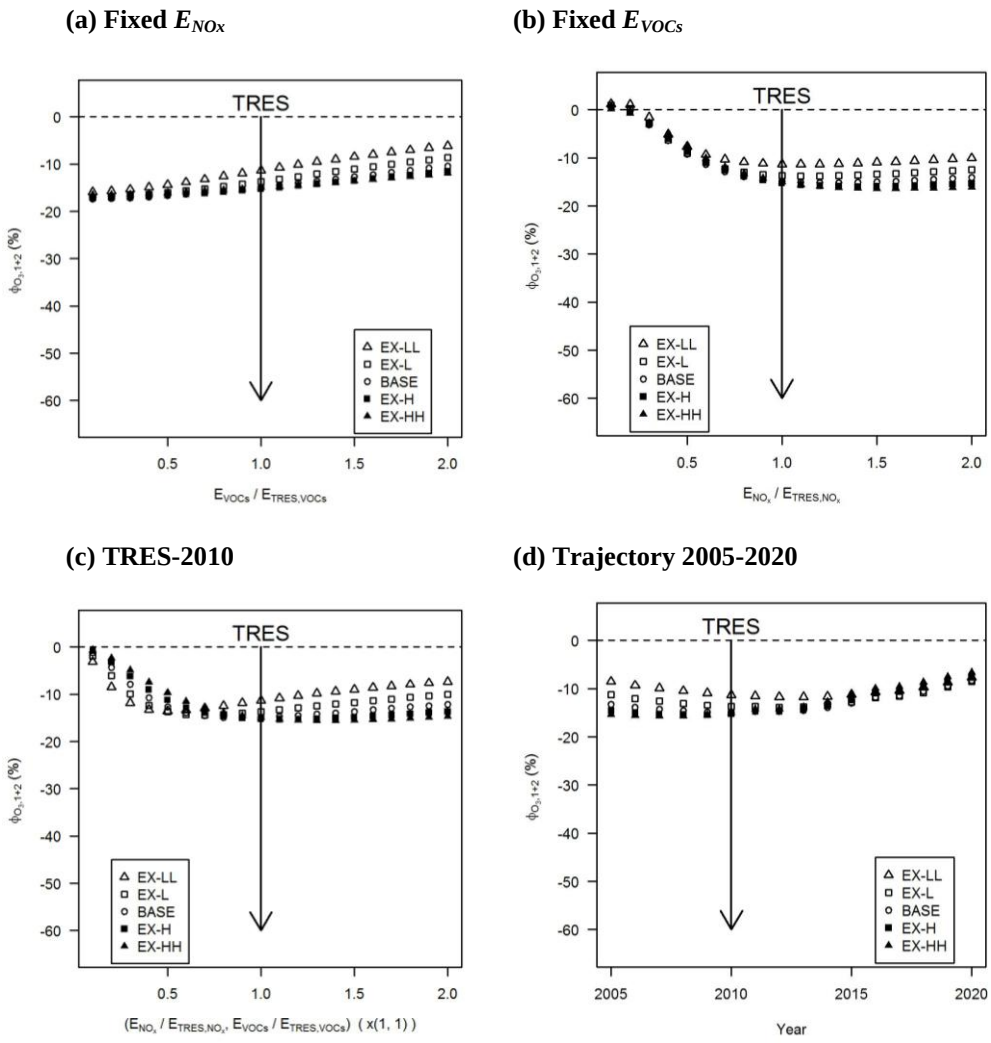

Figure 6.11 ϕ_{O_3} (%), the percentage of overestimation for O_3 by the 'one-box' model, for (a) "Fixed E_{NOx}" at a fixed NO_x emission of TRES, (b) "Fixed E_{VOCs}" at a fixed VOCs emission of TRES, (c) "TRES-2010" varying the total traffic volume only and (d) "Trajectory 2005-2020" assuming constant traffic volume and speed varying $w_{t,0}$. E_{VOCs} and E_{NOx} are normalised by those of the Typical Real-world Emission Scenario (TRES, represented by the solid arrow lines), for the year of 2010; The dashed line indicates the background O_3 level.

Figure 6.12 illustrates the effect of the exchange velocity ($w_{t,0}$) on $I_{S(O_3+NO)}$, i.e. the intensity of segregation between O_3 and NO. It is noted that there is also shifts of RPL with the change of $w_{t,0}$ and that the range of $I_{S(O_3+NO)}$ does not change significantly with the change of $w_{t,0}$ from 0.012 m s^{-1} to 0.028 m s^{-1} (Figure 6.12a-e). There is also strong correlation between $I_{S(O_3+NO)}$ (Figure 6.12) and ϕ_{O_3} (Figure 6.10). The findings indicate

(a) $I_{S(O_3+NO)}$ **(%) for Case EX-LL**

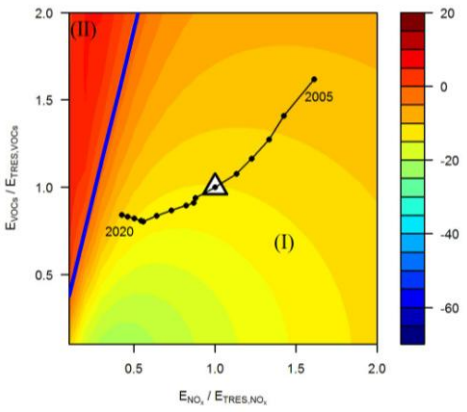

(b) $I_{S(O_3+NO)}$ **(%) for Case EX-L**

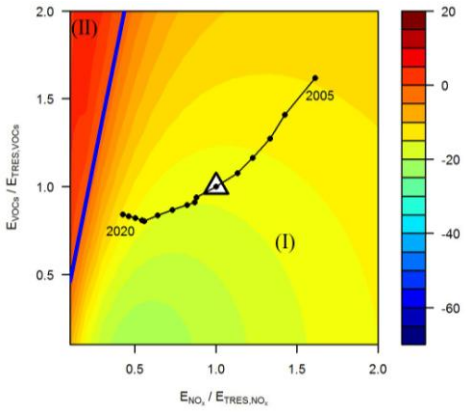

(c) $I_{S(O_3+NO)}$ **(%) for Case BASE**

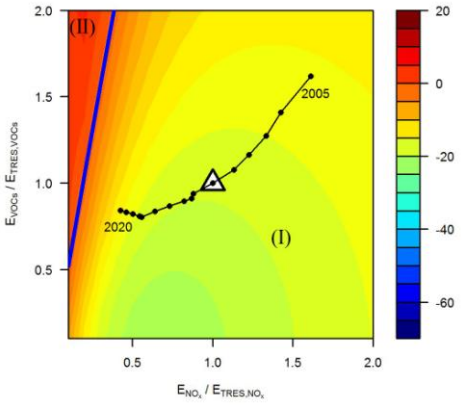

(d) $I_{S(O_3+NO)}$ **(%) for Case EX-H**

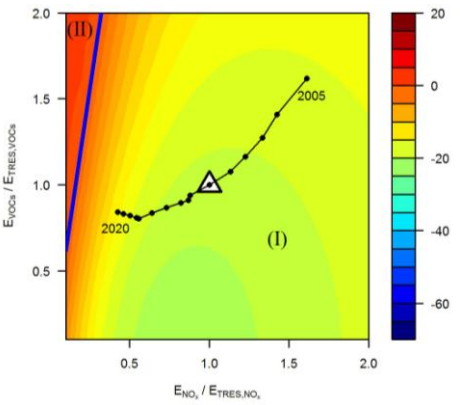

(e) $I_{S(O_3+NO)}$ **(%) for Case EX-HH**

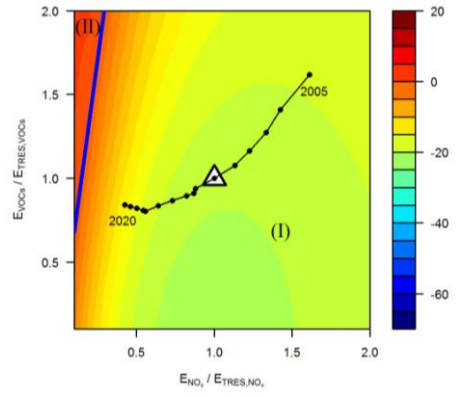

Figure 6.12 $I_{S(O_3+NO)}$ **(%), the intensity of segregation between O_3 and NO, in (a) Case EX-LL (** $w_{t,0}$ **=0.012 m s^{-1}), (b) Case EX-L (** $w_{t,0}$ **=0.016 m s^{-1}), (c) Case BASE (** $w_{t,0}$ **=0.02 m s^{-1}), (d) Case EX-H (** $w_{t,0}$ **=0.024 m s^{-1}) and (e) Case EX-HH (** $w_{t,0}$ **=0.028 m s^{-1}).** E_{VOCs} **and** E_{NOx} **are normalised by those of the Typical Real-world Emission Scenario (TRES, represented by △), for the year of 2010. Region Partition Line (RPL) is represented by the solid red line; Trajectory 2005-2020 represents the emission scenarios for 2005 to 2020, assuming constant traffic volume and speed.**

that the RPL is mainly determined by $w_{t,0}$ (discussed above), while the pattern and range of ϕ_{O_3} and $I_{S(O_3+NO)}$ in Region I and Region II depend more closely on ε. It appears that the impact of change in ε and w_t on ϕ_{O_3} and $I_{S(O_3+NO)}$ is nonlinear to E_{NOx} and E_{VOCs} due to the fact that O_3 is a secondary, rather than the primary, pollutant.

Figure 6.13 shows the cross-sectional analyses of $I_{S(O_3+NO)}$ (%) for cases with different $w_{t,0}$. Figure 6.13a shows that at the fixed NO_x emission, negative values of $I_{S(O_3+NO)}$ are observed and $I_{S(O_3+NO)}$ increases (becomes less negative) with the increase of E_{VOCs}. Figure 6.13b shows that positive (or negative) values of $I_{S(O_3+NO)}$ (Region II or Region I) are observed while E_{NOx} is below (or above) 0.3 of that for TRES. Figure 6.13a and Figure 6.13b indicate that the higher the exchange velocity is, the larger $I_{S(O_3+NO)}$ will be. Figure 6.13c shows that for less trafficked area/scenario, increasing $w_{t,0}$ will lead to the decrease of $I_{S(O_3+NO)}$ (less negative); likewise for more trafficked area/scenario, increasing $w_{t,0}$ will lead to the decrease of $I_{S(O_3+NO)}$ (more negative). Figure 6.13d shows that the effect of the exchange velocity is less significant for the future scenarios.

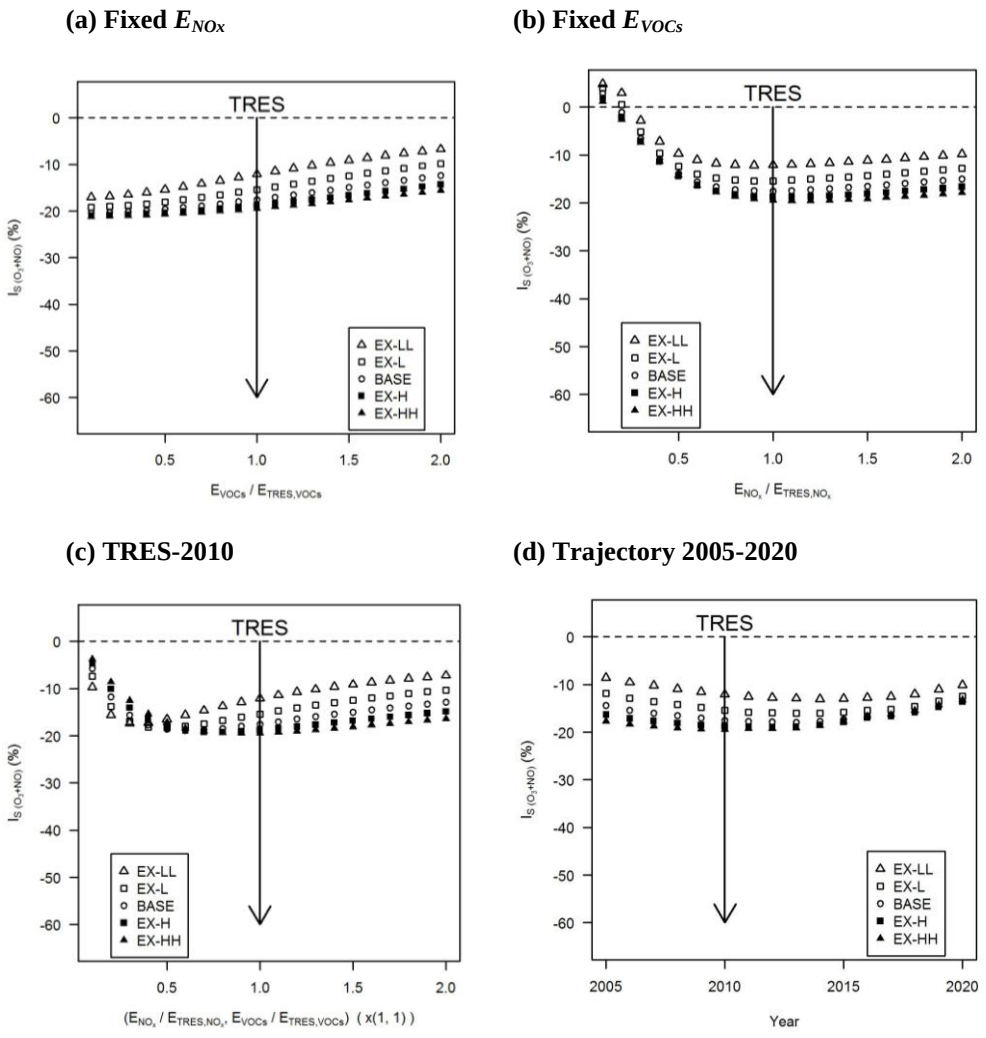

Figure 6.13 $I_{S(O_3+NO)}$ (%), the intensity of segregation between O_3 and NO, for (a) "Fixed E_{NOx}" at a fixed NO_x emission of TRES, (b) "Fixed E_{VOCs}" at a fixed VOCs emission of TRES, (c) "TRES-2010" varying the total traffic volume only and (d) "Trajectory 2005-2020" assuming constant traffic volume and speed varying $w_{t,0}$. E_{VOCs} and E_{NOx} are normalised by those of the Typical Real-world Emission Scenario (TRES, represented by the solid arrow lines), for the year of 2010.

6.4 Conclusions

Segregation effects of heterogeneous emissions have been examined by considering the surface sub-grid emission heterogeneity in two idealised urban street canyons within the urban canopy layer and investigated how differing chemical effects (arising from the heterogeneity of emissions) and dynamic effects (i.e. exchange velocity) influence the error in O_3 if implementing the grid-averaging parameterisation for heterogeneous

emissions. This study offers a better understanding of the parameterisation of raw emissions for urban air quality models by highlighting the importance of segregation effects of heterogeneous emissions within the typical city-blocks (i.e. urban street canyons) and by providing a 2D pattern of overestimation for O_3. The common situations in urban areas are found to fall into Region I where the modelled O_3 concentration in street canyons (lower than that in the overlying background atmosphere) determined by the 'one-box' model will be underestimated compared with the 'true' value by the 'two-box' model. Our findings also indicate that the performance of the 'one-box' model for O_3 concentration is better for a more 'green' area with extra VOCs sources (provided they are included in the inventory) and for the less trafficked area/scenario. Future emission trends are expected to lead to the error in the 'one-box' model approach falling. The error in ozone levels is strongly linked to segregation effects of heterogeneous emissions and is balanced by both dynamics and chemistry. There is a significant effect of the change of $w_{t,0}$ (representing dynamical effects) on the position of the Region Partition Line (RPL), while the change of ε (representing chemical effects) has a considerable effect on the pattern in Region I and Region II (with O_3 levels lower/higher than the background O_3 concentration, respectively). The error in ozone levels by the one-box model approach exhibits a rapid change with the change of ε, but a less significant change with the change of $w_{t,0}$.

7 Conclusions and future work

7.1 Summary and conclusions

The street canyon is a typical urban configuration with surrounding buildings along a street, where the majority of the outdoor activities of the urban populations occur. In such an atmospheric compartment, natural air ventilation is drastically constrained by surrounding buildings. Emissions from vehicles are reactive, undergoing chemical processing within urban street canyons to generate secondary pollutants. The combined effects of emissions sources, dynamical processes (reduced dispersion) and chemical processes (evolution of reactive primary and secondary pollutants) may lead to the deterioration of air quality within street canyons potentially in breach of air quality standards. Substantial human exposure to such environments tends to cause adverse public health effects. In addition, the fluxes of air pollutants at the roof level received by the urban boundary layer as the "emissions" input to urban-scale air pollution models are essential to a reliable prediction of air quality. Grid-average parameterisation of heterogeneous emissions, in which sub-grid scale processes and features are lost, may result in significant uncertainty, and systematic biases in the urban-scale air pollution models.

This thesis investigates the interaction of both dynamical and chemical processes for reactive pollutants in a street canyon and addresses selected scientific issues of air pollution levels inside the urban canopy that are significantly affected by local traffic emissions, mixing and chemical processes in the street canyon (reviewed in Chapter 2). In this thesis, two modelling approaches have been developed, i.e. the large-eddy simulations (LES) coupled with chemistry (Chapter 3 and Chapter 4) and the photochemical box

model methodology (Chapter 5 and Chapter 6). This thesis sought to address the core research questions proposed in the introductory chapter (Chapter 1):

1) *What is the turbulent flow pattern within a (deep) street canyon and how does it influence the turbulent mixing and chemical processes of reactive pollutants in such environment?*

The skimming flow (SF) regime representing the worst-case scenario for pollutant dispersion normally occurs in more tightly spaced buildings, especially deep street canyons. A large-eddy simulation (LES) coupled with chemistry (the LES-chemistry model) is developed to simulate the dispersion and transport of reactive pollutants in a deep street canyon with an aspect ratio of 2 under neutral meteorological conditions (Chapter 3). Turbulent flow in the deep street canyon reproduced by the LES dynamical model agrees well with a water channel experiment (Li et al., 2008a), which provides confidence that the simulated dynamics within the canyon is reasonable. Two vertically aligned vortices are observed with the vertical size of the upper one larger than that of the lower one. This is a major difference from the single-vortex flow for a street canyon with AR=1 (e.g. Bright et al., 2013). The two-vortex mean flow was also found by other studies for AR=2 using RANS, e.g. Kwak et al. (2013), but their RANS model generated a larger lower vortex than the one found in the water tank experiment and in the LES result in this study. The dispersion and transport of reactive pollutants within the deep street canyon is strongly determined by those two unsteady vertically aligned vortices (Chapter 4). Spatial and temporal variations of reactive pollutants are significant due to the existence of unsteady multiple vortices and pollutants exhibit significant contrasts within each vortex. The spatial patterns of pollutants for the upper vortex resemble those for the single vortex in a street canyon with AR=1 (e.g. Baker et al. (2004), Baik et al. (2007), Bright et al.,

2013, Garmory et al. (2009), Tong and Leung (2012), and Kwak and Baik (2012)). Emissions released at the ground level are largely trapped by the lower vortex, with weak dispersion to the upper vortex, resulting in high concentrations near the ground. Pollutants levels (e.g. NO_x) on the leeward wall are generally higher (around 1.5 to 2 times) than those on the windward wall for the upper canyon, but lower (around 50% to 70%) for the lower canyon. This finding could be of importance, which indicates that the results from the AR=1 canyon may be unreliable for the assessment of pollutant exposure at the pedestrian level for the AR=2 canyon.

2) *What are the differences in pollutant levels between the within-canyon atmosphere and the overlying background, and how are traffic emissions pre-processed by the street canyon dynamics and chemistry before entering into the overlying background atmosphere?*

Apart from pollutant characteristics driven by two unsteady vortices formed within the street canyon, there are also significant contrasts between the within-canyon atmosphere and the overlying background (Chapter 4). For emitted chemical species (such as NO and NO_2), higher levels are observed within the canyon than those at the overlying background. The general patterns of those species are dominated by the street canyon dynamics and emissions, while the conversions between them are dominated by the street canyon chemistry. The existence of multiple vortices (incomplete mixing) significantly enhances the retention time of pollutants, highlighting the more importance of chemistry. This chemical effect is more significant for deep street canyons than regular street canyons (AR=1). But for entrained chemical species (e.g. O_3), higher levels are observed in the overlying background than those within the canyon. Those species are more influenced by the overlying background. It is found that NO, NO_x, O_3, OH and HO_2 are chemically

consumed. For NO_2 and O_x, however, chemical production occurs inside the street canyon. There is evidence of the effect of two unsteady vortices on the pre-processing of traffic emissions through the street canyon dynamics and chemistry. Advective fluxes are dominant for both the upper vortex and the lower vortex, which play an important role for the transport of pollutant within a vortex. Turbulent fluxes are dominant for shear layer, which play an important role for the exchange of pollutant within the zone between the vortices. This finding is consistent with Cheng and Liu (2011) for LES simulations of a passive scalar in the AR=1 canyon. There is a positive (upward) total flux for NO and NO_2 from the canyon roof level into the background atmosphere aloft, and a negative (downward) total flux for O_3 indicating that O_3 is brought into the canyon from the overlying background atmosphere. The total flux generally decreases with height for NO, but increases for NO_2 indicating the conversion of NO to NO_2 within the street canyon pre-processing. This is also indicated by the NO/NO_2 total flux ratio changing from 9 (the raw emission ratio) near the emission region to 1.7 at the canyon roof level.

3) *What is the effect of HO_x chemical processing on pollutants levels within a street canyon?*

HO_x chemical processing plays an important role in reforming levels between reactive pollutants within a street canyon (Chapter 4). Compared with the complex chemical mechanism (RCS) considering HO_x chemical processing, simple NO_x-O_3 chemistry would overestimate the NO level (by about 30 %), but underestimate levels of NO_2 and O_3 (by about -38% and -52% respectively), indicating the additional conversion of NO to NO_2 through the VOCs oxidation chemistry by HO_x. Such findings suggest that using simple NO_x-O_3 chemistry may provide overly optimistic prediction of air pollution in street canyon while in reality NO_2 levels may already exceed the air quality standards, which

may delay the policy-maker to make effective decision on air quality management. The indirect approach to estimate ozone production rate based on the the photostationary state (PSS) of the NO_x-O_3 system gives the wrong results in street canyon environment, but instead reflects an artefact due to incomplete mixing.

4) *What is the human exposure to air pollutants within a street canyon environment?*

The potential exposure to air pollutants (e.g. NO, NO_2 and O_3) within the canyon is assessed, based on the time series output from the LES-chemistry model (Chapter 4). There are significant short-term concentration fluctuations for NO, NO_2 and O_3, which are strongly dependent upon the fluctuations of the flow turbulence inside the street canyon, the location of emissions (from ground level) and the nonlinear photochemistry. Those concentration fluctuations in the lower canyon are less pronounced (occur less frequently) than those in the upper canyon. There is a clear shift for different locations within the canyon. As expected, concentrations for a given percentile generally increase with the increase in percentiles. The percentile could serve as a guideline for determining air quality limits on assessing health impacts associated with differing exposure times, providing a better understanding of how people react to short-term exposure. Frequency histograms of pollutants shows multiple peaks, which are influenced by combined effect of primary emissions, chemical processing and turbulent mixing within the street canyon.

5) *What is the segregation effect due to incomplete mixing of reactive pollutants within a street canyon and how may this effect be captured?*

The segregation effect is of importance in the incomplete mixing environment in the presence of the street canyon chemical processing (Chapter 4). Intensities of segregation between A and B (where A=B), i.e. the auto-covariance of a chemical species, are positive

(e.g. with the largest value of 28.49 % for NO and the smallest value of 0.36 % for OH), which may reflect the spatial variability of the chemical species within the canyon due to incomplete mixing. Positive values are observed for intensities of segregation between the species with similar behaviour (either emitted chemical species or entrained chemical species). Negative values are found for intensities of segregation between emitted chemical species and entrained chemical species with the opposite behaviour. Auger and Legras (2007) suggested that due to the nonlinear nature of chemical processes, even a small value of intensity of segregation (e.g. 1 %) may lead to significant effects on the mean concentrations. This finding also supports the concept that segregation effects are very important and should be highlighted in the incomplete mixing environment (e.g. the street canyon), in which the interaction between the dynamics and nonlinear chemistry takes place. Intensities of segregation are separated by the two vortices formed in the street canyon and then increase both upwards to the canyon roof level and downwards to the street ground. Large segregation effects are observed at the regions close to the emission source and near the canyon roof level, where the spatial variability can be extremely significant.

In order to capture the significant concentration contrast between two vertically segregated vortices derived from the LES-chemistry model, an alternative simplified two-box model (Chapter 4) is developed and evaluated to represent key photo-chemical processes with timescales similar to and smaller than the turbulent mixing timescale. It is assumed that each vortex has sufficient intensity for the chemical species to be well-mixed within the corresponding box. The pollutant transfer between two adjacent boxes is expressed by the introduction of an ‘exchange velocity’. Segregation effects caused by incomplete mixing (i.e. spatial inhomogeneity represented by the LES-chemistry model) reduce the

conversion rate of NO to NO_2 through chemistry, the NO_x loss rate to other species and the rate of oxidation chemistry.

6) *What are the mean pollutant levels within a street canyon (exposure-related) under a variety of emission scenarios and meteorological conditions?*

The two-box model approach (vertically segregated) is extended to investigate bulk levels of air pollution in the lower canyon (i.e. the place of interest for the assessment of human health effect) (Chapter 5). The two-box model provides the capability of efficiently running a series of emission scenarios under a set of meteorological conditions so that the coupling effect between the flow dynamics and chemistry can be investigated. The findings identify the emission regimes and the meteorological conditions under which NO_2 at the lower canyon is in breach of air quality standards. Higher bulk NO_2 levels in the lower box were observed for cases with a higher heterogeneity coefficient. NO_2 levels are more likely to exceed UK air quality standards for NO_2 for scenarios with a higher heterogeneity coefficient. The 'one-box' model was found to underestimate NO_2 levels compared with those in the lower box by the 'two-box' model. This underestimation is relatively lower for cases with lower heterogeneity coefficients. The lower the exchange velocity is, the higher NO_2 levels in the lower box will be. Even lower emissions under the worst dispersion conditions can result in very poor air quality inside street canyons. There are extremely high levels of NO_2 for smaller box height ratio, which represents the case where pollutants are essentially trapped in the small lower part of the street canyon under poor ventilation conditions. The shading ratio coefficient has a considerable effect on NO_2 levels in the lower box for the two-box model. The effect of shading is found to be more significant for higher emissions scenarios.

7) *What are segregation effects of sub-grid heterogeneous emissions in urban air quality models if a grid-averaging parameterisation is adopted?*

Air quality models include representations of pollutant emissions, which necessarily entail spatial averaging to reflect the model grid size; such averaging may result in significant uncertainties and/or systematic biases in the model output. A photochemical model (the one-box model) with grid-averaged emissions of street canyons is compared with a two-box model considering each canyon independently (horizontally segregated) to investigate such uncertainties (Chapter 6), considering ozone concentrations in idealised street canyons within the urban canopy. The one-box model may significantly underestimate true (independent canyon mean) ozone concentrations for typical urban areas, and that the performance of the averaged model is improved for more 'green' and/or less trafficked areas. Our findings also suggest that the expected trends of 2005-2020 in vehicle emissions, in isolation, reduce the error inherent in the averaged-emissions treatment. The error in ozone levels is strongly linked to segregation effects of heterogeneous emissions and is balanced by both dynamics and chemistry. These new findings may be used to evaluate uncertainties in modelled urban ozone concentrations when grid-averaged emissions are adopted.

7.2 Implications of the research

The results presented in this thesis have several implications for both science and applications. The research is beneficial to scientists, researchers or model developers in the following aspects. The LES-chemistry model reveals the impacts of nonlinear photochemical processes in the incomplete mixing environment (e.g. street canyons) and provides a better understanding of the pre-processing of emissions by the street canyon

dynamics and chemistry. A methodology to predict the spatial and temporal variability of reactive pollutants in the canyon environment has been developed, which may be useful for the potential human exposure assessment. This research may also guide the siting procedure for new urban air quality stations, to ensure these are representative of human exposure and/or understand the measurement bias that may accrue from a particular location vs elsewhere in the canyon. The photochemical box model approach may provide guidance in the development of generic sub-grid scale schemes or models for urban canopy. This research may also help to derive effective bulk reaction rates which give more accurate overall chemical processing simulations for box models or sub-grid models in urban areas.

For applications, this research is beneficial to the end users of air quality models in the following aspects. This research helps those users be aware of the limitation of box models and to appropriately interpret model output. This research will also help them to understand the potential underestimation of NO_2 levels in urban street canyons, which is timely when the issue of NO_2 is becoming an urgent agenda for the UK air quality management. This research provides an evaluation of uncertainties and/or systematic biases in the urban air quality model output if the grid-averaged procedure of emissions is adopted. The box models can be run on a current desktop for general applications. By running the model, users are able to obtain pollution levels if a set of parameters are provided as the model's input (e.g. background wind speed, building geometry, traffic data, time of day (for shading calculation), etc.).

7.3 Future work

The large-eddy simulation (LES) coupled with chemistry presented here (Chapter 3 and Chapter 4) is limited to one typical emission scenarios with worst air ventilation (a deep street canyon of AR=2) under neutral meteorological conditions due to the high computational cost. However, turbulent mixing and photochemical processes are determined by other factors, such as the street canyon geometry, meteorological conditions, emissions and chemical transformation of pollutants. In order to investigate the extent of these factors, an alternative numerical modelling approach such as RANS models coupled with chemistry may be adopted. Thermal / shading effects (e.g. caused by solar radiation) on both the dynamic and chemical processing should be considered. More complex urban configurations effect (e.g. street intersections, irregular buildings, parking spaces and trees) on both the dynamic and chemical processing should be investigated. The two-box model approach (vertically segregated) is restricted to two boxes representing two vortices within a street canyon (Chapter 5). For even taller canyons, more vortices may be formed. Future studies should consider higher resolution (more photochemical boxes) and extend the range of scenarios to encompass the range encountered in reality. Also, a standard procedure for setting the parameters (representing real world parameter ranges) used in the two-box model should be developed. The analysis is limited to NO_2 concentrations in the lower box, reflecting the current air pollution issue caused by the breach of NO_2 air quality limits in urban areas. Further research may focus on analysis other key pollutants for practical application.

The two-box model approach (horizontally segregated) is also restricted to two boxes by considering only two typical street canyons with emission heterogeneity, which are totally segregated, neither transported nor mixed with each other (Chapter 6). It is only applicable

to the case in which the mean velocity is zero (the two boxes are totally segregated). Future work may consider the introduction of an advection velocity on the top of the exchange velocity between the two boxes, i.e. along streets and across intersections (in which the mean advection velocity is non-zero). A multi-box air quality model for a street canyon network may then be developed for practical applications. Also, the analysis is limited to model uncertainties of O_3, which is an important secondary pollutant. Further research may consider other key pollutants.

Finding an appropriate real-world dataset (or observational data) to evaluate the box-averaged concentrations of studies such as these in this research remains a challenge, in part as the concentrations of reactive chemical species (e.g. NO_2 and O_3) are highly non-uniform inside street canyons containing sources of reactive emissions. The traditional air quality monitoring networks are normally fixed and sparse with lower spatial resolution so that the tempo-spatial heterogeneity of air pollutants in street canyons can-not be captured (Sajani et al., 2004). High spatial density observations of pollutant concentrations inside street canyons are needed in support of rigorous evaluation of such modelling approaches (Williams et al., 2009). Recent development of low-cost sensors (Mead et al., 2013), which may be deployed in such networks (e.g. Kumar et al. (2015)), could provide a route to achieve this objective in the future.

Publications

Zhong, J., Cai, X.-M. and Bloss, W. J. 2015. Modelling the dispersion and transport of reactive pollutants in a deep urban street canyon: Using large-eddy simulation. Environmental Pollution, 200, 42-52.

Zhong, J., Cai X.-M. and Bloss W. J. 2014: Modelling segregation effects of heterogeneous emissions on ozone levels in idealised urban street canyons: Using photochemical box models, Environmental Pollution, 188, 132-143.

Appendix A: RCS mechanism

Table A1 - *All reactions and rate constants included in the Reduced Chemical Scheme (RCS). The units of rate constants are s^{-1} for first order reactions and ppb s^{-1} for second order reactions. The pressure is set to 10132.5 Pa and the temperature is set to 293 K.*

	Reactants				Products			Rate constant
1	O_3			→	OH	+	OH	3.40E-6
2	NO	+	O_3	→	NO_2			4.01E-4
3	NO	+	NO	→	NO_2	+	NO_2	2.63E-9
4	NO	+	NO_3	→	NO_2	+	NO_2	6.56E-1
5	OH	+	O_3	→	HO_2			1.72E-3
6	OH	+	H_2	→	HO_2			1.49E-4
7	OH	+	CO	→	HO_2			5.06E-3
8	H_2O_2	+	OH	→	HO_2			4.21E-2
9	HO_2	+	O_3	→	OH			4.86E-5
10	OH	+	HO_2	→				2.82E+0
11	HO_2	+	HO_2	→	H_2O_2			8.74E-2
12	HO_2	+	HO_2	→	H_2O_2			6.92E-2
13	OH	+	NO	→	HONO			2.54E-1
14	OH	+	NO_2	→	HNO_3			3.08E-1
15	OH	+	NO_3	→	HO_2	+	NO_2	5.01E-1
16	HO2	+	NO	→	OH	+	NO_2	2.27E-1
17	HO2	+	NO_2	→	HO_2 NO_2			3.59E-2
18	HO_2NO2			→	HO2	+	NO_2	3.74E-2
19	HO_2NO_2	+	OH	→	NO_2			1.20E-1
20	HONO	+	OH	→	NO_2			2.58E-2
21	HNO_3	+	OH	→	NO_3			4.08E-3

22	H_2O_2			→	OH	+	OH					7.11E-6
23	NO_2			→	NO	+	O_3					9.20E-3
24	NO_3			→	NO							2.34E-2
25	NO_3			→	NO_2	+	O_3					1.83E-1
26	HONO			→	OH	+	NO					2.02E-3
27	HNO_3			→	OH	+	NO_2					6.30E-7
28	CH_4	+	OH	→	CH_3O_2							1.39E-4
29	C_2H_4	+	OH	→	$HOCH_2CH_2O_2$							2.00E-1
30	C_3H_6	+	OH	→	RN_9O_2							7.19E-1
31	C_2H_4	+	O_3	→	HCHO	+	CO	+	HO_2	+	OH	4.46E-9
32	C_2H_4	+	O_3	→	HCHO	+	HCOOH					2.99E-8
33	C_3H_6	+	O_3	→	HCHO	+	CH_3O_2	+	CO	+	OH	8.18E-8
34	C_3H_6	+	O_3	→	HCHO	+	CH_3CO_2H					1.45E-7
35	C_5H_8	+	OH	→	RU14O2							2.58E+0
36	C_5H_8	+	O_3	→	UCARB10	+	CO	+	HO_2	+	OH	7.76E-8
37	C_5H_8	+	O_3	→	UCARB10	+	HCOOH					2.10E-7
38	HCHO			→	CO	+	HO_2	+	HO_2			3.05E-5
39	HCHO			→	H_2	+	CO					4.61E-5
40	CH_3CHO			→	CH_3O_2	+	HO_2	+	CO			5.07E-6
41	HCHO	+	OH	→	HO_2	+	CO					2.35E-1
42	CH_3CHO	+	OH	→	CH_3CO_3							4.02E-1
43	CH_3OH	+	OH	→	HO_2	+	HCHO					2.31E-2
44	C_2H_5OH	+	OH	→	CH_3CHO	+	HO_2					7.24E-2
45	C_2H_5OH	+	OH	→	$HOCH_2CH_2O_2$							9.23E-3
46	HCOOH	+	OH	→	HO_2							1.13E-2
47	CH_3CO_2H	+	OH	→	CH_3O_2							2.00E-2
48	CH_3O_2	+	NO	→	HCHO	+	HO_2	+	NO_2			1.95E-1
49	$HOCH_2CH_2O_2$	+	NO	→	HCHO	+	HCHO	+	HO_2	+	NO_2	1.68E-1
50	$HOCH_2CH_2O_2$	+	NO	→	$HOCH_2CHO$	+	HO_2	+	NO_2			4.84E-2
51	RN_9O_2	+	NO	→	CH_3CHO	+	HCHO	+	HO_2	+	NO_2	2.13E-1

52	CH_3CO_3	+	NO	→	CH_3O_2	+	NO_2					5.10E-1
53	$HOCH_2CO_3$	+	NO	→	HO_2	+	HCHO	+	NO_2			5.10E-1
54	$RU14O_2$	+	NO	→	UCARB12	+	HO_2	+	NO_2			4.93E-2
55	$RU14O_2$	+	NO	→	UCARB10	+	HCHO	+	HO_2	+	NO_2	1.46E-1
56	$RU12O_2$	+	NO	→	CH3CO3	+	$HOCH_2CHO$	+	NO_2			1.52E-1
57	$RU12O_2$	+	NO	→	CARB7	+	CO	+	HO_2	+	NO_2	6.52E-2
58	$RU10O_2$	+	NO	→	CH3CO3	+	$HOCH_2CHO$	+	NO_2			1.09E-1
59	$RU10O_2$	+	NO	→	CARB6	+	HCHO	+	HO_2	+	NO_2	6.52E-2
60	$RU10O_2$	+	NO	→	CARB7	+	HCHO	+	HO_2	+	NO_2	4.35E-2
61	CH_3O_2	+	NO	→	CH_3NO_3							1.95E-4
62	$HOCH_2CH_2O_2$	+	NO	→	$HOC_2H_4NO_3$							1.09E-3
63	RN_9O_2	+	NO	→	$RN9NO_3$							4.56E-3
64	$RU14O_2$	+	NO	→	$RU14NO_3$							2.17E-2
65	CH_3O_2	+	HO_2	→	CH_3OOH							1.52E-1
66	$HOCH_2CH_2O_2$	+	HO_2	→	HOC_2H_4OOH							3.62E-1
67	$RN9O_2$	+	HO_2	→	RN9OOH							3.20E-1
68	CH_3CO_3	+	HO_2	→	CH_3CO_3H							3.75E-1
69	$HOCH_2CO_3$	+	HO_2	→	$HOCH_2CO_3H$							3.75E-1
70	$RU14O_2$	+	HO_2	→	RU14OOH							4.74E-1
71	$RU12O_2$	+	HO_2	→	RU12OOH							4.35E-1
72	$RU10O_2$	+	HO_2	→	RU10OOH							3.85E-1
73	CH_3O_2			→	HCHO	+	HO_2					6.22E-3*
74	CH_3O_2			→	HCHO							6.32E-3*
75	CH_3O_2			→	CH_3OH							6.32E-3*
76	$HOCH_2CH_2O_2$			→	$HOCH_2CHO$	+	HO_2					1.12E-2*
77	$RN9O_2$			→	CH_3CHO	+	HCHO	+	HO_2			2.20E-2*
78	CH_3CO_3			→	CH_3O_2							2.50E-1*
79	$HOCH_2CO_3$			→	HCHO	+	HO_2					2.50E-1*
80	$RU14O_2$			→	UCARB12	+	HO_2					1.08E-2*
81	$RU14O_2$			→	UCARB10	+	HCHO	+	HO_2			3.20E-2*

82	$RU12O_2$			→	CH_3CO_3	+	HOCH2CHO					3.51E-2*
83	$RU12O_2$			→	CARB7	+	HOCH2CHO	+	HO_2			1.50E-2*
84	$RU10O_2$			→	CH_3CO_3	+	$HOCH_2CHO$					2.50E-2*
85	$RU10O_2$			→	CARB6	+	HCHO	+	HO_2			1.50E-2*
86	$RU10O_2$			→	CARB7	+	HCHO	+	HO_2			1.00E-2*
87	CARB7			→	CH3CO3	+	HCHO	+	HO_2			3.36E-6
88	$HOCH_2CHO$			→	HCHO	+	CO	+	HO_2	+	HO_2	1.77E-5
89	UCARB10			→	CH_3CO_3	+	HCHO	+	HO_2			1.62E-5
90	CARB6			→	CH_3CO_3	+	CO	+	HO2			1.26E-4
91	UCARB12			→	CH_3CO_3	+	HOCH2CHO	+	CO	+	HO2	1.62E-5
92	CARB7	+	OH	→	CARB6	+	HO_2					7.51E-2
93	UCARB10	+	OH	→	$RU10O_2$							6.26E-1
94	UCARB10	+	O_3	→	HCHO	+	CH_3CO_3	+	CO	+	OH	4.21E-8
95	UCARB10	+	O_3	→	HCHO	+	CARB6	+	H_2O_2			2.93E-8
96	$HOCH_2CHO$	+	OH	→	$HOCH_2CO_3$							2.50E-1
97	CARB6	+	OH	→	CH_3CO_3	+	CO					4.31E-1
98	UCARB12	+	OH	→	$RU12O_2$							1.13E-0
99	UCARB12	+	O_3	→	$HOCH_2CHO$	+	CH_3CO_3	+	CO	+	OH	5.35E-7
100	UCARB12	+	O_3	→	$HOCH_2CHO$	+	CARB6	+	H_2O_2			6.61E-8
101	CH_3NO_3			→	HCHO	+	HO_2	+	NO_2			8.96E-7
102	CH_3NO_3	+	OH	→	HCHO	+	NO_2					9.33E-3
103	$HOC_2H_4NO_3$	+	OH	→	$HOCH_2CHO$	+	NO_2					2.73E-2
104	$RN9NO_3$	+	OH	→	CARB7	+	NO_2					3.28E-2
105	$RU14NO_3$	+	OH	→	UCARB12	+	NO_2					1.39E+0
106	CH_3OOH			→	HCHO	+	HO_2	+	OH			5.44E-6
107	CH_3CO_3H			→	CH_3O_2	+	OH					5.44E-6
108	$HOCH_2CO_3H$			→	HCHO	+	HO_2	+	OH			5.44E-6
109	RU14OOH			→	UCARB12	+	HO_2	+	OH			1.37E-6
110	RU14OOH			→	UCARB10	+	HCHO	+	HO_2	+	OH	4.07E-6
111	RU12OOH			→	CARB6	+	HOCH2CHO	+	HO_2	+	OH	5.44E-6

112	RU10OOH			→	CH_3CO_3	+	HOCH2CHO	+	OH			5.44E-6
113	HOC_2H_4OOH			→	HCHO	+	HCHO	+	HO_2	+	OH	5.44E-6
114	RN9OOH			→	CH_3CHO	+	HCHO	+	HO_2	+	OH	5.44E-6
115	CH_3OOH	+	OH	→	CH_3O_2							9.10E-1
116	CH_3OOH	+	OH	→	HCHO	+	OH					4.79E-1
117	CH_3CO_3H	+	OH	→	CH_3CO_3							9.27E-2
118	$HOCH_2CO_3H$	+	OH	→	$HOCH_2CO_3$							1.55E-1
119	RU14OOH	+	OH	→	UCARB12	+	OH					1.88E+0
120	RU12OOH	+	OH	→	$RU12O_2$							7.51E-1
121	RU10OOH	+	OH	→	$RU10O_2$							7.51E-1
122	HOC_2H_4OOH	+	OH	→	$HOCH_2CHO$	+	OH					5.34E-1
123	RN9OOH	+	OH	→	CARB7	+	OH					6.26E-1
124	CH_3CO_3	+	NO_2	→	PAN							2.68E-1
125	PAN			→	CH_3CO_3	+	NO_2					1.51E-4
126	$HOCH_2CO_3$	+	NO_2	→	PHAN							2.68E-1
127	PHAN			→	$HOCH_2CO_3$	+	NO_2					1.51E-4
128	PAN	+	OH	→	HCHO	+	CO	+	NO_2			2.59E-3
129	PHAN	+	OH	→	HCHO	+	CO	+	NO_2			2.81E-2
130	$RU12O_2$	+	NO_2	→	RU12PAN							1.63E-2
131	RU12PAN			→	$RU12O_2$	+	NO_2					1.51E-4
132	$RU10O_2$	+	NO_2	→	MPAN							1.10E-2
133	MPAN			→	$RU10O_2$	+	NO_2					1.51E-4
134	MPAN	+	OH	→	CARB7	+	CO	+	NO_2			9.02E-2
135	RU12PAN	+	OH	→	UCARB10	+	NO_2					6.31E-1
136	NO_2	+	O_3	→	NO_3							7.65E-7

Note: * means peroxy radical summation, which is applied to the RO_2 permutation reactions.

[RO2] = [CH3O2] + [HOCH2CH2O2] + [RN9O2] + [CH3CO3] + [HOCH2CO3] + [RU14O2] + [RU12O2] + [RU10O2]

Appendix B: C++ chemistry code extracts

The Reduced Chemical Scheme (RCS) is coded using C++. Selected extracts from the chemistry code implementation are listed below.

```
//********************* For selected slower chemical species ******************//
// Chemical loss rates
LoNO=ck2*O3+2*ck3*NO+ck4*NO3+ck13*OH+ck16*HO2+ck48*CH3O2+ck49*HOCH2CH2O2
     +ck50*HOCH2CH2O2+ck51*RN9O2+ck52*CH3CO3+ck53*HOCH2CO3+ck54*RU14O2
     +ck55*RU14O2+ck56*RU12O2+ck57*RU12O2+ck58*RU10O2+ck59*RU10O2+ck60*RU10O2
     +ck61*CH3O2+ck62*HOCH2CH2O2+ck63*RN9O2+ck64*RU14O2;

LoNO2=ck14*OH+ck17*HO2+ck136*O3+ck23+ck124*CH3CO3+ck126*HOCH2CO3+ck130*RU12O2
      +ck132*RU10O2;

LoO3=ck1+ck2*NO+ck5*OH+ck9*HO2+ck31*C2H4+ck32*C2H4+ck33*C3H6+ck34*C3H6+ck36*C5H8
     +ck37*C5H8+ck94*UCARB10+ck95*UCARB10+ck99*UCARB12+ck100*UCARB12+ck136*NO2;

// Chemical production terms
PoNO=ck23*NO2+ck24*NO3+ck26*HONO;

PoNO2=ck2*NO*O3+2*ck3*NO*NO+2*ck4*NO*NO3+ck15*OH*NO3+ck16*HO2*NO+ck18*HO2NO2
      +ck19*OH*HO2NO2+ck20*OH*HONO+ck25*NO3+ck27*HNO3+ck48*CH3O2*NO
      +ck49*HOCH2CH2O2*NO+ck50*HOCH2CH2O2*NO+ck51*RN9O2*NO+ck52*CH3CO3*NO
      +ck53*HOCH2CO3*NO+ck54*RU14O2*NO+ck55*RU14O2*NO+ck56*RU12O2*NO
      +ck57*RU12O2*NO+ck58*RU10O2*NO+ck59*RU10O2*NO+ck60*RU10O2*NO+ck101*CH3NO3
      +ck102*OH*CH3NO3+ck103*OH*HOC2H4NO3+ck104*OH*RN9NO3+ck105*OH*RU14NO3
      +ck125*PAN+ck127*PHAN+ck128*OH*PAN+ck129*OH*PHAN+ck131*RU12PAN+ck133*MPAN
      +ck134*OH*MPAN+ck135*OH*RU12PAN;

PoO3=ck23*NO2+ck25*NO3;

//Update
NO= NO+(PoNO-LoNO*NO)*dtlong;

NO2= NO2+(PoNO2-LoNO2*NO2)*dtlong;

O3= O3+(PoO3-LoO3*O3)*dtlong;
//*****************************************************************************//



//********************* For selected faster chemical species ******************//
// Chemical loss rates
LoOH=ck5*O3+ck6*H2+ck7*CO+ck8*H2O2+ck10*HO2+ck13*NO+ck14*NO2+ck15*NO3
     +ck19*HO2NO2+ck20*HONO+ck21*HNO3+ck28*CH4+ck29*C2H4+ck30*C3H6
     +ck35*C5H8+ck41*HCHO+ck42*CH3CHO+ck43*CH3OH+ck44*C2H5OH+ck45*C2H5OH
     +ck46*HCOOH+ck47*CH3CO2H+ck92*CARB7+ck93*UCARB10+ck96*HOCH2CHO+ck97*CARB6
     +ck98*UCARB12+ck102*CH3NO3+ck103*HOC2H4NO3+ck104*RN9NO3+ck105*RU14NO3
     +ck115*CH3OOH+ck116*CH3OOH+ck117*CH3CO3H+ck118*HOCH2CO3H+ck119*RU14OOH
     +ck120*RU12OOH+ck121*RU10OOH+ck122*HOC2H4OOH+ck123*RN9OOH
     +ck128*PAN+ck129*PHAN+ck134*MPAN+ck135*RU12PAN;

LoHO2=ck9*O3+ck10*OH+2*ck11*HO2+2*ck12*HO2+ck16*NO+ck17*NO2
      +ck65*CH3O2+ck66*HOCH2CH2O2+ck67*RN9O2+ck68*CH3CO3+ck69*HOCH2CO3
      +ck70*RU14O2+ck71*RU12O2+ck72*RU10O2;
```

```
// Chemical production terms
PoOH=2*ck1*O3+ck9*HO2*O3+ck16*HO2*NO+2*ck22*H2O2+ck26*HONO+ck27*HNO3+ck31*O3*C2H4
     +ck33*O3*C3H6+ck36*O3*C5H8+ck94*O3*UCARB10+ck99*O3*UCARB12+ck106*CH3OOH
     +ck107*CH3CO3H+ck108*HOCH2CO3H+ck109*RU14OOH+ck110*RU14OOH+ck111*RU12OOH
     +ck112*RU10OOH+ck113*HOC2H4OOH+ck114*RN9OOH+ck116*OH*CH3OOH
     +ck119*OH*RU14OOH+ck122*OH*HOC2H4OOH+ck123*OH*RN9OOH;

PoHO2=ck5*OH*O3+ck6*OH*H2+ck7*OH*CO+ck8*OH*H2O2+ck15*OH*NO3+ck18*HO2NO2

+ck31*O3*C2H4+ck36*O3*C5H8+2*ck38*HCHO+ck40*CH3CHO+ck41*OH*HCHO+ck43*OH*CH3OH
     +ck44*OH*C2H5OH+ck46*HCOOH*OH+ck48*CH3O2*NO+ck49*HOCH2CH2O2*NO
     +ck50*HOCH2CH2O2*NO+ck51*RN9O2*NO+ck53*HOCH2CO3*NO+ck54*RU14O2*NO
     +ck55*RU14O2*NO+ck57*RU12O2*NO+ck59*RU10O2*NO+ck60*RU10O2*NO+ck73*CH3O2

+ck76*HOCH2CH2O2+ck77*RN9O2+ck79*HOCH2CO3+ck80*RU14O2+ck81*RU14O2+ck83*RU12O2
     +ck85*RU10O2+ck86*RU10O2+ck87*CARB7+2*ck88*HOCH2CHO+ck89*UCARB10+ck90*CARB6
     +ck91*UCARB12+ck92*OH*CARB7+ck101*CH3NO3+ck106*CH3OOH+ck108*HOCH2CO3H
     +ck109*RU14OOH+ck110*RU14OOH+ck111*RU12OOH+ck113*HOC2H4OOH+ck114*RN9OOH;

//Update
OH=(OH+(1.0+0.5*dtshort*LoOH)*dtshort*PoOH)/(1.0+dtshort*LoOH
  +0.5*dtshort*dtshort*LoOH*LoOH);

HO2=(HO2+(1.0+0.5*dtshort*LoHO2)*dtshort*PoHO2)/(1.0+dtshort*LoHO2
   +0.5*dtshort*dtshort*LoHO2*LoHO2);
//*********************************************************************//
```

References

ABAD, G. G., ALLEN, N. D. C., BERNATH, P. F., BOONE, C. D., MCLEOD, S. D., MANNEY, G. L., TOON, G. C., CAROUGE, C., WANG, Y., WU, S., BARKLEY, M. P., PALMER, P. I., XIAO, Y. & FU, T. M. 2011. Ethane, ethyne and carbon monoxide concentrations in the upper troposphere and lower stratosphere from ACE and GEOS-Chem: a comparison study. *Atmospheric Chemistry and Physics,* 11**,** 9927-9941.

AHMAD, K., KHARE, M. & CHAUDHRY, K. K. 2005. Wind tunnel simulation studies on dispersion at urban street canyons and intersections - a review. *Journal of Wind Engineering and Industrial Aerodynamics,* 93**,** 697-717.

ALEXANDROV, A., SAMEH, A., SIDDIQUE, Y. & ZLATEV, Z. 1997. Numerical integration of chemical ODE problems arising in air pollution models. *Environmental Modeling & Assessment,* 2**,** 365-377.

ARCISZEWSKA, C. & MCCLATCHEY, J. 2001. The importance of meteorological data for modelling air pollution using ADMS-Urban. *Meteorological Applications,* 8**,** 345-350.

ARNOLD, S. J., APSIMON, H., BARLOW, J., BELCHER, S., BELL, M., BODDY, J. W., BRITTER, R., CHENG, H., CLARK, R., COLVILE, R. N., DIMITROULOPOULOU, S., DOBRE, A., GREALLY, B., KAUR, S., KNIGHTS, A., LAWTON, T., MAKEPACE, A., MARTIN, D., NEOPHYTOU, M., NEVILLE, S., NIEUWENHUIJSEN, M., NICKLESS, G., PRICE, C., ROBINS, A., SHALLCROSS, D., SIMMONDS, P., SMALLEY, R. J., TATE, J., TOMLIN, A. S., WANG, H. & WALSH, P. 2004. Introduction to the DAPPLE Air Pollution Project. *Science of the Total Environment,* 332**,** 139-153.

ATKINSON, R. 2000. Atmospheric chemistry of VOCs and NOx. *Atmospheric Environment,* 34**,** 2063-2101.

AUGER, L. & LEGRAS, B. 2007. Chemical segregation by heterogeneous emissions. *Atmospheric Environment,* 41**,** 2303-2318.

BAIK, J.-J., KANG, Y.-S. & KIM, J.-J. 2007. Modeling reactive pollutant dispersion in an urban street canyon. *Atmospheric Environment,* 41**,** 934-949.

BAIK, J. J. & KIM, J. J. 1999. A numerical study of flow and pollutant dispersion characteristics in urban street canyons. *Journal of Applied Meteorology,* 38**,** 1576-1589.

BAIK, J. J. & KIM, J. J. 2002. On the escape of pollutants from urban street canyons. *Atmospheric Environment,* 36**,** 527-536.

BAIK, J. J., KIM, J. J. & FERNANDO, H. J. S. 2003. A CFD model for simulating urban flow and dispersion. *Journal of Applied Meteorology,* 42**,** 1636-1648.

BAIK, J. J., PARK, R. S., CHUN, H. Y. & KIM, J. J. 2000. A laboratory model of urban street-canyon flows. *Journal of Applied Meteorology,* 39**,** 1592-1600.

BAKER, J., WALKER, H. L. & CAI, X. M. 2004. A study of the dispersion and transport of reactive pollutants in and above street canyons - a large eddy simulation. *Atmospheric Environment,* 38**,** 6883-6892.

BARLOW, J. F. 2014. Progress in observing and modelling the urban boundary layer. *Urban Climate,* 10**,** 216-240.

BARLOW, J. F., DOBRE, A., SMALLEY, R. J., ARNOLD, S. J., TOMLIN, A. S. & BELCHER, S. E. 2009. Referencing of street-level flows measured during the DAPPLE 2004 campaign. *Atmospheric Environment,* 43**,** 5536-5544.

BARLOW, J. F., HARMAN, I. N. & BELCHER, S. E. 2004. Scalar fluxes from urban street canyons. Part I: Laboratory simulation. *Boundary-Layer Meteorology,* 113**,** 369-385.

BEEVERS, S. D., KITWIROON, N., WILLIAMS, M. L. & CARSLAW, D. C. 2012. One way coupling of CMAQ and a road source dispersion model for fine scale air pollution predictions. *Atmospheric Environment,* 59**,** 47-58.

BELCHER, S. E. 2005. Mixing and transport in urban areas. *Philosophical Transactions of the Royal Society a-Mathematical Physical and Engineering Sciences,* 363**,** 2947-2968.

BERKOWICZ, R. 2000. OSPM - A parameterised street pollution model. *Environmental Monitoring and Assessment,* 65**,** 323-331.

BEY, I., JACOB, D. J., YANTOSCA, R. M., LOGAN, J. A., FIELD, B. D., FIORE, A. M., LI, Q. B., LIU, H. G. Y., MICKLEY, L. J. & SCHULTZ, M. G. 2001. Global modeling of tropospheric chemistry with assimilated meteorology: Model description and evaluation. *Journal of Geophysical Research-Atmospheres,* 106**,** 23073-23095.

BLACKMAN, K., PERRET, L., SAVORY, E. & PIQUET, T. 2015. Field and wind tunnel modeling of an idealized street canyon flow. *Atmospheric Environment,* 106**,** 139-153.

BLOSS, C., WAGNER, V., JENKIN, M. E., VOLKAMER, R., BLOSS, W. J., LEE, J. D., HEARD, D. E., WIRTZ, K., MARTIN-REVIEJO, M., REA, G., WENGER, J. C. & PILLING, M. J. 2005. Development of a detailed chemical mechanism (MCMv3.1) for the atmospheric oxidation of aromatic hydrocarbons. *Atmospheric Chemistry and Physics,* 5**,** 641-664.

BLOSS, W. J. 2009. Atmospheric Chemical Processes of Importance in Cities. *In: Harrison, R. M. & Hester, R. E. (eds.) Air Quality in Urban Environments***,** Cambridge: The Royal Society of Chemistry.

BODDY, J. W. D., SMALLEY, R. J., DIXON, N. S., TATE, J. E. & TOMLIN, A. S. 2005. The spatial variability in concentrations of a traffic-related pollutant in two street canyons in York, UK - Part I: The influence of background winds. *Atmospheric Environment,* 39**,** 3147-3161.

BOULTER, P. G., BARLOW, T. J., LATHAM, S. & MCCRAE, I. S. 2009. Emission Factors 2009: Report 1 - a review of methods for determining hot exhaust emission factors for road vehicles. *TRL: Wokingham.*

BOULTER, P. G., BARLOW, T. J., S., L. & S., M. I. 2009b. Emission factors 2009: Report 1-a review of methods for determining hot exhaust emission factors for road vehicles. *TRL:Wokingham,UK.*

BOURBIA, F. & AWBI, H. B. 2004a. Building cluster and shading in urban canyon for hot dry climate - Part 1: Air and surface temperature measurements. *Renewable Energy,* 29**,** 249-262.

BOURBIA, F. & AWBI, H. B. 2004b. Building cluster and shading in urban canyon for hot dry climate Part 2: Shading simulations. *Renewable Energy,* 29**,** 291-301.

BRIGHT, V. B., BLOSS, W. J. & CAI, X. M. 2013. Urban street canyons: Coupling dynamics, chemistry and within-canyon chemical processing of emissions. *Atmospheric Environment,* 68**,** 127-142.

BRITTER, R. E. & HANNA, S. R. 2003. Flow and dispersion in urban areas. *Annual Review of Fluid Mechanics,* 35**,** 469-496.

BROWN, M. J., LAWSON JR., R. E., DECROIX, D. S. & LEE, R. L. 2000. MEAN FLOW AND TURBULENCE MEASUREMENTS AROUND A 2-D ARRAY OF BUILDINGS IN A WIND TUNNEL. *Presented at 11th Joint Conference on the Applications of Air Pollution Meteorology with the AWMA,* Long Beach, CA**,** January 9-14.

BUCKLAND, A. T. 1998. Validation of a street canyon model in two cities. *Environmental Monitoring and Assessment,* 52**,** 255-267.

CAI, X. 2012a. Effects of differential wall heating in street canyons on dispersion and ventilation characteristics of a passive scalar. *Atmospheric Environment,* 51**,** 268-277.

CAI, X. M. 2012b. Effects of Wall Heating on Flow Characteristics in a Street Canyon. *Boundary-Layer Meteorology,* 142**,** 443-467.

CAI, X. M., BARLOW, J. F. & BELCHER, S. E. 2008. Dispersion and transfer of passive scalars in and above street canyons - Large-eddy simulations. *Atmospheric Environment,* 42**,** 5885-5895.

CARPENTER, L. J., CLEMITSHAW, K. C., BURGESS, R. A., PENKETT, S. A., CAPE, J. N. & MCFADYEN, G. C. 1998. Investigation and evaluation of the NO_x/O_3 photochemical steady state. *Atmospheric Environment,* 32**,** 3353-3365.

CARSLAW, D. C. 2005. Evidence of an increasing NO2/NOX emissions ratio from road traffic emissions. *Atmospheric Environment,* 39**,** 4793-4802.

CARTER, W. P. L. 1990. A DETAILED MECHANISM FOR THE GAS-PHASE ATMOSPHERIC REACTIONS OF ORGANIC-COMPOUNDS. *Atmospheric Environment Part a-General Topics,* 24**,** 481-518.

CARTER, W. P. L. 2000b. Implementation of the SAPRC-99 chemical mechanism into the Models-3 Framework. *Report to the US Environmental Agency,* 29 January 2000.

CARTER, W. P. L. 2010. Development of a condensed SAPRC-07 chemical mechanism. *Atmospheric Environment,* 44**,** 5336-5345.

CASSIANI, M., VINUESA, J. F., GALMARINI, S. & DENBY, B. 2010. Stochastic fields method for sub-grid scale emission heterogeneity in mesoscale atmospheric dispersion models. *Atmospheric Chemistry and Physics,* 10**,** 267-277.

CATON, F., BRITTER, R. E. & DALZIEL, S. 2003. Dispersion mechanisms in a street canyon. *Atmospheric Environment,* 37**,** 693-702.

CHAN, T. L., DONG, G., LEUNG, C. W., CHEUNG, C. S. & HUNG, W. T. 2002. Validation of a two-dimensional pollutant dispersion model in an isolated street canyon. *Atmospheric Environment,* 36**,** 861-872.

CHANG, C. H. 2006. Computational fluid dynamics simulation of concentration distributions from a point source in the urban street canyons. *Journal of Aerospace Engineering,* 19**,** 80-86.

CHANG, C. H. & MERONEY, R. N. 2001. Numerical and physical modeling of bluff body flow and dispersion in urban street canyons. *Journal of Wind Engineering and Industrial Aerodynamics,* 89**,** 1325-1334.

CHEMEL, C., SOKHI, R. S., DORE, A. J., SUTTON, P., VINCENT, K. J., GRIFFITHS, S. J., HAYMAN, G. D., WRIGHT, R. D., BAGGALEY, M., HALLSWORTH, S., PRAIN, H. D. & FISHER, B. E. A. 2011. Predictions of UK Regulated Power Station Contributions to Regional Air Pollution and Deposition: A Model Comparison Exercise. *Journal of the Air & Waste Management Association,* 61**,** 1236-1245.

CHENG, W. C. & LIU, C.-H. 2011. Large-Eddy Simulation of Flow and Pollutant Transports in and Above Two-Dimensional Idealized Street Canyons. *Boundary-Layer Meteorology,* 139**,** 411-437.

CHENG, W. C., LIU, C.-H. & LEUNG, D. Y. C. 2008. Computational formulation for the evaluation of street canyon ventilation and pollutant removal performance. *Atmospheric Environment,* 42**,** 9041-9051.

CHENG, Y., LIEN, F. S., YEE, E. & SINCLAIR, R. 2003. A comparison of large Eddy simulations with a standard k-epsilon Reynolds-averaged Navier-Stokes model for the prediction of a fully developed turbulent flow over a matrix of cubes. *Journal of Wind Engineering and Industrial Aerodynamics,* 91**,** 1301-1328.

CHING, J., HERWEHE, J. & SWALL, J. 2006. On joint deterministic grid modeling and sub-grid variability conceptual framework for model evaluation. *Atmospheric Environment,* 40**,** 4935-4945.

CHRISTEN, A., VAN GORSEL, E. & VOGT, R. 2007. Coherent structures in urban roughness sublayer turbulence. *International Journal of Climatology,* 27**,** 1955-1968.

CHUNG, T. N. H. & LIU, C.-H. 2013. On the Mechanism of Air Pollutant Removal in Two-Dimensional Idealized Street Canyons: A Large-Eddy Simulation Approach. *Boundary-Layer Meteorology,* 148**,** 241-253.

COCEAL, O., THOMAS, T. G., CASTRO, I. P. & BELCHER, S. E. 2006. Mean flow and turbulence statistics over groups of urban-like cubical obstacles. *Boundary-Layer Meteorology,* 121**,** 491-519.

CONSTANTINESCU, E. M., SANDU, A. & CARMICHAEL, G. R. 2008. Modeling atmospheric chemistry and transport with dynamic adaptive resolution. *Computational Geosciences,* 12**,** 133-151.

CUI, P.-Y., LI, Z. & TAO, W.-Q. 2014. Investigation of Re-independence of turbulent flow and pollutant dispersion in urban street canyon using numerical wind tunnel (NWT) models. *International Journal of Heat and Mass Transfer,* 79**,** 176-188.

CUI, Z. Q., CAI, X. M. & BAKER, C. J. 2004. Large-eddy simulation of turbulent flow in a street canyon. *Quarterly Journal of the Royal Meteorological Society,* 130**,** 1373-1394.

CURTIS, A. R. & SWEETENHAM, W. P. 1987. FACSIMILE/CHECKMAT user's manual. *UKAEA Atomic Energy Research Establishment Computer Science and Systems Division*.

DEFRA 2008. The Air Quality Strategy for England, Scotland, Wales and Northern Ireland. Volume 1.

DEGUILLAUME, L., BEEKMANN, M. & DEROGNAT, C. 2008. Uncertainty evaluation of ozone production and its sensitivity to emission changes over the Ile-de-France region during summer periods. *Journal of Geophysical Research-Atmospheres,* 113.

DEJOAN, A., SANTIAGO, J. L., MARTILLI, A., MARTIN, F. & PINELLI, A. 2010. Comparison Between Large-Eddy Simulation and Reynolds-Averaged Navier-Stokes Computations for the MUST Field Experiment. Part II: Effects of Incident Wind Angle Deviation on the Mean Flow and Plume Dispersion. *Boundary-Layer Meteorology,* 135**,** 133-150.

DENBY, B., CASSIANI, M., DE SMET, P., DE LEEUW, F. & HORALEK, J. 2011. Sub-grid variability and its impact on European wide air quality exposure assessment. *Atmospheric Environment,* 45**,** 4220-4229.

DEPAUL, F. T. & SHEIH, C. M. 1986. MEASUREMENTS OF WIND VELOCITIES IN A STREET CANYON. *Atmospheric Environment,* 20**,** 455-459.

DERWENT, R. G., JENKIN, M. E., SAUNDERS, S. M. & PILLING, M. J. 1998. Photochemical ozone creation potentials for organic compounds in northwest Europe calculated with a master chemical mechanism. *Atmospheric Environment,* 32**,** 2429-2441.

DOBRE, A., ARNOLD, S. J., SMALLEY, R. J., BODDY, J. W. D., BARLOW, J. F., TOMLIN, A. S. & BELCHER, S. E. 2005. Flow field measurements in the proximity of an urban intersection in London, UK. *Atmospheric Environment,* 39**,** 4647-4657.

DUNKER, A. M., KOO, B. & YARWOOD, G. 2014. Sensitivity of atmospheric models to rate terms within complex chemical mechanisms. *Atmospheric Environment,* 98**,** 224-230.

DYER, C. 2015. Supreme Court tells UK government to cut nitrogen dioxide levels. *Bmj-British Medical Journal,* 350**,** h2329.

ELIASSON, I., OFFERLE, B., GRIMMOND, C. S. B. & LINDQVIST, S. 2006. Wind fields and turbulence statistics in an urban street canyon. *Atmospheric Environment,* 40**,** 1-16.

ELLER, P., SINGH, K., SANDU, A., BOWMAN, K., HENZE, D. K. & LEE, M. 2009. Implementation and evaluation of an array of chemical solvers in the Global Chemical Transport Model GEOS-Chem. *Geoscientific Model Development,* 2**,** 89-96.

EMMERSON, K. M. & EVANS, M. J. 2009. Comparison of tropospheric gas-phase chemistry schemes for use within global models. *Atmospheric Chemistry and Physics,* 9**,** 1831-1845.

EPA 1991. Guideline for regulatory application of the urban airshed model. EPA-450/4-91-013, US Environmental Protection Agency. Office of Air Quality Planning and Standards, Research Triangle Park, NC.

FENGER, J. 1999. Urban air quality. *Atmospheric Environment,* 33**,** 4877-4900.

FISHER, B., KUKKONEN, J., PIRINGER, M., ROTACH, M. W. & SCHATZMANN, M. 2006. Meteorology applied to urban air pollution problems: concepts from COST 715. *Atmospheric Chemistry and Physics,* 6**,** 555-564.

GALMARINI, S., VINUESA, J. F. & MARTILLI, A. 2008. Modeling the impact of sub-grid scale emission variability on upper-air concentration. *Atmospheric Chemistry and Physics,* 8**,** 141-158.

GARCIA-MENENDEZ, F. & ODMAN, M. T. 2011. Adaptive Grid Use in Air Quality Modeling. *Atmosphere,* 2**,** 484-509.

GARCIA-MENENDEZ, F., YANO, A., HU, Y. T. & ODMAN, M. T. 2010. An adaptive grid version of CMAQ for improving the resolution of plumes. *Atmospheric Pollution Research,* 1**,** 239-249.

GARMORY, A., KIM, I. S., BRITTER, R. E. & MASTORAKOS, E. 2009. Simulations of the dispersion of reactive pollutants in a street canyon, considering different chemical mechanisms and micromixing. *Atmospheric Environment,* 43**,** 4670-4680.

GERY, M. W., WHITTEN, G. Z., KILLUS, J. P. & DODGE, M. C. 1989. A photochemical kinetics mechanism for urban and regional scale computer modeling. *Journal of Geophysical Research,* 94**,** 12925-12956.

GRAWE, D., CAI, X.-M. & HARRISON, R. M. 2007. Large eddy simulation of shading effects on NO2 and O3 concentrations within an idealised street canyon. *Atmospheric Environment,* 41**,** 7304-7314.

GRELL, G. A., PECKHAM, S. E., SCHMITZ, R., MCKEEN, S. A., FROST, G., SKAMAROCK, W. C. & EDER, B. 2005. Fully coupled "online" chemistry within the WRF model. *Atmospheric Environment,* 39**,** 6957-6975.

GRIFFIN, R. J., DABDUB, D. & SEINFELD, J. H. 2002. Secondary organic aerosol - 1. Atmospheric chemical mechanism for production of molecular constituents. *Journal of Geophysical Research-Atmospheres,* 107.

GRIMMOND, C. S. B., KING, T. S., ROTH, M. & OKE, T. R. 1998. Aerodynamic roughness of urban areas derived from wind observations. *Boundary-Layer Meteorology,* 89**,** 1-24.

GROMKE, C. & BLOCKEN, B. 2015. Influence of avenue-trees on air quality at the urban neighborhood scale. Part I: Quality assurance studies and turbulent Schmidt number analysis for RANS CFD simulations. *Environmental Pollution,* 196**,** 214-223.

GROMKE, C. & RUCK, B. 2012. Pollutant Concentrations in Street Canyons of Different Aspect Ratio with Avenues of Trees for Various Wind Directions. *Boundary-Layer Meteorology,* 144**,** 41-64.

GRONTOFT, T. & RAYCHAUDHURI, M. R. 2004. Compilation of tables of surface deposition velocities for O-3, NO2 and SO2 to a range of indoor surfaces. *Atmospheric Environment,* 38**,** 533-544.

GROSS, A. & STOCKWELL, W. R. 2003. Comparison of the EMEP, RADM2 and RACM mechanisms. *Journal of Atmospheric Chemistry,* 44**,** 151-170.

HASSAN, A. A. & CROWTHER, J. M. 1998. Modelling of fluid flow and pollutant dispersion in a street canyon. *Environmental Monitoring and Assessment,* 52**,** 281-297.

HEARD, A. C., PILLING, M. J. & TOMLIN, A. S. 1998. Mechanism reduction techniques applied to tropospheric chemistry. *Atmospheric Environment,* 32**,** 1059-1073.

HERTEL, O., BERKOWICZ, R., CHRISTENSEN, J. & HOV, O. 1993. TEST OF 2 NUMERICAL SCHEMES FOR USE IN ATMOSPHERIC TRANSPORT-CHEMISTRY MODELS. *Atmospheric Environment Part a-General Topics,* 27**,** 2591-2611.

HESSTVEDT, E., HOV, O. & ISAKSEN, I. S. A. 1978. QUASI-STEADY-STATE APPROXIMATIONS IN AIR-POLLUTION MODELING - COMPARISON OF TWO NUMERICAL SCHEMES FOR OXIDANT PREDICTION. *International Journal of Chemical Kinetics,* 10**,** 971-994.

HILST, G. R. 1998. Segregation and chemical reaction rates in air quality models. *Atmospheric Environment,* 32**,** 3891-3895.

HOYDYSH, W. G. & DABBERDT, W. F. 1988. KINEMATICS AND DISPERSION CHARACTERISTICS OF FLOWS IN ASYMMETRIC STREET CANYONS. *Atmospheric Environment,* 22**,** 2677-2689.

HUANG, H., AKUTSU, Y., ARAI, M. & TAMURA, M. 2000. A two-dimensional air quality model in an urban street canyon: evaluation and sensitivity analysis. *Atmospheric Environment,* 34**,** 689-698.

HUQ, P., CARRILLO, A., WHITE, L. A., REDONDO, J., DHARMAVARAM, S. & HANNA, S. R. 2007. The shear layer above and in urban canopies. *Journal of Applied Meteorology and Climatology,* 46**,** 368-376.

HWANG, R.-L., LIN, T.-P. & MATZARAKIS, A. 2011. Seasonal effects of urban street shading on long-term outdoor thermal comfort. *Building and Environment,* 46**,** 863-870.

ISAKOV, V., TOUMA, J. S., BURKE, J., LOBDELL, D. T., PALMA, T., ROSENBAUM, A. & OZKAYNAK, H. 2009. Combining Regional- and Local-Scale Air Quality Models with Exposure Models for Use in Environmental Health Studies. *Journal of the Air & Waste Management Association,* 59**,** 461-472.

ITO, A., SILLMAN, S. & PENNER, J. E. 2007. Effects of additional nonmethane volatile organic compounds, organic nitrates, and direct emissions of oxygenated organic species on global tropospheric chemistry. *Journal of Geophysical Research-Atmospheres,* 112**,** doi:10.1029/2005JD006556.

JACOBSON, M. Z. 2005. *Fundamentals of Atmospheric Modeling,* New York, Cambridge University Press.

JENKIN, M. E., SAUNDERS, S. M., DERWENT, R. G. & PILLING, M. J. 1997. Construction and application of a master chemical mechanism (MCM) for modelling tropospheric chemistry. *Abstracts of Papers of the American Chemical Society,* 214**,** 116-COLL.

JENKIN, M. E., SAUNDERS, S. M., DERWENT, R. G. & PILLING, M. J. 2002. Development of a reduced speciated VOC degradation mechanism for use in ozone models. *Atmospheric Environment,* 36**,** 4725-4734.

JENKIN, M. E., SAUNDERS, S. M., WAGNER, V. & PILLING, M. J. 2003. Protocol for the development of the Master Chemical Mechanism, MCM v3 (Part B): tropospheric degradation of aromatic volatile organic compounds. *Atmospheric Chemistry and Physics,* 3**,** 181-193.

JENKIN, M. E., WATSON, L. A., UTEMBE, S. R. & SHALLCROSS, D. E. 2008. A Common Representative Intermediates (CRI) mechanism for VOC degradation. Part 1: Gas phase mechanism development. *Atmospheric Environment,* 42**,** 7185-7195.

JEONG, S. J. & ANDREWS, M. J. 2002. Application of the kappa-epsilon turbulence model to the high Reynolds number skimming flow field of an urban street canyon. *Atmospheric Environment,* 36**,** 1137-1145.

JICHA, M., POSPISIL, J. & KATOLICKY, J. 2000. Dispersion of pollutants in street canyon under traffic induced flow and turbulence. *Environmental Monitoring and Assessment,* 65**,** 343-351.

JIMENEZ, P., BALDASANO, J. M. & DABDUB, D. 2003. Comparison of photochemical mechanisms for air quality modeling. *Atmospheric Environment,* 37**,** 4179-4194.

JOHNSON, M., ISAKOV, V., TOUMA, J. S., MUKERJEE, S. & OZKAYNAK, H. 2010. Evaluation of land-use regression models used to predict air quality concentrations in an urban area. *Atmospheric Environment,* 44**,** 3660-3668.

JOHNSON, W. B., LUDWIG, F. L., DABBERDT, W. F. & ALLEN, R. J. 1973. URBAN DIFFUSION SIMULATION MODEL FOR CARBON-MONOXIDE. *Journal of the Air Pollution Control Association,* 23**,** 490-498.

KAKOSIMOS, K. E., HERTEL, O., KETZEL, M. & BERKOWICZ, R. 2010. Operational Street Pollution Model (OSPM) - a review of performed application and validation studies, and future prospects. *Environmental Chemistry,* 7**,** 485-503.

KANDA, M., MORIWAKI, R. & KASAMATSU, F. 2004. Large-eddy simulation of turbulent organized structures within and above explicitly resolved cube arrays. *Boundary-Layer Meteorology,* 112**,** 343-368.

KANG, Y.-S., BAIK, J.-J. & KIM, J.-J. 2008. Further studies of flow and reactive pollutant dispersion in a street canyon with bottom heating. *Atmospheric Environment,* 42**,** 4964-4975.

KARAMCHANDANI, P., SEIGNEUR, C., VIJAYARAGHAVAN, K. & WU, S. Y. 2002. Development and application of a state-of-the-science plume-in-grid model. *Journal of Geophysical Research-Atmospheres,* 107.

KARAMCHANDANI, P., VIJAYARAGHAVAN, K. & YARWOOD, G. 2011. Sub-Grid Scale Plume Modeling. *Atmosphere,* 2**,** 389-406.

KARAMCHANDANI, P., ZHANG, Y. & CHEN, S. Y. 2012. Development and initial application of a sub-grid scale plume treatment in a state-of-the-art online Multi-scale Air Quality and Weather Prediction Model. *Atmospheric Environment,* 63**,** 125-134.

KASTNER-KLEIN, P., BERKOWICZ, R. & PLATE, E. J. 2000. Modelling of vehicle-induced turbulence in air pollution studies for streets. *International Journal of Environment and Pollution,* 14**,** 496-507.

KASTNER-KLEIN, P., FEDOROVICH, E. & ROTACH, M. W. 2001. A wind tunnel study of organised and turbulent air motions in urban street canyons. *Journal of Wind Engineering and Industrial Aerodynamics,* 89**,** 849-861.

KASTNER-KLEIN, P. & PLATE, E. J. 1999. Wind-tunnel study of concentration fields in street canyons. *Atmospheric Environment,* 33**,** 3973-3979.

KESARKAR, A. P., DALVI, M., KAGINALKAR, A. & OJHA, A. 2007. Coupling of the Weather Research and Forecasting Model with AERMOD for pollutant dispersion modeling. A case study for PM10 dispersion over Pune, India. *Atmospheric Environment,* 41**,** 1976-1988.

KESSELMEIER, J. & STAUDT, M. 1999. Biogenic volatile organic compounds (VOC): An overview on emission, physiology and ecology. *Journal of Atmospheric Chemistry,* 33**,** 23-88.

KIKUMOTO, H. & OOKA, R. 2012. A numerical study of air pollutant dispersion with bimolecular chemical reactions in an urban street canyon using large-eddy simulation. *Atmospheric Environment,* 54**,** 456-464.

KIM, J. J. & BAIK, J. J. 2001. Urban street-canyon flows with bottom heating. *Atmospheric Environment,* 35**,** 3395-3404.

KIM, J. J. & BAIK, J. J. 2003. Effects of inflow turbulence intensity on flow and pollutant dispersion in an urban street canyon. *Journal of Wind Engineering and Industrial Aerodynamics,* 91**,** 309-329.

KIM, J. J. & BAIK, J. J. 2004. A numerical study of the effects of ambient wind direction on flow and dispersion in urban street canyons using the RNG k-epsilon turbulence model. *Atmospheric Environment,* 38**,** 3039-3048.

KIM, M. J., PARK, R. J. & KIM, J. J. 2012. Urban air quality modeling with full O-3-NOx-VOC chemistry: Implications for O-3 and PM air quality in a street canyon. *Atmospheric Environment,* 47**,** 330-340.

KOEPKE, P., GARHAMMER, M., HESS, M. & ROETH, E. P. 2010. NO2 photolysis frequencies in street canyons. *Atmospheric Chemistry and Physics,* 10**,** 7457-7466.

KOUTSOURAKIS, N., BARTZIS, J. G. & MARKATOS, N. C. 2012. Evaluation of Reynolds stress, k-epsilon and RNG k-epsilon turbulence models in street canyon

flows using various experimental datasets. *Environmental Fluid Mechanics,* 12**,** 379-403.

KOVAR-PANSKUS, A., LOUKA, P., SINI, J. F., SAVORY, E., CZECH, M., ABDELQARI, A., MESTAYER, P. G. & TOY, N. 2002a. Influence of geometry on the mean flow within urban street canyons - A comparison of wind tunnel experiments and numerical simulations. *Water, Air and Soil Pollution: Focus,* 2**,** 365-380.

KOVAR-PANSKUS, A., LOUKA, P., SINI, J. F., SAVORY, E., CZECH, M., ABDELQARI, A., MESTAYER, P. G. & TOY, N. 2002b. *Influence of geometry on the mean flow within urban street canyons - A comparison of wind tunnel experiments and numerical simulations*.

KROL, M. C., MOLEMAKER, M. J. & DE ARELLANO, J. V. G. 2000. Effects of turbulence and heterogeneous emissions on photochemically active species in the convective boundary layer. *Journal of Geophysical Research-Atmospheres,* 105**,** 6871-6884.

KUMAR, P., FENNELL, P. & BRITTER, R. 2008. Effect of wind direction and speed on the dispersion of nucleation and accumulation mode particles in an urban street canyon. *Science of the Total Environment,* 402**,** 82-94.

KUMAR, P., MORAWSKA, L., MARTANI, C., BISKOS, G., NEOPHYTOU, M., DI SABATINO, S., BELL, M., NORFORD, L. & BRITTER, R. 2015. The rise of low-cost sensing for managing air pollution in cities. *Environment International,* 75**,** 199-205.

KWAK, K. H. & BAIK, J. J. 2012. A CFD modeling study of the impacts of NOx and VOC emissions on reactive pollutant dispersion in and above a street canyon. *Atmospheric Environment,* 46**,** 71-80.

KWAK, K. H. & BAIK, J. J. 2014. Diurnal variation of NOx and ozone exchange between a street canyon and the overlying air. *Atmospheric Environment,* 86**,** 120-128.

KWAK, K. H., BAIK, J. J. & LEE, K. Y. 2013. Dispersion and photochemical evolution of reactive pollutants in street canyons. *Atmospheric Environment,* 70**,** 98-107.

LEE, J. D., LEWIS, A. C., MONKS, P. S., JACOB, M., HAMILTON, J. F., HOPKINS, J. R., WATSON, N. M., SAXTON, J. E., ENNIS, C., CARPENTER, L. J., CARSLAW, N., FLEMING, Z., BANDY, B. J., ORAM, D. E., PENKETT, S. A., SLEMR, J., NORTON, E., RICKARD, A. R., WHALLEY, L. K., HEARD, D. E., BLOSS, W. J., GRAVESTOCK, T., SMITH, S. C., STANTON, J., PILLING, M. J. & JENKIN, M. E. 2006. Ozone photochemistry and elevated isoprene during the UK heatwave of August 2003. *Atmospheric Environment,* 40**,** 7598-7613.

LEI, W., DE FOY, B., ZAVALA, M., VOLKAMER, R. & MOLINA, L. T. 2007. Characterizing ozone production in the Mexico City Metropolitan Area: a case study using a chemical transport model. *Atmospheric Chemistry and Physics,* 7**,** 1347-1366.

LI, X.-X., LEUNG, D. Y. C., LIU, C.-H. & LAM, K. M. 2008a. Physical modeling of flow field inside urban street canyons. *Journal of Applied Meteorology and Climatology,* 47**,** 2058-2067.

LI, X.-X., LIU, C.-H. & LEUNG, D. Y. C. 2008b. Large-eddy simulation of flow and pollutant dispersion in high-aspect-ratio urban street canyons with wall model. *Boundary-Layer Meteorology,* 129**,** 249-268.

LI, X. X., BRITTER, R. E., NORFORD, L. K., KOH, T. Y. & ENTEKHABI, D. 2012. Flow and Pollutant Transport in Urban Street Canyons of Different Aspect Ratios

with Ground Heating: Large-Eddy Simulation. *Boundary-Layer Meteorology,* 142**,** 289-304.

LI, X. X., LIU, C. H. & LEUNG, D. Y. C. 2009. Numerical investigation of pollutant transport characteristics inside deep urban street canyons. *Atmospheric Environment,* 43**,** 2410-2418.

LI, X. X., LIU, C. H., LEUNG, D. Y. C. & LAM, K. M. 2006. Recent progress in CFD modelling of wind field and pollutant transport in street canyons. *Atmospheric Environment,* 40**,** 5640-5658.

LIU, C.-H., CHENG, W. C., LEUNG, T. C. Y. & LEUNG, D. Y. C. 2011. On the mechanism of air pollutant re-entrainment in two-dimensional idealized street canyons. *Atmospheric Environment,* 45**,** 4763-4769.

LIU, C.-H. & LEUNG, D. Y. C. 2008. Numerical study on the ozone formation inside street canyons using a chemistry box model. *Journal of Environmental Sciences-China,* 20**,** 832-837.

LIU, C. H. & BARTH, M. C. 2002. Large-eddy simulation of flow and scalar transport in a modeled street canyon. *Journal of Applied Meteorology,* 41**,** 660-673.

LIU, C. H., BARTH, M. C. & LEUNG, D. Y. C. 2004. Large-eddy simulation of flow and pollutant transport in street canyons of different building-height-to-street-width ratios. *Journal of Applied Meteorology,* 43**,** 1410-1424.

LIU, C. H., LEUNG, D. Y. C. & BARTH, M. C. 2005. On the prediction of air and pollutant exchange rates in street canyons of different aspect ratios using large-eddy simulation. *Atmospheric Environment,* 39**,** 1567-1574.

LONGLEY, I. D., GALLAGHER, M. W., DORSEY, J. R., FLYNN, M. & BARLOW, J. F. 2004. Short-term measurements of airflow and turbulence in two street canyons in Manchester. *Atmospheric Environment,* 38**,** 69-79.

LOUGHNER, C. P., ALLEN, D. J., ZHANG, D.-L., PICKERING, K. E., DICKERSON, R. R. & LANDRY, L. 2012. Roles of Urban Tree Canopy and Buildings in Urban Heat Island Effects: Parameterization and Preliminary Results. *Journal of Applied Meteorology and Climatology,* 51**,** 1775-1793.

LOUKA, P., BELCHER, S. E. & HARRISON, R. G. 2000. Coupling between air flow in streets and the well-developed boundary layer aloft. *Atmospheric Environment,* 34**,** 2613-2621.

LOVAS, T., MASTORAKOS, E. & GOUSSIS, D. A. 2006. Reduction of the RACM scheme using computational singular perturbation analysis. *Journal of Geophysical Research-Atmospheres,* 111**,** doi:10.1029/2005JD006743.

MADALOZZO, D. M. S., BRAUN, A. L., AWRUCH, A. M. & MORSCH, I. B. 2014. Numerical simulation of pollutant dispersion in street canyons: Geometric and thermal effects. *Applied Mathematical Modelling,* 38**,** 5883-5909.

MAKAR, P. A. & POLAVARAPU, S. M. 1997. Analytic solutions for gas-phase chemical mechanism compression. *Atmospheric Environment,* 31**,** 1025-1039.

MAUERSBERGER, G. 2005. ISSA (iterative screening and structure analysis) - a new reduction method and its application to the tropospheric cloud chemical mechanism RACM/CAPRAM2.4. *Atmospheric Environment,* 39**,** 4341-4350.

MAYER, H. 1999. Air pollution in cities. *Atmospheric Environment,* 33**,** 4029-4037.

MCHUGH, C. A., CARRUTHERS, D. J. & EDMUNDS, H. A. 1997. ADMS-Urban: an air quality management system for traffic, domestic and industrial pollution. *International Journal of Environment and Pollution,* 8**,** 666-674.

MCNABOLA, A., BRODERICK, B. M. & GILL, L. W. 2009. A numerical investigation of the impact of low boundary walls on pedestrian exposure to air pollutants in urban street canyons. *Science of the Total Environment,* 407**,** 760-769.

MEAD, M. I., POPOOLA, O. A. M., STEWART, G. B., LANDSHOFF, P., CALLEJA, M., HAYES, M., BALDOVI, J. J., MCLEOD, M. W., HODGSON, T. F., DICKS, J., LEWIS, A., COHEN, J., BARON, R., SAFFELL, J. R. & JONES, R. L. 2013. The use of electrochemical sensors for monitoring urban air quality in low-cost, high-density networks. *Atmospheric Environment,* 70**,** 186-203.

MEMON, R. A., LEUNG, D. Y. C. & LIU, C.-H. 2010. Effects of building aspect ratio and wind speed on air temperatures in urban-like street canyons. *Building and Environment,* 45**,** 176-188.

MERONEY, R. N., PAVAGEAU, M., RAFAILIDIS, S. & SCHATZMANN, M. 1996. Study of line source characteristics for 2-D physical modelling of pollutant dispersion in street canyons. *Journal of Wind Engineering and Industrial Aerodynamics,* 62**,** 37-56.

MICHIOKA, T. & SATO, A. 2012. Effect of Incoming Turbulent Structure on Pollutant Removal from Two-Dimensional Street Canyon. *Boundary-Layer Meteorology,* 145**,** 469-484.

MICHIOKA, T., SATO, A., TAKIMOTO, H. & KANDA, M. 2011. Large-Eddy Simulation for the Mechanism of Pollutant Removal from a Two-Dimensional Street Canyon. *Boundary-Layer Meteorology,* 138**,** 195-213.

MUNIR, S., CHEN, H. & ROPKINS, K. 2013. Quantifying temporal trends in ground level ozone concentration in the UK. *Science of the Total Environment,* 458**,** 217-227.

MURENA, F. 2012. Monitoring and modelling carbon monoxide concentrations in a deep street canyon: application of a two-box model. *Atmospheric Pollution Research,* 3**,** 311-316.

MURENA, F., DI BENEDETTO, A., D'ONOFRIO, M. & VITIELLO, G. 2011. Mass Transfer Velocity and Momentum Vertical Exchange in Simulated Deep Street Canyons. *Boundary-Layer Meteorology,* 140**,** 125-142.

MURENA, F. & FAVALE, G. 2007. Continuous monitoring of carbon monoxide in a deep street canyon. *Atmospheric Environment,* 41**,** 2620-2629.

MURENA, F., FAVALE, G., VARDOULAKIS, S. & SOLAZZO, E. 2009. Modelling dispersion of traffic pollution in a deep street canyon: Application of CFD and operational models. *Atmospheric Environment,* 43**,** 2303-2311.

MURENA, F., GAROFALO, N. & FAVALE, G. 2008. Monitoring CO concentration at leeward and windward sides in a deep street canyon. *Atmospheric Environment,* 42**,** 8204-8210.

NAEI 2003. UK fleet composition projections. *URL: http://naei.defra.gov.uk/data/ef-transport*.

NAZRIDOUST, K. & AHMADI, G. 2006. Airflow and pollutant transport in street canyons. *Journal of Wind Engineering and Industrial Aerodynamics,* 94**,** 491-522.

NEOPHYTOU, M. K., GOUSSIS, D. A., VAN LOON, M. & MASTORAKOS, E. 2004. Reduced chemical mechanisms for atmospheric pollution using Computational Singular Perturbation analysis. *Atmospheric Environment,* 38**,** 3661-3673.

ODERBOLZ, D. C., AKSOYOGLU, S., KELLER, J., BARMPADIMOS, I., STEINBRECHER, R., SKJOTH, C. A., PLASS-DUELMER, C. & PREVOT, A. S. H. 2013. A comprehensive emission inventory of biogenic volatile organic

compounds in Europe: improved seasonality and land-cover. *Atmospheric Chemistry and Physics,* 13**,** 1689-1712.
OKE, T. R. 1987. Boundary Layer Climates. *second ed,* Methuen**,** London.
OKE, T. R. 1988. STREET DESIGN AND URBAN CANOPY LAYER CLIMATE. *Energy and Buildings,* 11**,** 103-113.
OPENFOAM 2012. http://www.openfoam.com/. Accessed May 2012.
OWEN, S. M., MACKENZIE, A. R., STEWART, H., DONOVAN, R. & HEWITT, C. N. 2003. Biogenic volatile organic compound (VOC) emission estimates from an urban tree canopy. *Ecological Applications,* 13**,** 927-938.
PARK, S.-J., KIM, J.-J., KIM, M. J., PARK, R. J. & CHEONG, H.-B. 2015. Characteristics of flow and reactive pollutant dispersion in urban street canyons. *Boundary-Layer Meteorology,* 108**,** 20-31.
PERRET, L. & SAVORY, E. 2013. Large-Scale Structures over a Single Street Canyon Immersed in an Urban-Type Boundary Layer. *Boundary-Layer Meteorology,* 148**,** 111-131.
PINHO, P. G., PIO, C. A., CARTER, W. P. L. & JENKIN, M. E. 2007. Evaluation of alpha- and beta-pinene degradation in the detailed tropospheric chemistry mechanism, MCM v3.1, using environmental chamber data. *Journal of Atmospheric Chemistry,* 57**,** 171-202.
PÖSCHL, U., VON KUHLMANN, R., POISSON, N. & CRUTZEN, P. J. 2000. Development and intercomparison of condensed isoprene oxidation mechanisms for global atmospheric modeling. *Journal of Atmospheric Chemistry,* 37**,** 29-52.
RAMAMURTHY, P., PARDYJAK, E. R. & KLEWICKI, J. C. 2007. Observations of the effects of atmospheric stability on turbulence statistics deep within an urban street canyon. *Journal of Applied Meteorology and Climatology,* 46**,** 2074-2085.
ROTACH, M. W., VOGT, R., BERNHOFER, C., BATCHVAROVA, E., CHRISTEN, A., CLAPPIER, A., FEDDERSEN, B., GRYNING, S. E., MARTUCCI, G., MAYER, H., MITEV, V., OKE, T. R., PARLOW, E., RICHNER, H., ROTH, M., ROULET, Y. A., RUFFIEUX, D., SALMOND, J. A., SCHATZMANN, M. & VOOGT, J. A. 2005. BUBBLE - An urban boundary layer meteorology project. *Theoretical and Applied Climatology,* 81**,** 231-261.
ROTH, M. 2000. Review of atmospheric turbulence over cities. *Quarterly Journal of the Royal Meteorological Society,* 126**,** 941-990.
SAHM, P., LOUKA, P., KETZEL, M., GUILLOTEAU, E. & SINI, J. F. 2002. *Intercomparison of numerical urban dispersion models - Part I: Street canyon and single building configurations*.
SAHU, L. K. 2012. Volatile organic compounds and their measurements in the troposphere. *Current Science,* 102**,** 1645-1649.
SAJANI, S. Z., SCOTTO, F., LAURIOLA, P., GALASSI, F. & MONTANARI, A. 2004. Urban air pollution monitoring and correlation properties between fixed-site stations. *Journal of the Air & Waste Management Association,* 54**,** 1236-1241.
SALIM, S. M., BUCCOLIERI, R., CHAN, A. & DI SABATINO, S. 2011a. Numerical simulation of atmospheric pollutant dispersion in an urban street canyon: Comparison between RANS and LES. *Journal of Wind Engineering and Industrial Aerodynamics,* 99**,** 103-113.
SALIM, S. M., CHEAH, S. C. & CHAN, A. 2011b. Numerical simulation of dispersion in urban street canyons with avenue-like tree plantings: Comparison between RANS and LES. *Building and Environment,* 46**,** 1735-1746.

SALIZZONI, P., MARRO, M., SOULHAC, L., GROSJEAN, N. & PERKINS, R. J. 2011. Turbulent Transfer Between Street Canyons and the Overlying Atmospheric Boundary Layer. *Boundary-Layer Meteorology,* 141**,** 393-414.

SALIZZONI, P., SOULHAC, L. & MEJEAN, P. 2009. Street canyon ventilation and atmospheric turbulence. *Atmospheric Environment,* 43**,** 5056-5067.

SANTIAGO, J. L., DEJOAN, A., MARTILLI, A., MARTIN, F. & PINELLI, A. 2010. Comparison Between Large-Eddy Simulation and Reynolds-Averaged Navier-Stokes Computations for the MUST Field Experiment. Part I: Study of the Flow for an Incident Wind Directed Perpendicularly to the Front Array of Containers. *Boundary-Layer Meteorology,* 135**,** 109-132.

SAUNDERS, S. M., JENKIN, M. E., DERWENT, R. G. & PILLING, M. J. 2003. Protocol for the development of the Master Chemical Mechanism, MCM v3 (Part A): tropospheric degradation of non-aromatic volatile organic compounds. *Atmospheric Chemistry and Physics,* 3**,** 161-180.

SCHATZMANN, M., BAECHLIN, W., EMEIS, S., KUEHLWEIN, J., LEITL, B., MUELLER, W. J., SCHAEFER, K. & SCHLUENZEN, H. 2006. Development and validation of tools for the implementation of european air quality policy in Germany (Project VALIUM). *Atmospheric Chemistry and Physics,* 6**,** 3077-3083.

SCHLICHTING, H. & GERSTEN, K. 2000. Boundary layer theory. *Springer***,** Berlin.

SEINFELD, J. H. & PANDIS, S. N. 1998. Atmospheric chemistry and physics: from air pollution to climate change. *Wiley***,** New York.

SHEN, J., WANG, X. S., LI, J. F., LI, Y. P. & ZHANG, Y. H. 2011. Evaluation and intercomparison of ozone simulations by Models-3/CMAQ and CAMx over the Pearl River Delta. *Science China-Chemistry,* 54**,** 1789-1800.

SHRESTHA, K. L., KONDO, A., KAGA, A. & INOUE, Y. 2009. High-resolution modeling and evaluation of ozone air quality of Osaka using MM5-CMAQ system. *Journal of Environmental Sciences-China,* 21**,** 782-789.

SINI, J. F., ANQUETIN, S. & MESTAYER, P. G. 1996. Pollutant dispersion and thermal effects in urban street canyons. *Atmospheric Environment,* 30**,** 2659-2677.

SMALLEY, R. J., TOMLIN, A. S., DIXON, N. S. & BODDY, J. W. D. 2008. The influence of background wind direction on the roadside turbulent velocity field within a complex urban street. *Quarterly Journal of the Royal Meteorological Society,* 134**,** 1371-1384.

SOKHI, R. S., SAN JOSE, R., KITWIROON, N., FRAGKOU, E., PEREZ, J. L. & MIDDLETON, D. R. 2006. Prediction of ozone levels in London using the MM5-CMAQ modelling system. *Environmental Modelling & Software,* 21**,** 566-576.

SOLAZZO, E. & BRITTER, R. E. 2007. Transfer processes in a simulated urban street canyon. *Boundary-Layer Meteorology,* 124**,** 43-60.

SOLAZZO, E., CAI, X. & VARDOULAKIS, S. 2008. Modelling wind flow and vehicle-induced turbulence in urban streets. *Atmospheric Environment,* 42**,** 4918-4931.

SOLAZZO, E., VARDOULAKIS, S. & CAI, X. 2011. A novel methodology for interpreting air quality measurements from urban streets using CFD modelling. *Atmospheric Environment,* 45**,** 5230-5239.

SONG, J., LEI, W., BEI, N., ZAVALA, M., DE FOY, B., VOLKAMER, R., CARDENAS, B., ZHENG, J., ZHANG, R. & MOLINA, L. T. 2010. Ozone response to emission changes: a modeling study during the MCMA-2006/MILAGRO Campaign. *Atmospheric Chemistry and Physics,* 10**,** 3827-3846.

SOULHAC, L., PERKINS, R. J. & SALIZZONI, P. 2008. Flow in a street canyon for any external wind direction. *Boundary-Layer Meteorology,* 126**,** 365-388.

SOULHAC, L. & SALIZZONI, P. 2010. Dispersion in a street canyon for a wind direction parallel to the street axis. *Journal of Wind Engineering and Industrial Aerodynamics,* 98**,** 903-910.

SRIVASTAVA, R. K., MCRAE, D. S. & ODMAN, M. T. 2000. An adaptive grid algorithm for air-quality modeling. *Journal of Computational Physics,* 165**,** 437-472.

STEIN, A. F., ISAKOV, V., GODOWITCH, J. & DRAXLER, R. R. 2007. A hybrid modeling approach to resolve pollutant concentrations in an urban area. *Atmospheric Environment,* 41**,** 9410-9426.

STOCKER, J., HOOD, C., CARRUTHERS, D. & MCHUGH, C. 2012. ADMS-Urban: developments in modelling dispersion from the city scale to the local scale. *International Journal of Environment and Pollution,* 50**,** 308-316.

STOCKWELL, W. R., KIRCHNER, F., KUHN, M. & SEEFELD, S. 1997. A new mechanism for regional atmospheric chemistry modeling. *Journal of Geophysical Research-Atmospheres,* 102**,** 25847-25879.

STOCKWELL, W. R., MIDDLETON, P., CHANG, J. S. & TANG, X. 1990. The second generation regional Acid Deposition Model chemical mechanism for regional air quality modeling. *J. Geophys. Res.,* 95**,** 16343-16367.

TARABORRELLI, D., LAWRENCE, M. G., BUTLER, T. M., SANDER, R. & LELIEVELD, J. 2009. Mainz Isoprene Mechanism 2 (MIM2): an isoprene oxidation mechanism for regional and global atmospheric modelling. *Atmospheric Chemistry and Physics,* 9**,** 2751-2777.

TIAN, S., LIANG, Z.-Y. & ZHANG, G.-B. 2009. Preliminary plan of numerical simulations of three dimensional flow-field in street canyons. *Icicta: 2009 Second International Conference on Intelligent Computation Technology and Automation, Vol Ii, Proceedings.*

TOMINAGA, Y. & STATHOPOULOS, T. 2010. Numerical simulation of dispersion around an isolated cubic building: Model evaluation of RANS and LES. *Building and Environment,* 45**,** 2231-2239.

TOMINAGA, Y. & STATHOPOULOS, T. 2011. CFD modeling of pollution dispersion in a street canyon: Comparison between LES and RANS. *Journal of Wind Engineering and Industrial Aerodynamics,* 99**,** 340-348.

TONG, N. Y. O. & LEUNG, D. Y. C. 2012. Effects of building aspect ratio, diurnal heating scenario, and wind speed on reactive pollutant dispersion in urban street canyons. *Journal of Environmental Sciences-China,* 24**,** 2091-2103.

TOUMA, J. S., ISAKOV, V., CHING, J. & SEIGNEUR, C. 2006. Air quality modeling of hazardous pollutants: Current status and future directions. *Journal of the Air & Waste Management Association,* 56**,** 547-558.

TSAI, M. Y. & CHEN, K. S. 2004. Measurements and three-dimensional modeling of air pollutant dispersion in an Urban Street Canyon. *Atmospheric Environment,* 38**,** 5911-5924.

UEHARA, K., MURAKAMI, S., OIKAWA, S. & WAKAMATSU, S. 2000. Wind tunnel experiments on how thermal stratification affects flow in and above urban street canyons. *Atmospheric Environment,* 34**,** 1553-1562.

VACHON, G., LOUKA, P., ROSANT, J. M., MESTAYER, P. G. & SINI, J. F. 2002. *Measurements of traffic-induced turbulence within a street canyon during the Nantes'99 experiment*.

VARDOULAKIS, S., FISHER, B. E. A., PERICLEOUS, K. & GONZALEZ-FLESCA, N. 2003. Modelling air quality in street canyons: a review. *Atmospheric Environment,* 37**,** 155-182.

VARDOULAKIS, S., VALIANTIS, M., MILNER, J. & APSIMON, H. 2007. Operational air pollution modelling in the UK - Street canyon applications and challenges. *Atmospheric Environment,* 41**,** 4622-4637.

VERSTEEG, H. K. & MALALASEKERA, W. 2007. An introduction to computational fluid dynamics: the finite volume method. *Pearson***,** Essex.

VERWER, J. G. & SIMPSON, D. 1995. EXPLICIT METHODS FOR STIFF ODES FROM ATMOSPHERIC CHEMISTRY. *Applied Numerical Mathematics,* 18**,** 413-430.

VERWER, J. G. & VANLOON, M. 1994. AN EVALUATION OF EXPLICIT PSEUDO-STEADY-STATE APPROXIMATION SCHEMES FOR STIFF ODE SYSTEMS FROM CHEMICAL-KINETICS. *Journal of Computational Physics,* 113**,** 347-352.

VIJAYARAGHAVAN, K., KARAMCHANDANI, P. & SEIGNEUR, C. 2006. Plume-in-grid modeling of summer air pollution in Central California. *Atmospheric Environment,* 40**,** 5097-5109.

VINUESA, J. F. & DE ARELLANO, J. V. G. 2005. Introducing effective reaction rates to account for the inefficient mixing of the convective boundary layer. *Atmospheric Environment,* 39**,** 445-461.

VOLZ-THOMAS, A., PATZ, H. W., HOUBEN, N., KONRAD, S., MIHELCIC, D., KLUPFEL, T. & PERNER, D. 2003. Inorganic trace gases and peroxy radicals during BERLIOZ at Pabstthum: An investigation of the photostationary state of NO_x and O_3. *Journal of Geophysical Research-Atmospheres,* 108.

WALTON, A. & CHENG, A. Y. S. 2002. Large-eddy simulation of pollution dispersion in an urban street canyon - Part II: idealised canyon simulation. *Atmospheric Environment,* 36**,** 3615-3627.

WALTON, A., CHENG, A. Y. S. & YEUNG, W. C. 2002. Large-eddy simulation of pollution dispersion in an urban street canyon - Part I: comparison with field data. *Atmospheric Environment,* 36**,** 3601-3613.

WATSON, L. A., SHALLCROSS, D. E., UTEMBE, S. R. & JENKIN, M. E. 2008. A Common Representative Intermediates (CRI) mechanism for VOC degradation. Part 2: Gas phase mechanism reduction. *Atmospheric Environment,* 42**,** 7196-7204.

WHITEHOUSE, L. E., TOMLIN, A. S. & PILLING, M. J. 2004. Systematic reduction of complex tropospheric chemical mechanisms, Part I: sensitivity and time-scale analyses. *Atmospheric Chemistry and Physics,* 4**,** 2025-2056.

WHO 2000. Air Quality Guidelines for Europe. *WHO Regional Publications, Europen series,* No. 91**,** Second ed.

WILLIAMS, D. E., SALMOND, J., YUNG, Y. F., AKAJI, J., WRIGHT, B., WILSON, J., HENSHAW, G. S., WELLS, D. B., DING, G., WAGNER, J., LAING, G. & IEEE 2009. *Development Of Low-Cost Ozone and Nitrogen Dioxide Measurement Instruments Suitable For Use In An Air Quality Monitoring Network*.

WOOD, E. C., HERNDON, S. C., ONASCH, T. B., KROLL, J. H., CANAGARATNA, M. R., KOLB, C. E., WORSNOP, D. R., NEUMAN, J. A., SEILA, R., ZAVALA, M. & KNIGHTON, W. B. 2009. A case study of ozone production, nitrogen oxides,

and the radical budget in Mexico City. *Atmospheric Chemistry and Physics,* 9**,** 2499-2516.

XIE, S. D., ZHANG, Y. H., LI, Q. & TANG, X. Y. 2003. Spatial distribution of traffic-related pollutant concentrations in street canyons. *Atmospheric Environment,* 37**,** 3213-3224.

XIE, X., LIU, C.-H., LEUNG, D. Y. C. & LEUNG, M. K. H. 2006. Characteristics of air exchange in a street canyon with ground heating. *Atmospheric Environment,* 40**,** 6396-6409.

XIE, X. M., HUANG, Z., WANG, J. S. & XIE, Z. 2005. The impact of solar radiation and street layout on pollutant dispersion in street canyon. *Building and Environment,* 40**,** 201-212.

XIE, X. M., WANG, J. S. & HUANG, Z. 2009. Traffic Emission Transportation in Street Canyons. *Journal of Hydrodynamics,* 21**,** 108-117.

XIE, Z. & CASTRO, I. P. 2006. LES and RANS for turbulent flow over arrays of wall-mounted obstacles. *Flow Turbulence and Combustion,* 76**,** 291-312.

YAZID, A. W. M., SIDIK, N. A. C., SALIM, S. M. & SAQR, K. M. 2014. A review on the flow structure and pollutant dispersion in urban street canyons for urban planning strategies. *Simulation-Transactions of the Society for Modeling and Simulation International,* 90**,** 892-916.

ZAVERI, R. A. & PETERS, L. K. 1999. A new lumped structure photochemical mechanism for large-scale applications. *Journal of Geophysical Research-Atmospheres,* 104**,** 30387-30415.

ZOU, B., ZHAN, F. B., WILSON, J. G. & ZENG, Y. N. 2010. Performance of AERMOD at different time scales. *Simulation Modelling Practice and Theory,* 18**,** 612-623.